Friction, Roughness and Boundary Layer Characteristics of Freshwater Biofilms in Hydraulic Conduits

Volume 1

By

Andrew F. Barton

BEng(Env)(Hons) *Deakin* MEngSc(Res) *Monash*

MIEAust, MASCE, MIAHR

Submitted in fulfilment of the requirements for the Degree of

Doctor of Philosophy, University of Tasmania, December 2006

Frontispiece

Clean and biofouled open channels

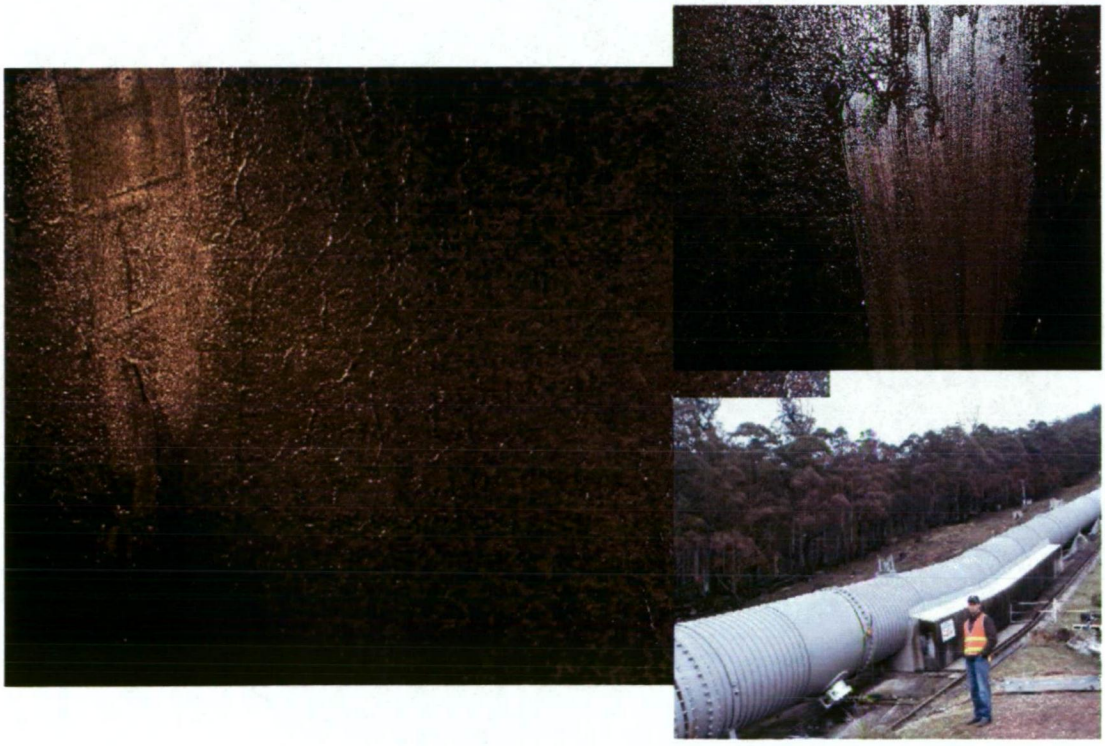

Clean and biofouled pipe walls

Statement Concerning Originality

This thesis contains no material which has been accepted for a degree or diploma by the University or any other institution, except by way of background information and duly acknowledged in the thesis, and to the best of the candidates knowledge and belief no material previously published or written by another person except where due acknowledgement is made in the text of the thesis.

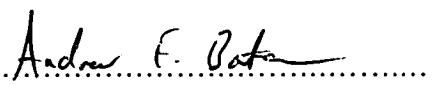

Andrew F. Barton
30/May/2007

Statement Concerning Authority Of Access

This thesis may be made available for loan and limited copying in accordance with the *Copyright Act 1968.*

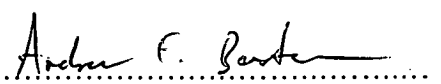

Andrew F. Barton
30/May/2007

Abstract

Hydraulic conduits are vulnerable to deterioration in their carrying capacity over time due to biofilm development and accumulation on internal surfaces. It is generally recognised that this is brought about by an increase in the effective roughness of the surface in contact with water. However, the detailed mechanisms by which biofilms affect the flow are poorly understood. This thesis presents the findings from a multi-faceted research program to investigate wall friction, roughness and boundary layer characteristics of freshwater biofilms in hydraulic conduits.

Field investigations included a series of headloss tests before and after cleaning of biofilm material from pipelines in three different hydroelectric schemes. Bacteria made up the majority of biofilm biomass in the pipelines studied. Results of the headloss testing show that improvements to hydraulic efficiency can be achieved from the removal of biofilms in the pipelines tested. Identifying the flow velocities at which hydraulically smooth, transitional or rough conditions occur was found to aid optimisation of conduit operating characteristics. The friction law for conduits roughened by biological growths did not always follow a Colebrook-White type relationship.

A purpose designed water tunnel was built and used to undertake total drag and boundary layer measurements of freshwater biofilms grown and conditioned in the field on test plates immersed in open channels. These measurements allowed a comparison between the flow behaviour of smooth and rough plates covered with biofilms with the same smooth and rough plates in their clean state. Instrumentation used in conjunction with the water tunnel included total pressure probes to determine the mean velocity boundary layer structure, a floating load-cell arrangement to measure total drag, wall tappings for static pressures, and pressure transducers. Turbulence measurements were undertaken using hot-film constant temperature anemometry, though results were inconclusive due to fouling problems with the probe. Unsteady pressure measurements were instead made to measure the turbulence character of the water tunnel working section. Observations of flow effects on biofilm behaviour were also made using the water tunnel. An increase in drag and local friction was measured for all fouled plates from their initially clean condition. Smooth plates coated with biofilms created

comparable levels of drag to rough plates coated with biofilms. The greatest relative increase in drag from the clean state was measured for a fouled smooth plate.

The increase in drag was related to the thickness and coverage of the biofilm over the test plate, and also the type of biofilm present. Low form gelatinous and filamentous algae made up the majority of biofilm biomass in these test plates. The greatest levels of drag were measured on test plates covered with filamentous biofilms. The non-uniform biofilm thickness encountered over the test plates affected the state of the boundary layer and complicated the roughness characterisation of the test plates. In all cases, the physical roughness of the biofilms was less than the effective roughness measured in the water tunnel.

An investigation into the physical character of freshwater biofilms was undertaken using data generated from close range photogrammetry. Biofilm surfaces were mapped, and the data were subsequently compared to the roughness information derived from water tunnel measurements. It was found that low form gelatinous biofilms are most amenable to close range photogrammetry studies. Filamentous biofilms lay flat when out of water, and so little value can be gained by studying their physical character in this condition. It was found that biofilms are able to change a rough surface to a physically smoother surface by growing in the gaps and valleys between roughness elements. It was also found that in some instances biofilms on coarse rough surfaces form peaks on the roughness elements. On heavily fouled test plates, the biofilm formed ripples transverse to the flow, not unlike a compliant or erodible surface. Algae made up the majority of biofilm biomass investigated in the photogrammetry studies.

This research shows that it is the uppermost surface of the biofilm exposed to the flow that most influences surface friction. This has implications for whether or not to refurbish concrete canals with a smooth coating. An appropriate smooth surface coating must also have good antifouling properties if gains in hydraulic efficiency are to be fully realised.

Acknowledgements

Special thanks to Dr Jane E. Sargison and Dr Gregory J. Walker, as supervisors for the PhD. Experimental research can be a demanding exercise, and Jane and Greg provided great mentoring and support.

An Australian government ARC large grant funded this project, with significant in-kind and financial support from Hydro Tasmania. Tony Denne, Principal Engineer (Civil) with Hydro Tasmania deserves a special mention for the considerable effort he made to drive the project.

My appreciation goes to the UTas School of Engineering, particularly Head of School Professor Frank Bullen, and the school secretaries Judy Bonsey and Mary Dixon for their assistance.

A huge thanks to Alex Buia, a fellow PhD student working on the microbiological aspects of the biofouling project. Alex and I spent many hours in the car travelling and in the field working together. We relied on each other many times to get work completed, and to develop the broader research program in general. I wish him success for the future.

Jon Osborn had the responsibility for developing much of the photogrammetric methods and equipment used in the present study. Some of this was done with the assistance of Yeon-Soung Bae, Anthony Sprent and Malcolm Grenness. The significant input from Jon to this project is gratefully acknowledged.

Leon Barmuta, Martin Line, Gustaaf Hallegraeff all provided input into the project by way of biofilm identification and general discussion on the nature of biofilms.

Michael Wallis, Craig Ludlow (Hydro Tasmania) and Michael Sylvester (no longer with Hydro Tasmania) provided support to the project, particularly in accommodating the biofouling research team for field headloss testing and conduit cleaning.

Many people made the design, construction and calibration of the water tunnel possible. I give my sincere thanks to:

- Ray LeFevre, Peter Seward and Nathan Smith (workshop technical staff).
- Dave Billings who worked on the water tunnel construction in 2004.
- Jane Sargison, who did much of the design work.
- Paul Brandner, manager of the cavitation tunnel at the Australian Maritime College, Launceston, brought much experience to the project and designed much of the working section and components.
- Greg Walker provided good oversight and input into the overall design specifications of the tunnel.
- Glenn Mayhew assisted with (non-trivial) electrical aspects during instrumentation of the tunnel.

Hydro Tasmania field staff, particularly Brian Knowles, helped greatly in the field at Tarraleah. Many station operators and field engineers (particularly Anthony McGuinness and Justin O'sullivan) gave support during the pipeline headloss testing program.

Thanks to the many honour students who worked on the biofouling project and contributed to its continuing success, including Lisa Commane, James Porter, Tim Bendall, Jessica Andrewartha and Kate Perkins.

Tim Bendall spent a substantial amount of his time on photography and the development of the photogrammetry models used in this thesis. Thanks to Tim for his effort. Jessica Andrewartha, Mark Morfew and Jon Osborn also contributed with photography and stereo plotting for the present study.

Michael Shultz of the Department of Naval Architecture and Ocean Engineering, US Naval Academy, provided assistance with the derivation of boundary layer parameters for rough walls. This is appreciated.

All of my family for their loving support, particularly my parents Samuel and Jennifer Barton. Also my brother Philip S. Barton for the frequent and motivating conversations.

Lastly, I would like to reserve my greatest thanks and love to my wife Lisa. I'm indebted to your kindness and understanding. The birth of our son Max and daughter Josephine made this PhD extra special.

Table of Contents

Volume 1

Volume 2

Publications Arising from this Thesis

(In order of appearance)

Conference Publications

Barton, A. F., Sylvester, M. W., Sargison, J. E., Walker, G. J. and Denne, A. B. (2004). "Deterioration of Conduit Efficiency Due to Biofouling." 8th National Conference on Hydraulics in Water Engineering, 13-16 July, ANA Hotel Gold Coast, Queensland, Australia, Engineers Australia (CD ROM).

Barton, A. F., Sargison, J. E., Walker, G. J., Osborn, J. E. and Brandner, P. A. (2005). "A Baseline Study of the Effect of Freshwater Biofilms in Hydraulic Conduits". Proceedings of the XXXI IAHR Congress, Seoul, Korea. (CD ROM.)

Osborne, J. E., Bae, Y.-S., Grenness, M. J., Sargison, J. E., Barton, A. F., Sprent, A. S., Walker, G. J. and Bendall, T. (2005). "Mapping Surface Biofilms to Improve the Efficiency of Water Conveyance." Spatial Sciences Congress, Melbourne, Spatial Sciences Institute of Australia, September 2005. (CD ROM)

Barton, A. F., Barmuta, L., Sargison, J., Walker, G. and Osborn, J. (2005). "Measuring the Near Wall Flow Characteristics of Freshwater Biofilms." The 44th ASL National Congress, University of Tasmania, Australian Society for Limnology. Hobart, Tasmania, Australia. (Conference abstract).

Barton, A. F., Sargison, J. E. and Walker, G. J. (2007). "Effects of Freshwater Biofilms on Flow over Rough Surfaces." IAHR 6th International Symposium on Ecohydraulics, Christchurch, New Zealand. (CD ROM).

Andrewartha, J., Sargison, J., Barton, A. F., Denne, T. and Cribbin, N. (2006). "Roughness Issues in Hydro Tasmania Water Conveyance Structures." Corrosion & Prevention 2006, "Steel & Concrete - Nothing Lasts Forever", Hotal Grand Chancellor, Hobart, Tasmania, Australia.

Technical Reports

Barton, A. F. and Sargison, J. (2003). "Wilmot Power Station - Penstock Cleaning and Power Conduit Headloss Estimation." University of Tasmania Report No. 17/03. Reviewed by, G. Walker and M. Wallis. Hobart, Tasmania, Australia.

Barton, A. F. and Sargison, J. (2004). "Tarraleah Headworks - Paint Trials in Canal No. 1 and Pond No. 1." University of Tasmania Report No. 20/04. Reviewed by, G. Walker and T. Denne. Hobart, Tasmania, Australia.

Barton, A. F. (2004). "Poatina Power Scheme - Penstock Cleaning and Power Conduit Headloss Estimation." University of Tasmania Report No. 21/04. Reviewed by, J. Sargison, G. Walker, C. Ludlow and M. Wallis. Hobart, Tasmania, Australia.

Barton, A. F. (2005). "Tarraleah Power Station - Hilltop Pipeline Cleaning and Headloss Estimation." University of Tasmania Report No. 18/03. Reviewed by, J. Sargison, G. Walker, C. Ludlow and M. Wallis. Hobart, Tasmania, Australia.

List of Figures

List of Tables

List of Abbreviations

AHD = Australian Height Datum (taken as mean sea level)

B3 = Bridge No. 3

B9 = Bridge No. 9

EPS = Extra Polymer (or polymeric) Substance

HGL = Hydraulic Grade Line

HTV = Hilltop Valve

MIV = Main Inlet Valve

P1 = Pond No. 1

RMS = Root Mean Square

SD = standard deviation

TEL = Total Energy Line

T4 = Transition No. 4

Nomenclature

A = law of the (smooth) wall constant or hot film calibration constant

B = law of the (rough) wall constant or hot film calibration constant

C = Chezy's resistance value

C_D = coefficient of drag

c_f = local coefficient of friction

D = pipe diameter

d = hot film diameter

E = Bridge voltage

f = friction factor (from Darcy-Weisbach equation)

G = velocity defect parameter

$H = \frac{\delta^*}{\theta}$ = shape factor

H_L = total headloss

h = heat transfer coefficient or height above datum

h_f = headloss due to friction

h_l = headloss due to minor losses

K = generic loss coefficient

k_s = equivalent sandgrain roughness

k_{water} = thermal conductivity of water

Nu = Nusselt number

n = Manning's roughness value

P = pressure

$Pstatic$ = static pressure (from wall tapping)

$Ptotal$ = total pressure (from Pitot or Preston tube)

p = local pressure

Δp = change in local pressure

Q = heat input (watts)

$R = \frac{A}{P}$ = hydraulic radius where A is flow area, P wetted perimeter

$\mathrm{Re}_D = \frac{\rho \bar{u} D}{\mu}$ = Reynolds number based on pipe diameter

$\mathrm{Re}_{film} = \frac{ud}{\nu}$ = Reynolds number based on hot film diameter

$\mathrm{Re}_k = \frac{k_s u^*}{\nu}$ = Reynolds roughness number

$\mathrm{Re}_{Plate} = \frac{\rho U x_{Plate}}{\mu}$ = Reynolds number based on plate length

$\mathrm{Re}_{Plug} = \frac{\rho U x_{Plug}}{\mu}$ = Reynolds number based on distance to plug

$\mathrm{Re}_x = \frac{\rho U x}{\mu}$ = Reynolds number for characteristic length, x.

$\mathrm{Re}_\delta = \frac{\rho U \delta}{\mu}$ = Reynolds number based on boundary layer thickness

$\mathrm{Re}_{\delta^*} = \frac{\rho U \delta^*}{\mu}$ = Reynolds number based on boundary layer displacement thickness

$\mathrm{Re}_\theta = \frac{\rho U \theta}{\mu}$ = Reynolds number based on boundary layer momentum thickness

Ra = arithmetic mean

Rca = cable resistance

Rp = ean to peak distance or probe resistance

Rq = RMS

Rt = valley to peak distance

Rv = mean to valley distance

T = temperature

Ta = ambient air temperature

U = free stream velocity

u = local velocity

Δu = change in local velocity

$\bar{u}$ = mean velocity

u^* = wall shear (or friction) velocity

V = volts

X, Y, Z = three dimensional distances used to describe surface topography

x = streamwise or longitudinal distance

y = distance from wall

Π = Clauser pressure gradient parameter

δ = boundary layer thickness

δ^* = boundary layer displacement thickness

δ_v = thickness of viscous sublayer

ε = origin error

θ = boundary layer momentum thickness

κ = 0.41 = von Karman constant

μ = dynamic viscosity

ν = kinematic viscosity

ρ = fluid density

τ_0 = wall shear stress

Chapter 1 Introduction

This thesis contains the details on investigations into freshwater biofouling in hydraulic conduits. This distinction of freshwater is important, as most engineering studies of biofilms have looked at marine biofouling with application to ship hulls and anti-fouling paints. This thesis is concerned with the effects of biofouling on civil engineering hydraulic structures such as pipes and open channels.

Biofouling causes significant problems in engineered structures, mostly related to reductions in efficiency. Biofilms can greatly change the wall roughness properties and associated frictional drag.

A biofilm is the layer of biological growth that attaches itself to the internal walls and forms an interface with the water. It may be any combination of bacteria, algae, protozoa, fungi, mosses and invertebrate organisms. When unwanted, the biological growth is called biofouling, and occurs wherever it is sufficiently wet. Figure 1.1 shows a severely biofouled canal. Growth is mostly on the floor with some dried on the vertical walls.

Figure 1.1: Photo showing a severely biofouled canal.

As demand for electricity increases, hydroelectric power scheme operators are struggling to find ways to increase their output without embarking on new construction ventures. Much like the economic losses incurred in the marine industry, the hydroelectric industry wishes to reduce their biofouling problems and associated costs.

Biofouling also creates safety and maintenance issues. Figure 1.2 shows the devastating result of a major canal failing due to over topping. As the fouling causes a reduction in velocity in the canal, to maintain flow rates, water levels must rise.

Figure 1.2: Failure of a canal due to overtopping and subsequent erosion of soil. Significant water and economic losses occurred due to the failure and following asset outage for repair (photo courtesy Hydro Tasmania).

There exists a large body of work on the problems of marine biofouling and this present study aims to add to the body of knowledge on freshwater biofouling with particular focus on the problem in hydraulic conduits.

The present study aims to develop a better understanding of the relationships between the physical roughness of biological fouling material and friction effects on flow. Field studies, water tunnel measurements and photogrammetric data were used in this endeavour.

Wall roughness in fluid mechanics and hydraulics is usually equated to a general hydraulic roughness or equivalent sandgrain roughness through the work of Nikuradse (1933). This may not be appropriate for a complex surface like a biofilm. A multi-disciplinary approach has been used to research the problem of biofouling, based primarily on the use of experimental measurements in a laboratory setting, the use of close range photogrammetry, field studies, and elements of microbiology, freshwater ecology, and plant science.

The thesis begins with an introduction and review of the literature relevant (Chapter 2) to this study. An overview of the biofouling problem and the complexities involved is given. Case studies of reported biofouling problems are summarised. Techniques used to measure the effects of biofouling and an introduction to the theory used in this study to measure the effect of biofilms is presented. Finally, a summary of the work especially related to the present study and where this study fits amongst is defined.

Chapter 3 provides an outline of the fieldwork conducted over the course of this study. A series of headloss test were conducted on low and high pressure pipelines and the results are presented here. Paint trials were also undertaken, and these results are shown. This chapter presents industrial applications of the freshwater biofouling problem.

Chapter 4 contains details on the series of test plates used to grow biofilms and conduct laboratory measurements. Different types were used and the strategy for their deployment and measurement is reported.

Close range photography and the photogrammetric methods to obtain surface topography data of clean and biofouled test plates are explained in Chapter 5. Results are also presented for a study of biofilm characteristics on small rough test plates.

Chapter 6 introduces the purpose built water tunnel used to conduct the detailed drag and boundary layer measurements on the series of biofouled test plates. The water tunnel and instrumentation is described, and results for the calibration of the tunnel and working section using a smooth flat plate is presented.

Chapter 7 presents results for clean and biofouled smooth painted plates. Both water tunnel measurements and photogrammetry results are presented and comparisons between the physical roughness from the photogrammetry and measured roughness from the water tunnel experiments are made.

Chapter 8 present the results from work with the rough plates, both clean and biofouled. Results are in the same format as Chapter 7 with a comparison of roughness information made.

Chapter 9 provides a discussion and synthesis of the results presented in this thesis.

Chapter 10 gives the conclusions and recommendations for the study.

References are included at the back of this thesis.

This thesis is a two-part volume. The main body of the thesis is contained in volume 1; appendices and publications arising from the thesis are included in Volume 2.

Chapter 2 Literature Review: The Problem of Biofouling in Hydraulic Conduits

2.1 Introduction

A review of the literature is presented in this chapter, with the purpose of outlining the significance of the present work.

The chapter begins with an introduction to the nature of biofouling and an overview of the problems biofouling can cause. Historical case studies of afflicted conduits are presented leading to the problem of biofouling in the Hydro Tasmania hydroelectric scheme.

An overview of methods and the important parameters to study the effects of biofilms, and the techniques used in this study are presented.

Strengths and points of difference of the current study are shown.

The chapter finishes with a summary.

2.2 The Nature of Biofouling

Biofouling is the process whereby biological material accumulates over time on a surface exposed to water or moisture. The biofouling may include any combination of bacteria, algae, protozoa, fungi, mosses and invertebrate organisms. This biological layer covering a surface is termed the biofilm.

The process of biofouling on a clean surface begins with the spontaneous adsorption of a conditioning film of organic molecules (Baire, 1980; cited in Callow, 2000). Chamberlain (1992) reports that this film may also contain inorganic materials such as

metallic oxides or very fine clay material particles (cited in Callow, 1993). Primary colonisers then follow including bacteria and algal cells or spores (Callow, 2000).

The initial colonisation of a surface may consist of just a few cells, where subsequent rapid cell division gives rise to colonies which eventually form compact biofilms (Callow, 2000).

In the process of forming the biofilm, these organisms secrete Extracellular Polymeric Substances or Slimes (EPS). The EPS binds together the microbial aggregates, and mediates cohesion as well as adhesion to surfaces (Flemming *et al.*, 1999). It is the EPS that give the biofilm its "slime" characteristics, and may ultimately constitute approximately 50% to 80% of the overall biofilm organic matter (Flemming *et al.*, 1999).

Over time, further colonisation takes place, and depending on the prevailing conditions of the fouled site, may include multi-celled organisms such as filamentous algae and mosses, invertebrates (which may or may not graze on the biofilms itself) and decomposers.

Biofilm species are in constant competition with each other to colonise surfaces suitable for biofouling. Biofilm properties may therefore change over time, and display varying characteristics, such as a varying surface topography, which will influence important hydraulic parameters such as wall roughness. The most general biofilm characteristic that will change over time is its thickness.

2.3 Overview of the Problem of Biofouling

The problem of biofouling has been extensively investigated in the marine industry due to the heavy economic and efficiency losses fouling can impose. Fouling on ship hulls, for example, cause many millions of dollars in lost revenue per year due to the costs involved from the increase in drag and therefore extra energy required to move hulls through water. The removal of fouling material and the special consideration and expense going into producing effective antifouling paints and surface coatings also adds significant costs. The problem has long been recognised (McEntree, 1915), and the

problem still exists (Jones, 1999; Schultz and Swain, 2000; Townsin, 2003; Schultz, 2004; Candries and Atlar, 2005).

The problem of biofouling in freshwater conduits, like the marine biofouling problem, manifests itself in the eventual inefficient hydraulic performance and operation. It does this through growth and accumulation of biological materials over time, which constricts the flow by reducing the cross sectional area, and changes the wall roughness properties from the original design values, which in turn affect wall friction and conduit headloss characteristics. Colebrook and White (1937-38) demonstrate that it is the increase in wall roughness rather than the reduction in pipe cross section that is largely responsible for pipe flow reduction. For a ten-fold increase in wall roughness (0.01 to 0.1 inch), Colebrook and White (1937-38) report that the corresponding reduction in area gives only a 2.6% decrease in flow capacity, whereas the wall roughness change causes a 30% reduction.

The focus of the present study is to look at the effect of biofouling as a wall roughness problem, and to develop a better understanding of the physical roughness of the biofilm and associated friction effects on the flow. This requires study of the boundary layer, and a water tunnel (see Chapter 6) was designed specifically for this purpose.

Methods to combat biofouling in potable freshwater conduits are not as well established as they are in the marine industry. Surfaces in need of protection can take the form of new or aged rough concrete, steel, or even wood staves.

The problem of marine biofouling is based on biological growth over generally smooth coated surfaces such as ship hulls. In freshwater conduits, the surfaces can be smooth or rough and is why both smooth and rough surfaces (see Chapter 4) were studied in this thesis.

To further complicate the problem, often the water can be in environmentally sensitive areas, and is required for potable water supplies precluding the use of harsh chemicals as a control method. Novel methods for control will be required.

2.4 Case Studies of Freshwater Biofouling in Hydraulic Conduits

There have been several reports of biofouling problems in conduits dating back to at least 1903 where an early example of the acknowledged effects fouling has on flow in hydraulic conduits was reported by Brown (1903-1904), who described general cases of deposits in pipes and channels. Brown included an account of the effect slimes had on the carrying ability of conduits, with the paper demonstrating a very basic level of knowledge of the problem in terms of causes and effects of slime growths. However Brown (1903-1904) did demonstrate clearly, that biological growths reduce cross section and velocity. He made the conclusion that "it is far better to prevent the growth of slime, in water favourable to it."

Minkus (1954) reports on the reduction of carrying capacity of two pipes. The carrying capacity of a newly constructed 36 inch concrete pipeline was reduced by 23% in just 5 years. Testing on a 42 inch cast iron pipe found the carrying capacity reduced by 12% in two years. It was found that slime layers of 1/32 to 1/16 of one inch in thickness were growing on the inside surface of the pipes. Minkus (1954) describes the slime as looking and feeling very smooth, though "with a little imagination there was a rougher feeling to the deposit." Minkus (1954) concluded it was the character of the biological deposits in the pipe which reduced the capacity of the pipes. From chemical analysis, the biological deposits were found to be mostly iron and manganese.

Pollard and House (1959) reports on the analysis of "an unusual deposit in a hydraulic tunnel." The analysis undertaken by Pollard and House (1959) showed that the deposit was primarily made up of metallic oxides, the most abundant of which was manganese. It was estimated by Pollard that the biological deposits were responsible for an annual power loss of 5,000,000 KWh for the power scheme in question. Adequate consideration was not given for the potential of biofouling in the conduit as it was only after excessive headloss was discovered that an investigation was undertaken.

Biofouling in conduits and the associated changes in the flow resistance started to get greater factual attention by Ackers *et al.* (1961; 1964). Ackers' *et al.* work included a brief section on the reduction of carrying capacity over time due to sliming and

deposits. Limited knowledge of biofouling growth rates were shown, with only very general values given for increases in equivalent sandgrain roughness, k_s, over time.

Changes in flow capacity due to biofouling were given some consideration by The American Society of Civil Engineers (ASCE, 1965) and the United States Department of the Interior (U.S. Bureau of Reclamation, 1965). These reports make a clear reference to the impact biological growths have on surface roughness and consequently the importance of friction factors used for design.

Further investigations followed by Bland *et al.* (1975) who experimented with six different types of pipe material, with sewage pumped through the arrangement to study the accumulation of slime. This worked complemented the earlier work of Ackers *et al.* (1961; 1964), and the work by Perkins and Gardiner (1985) who then made recommendations for roughness values to be used in the design of fouled sewers by drainage engineers.

It perhaps was not until the work of Characklis (1973) and Picologlou *et al.* (1980) that the mechanisms for energy loss by biofilms in freshwater conduits were beginning to be identified. Picologlou *et al.* (1980) introduced several concepts important to the present study. These include:

- The effect different shear forces have on the morphology and thickness of the biofilm layer;
- The visco-elastic nature of the biofilms and how this may be responsible for additional energy dissipation mechanisms,
- An increase in frictional resistance and sandgrain roughness corresponds to an increase in biofilm thickness; and importantly;
- From a design point of view, a single equivalent sand grain roughness value may be inadequate over the entire range of operating conditions.

Picologlou *et al.* (1980) completed the study on a small laboratory scale set up where the test sections used to conduct the frictional resistance measurements were between 76cm and 100cm in length with an internal diameter of 1.9cm-1.95cm.

Three authors have special significance to the present study. The papers by Brett (1980) and McFie (1973; 1976) and the Doctoral thesis by Tyler (1967) are important, as many of the same conduits investigated by them, were again investigated for this thesis.

T. Maxwell Brett (1980) presented headloss test information for a range of conduits within the Hydro Tasmania system. Brett found through a series of tests that friction factors varied greatly over time due mainly to biological growths, and established that the problems associated with biofouled conduits were significant.

McFie's paper of (1976) in particular talked about hydraulic losses in conduits due to biological growths. He discussed methods of control of biological growth by scrubbing and chemical spraying, and reported an increase in output in the Tarraleah hydro-electric system of more than 10% or 7MW as a result of cleaning. Tarraleah investigations are also shown in Chapter 3.

Tyler's (1967) studies focused on the microbial aspect of the biofouling in some of Hydro Tasmania hydraulic conduits. He identified many of the species present in the biofilms, and looked specifically at manganese depositing bacteria.

Hydro Tasmania has 27 large hydroelectric power stations, 2 mini hydro stations and 9 pump stations in its generating system, generating in excess of 2200MW of power. An extensive network of open and closed hydraulic conduits is maintained. There are 66 pipelines, with a combined approximate length of 105 kilometres. They vary in length from 49 meters to 8.93 kilometres, and in diameter between 1.2 metres to 9.1 metres. The majority are constructed from steel, though a number are concrete lined and unlined tunnel sections, and four are of wood stave construction. There are also 17 open channel systems with a combined approximate length of 114 kilometres. The majority are unlined, however, there is a significant portion that are concrete lined.

The problem of biofouling for Hydro Tasmania relates directly to the economic returns it can get from its hydropower systems. As examples, for the open channel networks to overcome the increase in wall resistance due to biofilms, increased flow depths must be maintained to sustain design flows. This increased depth means less freeboard which increases the risk of overtopping and subsequent damage to the structure and surrounding environment (as shown in Figure 1.2, Chapter 1). Alternatively, to maintain

freeboard, less water is conveyed through the structure directly reducing the revenue potential of power stations.

For the case of pipe networks, especially those leading to power stations, the increase in wall resistance results in increased headloss. A reduction in head at a power station equates to a reduction in power generating capacity, and reduced generation revenue. Chapter 3 looks at this problem in greater detail.

There is currently no systemic maintenance program in place to keep friction losses due to biofouling to an acceptable level in Hydro Tasmania's hydraulic conduit systems (Hydro Consulting, 2000). This is primarily due to a limited understanding of the effect biofouling has within the hydraulic conduit system. In general, current understanding has little theoretical emphasis and is based more on immediate costs and savings rather than longer term improvements in efficiency and benefits that result.

2.5 Typical Biofouling Forms

Biofouling deposits typically found in freshwater environments related to the present study (hydraulic conduits) are given a general description here.

The biological material responsible for freshwater fouling can be classified into two groups.

1. For closed conduit biofouling (e.g. pipes/tunnels/penstocks)
    - Predominantly bacteria (no sunlight)
2. For open conduit biofouling (e.g. open channels)
    - Predominantly algae (exposed to sunlight)

Each conduit will have its own characteristic biological fouling material, and from the types observed for the present study, may be further classified into:

A. Soft gelatinous material or slime (see Figure 2.1). This material is dominated by EPS material produced by the biological growths. Biofilms of this type will display visco-elastic properties.
B. Hard deposits, usually a product of bacterial activity (see Figure 2.2) (calcite, manganese, iron deposits and associated encrustation) or possibly invertebrates.

Often the living portion of a biofilm is only on the very outer layer in contact with the flowing water. Bacteria lay down deposits with seasonal cycles, much like growth rings on a tree.

C. Filamentous growths usually associated with algae and mosses (see Figure 2.3). Filamentous "streamers" are also created by flow over soft EPS dominated biofilms. This phenomenon is further discussed in section 2.5.2 and is described by (Stoodley *et al.*, 1988; Lewandowski and Stoodley, 1995; Stoodley *et al.*, 1999c).

Figure 2.1 shows type A fouling. Figure 2.2 shows type B fouling. Figure 2.3 shows type C fouling. This is a general classification, and any combination may be found in any conduit.

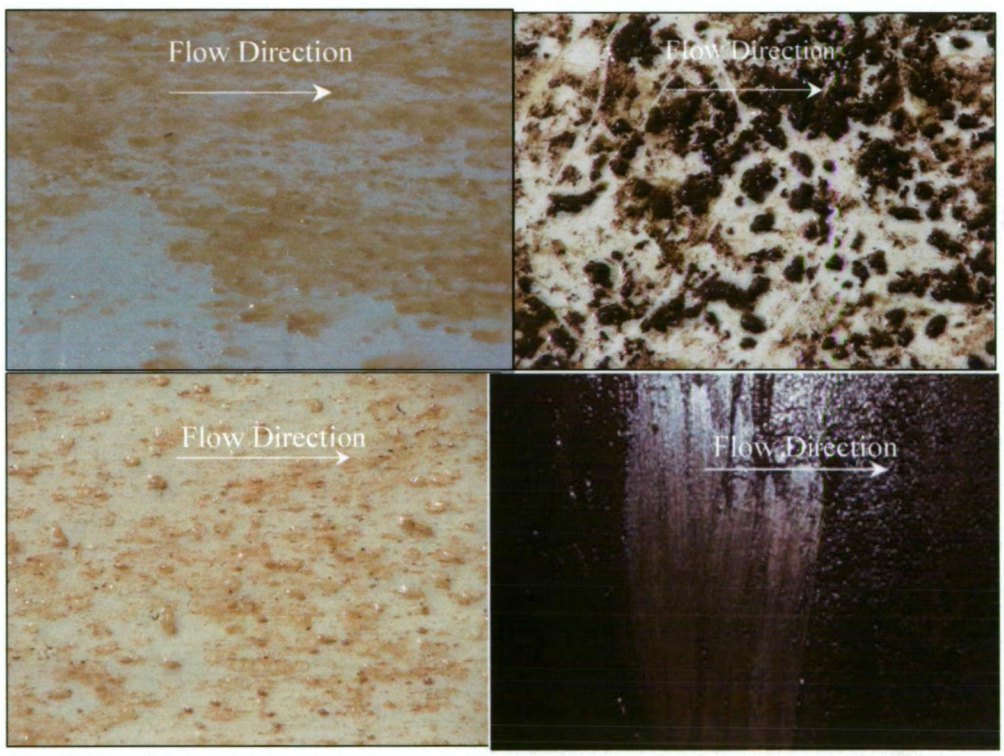

Figure 2.1: These photos shows type A biofilm deposits (soft gelatinous algae or bacterial deposits) found on smooth walls in canals and pipes.

Figure 2.2: Type B biofilm showing hard deposits found inside pipelines.

Figure 2.3: These photos shows filamentous mosses and algae (Type C biofilms) found on concrete walls in open channels.

Algal biofilms exist in sunlit areas only as they require photosynthesis for growth (obligate phototrophs). Algal biofilms display more aggressive growth patterns and are usually thicker than bacterial biofilms.

Bacterial biofilms are almost always present in any environment; however, bacterial biofilms dominate in closed pipe systems such as penstocks as there is no sunlight for algae growth (strictly speaking some species of cyanobacteria (blue-green algae) can exist in the absence of sunlight given the right nutrients). Most bacteria found in pipelines are organochemotrophs, meaning they use chemical nutrients as their prime energy source. Commonly, as is shown in Chapter 3 and the reviewed literature, iron and manganese reducing bacteria are dominant.

2.5.1 Biofilms as an Engineering Roughness

Biofilms differ greatly from typical engineering materials such as concrete or steel. The usual methods for dealing with friction in pipelines are by using the Darcy-Weisbach equation (Darcy, 1857) and the Moody Diagram (Moody, 1944). The internal surface of pipes is usually described with a one dimensional roughness parameter such as an equivalent sandgrain roughness (Nikuradse, 1933). The Colebrook-White equation is normally used to relate the friction factor, f, and equivalent sandgrain roughness, k_s, (Colebrook and White, 1937).

For open channels, Manning's equation (Manning, 1889) is most commonly used to evaluate a roughness value for design using the Manning's "n" resistance value. Chezy's equation (Chezy, 1775) and resistance coefficients are also used by some practitioners.

These methods use one dimensional and empirical information in the prediction of the surface friction and roughness character, and is based mostly on engineered materials such as steel, concrete, PVC's and other man-made surfaces such as earth lined channels.

However as seen in Figure 2.4, the surface topography of a biofilm (in contact with the water) is typically uneven. Moreover, the topography may also change with time as the

biofilm matures from a combination of growth and sloughing (removal by fluid shear) and other factors. Nikora *et al.* (2004), for example, discuss the thinning of the "canopy" or biofilm layer in higher flows due to shear forces. This is also reported by Stoodley *et al.* (1999c). Having such a dynamic surface complicates its characterisation.

In the case of some biofilms, particularly filamentous growths, surface topography constantly changes as the submerged filaments (or streamers) move about in the flow.

These roughness types impart different roughness effects on the flow through different energy dissipation mechanisms.

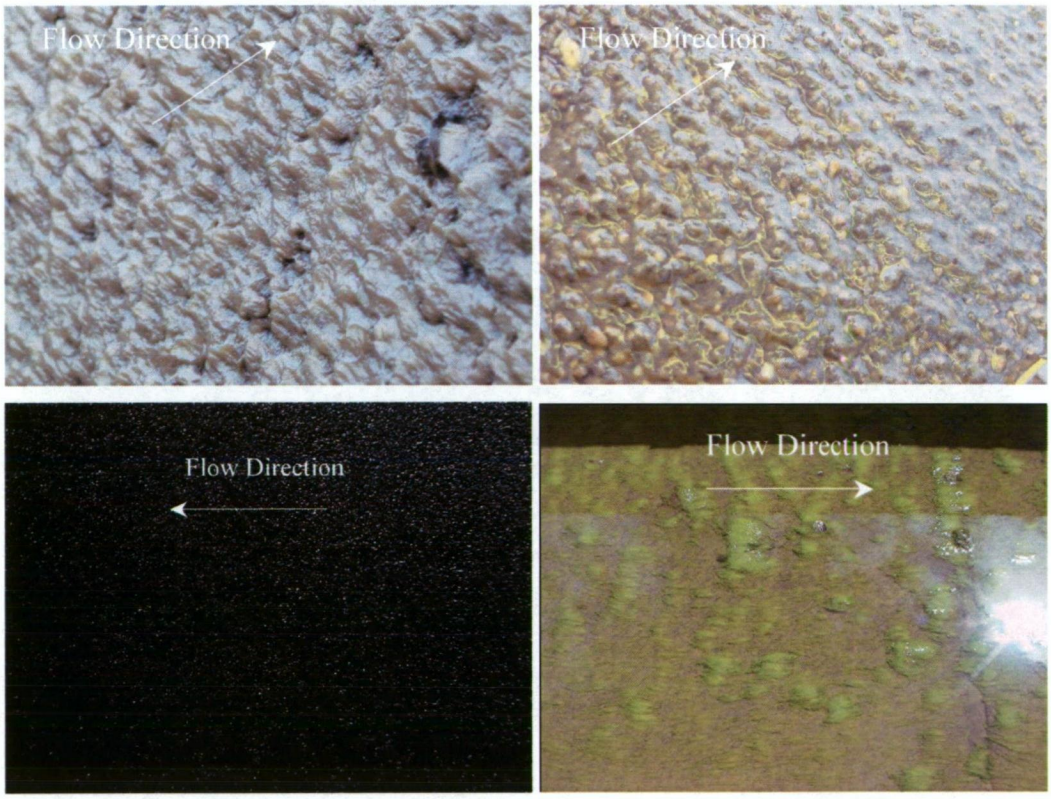

Figure 2.4: The surface topography of biofilms can take various shapes.

Studies have been conducted investigating the behaviour of biofilms in moving water (Stoodley *et al.*, 1988; Schultz, 1999; Stoodley *et al.*, 1999c; Schultz, 2000; Stoodley *et al.*, 2001). The most significant finding has been that biofilms have the capacity to move and gyrate in the flow, most unlike the surfaces on which f, k_s, and n are historically based and used. This may make the use of wall roughness parameters used in typical engineering calculations insufficient when considering the effects of biofilms.

Another significant aspect is that the surface characteristics biofilms display is dependant on the biofilm species present, and the prevailing flow conditions through the conduit, in terms of both the near wall flow and nutrient sources. This means the environment in which the biofilm grows must also be well understood. For example the flow boundary layer in an aquatic environment is able to cause limiting of nutrients (Liehr *et al.*, 1989), affecting biofilm development.

The detail in this is that no two conduits will be exactly the same. Indeed, two points in the one conduit may not be exactly the same. How this variability can be accounted for in conduit design and maintenance is a target for biofilm research.

2.5.2 Biofilm Visco-Elasticity

The EPS material which binds and attaches biofilms to the surface has been established to be visco-elastic (Zelver, 1979; Picologlou *et al.*, 1980; Stoodley *et al.*, 1999c), meaning they display both viscous and elastic properties. Visco-elastic (from viscous – fluid, and elastic – solid) behaviour is considered unique, and is something that can not be easily related back to the sand grain roughness of Nikuradse (1933) or other engineering roughness parameters based on geometric similarity.

A further consequence of the EPS material of biofilms is that filaments may form. Stoodley (1999c) describes the EPS as having extensions forced by the flow regime into a "streamer" which then extends into the flow and displays similar properties to a filamentous component. Towler (2004) and Stoodley *et al.* (1988; 1999c) have done some work on investigating creep and movement of biofilms to further understand the visco-elastic behaviour. The rheology of biofilms and biofilm structure is thought to play a significant role in energy loses in conduits. Stoodley *et al.* (1999c) concludes this is because of the visco-elastic nature of biofilms.

The most significant finding of this visco-elastic nature, and filamentous streamer formation, is that the roughness effects of the biofilm may be larger than the physical roughness height may otherwise suggest, using current engineering methods such as sandgrain height (Picologlou *et al.*, 1980; Schultz, 1999; Schultz, 2000). This finding is

the prime reason for the present study, which is aimed at developing a better understanding between physical and measured roughness.

How to best characterise the surface roughness of biofilms, therefore, is not straight forward, and there may need to be qualitative descriptions in addition to quantitative measurements in texture and physical height. This study uses close range photogrammetry and water tunnel measurements to investigate this.

2.6 Methods of Control and Management

It is worth summarising the range of methods used to clean biofouling material from conduits to appreciate the considerable effort and expense put into the control of freshwater fouling. The most common method is mechanical scrubbing and removal. Figure 2.5 and 2.6 shows various brushing techniques to scrub biofilms off canal walls.

Figure 2.5: Tractor mounted brushes scrubbing the wall. The photo on the left clearly shows the clean section of canal behind the brush

Figure 2.6: A rotating wire brush is used here to remove biofouling material.

Another method used is very high-pressure water spray. Figure 2.7 shows a spray rig mounted in a half pipe for demonstration purposes. The high-pressure spray is seen shooting of to the top left hand side of the photo. High-pressure sprays were successfully used when cleaning pipelines for the present study, with results show in Chapter 3.

Figure 2.7: Spray arrangement in operation.

Other reported techniques have been the chemical control of slimes including the use of "slimicides" (McFie, 1956; Characklis, 1973), and allowing air to pass through pipes and dry out the biofouling material (pers. com. Denne, 2005), to be later flushed out when the conduit returns to service.

Surface coatings (paints) can be used to control or inhibit biofilm growth either by control of surface properties, biocidal properties or a combination of these. Based on the success of antifouling surface coatings used in the marine industry, trials of different coatings were undertaken as part of the present study and are presented in Chapter 3. Figure 2.8 shows an example of a refurbished canal. A coating was used here to both restore the canal to improve its structural integrity, and also to improve the hydraulic performance, and retard the growth of biological material. Only non-toxic paints were trialled in the present study. These coatings (and the associated surface preparation) create a very smooth surface that inhibits biofilm growth by preventing initital colonisation of the surface.

Figure 2.8: A refurbished canal with a very smooth cementitous surface coating.

Plugs, or pigs as they are sometimes known, have also been used for cleaning pipelines. This is usually based on the use of an inflatable balloon type arrangement where the pig forms a tight fit in the pipe, is pulled through the pipe, and consequently cleans material from the pipe wall. This is a different form of scrubbing.

2.7 Measuring the Effects of Biofilms

The impact biofouling has on the deterioration of hydraulic efficiency has not been frequently studied. Previous findings have been derived mostly from field measurements and observations of conduits subject to biofouling, for example by Brett (1980) and Pollard and House (1959). Though these types of studies are useful to gain an overall understanding of the problem of biofouling in a pipeline, detailed near wall measurements are also required to further current understanding of the problem. This is not generally feasible in the field. Both approaches are used in the present study, with field studies presented in Chapter 3, and detailed boundary layer studies presented in Chapters 6, 7 and 8.

Schultz (1998; 1999; 2000) and Schultz and Swain (2000) contain probably the best contemporary examples of detailed boundary layer studies of flow over biofilms. Schultz used a recirculating water tunnel to undertake his measurements (like the present study), and found that biofilms had a significant impact on the velocity structure of the turbulent boundary layer, dependent mostly on biofilm thickness and morphology. Schultz's work is referenced throughout this thesis for comparison with results.

Schultz (1998) studied three fouled test plates, all on a smooth surfaces. This is because Schultz was interested in marine fouling of smooth ship hulls. The present study uses a recirculating water tunnel to look at clean smooth and fouled smooth plates, and clean rough and fouled rough plates. This is because freshwater biofouling occurs on smooth and rough surfaces.

Detailed measurement of biofilm surfaces is not common due to the biofilm being fragile and easily moved or damaged. For example Schultz (1998) used a wet film thickness gauge to obtain the mean thickness of the biofilm, a tool used to measure the

thickness of paint coatings while still wet. This would have disturbed the biofilm at locations where the gauge was used.

Lewkowicz and Das (1985) completed detailed wind tunnel measurements looking at turbulent boundary layers over rough surfaces, including a rough surface overlaid with a large number of deformable nylon tufts. These nylon tufts were not visco-elastic like biofilms, but were nonetheless used to simulate marine biofouling. Lewkowicz and Das (1985) found that significant changes in the boundary layer were brought about by the addition of the nylon tufts, most noticeably the physical growth of the boundary layer, and changes in wall friction.

Other studies on skin friction due to biofouling have mostly come from marine problems and ship hulls (see for example Lewthwaite *et al.*, 1985; see for example Haslbeck and Bohlander, 1992). These studies lack the detailed boundary layer work of Schultz (1998), Lewkowicz and Das (1985) or the present study.

It is worth noting the work of Candries (2001; 2003; 2005) who has produced work using similar methods of the present study, though with more focus on the antifouling paints rather than the biofouling itself. Candries undertook surface roughness measurements using a hull roughness analyser to compare with his laboratory measurements, much in the same way the present study use independent surface roughness data from photogrammetry to compare to water tunnel measurements.

Groenenboom (2000) studied the frictional resistance due to biofilms of flow in pipelines. No detailed boundary layer investigations were completed, only general friction studies, with no measurements of biofilm roughness. This work did support the notion of a visco-elastic biofilm causing frictional losses.

Stoodley *et al.* (1988; 1999a; 1999b; 1999c; 2001) undertook many studies looking at biofilm characteristics under laminar and turbulent flow regimes. These experiments were conducted in very small-scale laboratory set ups using flow cells measuring only 200mm in length and 3mm by 3mm square in section. Tests were conducted at very low Reynolds numbers, and were more for a microbiological than engineering perspective. Boundary layer measurements were not completed with these studies, and roughness measurements were simple thicknesses of the biofilm.

The very small size of these experiments by Stoodley *et al.* (1988; 1999a; 1999b; 1999c; 2001) brings scaling issues and relevance to large scale problems in question. However, the results have widely supported the phenomena of the visco-elastic nature of biofilms, the formation of streamers from EPS material, and insight into the influence of nutrients on biofilm development.

It has been speculated that longitudinal movement, or creep, of biofilms within conduits is a source of energy dissipation, much in the same way Brauer (1963) investigated longitudinal movement of asphalt in the internal surface of a pipeline. It was concluded by Picologlou *et al.* (1980) that this type of energy dissipation is not likely for a biofouled system, and that more likely forms of energy dissipation mechanisms are:

- Viscous dissipation by biofilms from an oscillatory response to turbulent flow.
- Increased dissipation due to increased surface roughness.
- Pressure drop due to conduit constriction.

It was previously stated in section 2.3 that pipe constriction accounts only for a small reduction in conduit capacity compared to wall roughness effects, and so this is not investigated in the present study.

The oscillatory response of biofilms from turbulent flow was concluded by Picologlou *et al.* (1980) to be due to the visco-elastic nature of the biofilm which agrees with work by Stoodley *et al.* (1988). This phenomenon was clearly observed in the present study, and is discussed in Chapter 7 and 8. A CD is attached in Appendix A of this thesis which shows some video footage of biofilms in motion.

Increased energy dissipation due to increased surface roughness effects by biofilm is a widely held view (Picologlou *et al.*, 1980; Schultz, 1999; Schultz, 2000), and is also associated with a general increase in biofilm thickness. The present study aims to better quantify biofilm roughness by using close range photogrammetry to characterise biofilm growths, measure its thickness, analysis the biofilm surface for statistical and roughness information. These results are compared with water tunnel measurements of the same biofilms.

In summary, five features make the present study unique and significant. They are:

1. The present study investigates freshwater biofilms.
2. The focus of the present study is for hydraulic conduits, not marine surfaces such as ship hulls.
3. The present study uses conditioned biofilms grown in flowing water in large conduits rather than biofilms grown in still water as for Shultz (1998) or in very small laboratory glass tubes and flumes as for Stoodley *et al.* (1988) or Picologlou *et al.* (1980).
4. A comprehensive suite of laboratory measurements is used to determine the friction and roughness properties of biofilms, and the effect these have on flow.
5. A new and innovative method to obtain information on the surface character of the biofilm without interfering with the biofilm itself.

2.8 Important Concepts on Flow Boundary Layers, Wall Roughness and Drag

2.8.1 The Boundary Layer

It is well established that skin friction is influenced by wall surface roughness, which in turn can be related to boundary layer theory (see Schlichting, 1979 for example). The problem of biofouling occurs at the wall, and therefore, boundary layer studies are required to assist in the understanding the effects of biofilms.

For a smooth wall, the mean flow velocity profile for a turbulent boundary layer is usually described by the log-law of Equation 2.1 or the power law of Equation 2.2. Here, $\kappa \approx 0.41$ and $A \approx 5.0$ respectively for a hydraulically smooth wall (Streeter and Wylie, 1986). For the power law, n is usually taken as 7, giving the $1/7^{th}$ power law. δ, is the boundary layer thickness. Equation 2.1 is particularly useful because the wall shear velocity, u^*, can be used to describe the local friction properties, where $u^* = \sqrt{\frac{\tau_o}{\rho}}$

(where τ_o is the fluid shear at the wall).

$$\frac{u}{u^*} = \frac{1}{\kappa} \ln \frac{yu^*}{\nu} + A \qquad \text{Equation 2.1}$$

$$\frac{u}{U} = \left(\frac{y}{\delta}\right)^{\frac{1}{n}} \qquad \text{Equation 2.2}$$

Chapter 6 describes the method used in the present study to find u^* for smooth walls.

For a rough wall, the boundary conditions become much more complex. Roughness elements cause greater turbulence and fluid mixing in the boundary layer (Schlichting, 1979) than smooth boundaries, and therefore adds significantly to flow resistance. This is a major area of research (summarised well by Rouse, 1965; and Yen, 2002), of which the problem of biofouling is a part.

The determination of u^* is more difficult for rough walls (using Equation 2.1), and introduces two additional variables; the roughness function, $\Delta u^+ = \frac{\Delta u}{u^*}$ (which describes the downward velocity shift from the corresponding smooth wall profile, where Δu is a change in velocity), and a change in wall origin, ε, some distance below the crests of the roughness elements (Perry *et al.*, 1969). Chapter 7 describes the method used in the present study to determine u^*, and consequently the determination of Δu^+ and ε.

For a rough wall, Equation 2.1 can be expressed as Equation 2.3, where ΔB is the vertical axis intercept, shifted downward by the amount Δu^+ due to wall roughness effects.

$$\frac{u}{u^*} = \frac{1}{\kappa} \ln \frac{(y+\varepsilon)u^*}{\nu} + A - \Delta B \qquad \text{Equation 2.3}$$

Surface roughness effects are usually classified into three types, depending on the flow conditions, and can be measured by the ratio of physical roughness height, k, to the thickness of the viscous sublayer, δ_v. Where $\delta_v = \frac{\nu}{u^*}$ and ν is the kinematic viscosity.

When the roughness Reynolds number, $\mathrm{Re}_k = \frac{ku^*}{\nu}$, is approximately < 5, roughness elements are totally submerged in the viscous sublayer, and the conduit may be considered hydraulically smooth, where friction is a function of Reynolds number only.

In the transitional or intermediate regime at $5 < \mathrm{Re}_k < 60$, friction is dependant on both Reynolds number and roughness, as the roughness elements are only partly submerged in the viscous sublayer.

When Re_k is approximately > 60, roughness elements project above the viscous sublayer and the conduit may be considered hydraulically rough (White, 2006). It should be noted that some use a value for the hydraulically rough condition closer to $\mathrm{Re}_k = 70$ or even $\mathrm{Re}_k = 80$. For fully rough conditions, form drag dominates and effects of roughness induced flow separation and eddy shedding completely overwhelms the viscous effect, and there is no longer a Reynolds number dependency.

Figure 2.9 graphically presents these three conditions.

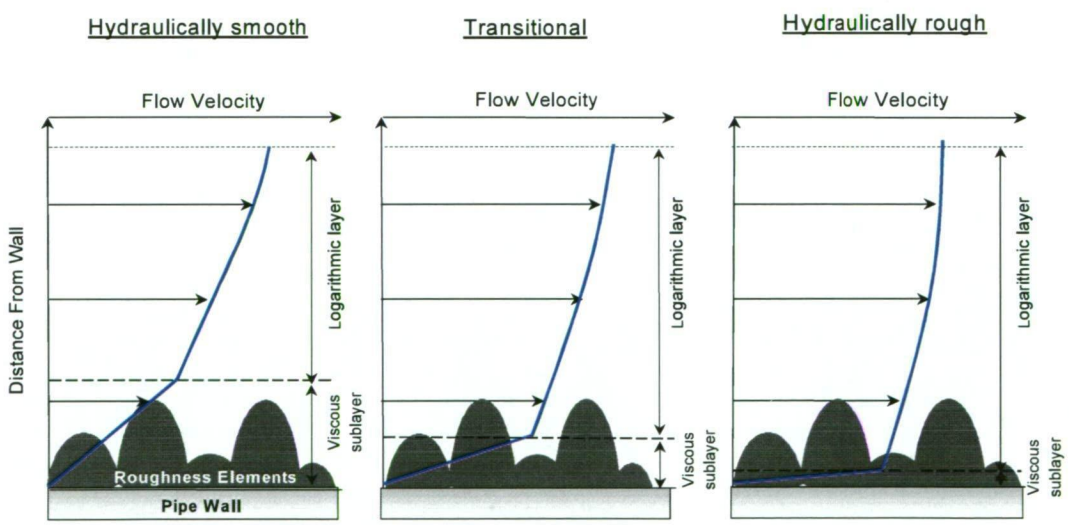

Figure 2.9: Hydraulically rough behaviour.

An alternative way to represent a rough wall boundary layer is to replace the dimensionless term, $\frac{yu^*}{\nu}$, of the smooth wall, with a roughness height, k_s, called the equivalent sandgrain roughness of Nikuradse (1933). The resultant form of the mean

velocity profile then becomes Equation 2.4, where typically $B \approx 8.5$ (Streeter and Wylie, 1986).

$$\frac{u}{u^*} = \frac{1}{\kappa} \ln\left(\frac{y+\varepsilon}{k_s}\right) + B \qquad \text{Equation 2.4}$$

The roughness height, k_s, in Equation 2.4 has been shown to be a useful approximation for rough surfaces with geometrically similar roughness elements (like that of the uniform sandgrain roughness. Surfaces with characteristics other than a sandgrain type roughness may not be reliably represented by k_s in Equation 2.4. The roughness function, Δu^+, accommodated for in Equation 2.3 is therefore particularly important when considering the roughness characteristics of non-uniform surfaces, and appropriate attention is devoted to this in the present study for biofilm covered surfaces.

A number of relationships may exist between roughness and its effect on flow. The studies by Nikuradse (1933) found that the ratio of roughness height to pipe diameter, for uniform type roughness k_s, is a good approximation. Morris (1955) suggested that the distance between roughness elements can provide a useful measure of roughness effects. Many other studies have investigated useful length scales to characterise roughness effects (Hama, 1954; Perry *et al.*, 1969; Ligrani, 1986; Krogstad *et al.*, 1992).

In summary, there is no universal length scale to characterise a range of roughness effects, especially so for non-uniform roughness. However, better approximations can be obtained after detailed studies measure the roughness effects. There are few of these types of studies investigating biofilm, and this study aims to add to the current body of knowledge in this area.

From a practical perspective, Young (1992), Gordon *et al.* (2004), Carling (1992) and Davis and Barmuta (1989) state that surface roughness has an important role to play in the distribution and abundance of stream organisms. This would include biofilms on conduit walls. Chapter 4 proposes a number of scenarios where biofilms may change the physical surface character of a wall, either smooth or rough. Better knowledge of how and where biofilms grow is important in understanding the roughness effects of biofilms.

2.8.2 Measurement of Drag Due to Friction

Surface roughness information can also be derived from drag measurements of a flat plate. For the present study all measurements were undertaken on flat plates with mild adverse pressure gradients. Chapter 6 describes the water tunnel working section where measurements for the present study were undertaken.

Winter (1977) describes several techniques available for the measurement of skin friction in turbulent boundary layers, one of which has been adopted for the present study. The direct force measurement of drag on a test plate by the use of a force balance system. The drag rig used is described in Chapter 6. The basic drag equation for a flat plate can be described by Equation 2.5 (Schlichting, 1979), where C_D is the coefficient of drag for the test plate (where the plate is parallel with the flowing water), ρ is the water density, b is the plate width, l is the plate length, g is the gravitational acceleration and U is the bulk flow mean velocity.

$$Drag = C_D \rho b l \frac{U^2}{2g} \qquad \text{Equation 2.5}$$

For a hydraulically smooth plate Equation 2.6 can be used to find the drag coefficient

$$C_D = \frac{0.074}{\mathrm{Re}_l^{\frac{1}{5}}} \qquad \text{Equation 2.6}$$

For a hydraulically rough plate, a k_s roughness value can also be used to describe the drag coefficient (Schlichting, 1979) as shown in Equation 2.7.

$$C_D = \left(1.89 + 1.62 \log \frac{l}{k_s}\right)^{-2.5} \qquad \text{Equation 2.7}$$

Various corrections and other considerations are important for the measurement of total drag on test plates. These are described in Chapters 6, 7 and 8.

With the use of both boundary layer mean velocity profiles and total drag measurements, skin friction and roughness characteristics were determined from a range a biofouled test plates. These measurements complemented the results from the surface characterisations using close range photogrammetry. The approach used in the present study to research the biofouling problem provides multiple data sets to compare. This was considered essential to successfully investigate the problem of freshwater biofouling in hydraulic conduits.

2.8.3 Roughness Characterisation of Biofilms

Close range photogrammetry has been used in this study to obtain the surface character of clean and biofouled surfaces. Roughness parameters and statistical moments were derived from this data for analysis and comparison with water tunnel measurements. More detail is provided on this in Chapter 5.

The diversity of the surface character of biofilms has been shown in section 2.5.1. As such, other information beyond roughness height and spacing may be useful in the roughness characterisation of biofilms. Qualitative features such as texture, or percent coverage of biofilm over an area may also be important to infer relative effects.

Previous studies have been limited mostly to mean thickness, standard deviations of the mean, and local observations of roughness height. Schultz's (1998) use of a wet film thickness gauge used to obtain basic biofilm thickness information has been mentioned previously. Resolution of this gauge was between 25 and 127 microns depending on the thickness of the film. Schultz reports no detailed method to obtain the biofilm thickness data, other than taking 60 samples at the forward, middle and rear section of the test plates. A more methodical approach is probably required.

Picologlou *et al.* (1980) also measured biofilm thickness. He did this not directly, but rather by estimating biofilm volume and dividing by the surface area the biofilm was attached to. This did not produce much in the way of roughness information. These measurements were also made in very small scale laboratory setting, limiting full scale application understanding of what was found.

It is typical to measure angles of deformation, and the length of roughness elements for studies of flexible roughness (Lewkowicz and Das, 1985; Lopez and Garcia, 2001). Microbiological experiments involving biofilms have looked at biofilms from this perspective including primarily those studies by Stoodley *et al.* (1988; 1999a; 1999c; 2001). Stoodley *et al.* has measured filament length, deformation properties, attachment and detachment characteristics, and oscillation characteristics of biofilms. However, this work has been put in only a limited context for boundary layer type flows and other engineering type problems.

The present study was limited to the proving of a new technique for the measurement of stationary surfaces, although the method could be extended to in situ measurement with further development. Chapters 5 and 9 provide more discussion on this.

Much can be improved on the methods to obtain surface data from biofilms, and the methods to process the data for appropriate roughness information. Half the challenge for such unfamiliar surfaces as biofilms, seems to be knowing what to measure, not just how to measure it. The photogrammetric method used in the present study is novel; has previously been shown to have high potential by Mitchell *et al.* (1999) and Grenness *et al.* (2005); and the production of three-dimensional surface data, at sub millimetre resolution, allows better quantification of roughness height and texture. Digital methods allow for the production of height information for surface areas fast and reliably. This forms the basis of obtaining more useful information on biofilms surfaces than has previously been available, making this study a leap forward in this regard.

2.9 Chapter Summary

The complexity of the biofouling process and associated problems has been explained in this chapter. Biofilms are very different to standard engineering materials primarily due to their varying surface topography, visco-elastic properties and sometimes filamentous components.

Past studies have been useful, but limited in quantifying the effects biofilms have in practical applications. Over time, more emphasis has been placed on the significance

biological material has on the efficiency of hydraulic conduits. Yet there is no definitive method to derive appropriate friction or roughness values for the design of pipes or open channels subject to biofouling. Nor are there any prescriptive measures to control biofouling in hydraulic conduits.

This study aims to find a better understanding of the relation between physical roughness of biofilms and effects of flow, and investigate the mechanisms of energy loss. A purpose built water tunnel has been used to obtain boundary layer and total drag information from biofouled test plates. And an innovative method to acquire surface roughness data by using close range photogrammetry has been utilised which gives greater flexibility than previous work. This research approach has been complemented with results from headloss tests on large hydroelectric pipelines. All biofilms studied in this thesis were conditioned biofilms, grown in flowing freshwater hydraulic conduits, again separating the present study from those completed previously.

Chapter 3 Field Headloss Studies and Paint Trials

3.1 Introduction

This chapter describes fieldwork carried out in parallel with the laboratory program, to investigate the effect of biofouling in pipelines, and to trial various surface coatings with the aim of finding a suitable refurbishment option to line open channels.

In a hydroelectric system, biofouling causes a reduction in power output generation capacity, lost revenue through reduced available output, and costs are incurred through the cleaning and removal of biofouling, and associated down time for the system affected. Hydro Tasmania embarked upon a program of headloss testing in 2002/03 to investigate the effectiveness of cleaning conduits. Many of the conduits were previously studied by Brett (1980). However, the present study gives new information on the cleaning of conduits, and the direct consequence of the removal of biofouling.

With increased reliability and accuracy of flow metering and pressure measurements, coupled with microbiology expertise, a more sophisticated analysis of the problem is now achievable. The present chapter reports on the cleaning of three large diameter pipelines and the headloss testing undertaken both pre-cleaning and post-cleaning. Two of the pipelines were high pressure penstocks, and the other was a low pressure hilltop pipeline. All pipelines were part of different hydroelectric schemes, and so the effects of cleaning were also evaluated in terms of improvements in power station generating capacity.

This Chapter presents an overview of the characteristics for each of the pipelines studied, the methods for field headloss testing, headloss test results, an overview of the microbiological properties of the biofouling material, results analysis, discussion and conclusions.

Also presented in this chapter are the methods and results for a paint trial program to identify the best performing surface coating to retard biofouling. From this study, in

addition to making recommendations to the end user, a paint was chosen for subsequent use in later laboratory studies looking at the growth of biofilms on a smooth plate.

The chapter closes with a summary

3.2 Headloss Studies

Three pipelines were cleaned and tested. The pipelines are located in three different hydroelectric power schemes that are owned and operated by Hydro Tasmania in Tasmania, Australia. Figure 3.1 shows the location of the three sites, Wilmot, Poatina and Tarraleah.

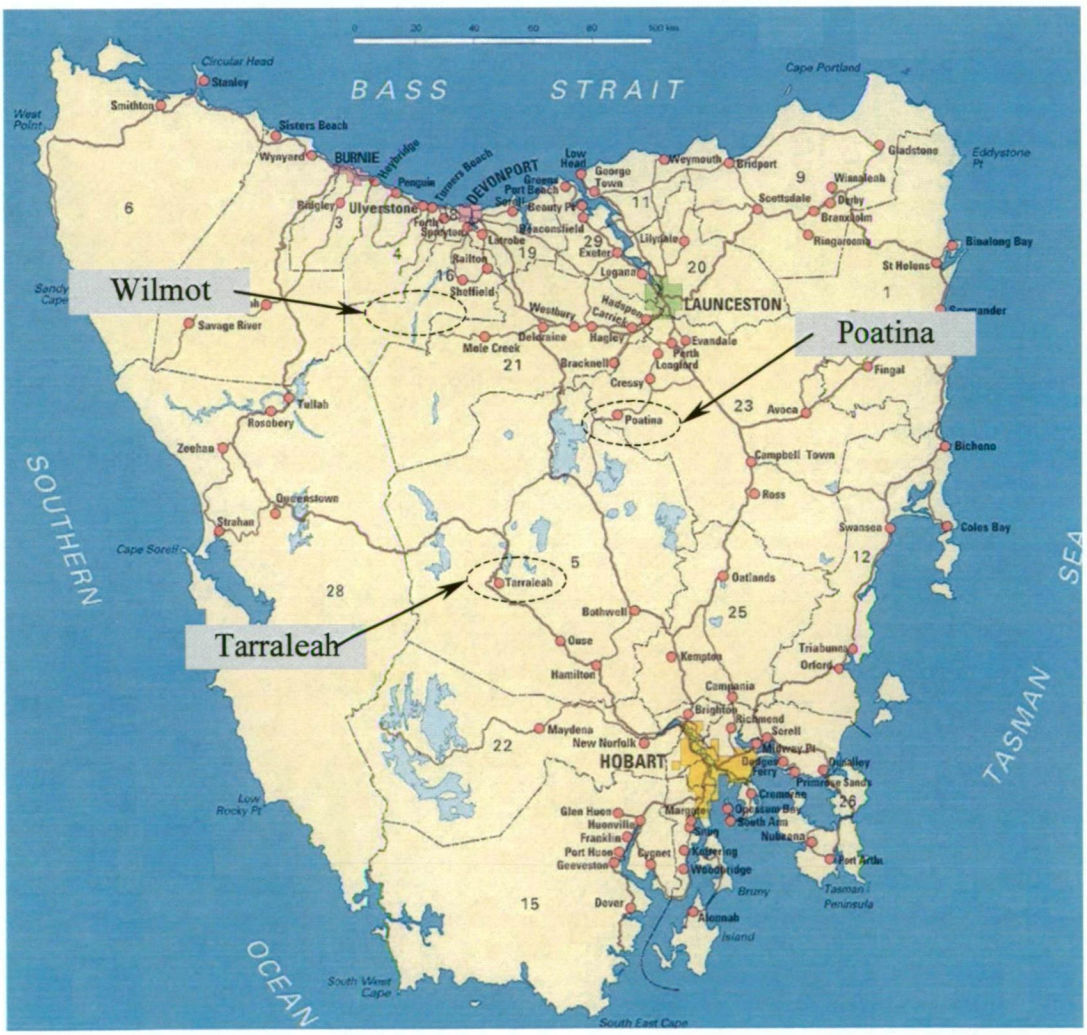
Wilmot
Poatina
Tarraleah
BASS STRAIT
SOUTHERN OCEAN
TASMAN SEA
LAUNCESTON
HOBART
DEVONPORT
BURNIE
Stanley
Smithton
Sisters Beach
Wynyard
Ulverstone
Penguin
Latrobe
Railton
Sheffield
Savage River
Mole Creek
Deloraine
Westbury
Hadspen
Carrick
Hagley
Evandale
Perth
Longford
Bracknell
Cressy
Poatina
Avoca
Fingal
Campbell Town
Ross
Oatlands
Bothwell
Ouse
Hamilton
Kempton
Tarraleah
Strahan
Queenstown
Zeehan
Rosebery
Tullah
Cape Sorell
Maydena
New Norfolk
Glen Huon
Huonville
Franklin
Port Huon
Geeveston
Dover
Brighton
Richmond
Sorell
Triabunna
Orford
Swansea
Coles Bay
Bicheno
Scottsdale
Derby
Branxholm
Ringarooma
Gladstone
Weymouth
Bridport
George Town
Low Head
Beaconsfield
Exeter
Lilydale
Legana
St Helens
Binalong Bay
Eddystone Pt
Cape Portland
Circular Head
West Point
Sandy Cape
South West Cape
South East Cape
Low Rocky Pt
Tasman Peninsula
Port Arthur
Bruny Island
Alonnah
Cygnet
Margate
Kettering
Woodbridge
Nubeena
Primrose Sands
Cremorne
Opossum Bay
South Arm
Sandy Bay
Dunalley
Midway Pt
Howrah
Lindisfarne
Clarence
Glenorchy
Claremont
Granton
Bridgewater
Brighton
Tea Tree
Campania
Colebrook
Jericho
Oatlands
Ross
Campbell Town
Fingal
Avoca
Poatina
Cressy
Longford
Perth
Evandale
Hagley
Carrick
Hadspen
Westbury
Deloraine
Mole Creek
Sheffield
Railton
Latrobe
Ulverstone
Penguin
Turners Beach
Port Sorell
Greens Beach
Port Beach
Beauty Pt
Forth
Spreyton
Wynyard
Sisters Beach
Smithton
Stanley
Circular Head
Savage River
Zeehan
Queenstown
Strahan
Rosebery
Tullah
Derwent Bridge
Maydena
New Norfolk
Glen Huon
Huonville
Franklin
Port Huon
Geeveston
Dover
Cygnet
Kettering
Woodbridge
Nubeena
Port Arthur
Bruny Island
Alonnah
Margate
Opossum Bay
South Arm
Sandy Bay
Dunalley
Midway Pt
Howrah
Lindisfarne
Clarence
Glenorchy
Claremont
Granton
Bridgewater
Brighton
Tea Tree
Campania
Colebrook
Jericho
Primrose Sands
Cremorne
Swansea
Coles Bay
Bicheno
Fingal
Avoca
Campbell Town
Ross
Oatlands
Bothwell
Ouse
Hamilton
Kempton
Triabunna
Orford
Sorell
Richmond
Brighton
Campania
Colebrook
Jericho
Tea Tree
Bridgewater
Granton
Claremont
Glenorchy
Clarence
Lindisfarne
Howrah
Midway Pt
Dunalley
Sandy Bay
South Arm
Opossum Bay
Cremorne
Primrose Sands

3.2.1 Wilmot Penstock

The first conduit to be studied was Wilmot Penstock, which leads to Wilmot Power Station. This penstock was commissioned in 1971 and is located on Hydro Tasmania's Mersey-Forth Power Development. Wilmot consists of one Francis turbine with an operating head of nominally 252m. Figure 3.2 shows a photo of the penstock studied.

The power scheme details are contained in Table 3.1. The dimensions of the tunnel and penstock are shown in Table 3.2.

Figure 3.2: Wilmot Penstock looking uphill.

Wilmot Power Station gains its water supply from Lake Gairdner. Water then travels through an intake structure into a tunnel of horseshoe cross section. Flow then enters a transition and penstock, which is lined with coal-tar enamel on its internal surface. The pipe is fixed at a slope of approximately 34.6 degrees from the horizontal on a hillside.

The flow then passes through, and incurs energy losses at each of the hilltop valve (HTV), four vertical bends, a pipe off-take, and the machine inlet valve (MIV).

Table 3.1: Characteristics of Wilmot Power Scheme.

Power Scheme Feature	Value
Lake full supply level (m, AHD)	472.44
Power station turbine centreline (m, AHD)	214.88
Rated power station output capacity (MW)	30.60
Number of turbines (Francis type)	1

Table 3.2: Wilmot penstock general information.

Conduit Section Description	Length (m)	Diameter (m)	Area (m^2)
Tunnel - unlined	3688.00	3.51 (equivalent)	11.09
Tunnel - lined with unlined invert	299.00	3.45 (equivalent)	10.68
Tunnel - lined with lined invert	89.60	3.20 (equivalent)	9.14
Start of penstock to HTV	132.00	1.98	3.08
HTV to test section	31.37	1.98	3.08
Test section	331.88	1.98	3.08
Test section to bottom of vertical bend	29.15	1.98	3.08
Bottom of vertical bend to MIV	1.80	1.30	1.33
Total length of penstock	526.20		

Wilmot Penstock has been partially cleaned in the past by dewatering of the pipe as part of scheduled maintenance, but the effectiveness was never quantified. While empty of water, the pipeline was open at the top and bottom allowing air to circulate and dry out the biofilm, significant amounts of which then flaked off.

Only the penstock, between the hilltop valve and the main inlet valve (394m), was cleaned for the present study. It should be noted that the pipe was dewatered approximately 12 months prior to the present headloss tests and cleaning, where the biofouling was allowed to dry out and flake off. So effectively, the penstock had only 12 months of fouling prior to the pre-cleaning headloss test.

3.2.2 Poatina Penstock

The second pipeline studied was the Poatina Penstock. Poatina Power Scheme was commissioned in 1964 and the penstock has never been cleaned with high pressure

water spray, although it has been drained on occasions allowing partial cleaning by air drying. Poatina Power Station consists of five 51.6MW Pelton turbines and one 54.5MW with a nominal operating head of 835m. Figure 3.3 shows the penstock.

Figure 3.3: Poatina Penstock looking uphill.

The general characteristics of the Poatina Power Scheme are presented in Table 3.3. The Poatina headrace conduit begins at Great Lake intake structure. Flow passes through a trash rack and enters sections of unlined and lined horseshoe shaped tunnel, lined circular tunnel, steel lined tunnel penstock, coal-tar enamel lined steel surface penstock, a vertical shaft, distributor and penstock off-takes to turbines. The details for each of these sections are shown in Table 3.4. Only the penstock, between the hilltop valve and the offtake to turbine No. 1 (2718m), was cleaned in the present study.

Table 3.3: Characteristics of Poatina Power Scheme.

Power Scheme Feature	Value
Great Lake full supply level (m, AHD)	1039.37
Normal minimum operating level (m, AHD)	1018.03
Power station turbine centreline (m, AHD)	204.52
Maximum gross head (m)	834.85
Minimum gross head (m)	813.51
Rated power station output capacity (MW)	>300
Number of turbines (Pelton type)	6

Table 3.4: Details of headrace conduit.

Conduit Section Description	Length (m)	Diameter (m)	Area (m^2)
Tunnel – unlined (horseshoe)	2338	5.74 (equivalent)	28.71
Tunnel - lined (circular)	3280	4.42	15.34
Tunnel – lined (horseshoe)	151	6.47 (equivalent)	37.07
Penstock (tunnel)	1008	3.05	7.30
Penstock (surface)	1684	2.93 – 2.58	6.74 – 5.23
Distributor	48	2.58 – 1.49	5.23 – 1.74
Penstock offtake	15 × 5 and 1 × 26	0.92 – 1.15	0.66 – 1.04
Total length of penstock	2755-2766		

3.2.3 Tarraleah Hilltop Pipeline

The third pipeline studied was the Tarraleah No.1 Hilltop Pipeline. Tarraleah Power Station was commissioned between 1938 and 1958 and is located on Hydro Tasmania's Upper Derwent Power Development. Tarraleah Power Station consists of six Pelton turbines with a nominal operating head of 299m.

Tarraleah Power Station gains its water supply from Lake King William. Water is released at Clark Dam where it passes through Butlers Gorge Power Station into the low level No. 1 Canal. Water is also released into a high level No. 2 Canal.

Flow from No. 1 and No. 2 Canals join at No. 1 Pond, which flows to the Tarraleah Forebay. Water from the Forebay flows into large diameter low pressure No. 1 and No. 2 Hilltop Pipelines (Figure 3.4). No. 1 Hilltop Pipeline is the subject of the current headloss tests and was the candidate for the cleaning of biofouling material. The pipeline was cleaned between the Forebay and the hilltop valves (2141m).

Figure 3.4: Tarraleah No. 1 and No. 2 Hilltop Pipelines looking downstream.

Each of the Hilltop Pipelines has a large surge tower at their approximate halfway point. Flow also passes an interconnecting valve for the hilltop pipelines, then is split between six high pressure penstock pipelines, passes through hilltop valves (HTV) which feed the six Pelton turbines. Table 3.5 provides the general characteristics of the system.

Table 3.5: Characteristics of Tarraleah Power Scheme beginning from forebay.

Power Scheme Feature	Value
Normal forebay operating level (m, AHD)	643
Power station turbine centreline (m, AHD)	344
Nominal operating head (m, AHD)	299
Rated power station output capacity (MW)	90
Number of turbines (Pelton type)	6

There has been previous testing of the Tarraleah hilltop pipelines to investigate the issue of varying hydraulic roughness and associated hydraulic efficiency over time. The results are best summarised in the work by Brett (1980). Both the Manning "n" roughness coefficient and the Darcy friction factor "f" were presented in this paper as flow resistance variables, and were shown to vary significantly over time. Special events such as periods when the pipes were cleaned (1960 and 1967), or dewatered and

air dried (1963), appreciably influenced the hydraulic roughness of the pipe. The paper by Brett (1980) should be regarded as a companion to this present work.

Table 3.6 shows the general characteristics of No. 1 Hilltop Pipeline leading to Tarraleah Power Station commencing from the forebay.

Table 3.6: Tarraleah No. 1 Hilltop Pipeline general information.

Conduit Section Description	Length (m)	Diameter (m)	Area (m^2)
From forebay to surge towers (No. 1 Hilltop Pipeline)	1067	2.59	5.27
Surge towers to HTV house (No. 1 Hilltop Pipeline)	1074	2.59	5.27
HTV house to power station (Penstock pipelines)	584	1.51-1.24	1.82-1.20
Total length of conduit	2725		

Both No. 1 and No. 2 Hilltop Pipelines originally had internal coatings of horizontal retort tar. The pipelines were relined in 1974 with Zincanode 206 primer and Luxatar 5 coal-tar epoxy (Pers. Com. Denne, 2005).

3.3 Method and Instrumentation

3.3.1 Methods

The energy equation used to evaluate the headloss due to friction is given by Equation 3.1.

$$\frac{P_1}{\rho g}+\frac{\bar{u}_1^2}{2g}+y_1=\frac{P_2}{\rho g}+\frac{\bar{u}_2^2}{2g}+y_2+H_L \qquad \text{Equation 3.1}$$

where P is pressure (Pa), $\bar{u}$ is the mean velocity (m/s), g is gravitational acceleration (m/s^2), ρ is the water density (kg/m^3), y is the height to a horizontal datum (m) taken as the supply water level, and H_L is the total headloss (m). The total head loss was first evaluated from the field measurements between points 1 (upstream) and 2 (downstream).

Minor losses, h_l, due to valves, pipe branches, bends, and pipe transitions were then subtracted from the total headloss to determine the headloss due to friction, h_f, given by $h_f = H_L - h_l$. The minor losses are given in terms of a generic loss coefficient, K. This coefficient can be applied to the velocity head at the point of interest in the pipe, as Equation 3.2.

$$h_l = \sum_i K_i \frac{\bar{u}_i^2}{2g} \qquad \text{Equation 3.2}$$

where the subscript, i, denotes the pipe section of interest.

Friction factors, f, and equivalent sand grain roughness height, k_s (Nikuradse, 1933), are then determined using the Darcy-Weisbach equiation (Equation 3.3)

$$h_f = f \frac{L}{D} \frac{\bar{u}^2}{2g} \qquad \text{Equation 3.3}$$

and the Colebrook-White equation (Equation 3.4) from Colebrook (1939).

$$\frac{1}{\sqrt{f}} = -2\log\left(\frac{k_s}{3.7D} + \frac{2.51}{R_e\sqrt{f}}\right) \qquad \text{Equation 3.4}$$

where h_f = headloss due to friction (m), $\bar{u}$ is mean flow velocity (m/s), L is pipe length (m), D is pipe diameter (m), and R_e is the Reynolds number defined by Equation 3.5.

$$R_e = \frac{\rho \bar{u} D}{\mu} \qquad \text{Equation 3.5}$$

where μ is the dynamic viscosity of the water (N.s/m^2).

Additional data required to complete the analysis were obtained from Hydro Tasmania's centralised time series database. This was used to obtain information such as lake and

tailwater levels. This information is contained in Barton and Sargison (2003), Barton (2004) and Barton and Buia (2005) for Wilmot, Poatina and Tarraleah respectively.

3.3.2 Pressure Transducers for Pressure Measurement

Pressure tappings were used at various locations for the present study. For each conduit two locations were chosen at upstream and downstream points covering the greatest possible length of conduit. Ring tappings were used to gain a circumferential average reading allowing for uneven flow distributions in the pipe. Two pressure transducers were attached to each ring bus where possible and an average reading taken.

Druck type PTX Industrial pressure transmitters were used. The accuracy of the transducers is a typical 0.15% full scale (Druck Limited, 2002). Details of this instrument can be found on the data sheet included with in Barton and Buia (2005) in volume two of this thesis. Figure 3.5 shows a typical arrangement for pressure measurement on a pipe.

Zero error was eliminated from each pressure measurement by conducting a zero flow (or static) observation for each of the pre- and post-clean studies. Calculations were undertaken to determine the offset for each pressure transducer. In addition, where possible, each pressure transducer was calibrated on a dead-weight tester by Hydro Tasmania engineers before and after completion of each series of tests to re-check the transducer performance for gross errors. The height level of each pressure transducer was surveyed prior to the pre-clean tests to obtain a reference to the datum.

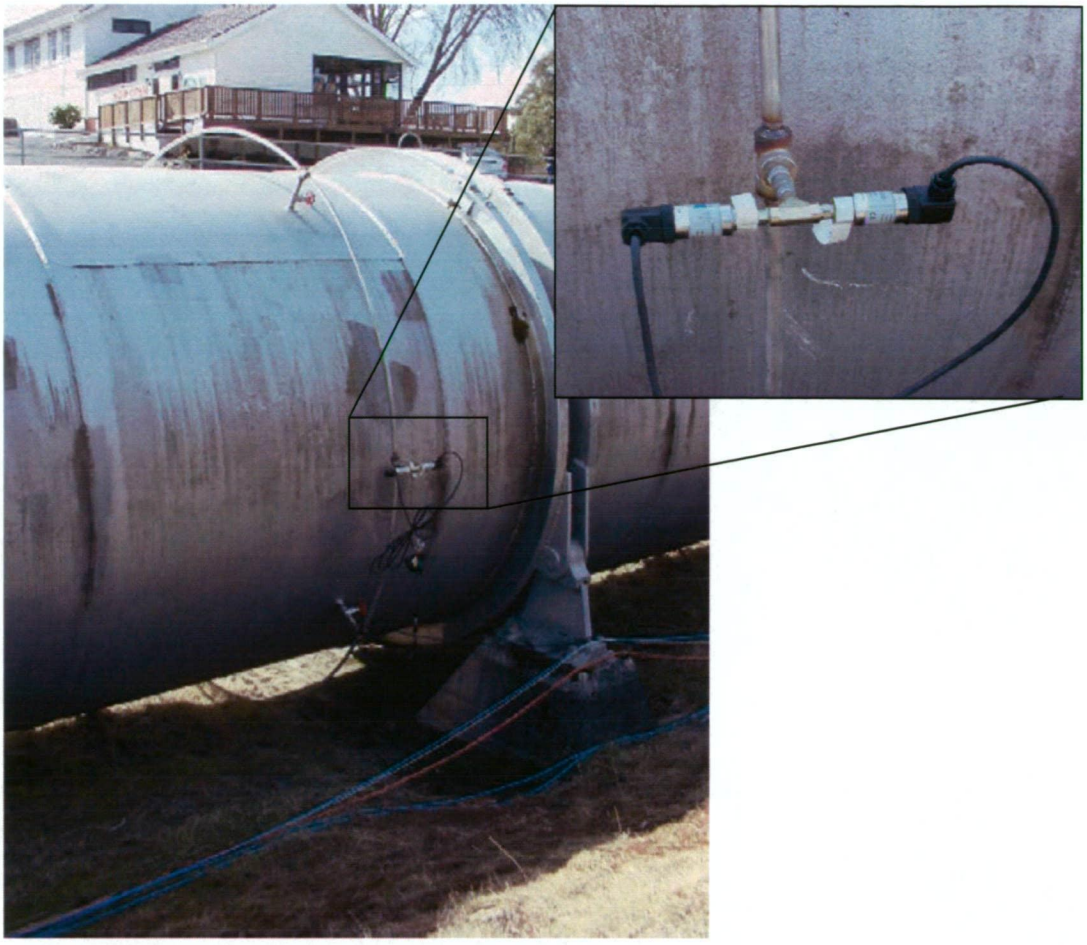

Figure 3.5: Typical pressure transducer arrangement attached to ring bus to obtain circumferential average.

3.3.3 Flow Measurement

Flows were recorded using ultrasonic Panametrics type flowmeters (Panametrics, 2001). Two sets of flowmeters were used, aligned with the pipe longitudinal axis, mounted at the centreline, or mounted diagonally opposite, in line with practical limitations. Average values for the two flowmeter recordings were taken in the result analysis. The accuracy of the flowmeters is 2% of reading typical. Practical considerations precluded calibration of these flowmeters. However, a check was performed where possible using other data (see Barton and Sargison, 2003; Barton, 2004; Barton and Buia, 2005). Figure 3.5 shows a typical flow transducer set up.

Figure 3.6: Panametrics flowmeters attached to pipe wall.

3.3.4 Measurement of Individual Machine and Total Power Station Output

Individual turbine power output was measured from within the power stations. Machine electrical power output was measured at the machine electrical circuits. The net output from each turbine was taken as the total station output.

3.3.5 Dataloggers and Data Quality

All data was quality checked by monitoring all data traces for inconsistencies such as signal drop out or effects from transient pressures in the penstock. All data were logged directly to a PC for storage at 10 Hz over either a 5 or 10 minute period. Figures 3.7 shows a typical data acquisition setup to a portable computer.

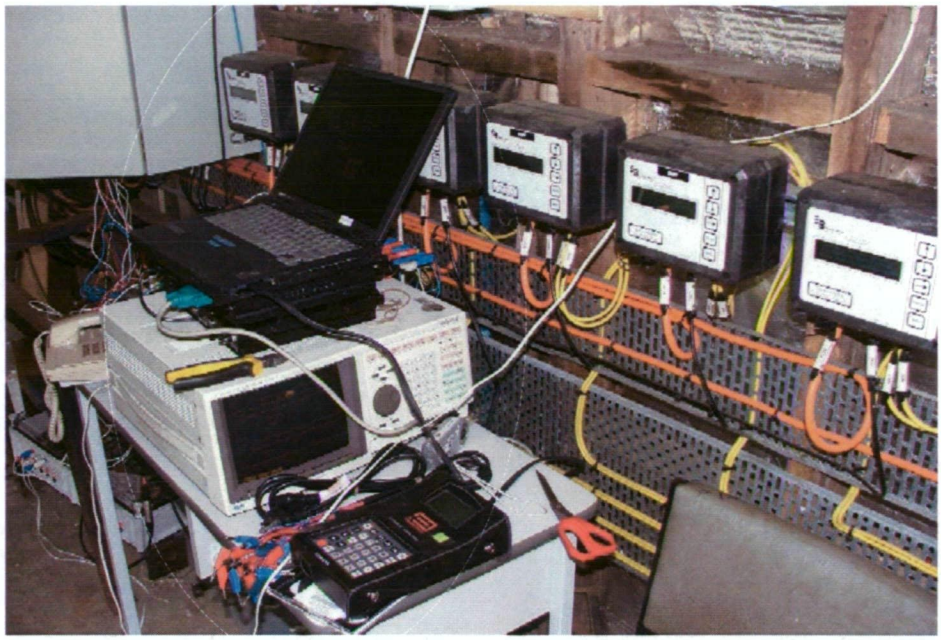

Figure 3.7: Photo showing the typical data logging equipment.

3.3.6 Water Level Measurement

Where water surface levels were required, data were obtained from either ultrasonic level sensors or from Hydro Tasmania time series database linked by telemetry to ultrasonic depth sensors at lakes or other storages.

Figure 3.7 shows a Milltronics 5m ultrasonic level sensor used at the forebay to measure water surface level at the entrance to No. 1 Hilltop Pipeline (accuracy of 0.25% of full scale (Milltronics, 2001)). The instrument specification sheet and other information can be obtained from Barton and Buia (2005) contained in Volume two of this thesis.

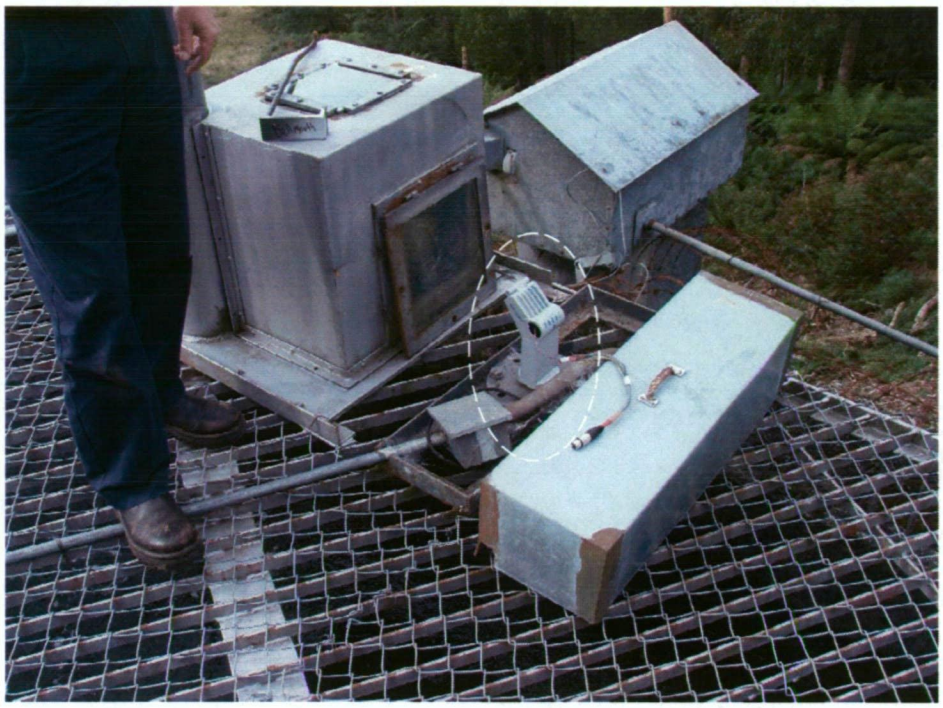

Figure 3.8: The water level sensor (in dashed circle) used for the forebay level measurements for the Tarraleah headloss studies.

3.3.7 Temperature Measurement

A Center 305 data logger thermometer was used to record ambient and pipeline water temperatures (where available) periodically for both pre- and post-clean testing. This enabled more accurate determination of water density and viscosity.

3.3.8 Microbiological Methods

Molecular analysis was undertaken on biofilm samples from Poatina and Tarraleah by Buia (2006). Only brief details will be given here. *DNA* extraction methods were used, clone libraries generated and DNA sequencing carried out. Determination of the closest match to the partial rRNA sequences was performed by performing n-BLAST searches on the National Center for Biotechnology Information (NCBI) website (www.ncbi.nlm.nih.gov) accessed by Buia (2006) throughout 2005 and 2006 (Altchul *et al.*, 1997).

3.3.9 Cleaning Method

The cleaning was performed by a proprietary system consisting of a rotating high-pressure water spray. First the pipeline headloss was measured, then the pipeline cleaned, then the pipeline headloss re-measured.

The cleaning system was traversed through the conduits at a rate deemed the most effective at removing the biological fouling, yet without causing damage to the underlying surface coating. The arrangement was collapsible to <0.5m to fit through a range of access points along the pipeline, and expands to fit pipes greater than 3m in diameter.

3.4 Results

Results for the headloss tests are presented here. The two key results from the field studies are shown as headloss (m) versus flow rate (m^3/s) and power output (MW) versus flow rate (m^3/s). Also presented are the limits of hydraulically smooth and rough behaviour for the respective pipelines, and Moody diagrams for the results obtained.

3.4.1 Wilmot Penstock

Figures 3.9 to 3.12 show the results for the Wilmot Penstock headloss testing. Note that both the pre-clean and post-cleaning results are shown.

Figure 3.9 shows the measured headloss for the penstock against the measured flow. There are two sets of results with each showing the pre- (fouled pipe) and post-clean (cleaned pipe) results. The measurements for the penstock section show a reduction in headloss of approximately 1m at full flow. There is a reduction of approximately 1.5m if the results for the penstock test section are extrapolated to the entire section of cleaned penstock and also the upstream tunnel sections (which were not cleaned). The data which show the headloss of the clean penstock greater than the fouled penstock is mostly a reflection of the uncertainty in the measured flow rate, which is highest at low flows.

Figure 3.10 presents the power output (in MW) measured in the power station against the flow rate. For the cleaned penstock there is increased power output for the respective flow rates. Alternatively, less flow is required to maintain the same power output. Approximately, an additional 0.5MW is available at $15m^3/s$. Further detail may be found in Barton and Sargison (2003).

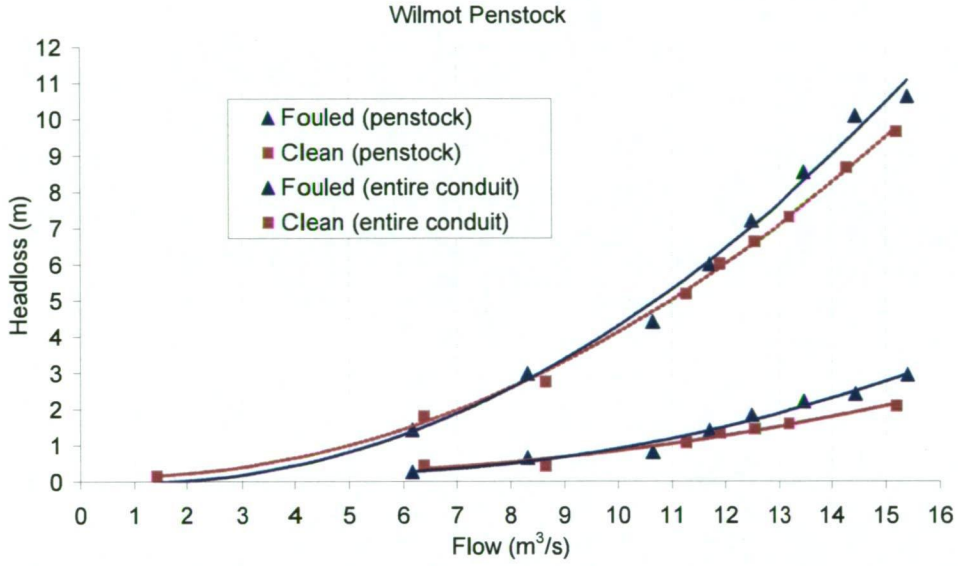

Figure 3.9: Headloss versus flow rate for Wilmot Penstock.

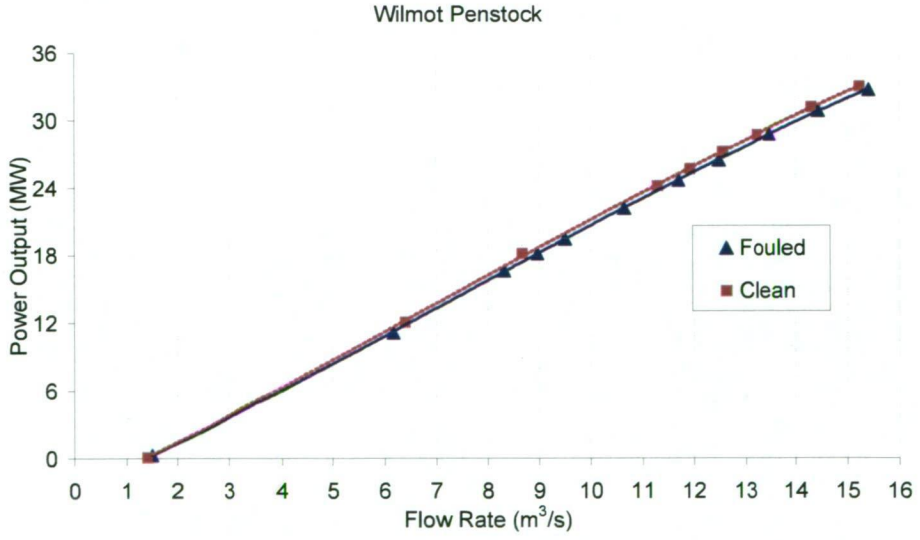

Figure 3.10: Power output versus flow rate for Wilmot Penstock.

The limits of hydraulically rough and smooth behaviour are shown in Figure 3.11. This plot is significant as it shows at what flow most headloss will occur. Figure 3.11 shows that the fouled pipe hydraulic roughness of 0.27mm measured in the penstock means

hydraulically rough behaviour may never be reached, though it is closely approached near maximum flow.

Figure 3.12 shows a Moody diagram plot of friction factor against Reynolds number (based on pipe diameter). This suggests that the fouled pipe condition may not follow a Colebrook-White friction type law in the smooth-rough transition regime, which is typically used in engineering calculations to determine the hydraulic roughness from the friction factor. Clean pipe measurements show a better data trend in line with a typical engineering material (coal tar enamel).

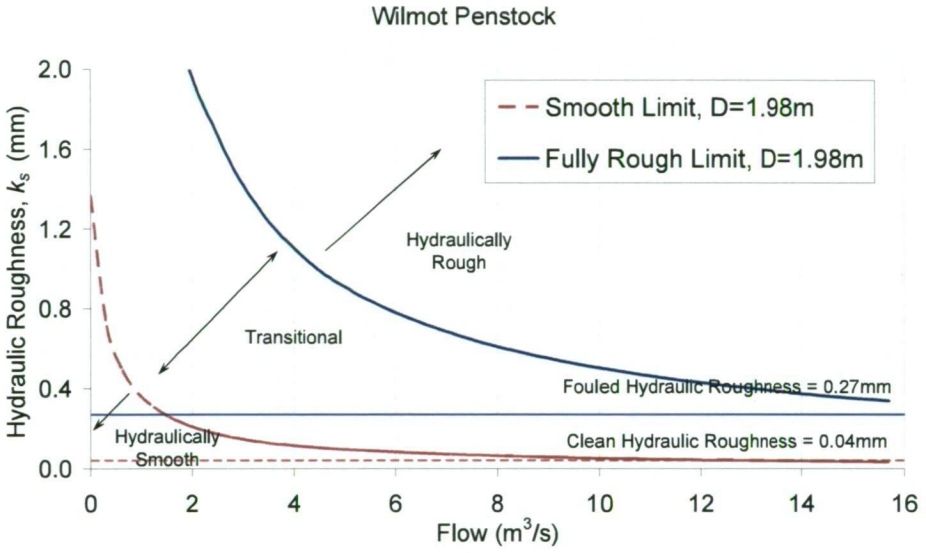

Figure 3.11: Hydraulically smooth and rough behaviour for Wilmot Penstock.

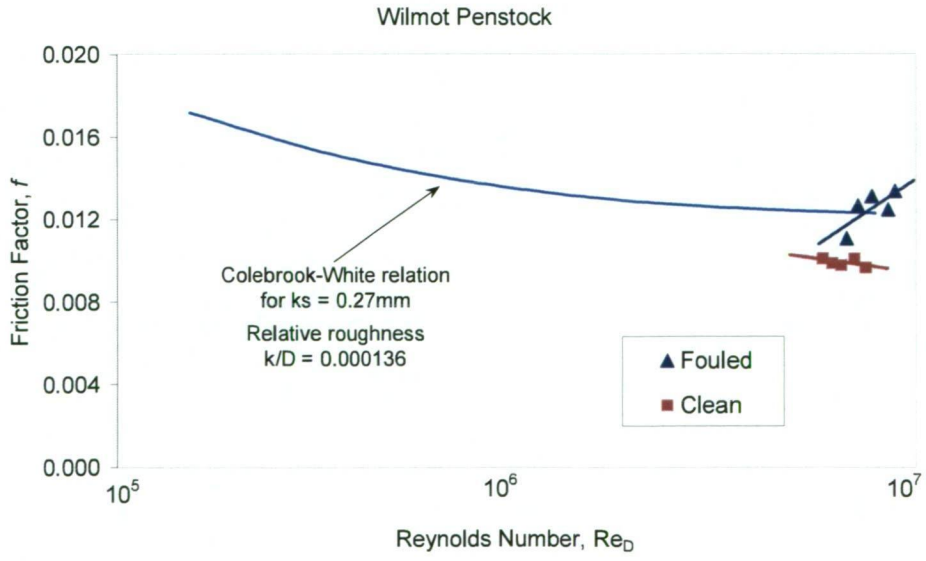

Figure 3.12: Moody diagram for Wilmot Penstock.

The friction factors and hydraulic roughness derived from the headloss tests are summarised in Table 3.7. The table shows a clear reduction in wall roughness.

Table 3.7: Friction and hydraulic roughness for Wilmot Penstock.

Test	Friction factor f	Hydraulic roughness k_s (mm)
Pre-Clean (Fouled)	0.0129	0.27
Post-Clean (Clean)	0.0099	0.04

3.4.2 Poatina Penstock

Figures 3.13 to 3.16 show the results for the Poatina Penstock headloss testing. For each plot both the fouled and clean penstock measurements are shown.

Figure 3.13 shows the headloss versus flow rate in the same format as for the Wilmot results. Over the flow rates where measurements were made there is very little difference between fouled and clean pipe conditions. Results are obscured by the lack of measurements at higher flows for the fouled pipe (pre-clean) conditions. The reason for the negligible improvement seemed to be the interior coal-tar enamel coating which was found to be in very poor condition in the surface section of the penstock.

The results plotted in Figure 3.14 are for power output versus flow rate. This plot also shows negligible difference between the fouled and clean pipe measurements. It should be noted that the fouled pipe tests were undertaken using four turbines, and as such were operating slightly differently in their efficiency curves to the clean pipe tests using five turbines. The effects of turbine efficiency were found to have no discernable impact on the results at the measured flow rates.

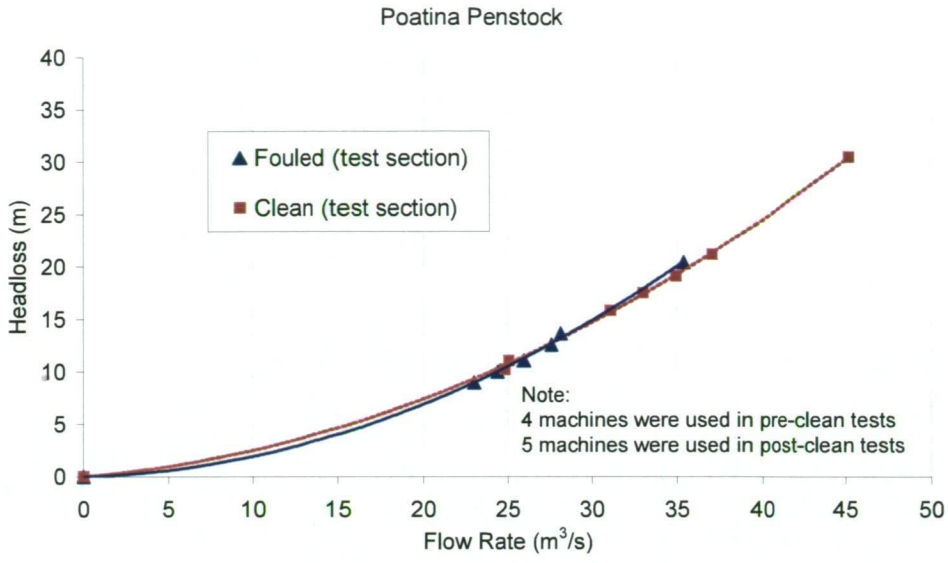

Figure 3.13: Headloss versus flow for Poatina Penstock.

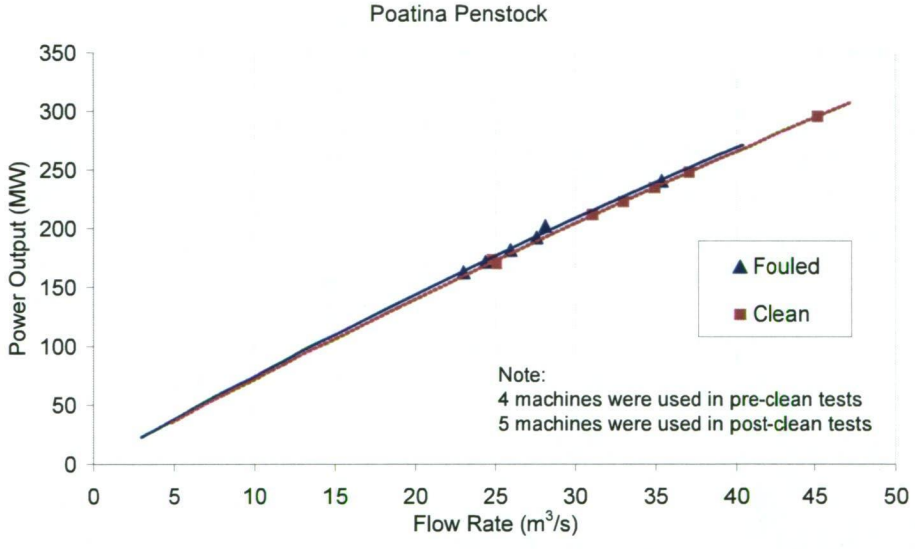

Figure 3.14: Power output versus flow for Poatina Penstock.

Separate consideration of friction and roughness information for the tunnel and surface sections of the penstock (Table 3.8) gives a better indication of the degree of deterioration of the interior coating of the surface penstock.

Figure 3.15 shows that for much of the operating flow range, conditions are hydraulically rough for the tunnel section of the penstock where the biofilm thickness was noted to be thicker. Conditions for the tunnel section improved after cleaning.

The surface section of the penstock, however, displayed different behaviour, where the fouled pipe hydraulic roughness was less than for clean pipe measurements. For the fouled surface penstock tests, much of the flow was in the transition region, and the friction law (Figure 3.16) exhibited a positive slope similar to the behaviour of the Wilmot and Tarraleah pipelines.

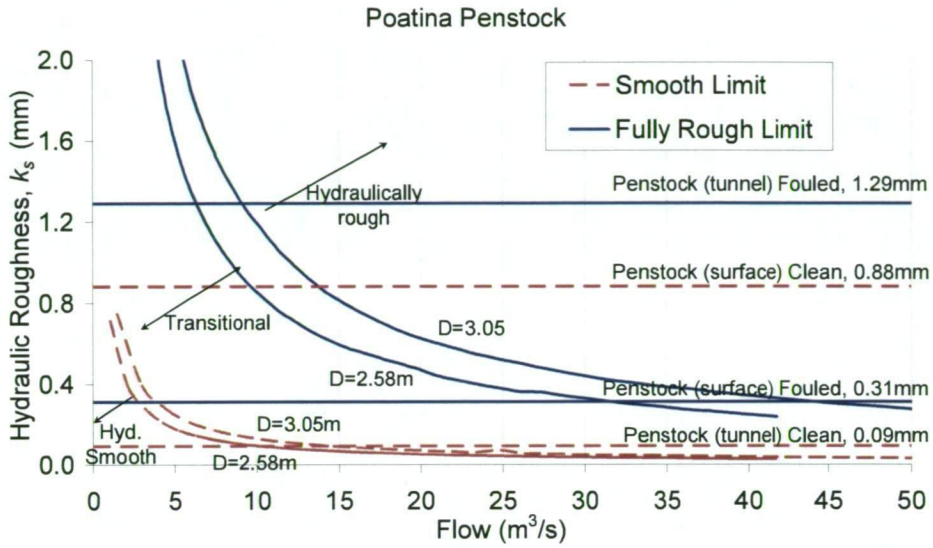

Figure 3.15: Hydraulically smooth and rough behaviour for Poatina Penstock.

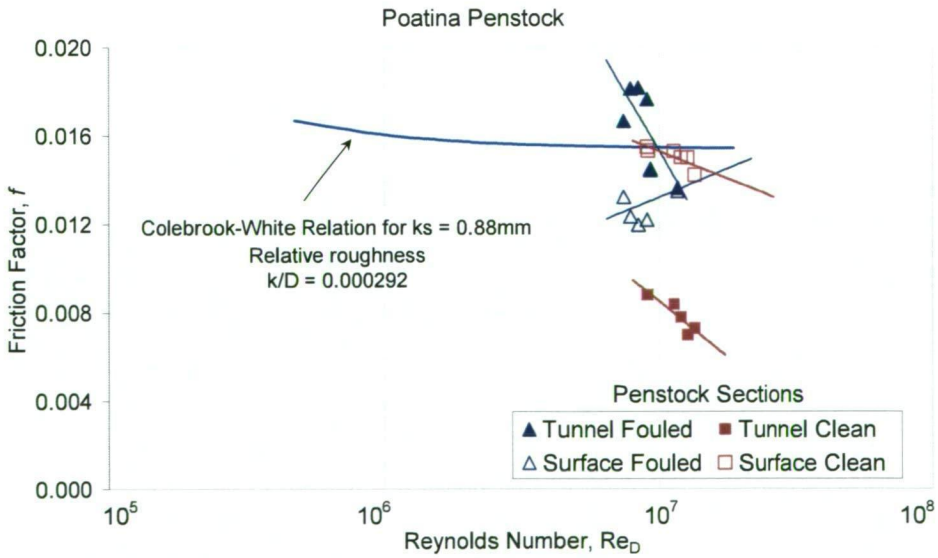

Figure 3.16: Moody diagram for Poatina Penstock.

Table 3.8: Friction and hydraulic roughness for Poatina Penstock.

Test	Friction factor f			Hydraulic roughness k_s (mm)		
	Total	Tunnel	Surface	Total	Tunnel	Surface
Pre-Clean (Fouled)	0.0150	0.0164	0.0129	0.89	1.29	0.31
Post-Clean (Clean)	0.0147	0.0089	0.0150	0.81	0.09	0.88

Figure 3.17 shows photos of the internal surface of the penstock after cleaning off the biofouling material. Crazing and lifting of the surface is very apparent for the surface penstock. The internal surface of tunnel penstock section is much more intact and smooth. These results show that it is important to know the underlying condition of the pipe surface if improvements in pipe performance are to be realised by the cleaning off of biofouling material. In this case the underlying surface was in particularly poor condition and the substrate roughness was in fact greater than the roughness of the biofouled surface.

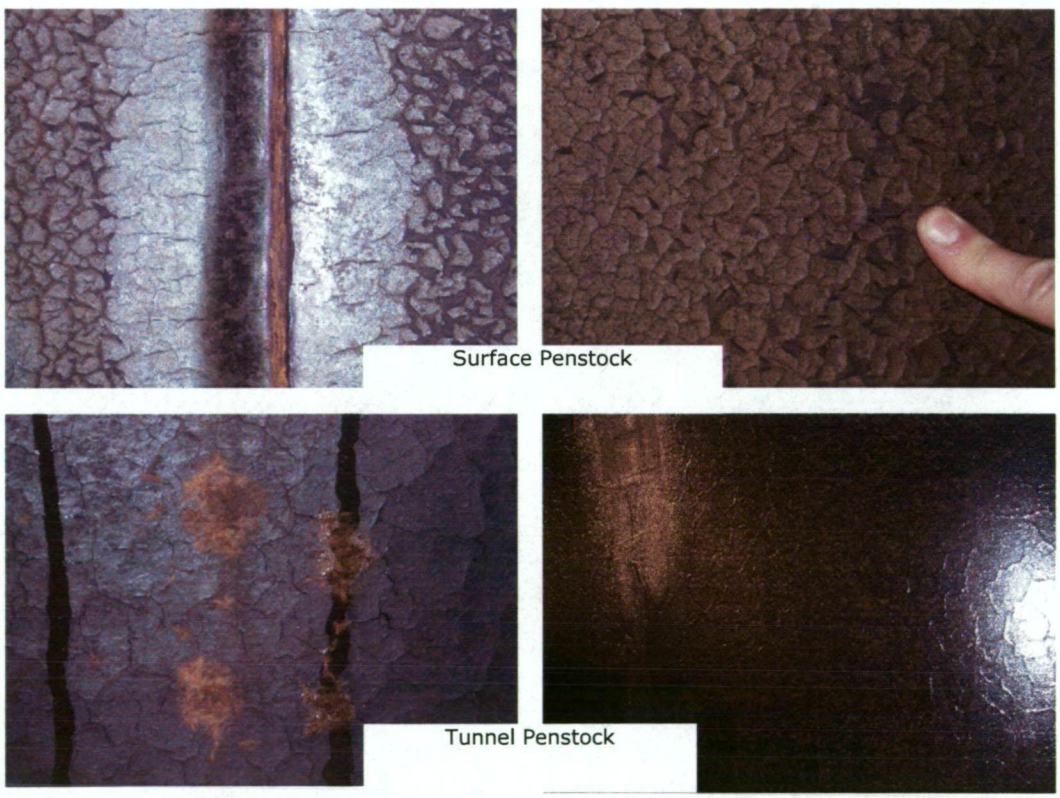

Figure 3.17: Photos of the internal surface of Poatina Penstock.

3.4.3 Tarraleah Hilltop Pipeline

Tarraleah showed the most significant results from the cleaning of biofouling material. Figure 3.18 shows the headloss versus flow measured during the tests. A 25% reduction

in headloss was recorded over the fouled pipe condition. Note that results are presented for the test section, which was approximately half of the full length of the hilltop pipeline, and the full length of the pipeline. Results from Figure 3.19 clearly show a consistent improvement in power output for clean pipe conditions. At a flow rate of $20m^3/s$ an improvement of approximately 2MW was recorded.

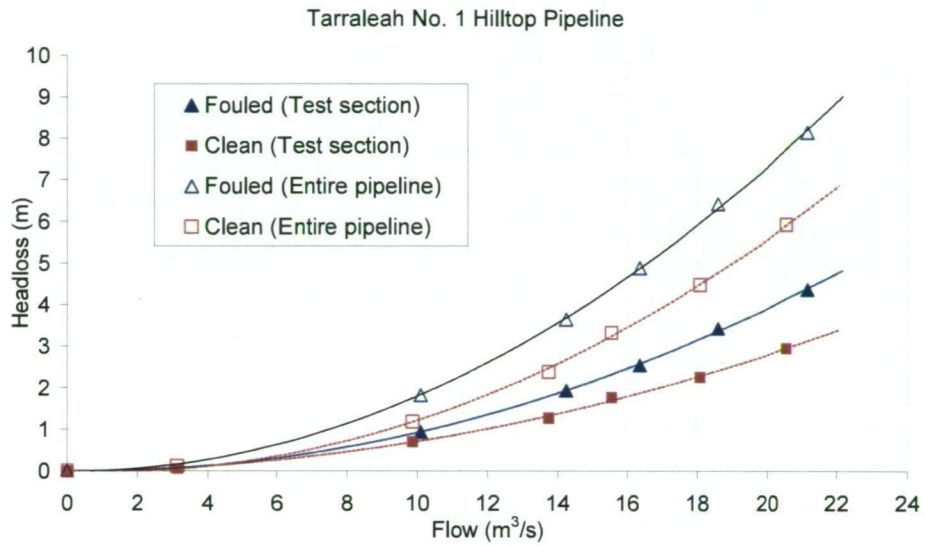

Figure 3.18: Headloss versus flow for Tarraleah No. 1 Hilltop Pipeline.

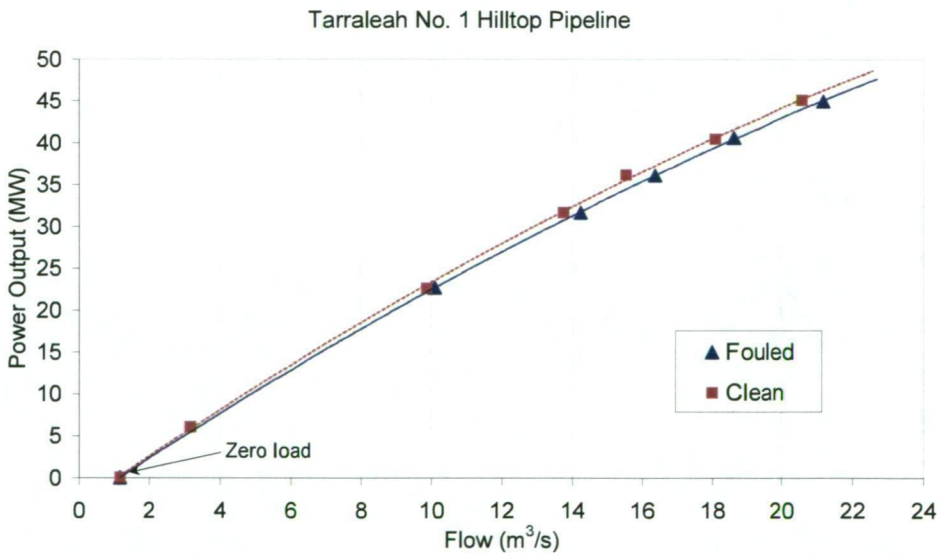

Figure 3.19: Power output versus flow for Tarraleah No. 1 Hilltop Pipeline.

The plot of hydraulic roughness limits (Figure 3.20) shows that, like Wilmot, fully hydraulic rough conditions are never actually reached, though approached at the higher flow rates.

The friction data shown in the Moody diagram, Figure 3.21, exhibited similar behaviour to the Wilmot Penstock result where the fouled pipe results have a positive slope, and the clean pipe results show a more negative slope, better following a Colebrook-White relation.

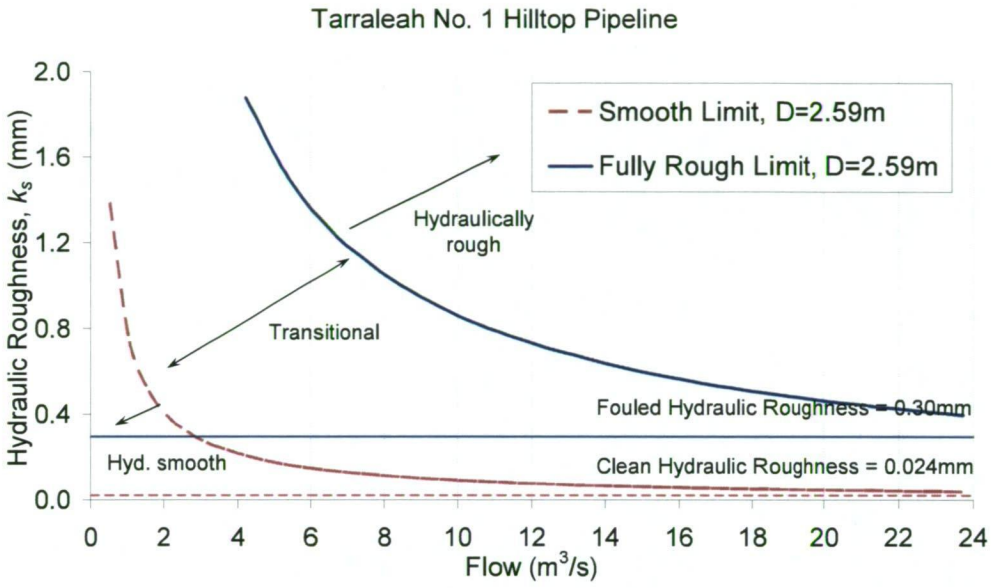

Figure 3.20: Hydraulically smooth and rough behaviour for Tarraleah No. 1 Hilltop Pipeline.

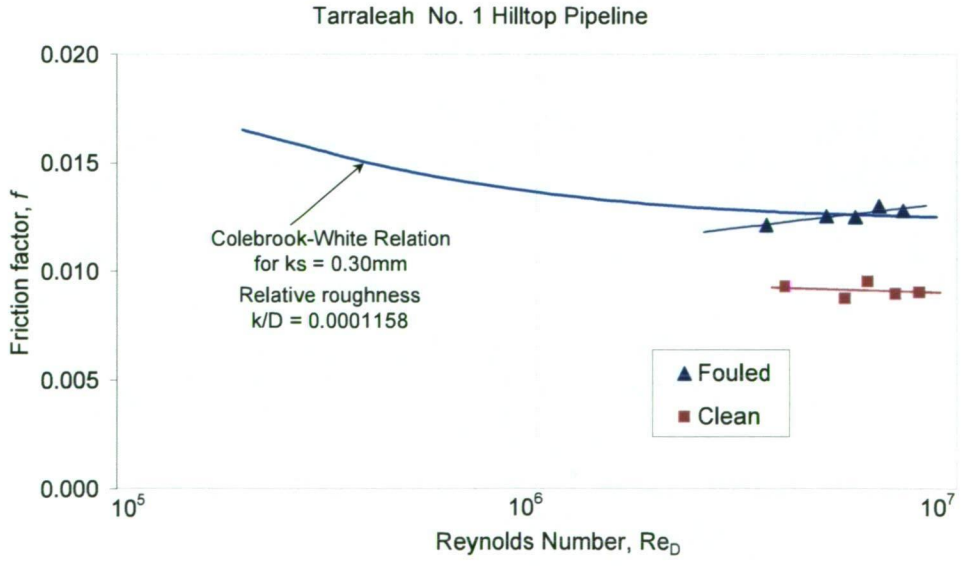

Figure 3.21: Moody diagram for Tarraleah No. 1 Hilltop Pipeline.

Table 3.9 summarises the roughness and friction data for the headloss tests. It should be noted that the results are much lower than those of (Brett, 1980), although he presented results for No. 2 Hilltop Pipeline.

Table 3.9: Friction and hydraulic roughness for Tarraleah No. 1 Hilltop Pipeline.

Test	Friction factor f	Hydraulic roughness k_s (mm)
Pre-Clean (Fouled)	0.0126	0.30
Post-Clean (Clean)	0.0088	0.02

3.5 Economic Analysis

For both Wilmot and Tarraleah pipeline test, an economic analysis was undertaken based on the measured improvements in power output. No analysis was undertaken for Poatina as no noticeable improvement was recorded. Information on the economic analysis can be found in Volume 2 of this thesis in Barton and Sargison (2003) and Barton and Buia (2005).

3.6 Biofilm Analysis

Buia (2005) obtained biofilm samples from the internal walls of all three pipelines. All pipes had a relatively uniform covering of 2-5 mm thick biofilm, although smaller areas of thicker biofilm of up to 10-12 mm were observed. The biofilm had a dark, almost black colour on the internal coal-tar enamel walls and was well hydrated. Brown deposits were found on field welds and exposed steel surfaces. Samples for DNA analysis were taken by Buia (2005) using aseptic techniques, transported on ice, and stored at -80°C until analysis. Chemical analyses were undertaken on the samples and are shown in Table 3.10. The metal content of all samples was predominantly iron and manganese, supporting previous findings of Minkus (1954), Tyler (1967) and Pollard and House (1959). Aluminium levels were also high.

Buia (2005) undertook direct microscopic examination of the biofilm from Tarraleah No. 1 Hilltop Pipeline using transmitted light microscopy. This examination revealed a variety of bacterial morphotypes (rods, cocci, filaments), as well as a small number of

diatoms (including *Gomphonema sp.*), possibly washed into the pipeline from upstream open channel inflow.

Barton *et al.* (2007) and Buia (2006) report that Proteobacteria were found to represent the most dominant bacterial phylum associated with the Poatina conduit biofilm. Of the Proteobacteria detected, the majority were of the class Alphaproteobacteria. Based on clone library information, the biofilm was quite diverse as it contained clones of several other bacterial phyla including: Acidobacteria, Chloroflexi, Planctomycetes, Bacteroidetes, Verrucomicrobia, Firmicutes and Actinobacteria.

The Tarraleah No. 1 Hilltop Pipeline biofilm was also dominated by Proteobacteria, and in particular Alphaproteobacteria. Like the Poatina conduit, this biofilm also possessed a very diverse microbial community. Clones associated with the phylum Chloroflexi was detected at a high incidence and the biofilm also contained several clones belonging to the recently discovered phylum Gemmatimonadetes (Zhang *et al.*, 2003).

No microbiological assessment was performed on the Wilmot Penstock biofilm.

Table 3.10: Results for the chemical analyses of biofilm samples.

		Wilmot Penstock		Poatina Penstock		Tarraleah No. 1 Hilltop Pipeline
Analyte	Units	**Black Deposit**	**Brown Deposit**	**Black Deposit**	**Brown Deposit**	**Black Deposit**
C Total	% w/w	-	-	20	13	15
Nitrogen, (Total)	% w/w	-	-	2	1	2
Phosphorus	mg/kg	-	-	610	1410	958
S	mg/kg	-	-	4090	2580	2260
Al	mg/kg	-	-	30600	37900	54400
As	mg/kg	-	-	11	3	28
Cd	mg/kg	65	1	6	<1	14
Co	mg/kg	831	34	185	63	280
Cr	mg/kg	29	42	61	92	110
Cu	mg/kg	140	36	200	73	91
Fe	mg/kg	169000	579000	22600	51500	32400
Mn	mg/kg	230000	6510	145000	24500	208000
Ni	mg/kg	417	21	654	186	338
Pb	mg/kg	228	95	37	18	56
Zn	mg/kg	2600	1810	577	165	664
Ca	mg/kg	-	-	13400	4390	10200
K	mg/kg	-	-	728	948	742
Mg	mg/kg	-	-	3490	5720	2410
Na	mg/kg	-	-	305	408	303

3.7 Discussion for Headloss Studies

Results from the headloss tests of the present study show that as long as the underlying surface condition of the pipe is good, gains can be made from cleaning off the biofouling material both in terms of hydraulic and economic efficiency.

Although the thickness of the biofilms observed were anywhere from 2mm to 10mm in thickness, the surface was relatively smooth as could be expected from a slime type surface. However, the measurements indicated an equivalent sandgrain roughness greater than the underlying surface coating of the pipelines. This may be due to the visco-elastic film behaviour, the non-homogeneous cover of the biofilms of thin and thick patches, and possible streamer effects of EPS material interacting with the boundary layer flow as discussed by Picologlou *et al.* (1980) and Stoodley *et al.* (1988).

It was shown in Figures 3.12, 3.16 and 3.21 that behaviour of the fouled pipes may not follow a Colebrook-White type relationship in the smooth-rough transition regime, although results are probably too narrow in Reynolds number range to be conclusive. This is significant as the current testing methodologies and procedures usually use the Colebrook-White equation for analysis. For the conduits studies here, the majority of the flow regime operated within the transition regime.

Hydraulically rough or smooth limits are important where considering the optimal operating schedule for individual pipelines. It makes sense to keep pipes within the hydraulically smooth area to minimise energy loss in the power-generating scheme. This may require a maintenance program to better monitor biofouling, and schedule cleaning when the hydraulic roughness begins to enter too far into the transitional flow range.

Barton *et al.* (2007) and Buia (2006) report that the biofilm samples collected from Poatina and Tarraleah represent mature biofilms with complex spatial structure, believed to facilitate a high diversity. Such biofilms possess high niche-availability in terms of more physical habitats (i.e. from the formation of anaerobic pockets within the biofilm), and in utilisation of the variety of carbon sources available (Colin *et al.*, 2001). Masurat *et al.* (2005) found that low levels of total organic carbon (TOC) in water do

not prevent the formation of biofilms and that the most prolific bacterial growth occurred on surfaces exposed to the highest water flow, indicating that a high carbon flux past a surface benefits biofilm growth. Biofilm formation is also a common survival strategy of microorganisms in extreme environments (Costerton *et al.*, 1995).

The ratio of Carbon: Nitrogen: Phosphorous (C:N:P) of bacterial biomass in environmental biofilms has been reported to be approximately 50:10:1 (Chenier *et al.*, 2003). In contrast, the C:N:P of the biofilm of the Tarraleah No. 1 Hilltop Pipeline was 15:2:958. Phosphorous is clearly present in abundance in this pipeline, greatly exceeding microbial requirements. It is concluded that Phosphorous is probably present as an adsorbed component of the biofilm, with perhaps a smaller amount being immobilised within the microbial cells as crystalline phosphate (Barton *et al.*, 2007). Lower levels of phosphorus were found in the Poatina Penstock biofilm, but the sample showed higher levels of Carbon and Nitrogen than the Tarraleah sample.

Sulphur was similarly well in excess of microbial requirements in both samples, and Barton *et al.* (2007) states the same conclusions apply. High levels of adsorption of other metals within the biofilm were also indicated. Since these metals were probably present in oxidized states in the water, they are not likely to have been used as sources of energy by the biofilm organisms (Barton *et al.*, 2007).

Most of the detected bacteria in both biofilm pipelines are uncultured bacteria and typical of freshwater ecosystems (Rickard *et al.*, 2002). Many of the Alphaproteobacterial clones detected were closely related to the metal-depositing-bacterium *Pedomicrobium sp.* These have the capacity to incorporate oxides of iron or manganese or both on their cell-surfaces or within hyphae (Holt *et al.*, 1994) using an enzymatic process (Larsen *et al.*, 1999). This may explain the high level of these metals found in the biofilms. Buia (2006) contains further details on the microbiological aspects of the biofouling in the conduits studied.

3.8 Surface Coating Trials

3.8.1 Introduction

It was reported in Chapter 2 that biological growths affect the performance of Hydro Tasmania hydraulic conduit assets. These growths change wall surface properties over time and reduce the efficiency of open channel and pipe systems. Hydro Tasmania has known this for some time (see McFie, 1956; McFie, 1973; McFie, 1976; see Brett, 1980), and subsequently commissioned an investigation in partnership with the University of Tasmania, School of Engineering looking at ways to control biological growths. As part of this study, trials of different paints commenced in late 2001 and early 2002. Over the course of the study, approximately monthly site visits took place to photo document the ability of these paints to retard biological growths. This section gives the findings of the study, and recommends some paints that performed better than others.

The location of the study was the Tarraleah No. 1 Canal system. Tarraleah is shown in the map of Figure 3.1. This canal is subject to regular cleaning at approximately 6 monthly intervals. Such cleans (mechanical scrubbings) are a costly event, also requiring considerable downtime. As such, the Tarraleah No. 1 Canal was an ideal candidate to undertake paint trials as the eventual recipient of the successful paint.

Three locations (two along the canal and one at the pond) were selected, broadly described as an exposed area, a shaded area and a low velocity area to undertake the studies. These locations are described fully in Chapter 4.

The trial period of over two years enabled detailed observations and conclusions to be made on a surface coating.

3.8.2 Method

The method behind the paint trial study involved the installation at different sites along the Tarraleah No. 1 Canal and No. 1 Pond of test plates (see Chapter 4). These test

plates were arranged in a frame on the canal wall (see drawing in Barton and Sargison (2004)), shown in the photo of Figure 3.22. When submerged in water they were at an approximate depth of between 0.3m for the top plates to 1.0m for those at the bottom (Figure 3.23a). They were hauled out with hooks, photographed on the ground (Figure 3.23b), and then quickly re-deployed in the canal. No biofilm samples were taken from these plates for biological analysis.

The test plates were made of mild steel and were the substrate for the paints. Some plates had a rapid set cement applied to replicate a canal wall concrete mortar lining. The surface coatings were applied to the plates according to manufacturer specifications. Some plates were also marked to allow photogrammetric measurement, described in Chapter 5, to map the growth and surface roughness of biofouling material over time.

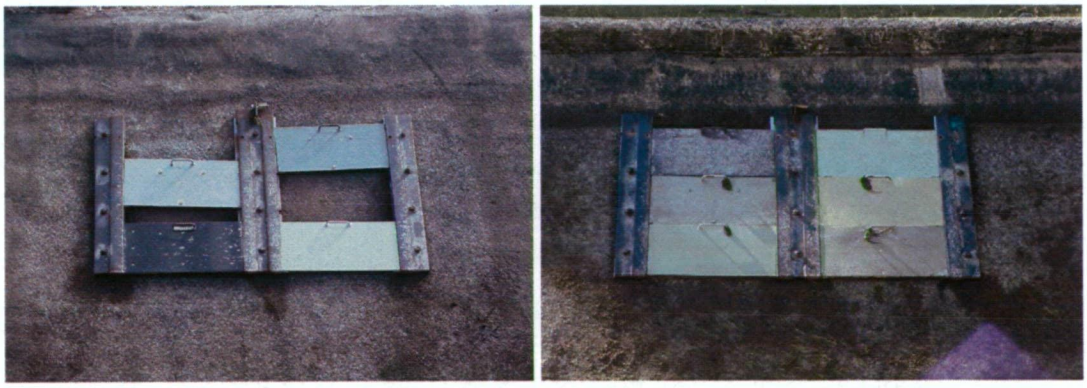

Figure 3.22: Typical test plate arrangement installed in Tarraleah canal system.

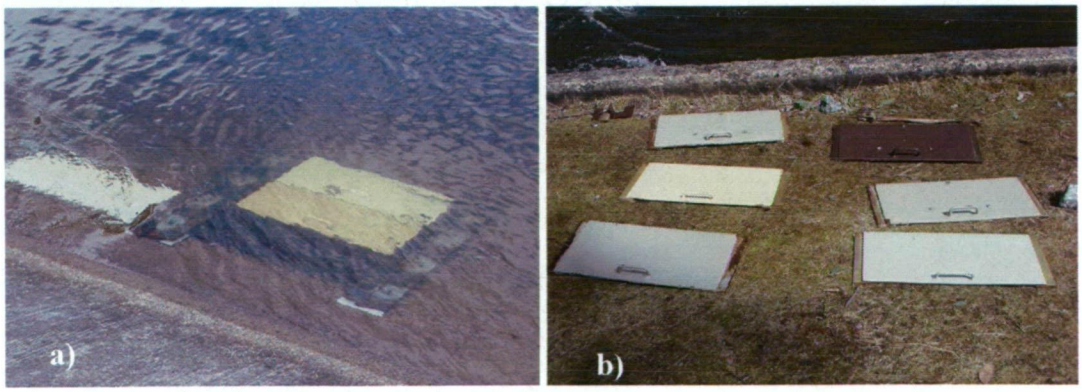

Figure 3.23: Submerged test plates in Tarraleah canal (a), and the test plates on the canal bank ready to be photographed (b).

As much as practicable, visits were made approximately monthly to photo document the performance of each of the test plates and respective coatings. The complete photo documentation is included in Barton and Sargison (2004) in Volume 2 of this thesis.

The comparative performance of paints was tested by deploying an initial set of plates with different paints in Tarraleah No. 1 Canal. This set represented the coatings under test, and where multiples of one coating was available, these were placed at different depths and/or different sites to remove bias from the test.

After 6 months this initial test was concluded. All plates were removed and cleaned (to grading A, explained subsequently). The coating locations were rearranged, coatings with less than grading C were removed from the test and new coatings were installed. Superior coatings were retained as controls and at each site a plate was returned to the same location as previous tests to act as controls.

3.8.3 Site Locations for Paint Trials and Test Plates for Laboratory

Three sites were chosen to trial the different surface coatings and paints. Chapter 4 outlines these sites in more details. Only a brief overview is given here.

The three sites were chosen due to the observed difference in growth which occurred at the sites. Also, they all displayed different environmental or flow conditions.

The first, at the most upstream location was at No. 9 Bridge (see Figure 4.10 in Chapter 4). This is a long straight section exposed to full sunlight for most of the day. Flow velocity at the water surface was approximately 2m/s.

The second site was just downstream of Transition No. 4 (see Figure 4.12) where the above ground flume section transitions to an in-ground trapezoidal section. The site was located on a bend, and had a mix of shade and sunlight throughout the day. Flow was clearly turbulent and large eddies and up welling was apparent due to the secondary flows.

The most downstream location was No. 1 Pond, which forms the confluence of No. 1, and No. 2 Canals (Figure 4.14). This location had full sun all day, and being a large

pond, the hydraulic conditions were different. Flow velocities were approximately 0.5m/s to 1m/s depending on the relative contributions of flow from the two inflowing canals.

Its important to note that although both canals receive water at Butlers Gorge dam at Lake King William, No. 2 Canal also has some natural inflow from local catchments. Sections of the canal are also earth lined (No. 1 canal is concrete lined the entire way except for two inverted siphons), making the water quality more variable and most likely with higher nutrient levels.

3.8.4 Paint Performance Grading

To assess the performance of the various paints trialled, a grading system was devised. The grading system is based on the relative performance of the paints, with the worst performing paint awarded an F, the best awarded an A. Therefore, gradings of F, E, D, C, B and A denote incrementally better performing paints. More detail of the grading method is explained subsequently and can also be found in Barton and Sargison (2004).

A test plate with a grading of F (Figure 3.24) indicates a fully fouled plate, with the biofilm thickness in the order of several millimeters. The biofilm consists of large and numerous clumps of gelatinous algae formations, with a coverage over the entire plate. A test plate with a grading of E (Figure 3.25) indicates a very fouled plate, with the biofilm thickness in the order of several millimeters. The biofilm consists of large and numerous clumps of gelatinous algae formations, however, the biofilm may not cover the entire plate and may appear as patches.

Figure 3.24: Plate with grading F.

Figure 3.25: Plate with grading E.

A test plate with a grading of D (Figure 3.26) indicates a moderately fouled plate, with the biofilm typically a few millimeters thick. The biofilm consists of a thin layer of biofilm with some clumps of gelatinous algae formations. The biofilm may not cover the entire plate and may appear as patches. A test plate with a grading of C (Figure 3.27) indicates a lightly fouled plate, with the biofilm less than a few millimeters thick. The biofilm consists only of a thin layer of biofilm with no clumps of algae present. The biofilm may not cover the entire plate.

Figure 3.26: Plate with grading D.

Figure 3.27: Plate with grading C.

A test plate with a grading of B (Figure 3.28) indicates a very lightly fouled plate, with the biofilm found to be present by wiping a finger across the surface and looking at the residue. The biofilm may not cover the entire plate. A test plate with a grading of A (Figure 3.29) indicates a clean plate, with no biofilm present.

Figure 3.28: Plate with grading B.

Figure 3.29: Plate with grading A.

Other grades were used to describe paints that were not appropriate for the aforementioned grading system. A test plate with a grading of X_p (Figure 3.30) indicates a test plate where the paint has failed and detached. A test plate with a grading of X_c (Figure 3.31) indicates a test plate failure due to the rapid set cement under the paint detaching.

Figure 3.30: Plate with grading X_p.

Figure 3.31: Plate with grading X_c.

3.8.5 Results

Only a concise account of the results are provided here, the full set of results for the study are presented in Barton and Sargison (2004) in Volume 2 of this thesis. From the more than 20 paint and surface preparation combinations, 5 paints were selected as clear standouts. In order of the best performing, the top five were:

- Polythene, 5mm thick sheet (widely available)
- Sigma Jotamastic 87 (Jotun brand), two-component epoxy mastic coating
- Wattyl Sigma/Seaslide (Wattyl brand), two-component solvent free amine cured epoxy coating
- Bio-Dur 561 (MRJ Industrial Services), high performance Kevlar reinforced epoxy coating
- Bio-Gard 258 (MRJ Industrial Services), high performance Kevlar reinforced epoxy coating

3.8.6 Discussion

General observations were made during the course of the paint trials. They are:

- There was increased growth with depth, thought to be related to the amount of ultra-violet light able to penetrate into the water (Buia, 2005).
- There was more growth at Transition No. 4 due to more shading (less UV light), influenced by different flow regime with secondary currents.
- No. 1 Pond had the greatest growth of the three sites thought to be primarily due to lower velocities, higher nutrient levels, and kinder environment for growth in general. Note that due to the lower velocities a larger growth in this region is permissible.

- Winter months see noticeable reduction in biofilm activity, with little or no growth. This is thought to be due to the decrease in mean daily temperatures.
- There may be a reduction in fouling material due to new growth not able to keep up with shear forces sloughing off growths.
- Warmer summer months see generally greater growth activity.
- The biofilms were observed to be low form gelatinous clumps, consistent with Type A biofilms described in Chapter 2. No filamentous growths were observed.
- At times, significant numbers of invertebrate organisms were present on the canal walls. Immediately after cleaning of the canal Black Fly larvae (Barmuta, 2005) populated the vacant surfaces of the canal wall. Its seems some invertebrates compete for wall space with biofouling material, with the biofilms eventually winning out. This is thought to be opportunistic behaviour, as the invertebrates were observed in both warm and cold months.

Due to the qualitative nature of the grading system (Figure 3.24 to 3.31) based on photos of the plates over time with field inspections, the recommended paints could be argued to not be a definitive result. Other factors such as the friction characteristics of the paints, were not studied, nor the economic/cost characteristics of the paints. These details are the subject of further related studies as part of the joint research project between Hydro Tasmania and the University of Tasmania.

Further comments are made on individual paint performance in Barton and Sargison (2004) in volume 2 of this thesis.

3.9 Chapter Summary and Conclusions

This chapter has demonstrated the industrial application of this research and identified the impact of biofouling on the operation of pipelines and canals. This type of investigation has been highlighted by Groenenboom (2000) as necessary to complement laboratory scale experiments. The principal biofilm species in this application have been identified with ongoing work being done by Buia (2006) and Perkins (2006). Work is also continuing on the selection of paint for their antifouling and low friction properties by Andrewartha (2006). Hydro Tasmania is also continuing a conduit cleaning and

headloss testing program aimed at improving the current scheduled maintenance practices.

3.9.1 Headloss Studies

Better understanding of biofouling problems requires regular monitoring of pipeline headloss characteristics, and further efforts to quantify the level of growth on internal surfaces. Accurate field tests of large conduits pose significant problems.

The friction behaviour of biofouled surfaces may not follow a Colebrook-White type relationship in the smooth-rough transition regime. Designers of hydraulic conduits should take this into account.

Better understanding is still needed on the causes of biofilm growth and variables which influence on biofouling character. Headloss tests of individual conduits are the best method of determining roughness character and re-growth properties in conjunction with more fundamental laboratory based research on the problem.

3.9.2 Paint Trials

The trials of different paints to study their performance over time with regards to biofilm growths has been described. The trials form part of a larger program investigating ways in which to understand and control the problem of biofouling of hydraulic conduits within Hydro Tasmania power schemes.

The study was based on the photo documentation of various paints for a period of up to two years in Tarraleah No. 1 Canal and No. 1 Pond. Approximately monthly site visits enabled an assessment of the ability of the paints to impede biological growth.

This study is able to conclude that there are a group of paints that clearly failed, and a group that has a good ability to resist fouling. There were also many paints with moderate to poor performance ratings.

Further investigation into the friction characteristics of the paints is required, along with a cost-benefit analysis to determine the economic viability of relining various conduits. This introductory work identified the basis for ongoing work on biofilm character and surface roughness properties outlined in the succeeding chapters of this thesis.

Chapter 4 Test Plate Details, Deployment Strategy and Schedule for Testing

4.1 Introduction

Five types of test plate were used in the present study using two sizes of panel. They were:

Small plate:	fine grit
	coarse grit
	smooth painted
Large plate:	fine grit
	smooth painted

The small sized test plates were used for the paint trials (presented in Chapter 3) and photogrammetric studies (presented in Chapter 5). The large plate were used for the photogrammetric studies (Presented in Chapters 7 and 8) and the laboratory measurements using the water tunnel (introduced in Chapter 6 with results also presented in Chapters 7 and 8).

This chapter introduces each type of plate and the reason the surface finish on each plate was chosen. Other details such as dimensions are also presented. The strategy for the deployment of each plate is explained, with the field locations used for deployment described. A summary of the testing schedule is presented for the photography and measurement in the laboratory.

4.2 Simulation of Surface Conditions Using Test Plates

The smooth and rough plates represent a refurbished canal wall, and an aged canal wall respectively. The smooth and rough plates also present interesting research questions such as "how the biofilm will change the surface in the long term?"

For example, Figure 4.1 shows at top a clean, unfouled rough surface. Over time will the surface gain a general layer of growth that covers everything (middle), or will the biofilm show more specialised properties such as at the bottom? Nikora *et al.* (2002) described the phenomenon of biofilms growing on top of roughness elements, and proposed that this may be due to the biofilm placed on top have a competitive advantage over those biofilms in the valleys due to the better uptake of nutrients from the closer proximity to the diffusive sublayer. This complements the work of Stoodley, P *et al.* (1999) who discusses the process of biofilm nutrient uptake in the context of flow hydrodynamics.

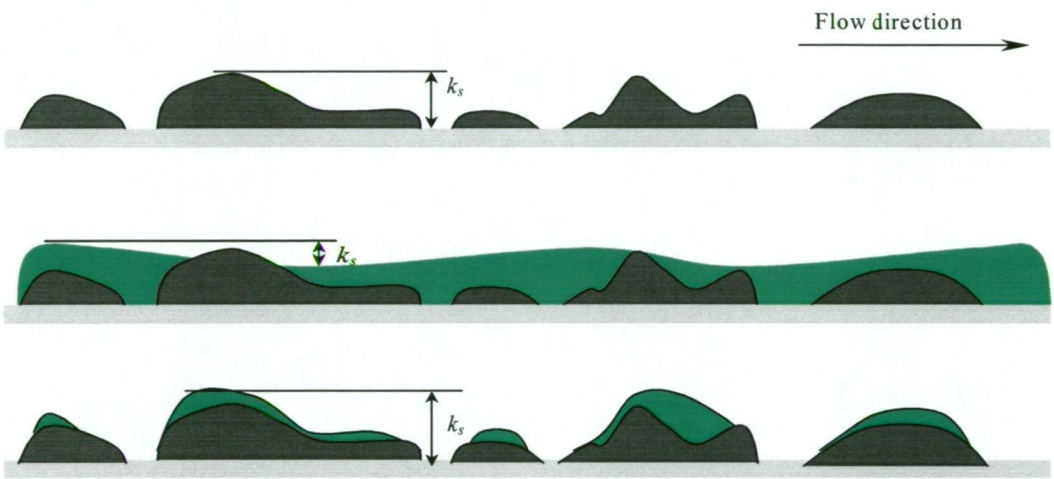

Figure 4.1: Biofilms growing on a rough surface showing different possible scenarios.

A smooth wall, such as that represented at the top of Figure 4.2, will over time gain a biofilm that will change the surface roughness regardless of any special biofilm properties. No biofilm will develop a surface exactly parallel to the clean surface, be of a homogeneous nature, and be hard non-elastic like the surface beneath. So, would refurbishing a rough concrete surface with a smooth surface be a worthwhile exercise?

This thesis looks at this further by studying biofilms on smooth and rough plate surfaces.

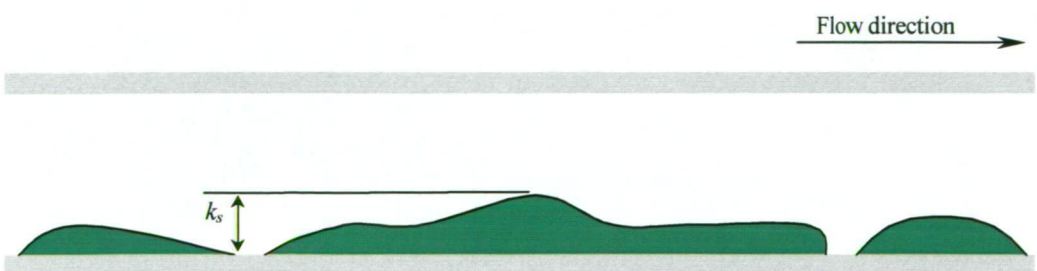

Figure 4.2: Biofilms on a smooth surface.

4.3 Small Test Plates

The small test plates used measured 600mm long, 300mm wide, and 6mm thick and were fabricated from mild steel. They were used for paint trials (Chapter 3) and for photogrammetric studies (Chapter 5). Figure 4.3 shows two photos of the small plates mounted in Tarraleah No.1 Canal. The plates were fixed to the canal wall by rails, enabling the plates to be placed in or pulled out easily. The same rail mounting arrangement was used for both the small and large test plates. A maximum of six plates could be mounted at each location at any one time. The locations are discussed in section 4.5 of this chapter.

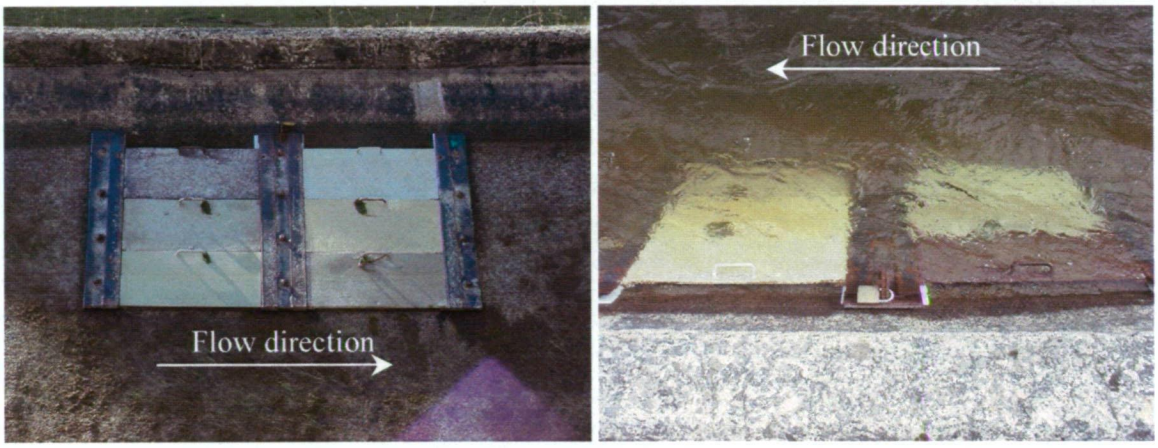

Figure 4.3: Small test plate arrangement in the Tarraleah canal system.

4.4 Large Test Plates

The large test plates were used for water tunnel measurements and complementary photogrammetry studies. They were constructed of stainless steel and measured 997mm long, 597mm wide and 3mm thick. Six were manufactured: three with a smooth painted surface, and three with fine grit, artificially rough surface, the same as the fine grit small plates. One each of the smooth and rough plates acted as controls and remained in the laboratory. The other four were deployed in Tarraleah canal system, allowing biofilms to grow and develop before being brought back to the laboratory for photography and water tunnel measurements. Figure 4.4 shows both the smooth and rough large plates in their clean condition.

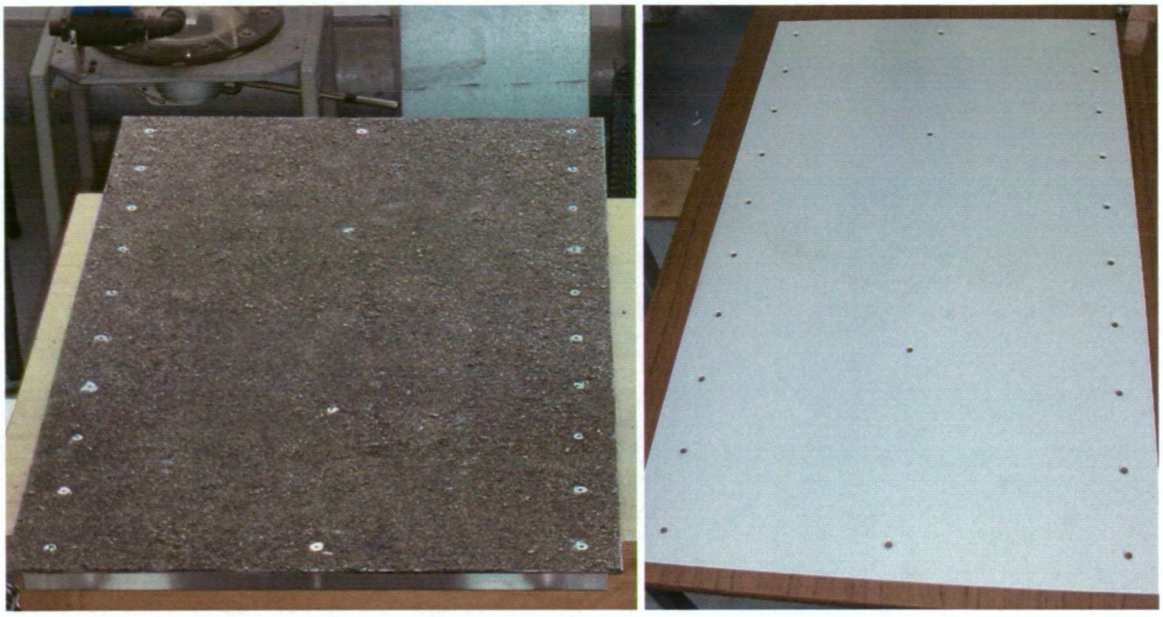

Figure 4.4: Large test plates in their clean condition. Artificially rough surface (a) and smooth painted surface (b).

The large test plates had special backing plates for their deployment in the field. This was to allow their mounting at the same locations as the small plates, and to provide extra protection whilst in transit and during handling. Figure 4.5 shows the aluminium backing plates. These were 5mm thick, and 600mm wide by 1010mm long.

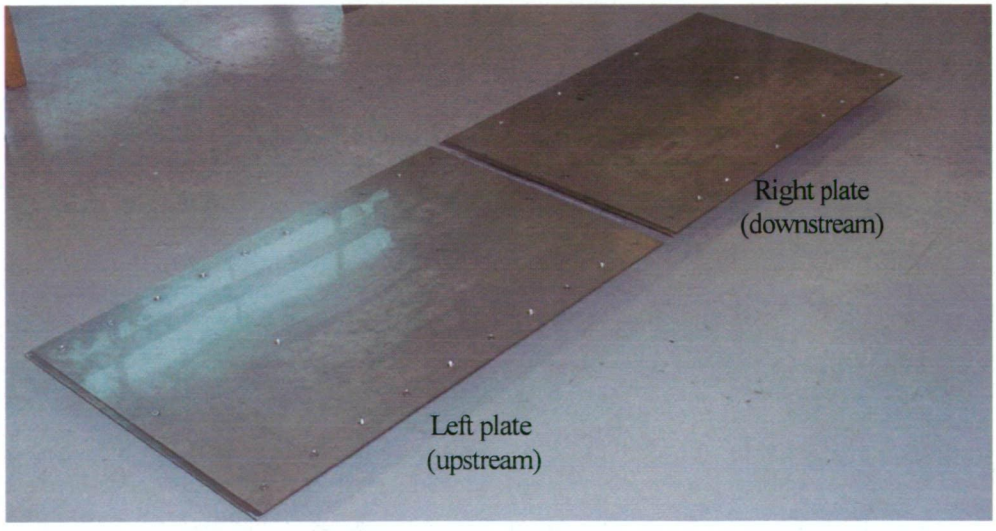

Figure 4.5: Test plate support plates used for deployment in the field.

4.5 Field Installation of Test Plates

The typical arrangement of the test plates while deployed in the field is shown in Figure 4.6. This changed when individual plates were withdrawn and taken to the laboratory for photography and/or water tunnel measurements. Large plates were always placed at the bottom. The approximate high water line can be seen on the photo.

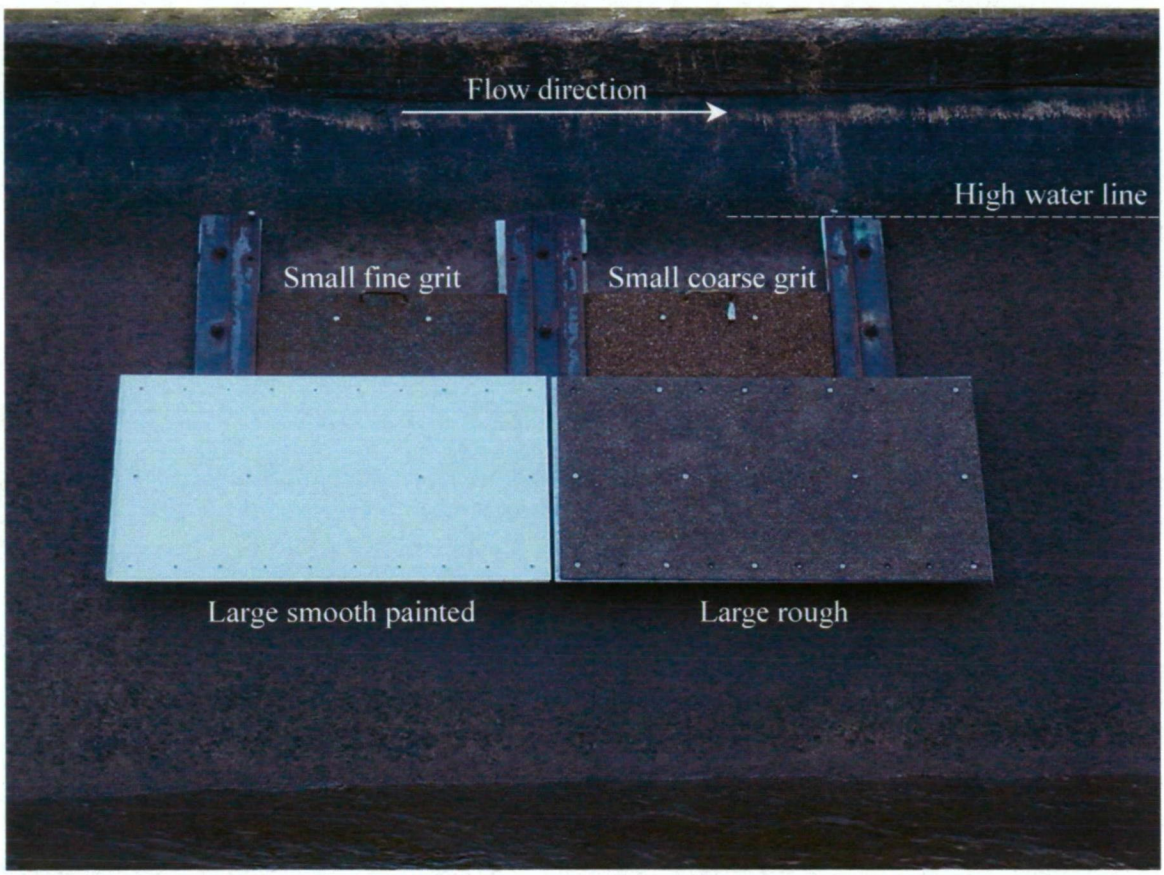

Figure 4.6: Large and small test plate general arrangement in Tarraleah No. 1 Canal.

Figure 4.7 shows more clearly at what depths the plates were mounted in water. The canal water line when flowing full can be seen, and is approximately 300mm (vertically) above the top of the small plates. The plates could not be mounted any lower as they would not then be able to be retrieved easily and safely.

Figure 4.7: General arrangement of test plate mounting in canal.

The mounting of the plates was designed so that the plates were as close to the wall as possible to best replicate the wall shear and prevailing flow velocities (Figure 4.8). The large plates projected about 60mm into the flow, the small plates about 20mm.

Figure 4.8: The plates were mounted as close to the wall as practicable.

4.6 Field Locations for Test Plate Deployment and Data Collection

The work reported in this chapter was undertaken on the Tarraleah canal system. Figure 4.9 shows a schematic of Tarraleah Canal No. 1 and Pond No. 1. The black dots indicate the approximate locations described, where B9 is Bridge No. 9, T4 is Transition No. 4, B3 is Bridge No. 3 and P1 is Pond No. 1.

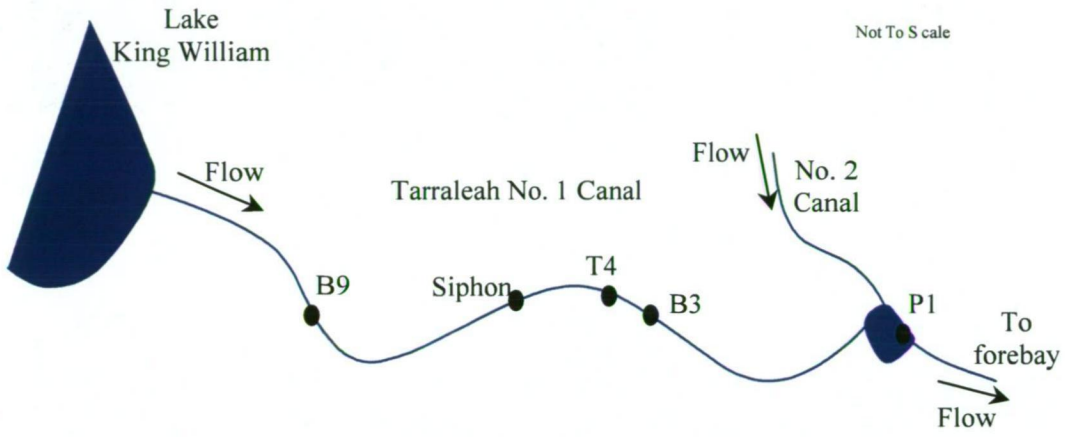

Figure 4.9: Schematic layout of the Tarraleah canal system showing the various locations where data were collected and test plates deployed.

Water is released into Canal No. 1 at Clark Dam where it first passes through Butlers Gorge Power Station. Water is also released into both the high level Canal No. 2 and the start of the Derwent River.

Canal No. 1 is approximately 20 km long with a design capacity of 25.6 m^3/s. It is mostly trapezoidal in cross section with some above ground rectangular flume sections, and a steel inverted siphon takes it across a deep valley.

Canal No. 2 is approximately 11 km long with a design capacity of 8.5 m^3/s. Canal No. 2 takes a different route from Canal No. 1, passing through a series of tunnels, inverted siphons and canal sections. Canal No. 2 also has inflow at several locations from naturally occurring local catchment runoff. Canal No. 2 flows into Pond No. 2.

Flow from Canals No. 1 and No. 2 join at Pond No. 1, which flows to the Tarraleah Forebay. Water from the Forebay flows into large low pressure Hilltop Pipelines No. 1 and No. 2, which were the subject of headloss testing, discussed in Chapter 3.

Flow passes through the Hilltop Pipelines past two large surge towers at their approximate halfway point, Hilltop Valves, before flowing into six high pressure penstock pipelines, which feed six Pelton turbines at Tarraleah Power Station. Flow from the power station then flows to the Nive River and on to Lake Liapootah.

Table 4.1 details the use of, and information gathered at, each location on the Tarraleah canal system. Each location can be found on Figure 4.9. Surface roughness data at the inverted siphon shown in Figure 4.9 is presented in Chapter 5.

Table 4.1: Study locations and parameters measured.

Bridge No. 9	**Transition No. 4**	**Bridge No. 3**	**Pond No. 1**
Paint Trials	Paint Trials	Water Quality Sampling	Paint Trials
Water Quality Sampling	Test Plate deployment	Microbiological studies (see Buia (2006))	Test plate Deployment
	Temperature Monitoring	Temperature monitoring	Temperature Monitoring

4.6.1 Bridge No. 9

Tarraleah Bridge No. 9 was the most upstream location on the canal system. Figure 4.10 shows the site is located on a long straight section. Figure 4.11 shows the dimensions for the trapezoidal section. The site is exposed to full sun for the entire day. The water surface velocity is approximately 2m/s.

Figure 4.10: Photo showing Bridge No. 9. Note the exposed, straight section location.

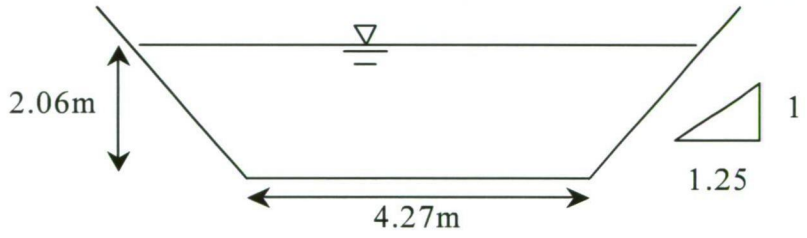

Figure 4.11: Dimensions for Tarraleah Canal No. 1 trapezoidal channel section.

4.6.2 Transition No. 4

Tarraleah Transition No. 4 is the next location several kilometres downstream from Bridge No. 9. Dimensions are the same as shown in Figure 4.11. The site is located on a bend as shown in Figure 4.12. The transition is so called as the cross section changes from a rectangular flume section upstream to a trapezoidal section. The site is exposed to direct sunlight for a period typically shorter than Bridge No. 9, as the surrounding vegetation increases shading in the early morning and late afternoon. Because the section is sinuous,

secondary currents are present, with large eddies and upwelling observed washing past the site.

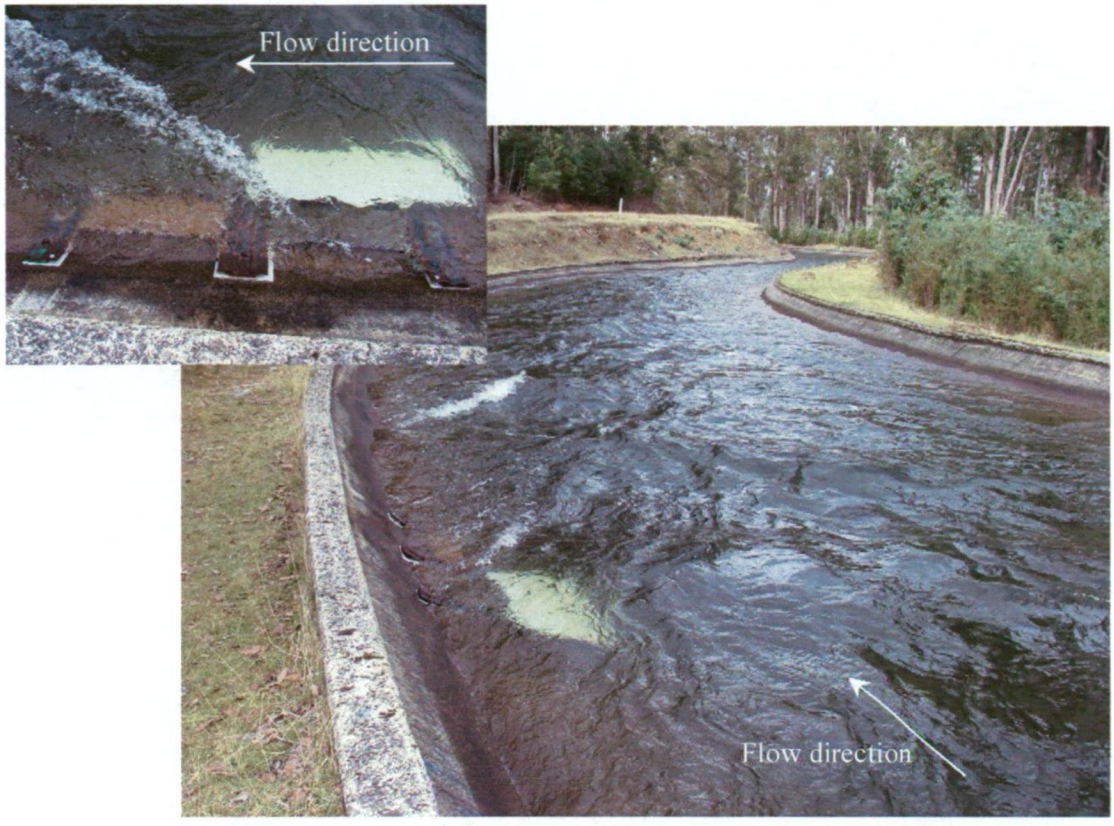

Figure 4.12: Test plates mounted at Transition No. 4 shown while canal full.

This site was chosen to deploy the small test plates for photogrammetry and also to the large smooth and rough plates for laboratory measurements. The plates deployed here grow biofilms conditioned to high flow velocities.

4.6.3 Bridge No. 3

Tarraleah Bridge No. 3 is just downstream of Transition No. 4. This site was not used extensively for the present study, however water samples were taken here for chemical analysis and water temperatures were also monitored. This location is significant mostly as this is where a major microbiological investigation is underway by Buia (2006). Figure 4.13 shows the site. The steel frame suspended from the bridge is for the microbiological investigation.

The site is on very gentle, long radius bend. It receives sun for only part of the day due to the encroachment of vegetation.

Figure 4.13: Photo showing Bridge No. 3.

4.6.4 Pond No. 1

Tarraleah Pond No. 1 shown in Figure 4.14 is exposed to sunlight for the entire day. The flow is significantly slower than the other two sites, at only approximately 1m/s. The pond forms the confluence of Canals No. 1 and No. 2. Canal No. 2, has sections of earth lining, and will have different water quality characteristics to Canal No. 1, which is concrete lined the entire length.

The pond itself also has rock and earth lined sections. When empty, the vegetation and earth lined sections are clearly seen (Figure 4.15).

This site was chosen to deploy the small test plates for photogrammetry and also large smooth and rough plates for laboratory measurements.

The biofilms that grow here are conditioned to lower flow velocities.

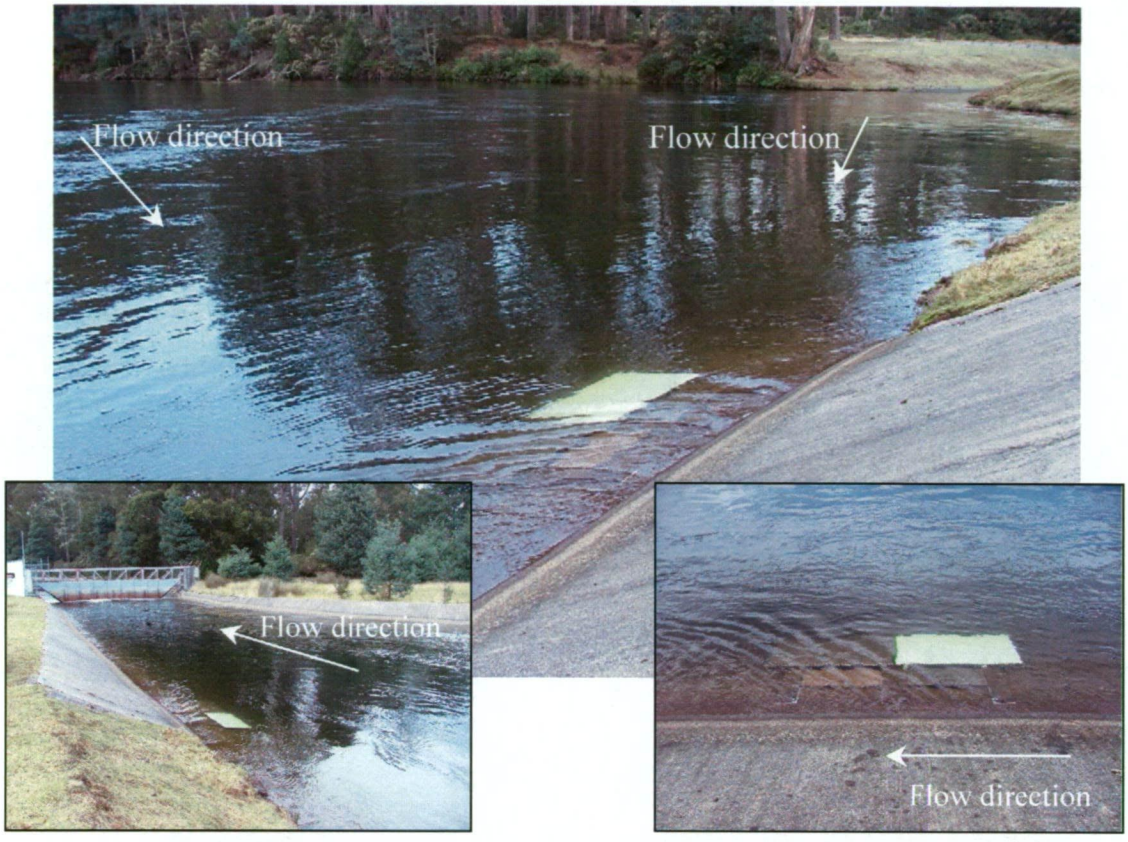

Figure 4.14: Test plates at Pond No. 1 shown while pond full.

Figure 4.15: Tarraleah Pond No. 1 when empty, displaying earth lined sections and large amounts of aquatic vegetation. The dashed circle shows where the test plates were mounted.

4.6.5 Plate Retrieval

All plates were made with either a handle or large loops to allow them to be removed from the canal with long handled hooks. Figure 4.16 shows the removal of a test plate with one of these hooks. Care was taken when retrieving plates so as not to damage plate surface, particularly the biofilm growths.

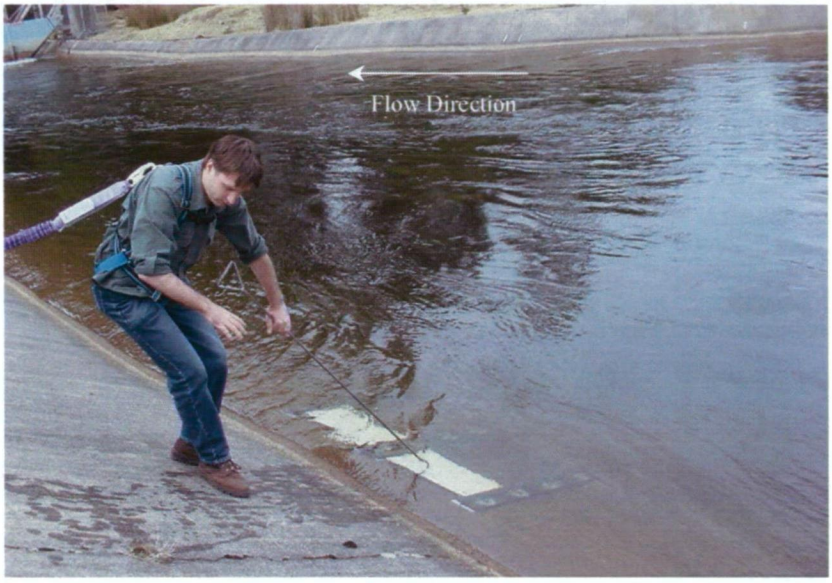

Figure 4.16: Photo showing retrieval of test plates with fall arrest harness and hook.

4.7 Test Plate Surface Coating Details

As discussed in the Introduction (section 4.1), there were five types of test plate used in the present study.

An artificially rough surface was developed to provide a likeness to the surface finish of the aged concrete open channels being studied, while also providing a finish not unlike the sandgrain roughness of Nikuradse (1933).

In collaboration with Osborn (2006), different surfaces were trialled to find material with appropriate optical texture for the photogrammetry requirements (see Chapter 5) and

robustness for deployment in the field. Various types of sandpaper were found unsatisfactory (Stanborough, 2003) as these did not have enough contrast or texture. Eventually two types of sand were found to have a good mix of grain texture and particle size to provide two types of artificially rough surface. Figures 4.17 and 4.18 show photos of the coarse grit and fine grit respectively with a rule inset as a scale.

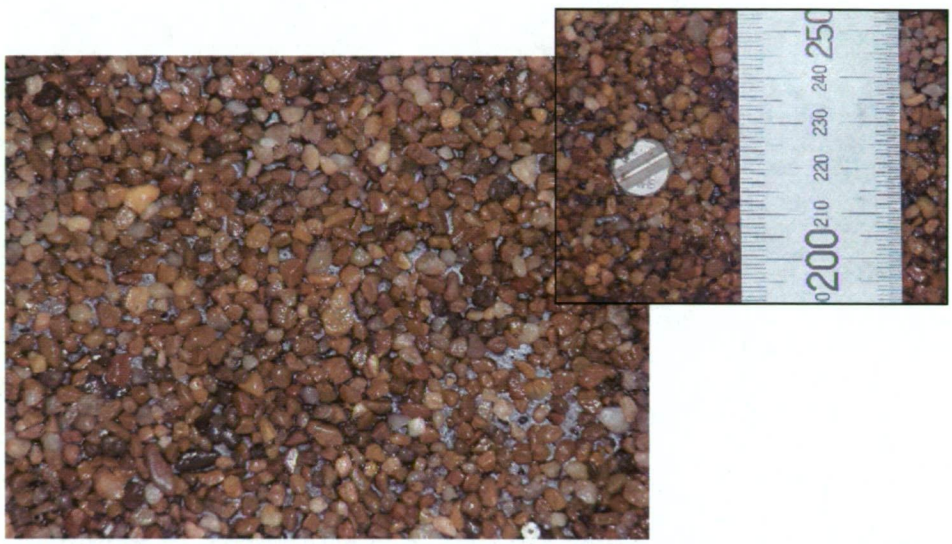

Figure 4.17: The coarse grit finish used on the small test plates showing scale in mm.

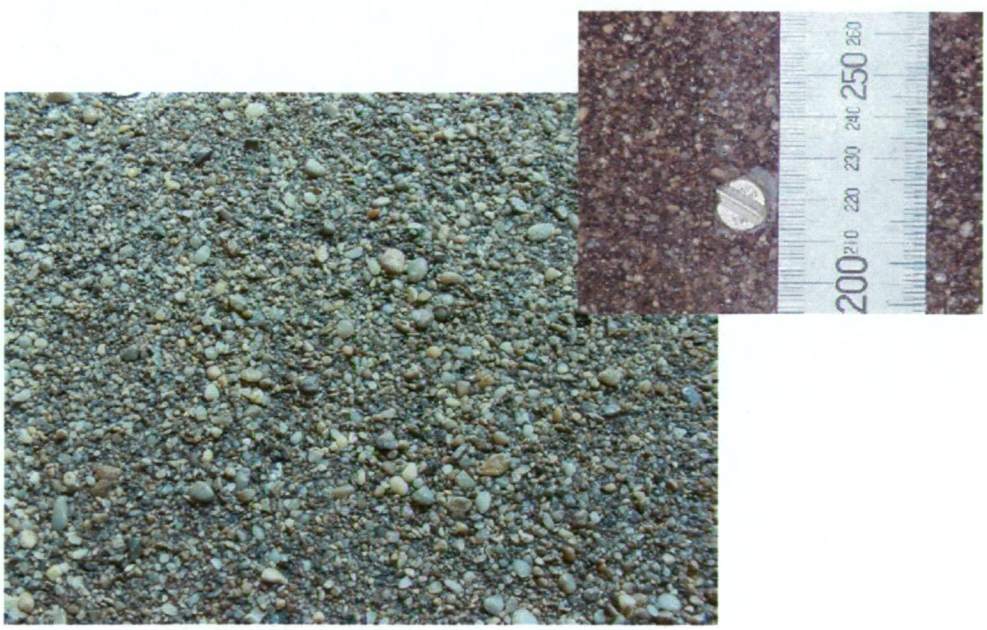

Figure 4.18: The fine grit finish used on the small test plates showing scale in mm.

The two types of grit were used, primarily as an aid to develop the photogrammetry in collaboration with Bendall (2005) and Osborn *et al.* (2005), and also to study the effect of biofilm growth on different grades of roughness (presented in Chapter 5).

A study of particle size distribution was undertaken on the two grits. Using standard soils science methods, several sieves of different aperture were used to determine the percent mass of each. These are presented in Figures 4.19 and 4.20 for the coarse and fine grits respectively, with the data shown Table 4.2.

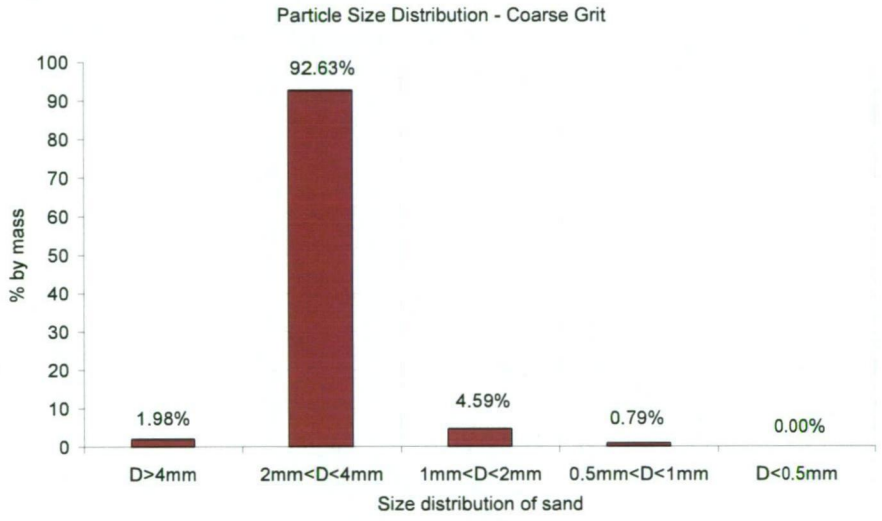

Figure 4.19: Particle size distribution for coarse grit.

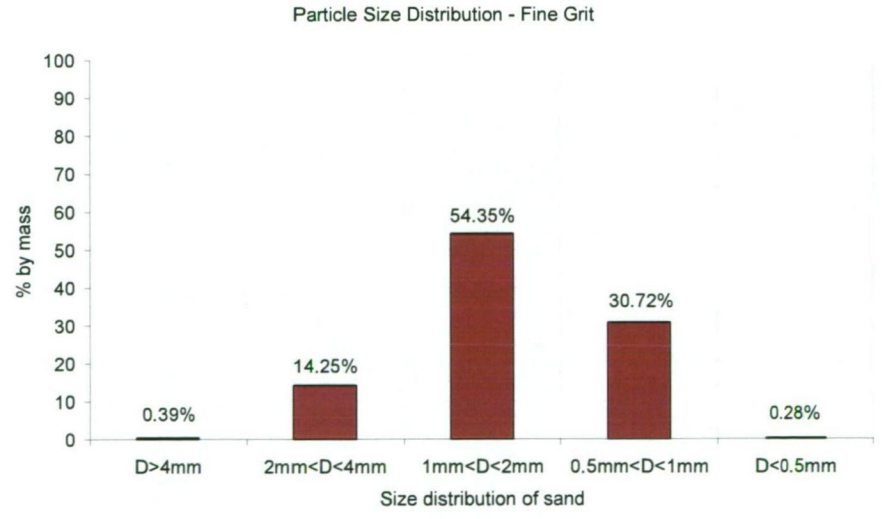

Figure 4.20: Particle size distribution for fine grit.

Particle size distribution analysis shows that the coarse grit is more uniform in its diameter than the fine grit. The fine grit is a washed river sand, horticultural propagating mix, whereas the coarse grit is screened (for size) sand that was made for use as bed gravel for fish aquariums. This data is used to compare the results of water tunnel and photogrammetry roughness characterisation in later chapters.

Table 4.2: Results for the particle size distribution analysis.

Propagating Sand Mix					
Artificially Rough Surface - Fine Grit					
Sieve Aperture Size	Size Distribution of Particles	Total Mass (grams)	Sieve Mass (grams)	Sand Mass (grams)	% Total Mass
1st Sieve (4mm)	D>4mm	423.00	418.80	4.20	**0.39**
2nd Sieve (2mm)	2mm<D<4mm	552.10	400.20	151.90	**14.25**
3rd Sieve (1mm)	1mm<D<2mm	930.40	351.20	579.20	**54.35**
4th Sieve (0.5mm)	0.5mm<D<1mm	625.70	298.40	327.30	**30.72**
Remaining	D<0.5mm	246.60	243.60	3.00	**0.28**
			Total:	**1065.60**	
Artificially Rough Surface - Coarse Grit					
Sieve Aperture Size	Size Distribution of Particles	Total Mass (grams)	Sieve Mass (grams)	Sand Mass (grams)	% Total Mass
1st Sieve (4mm)	D>4mm	434.50	418.80	15.70	**1.98**
2nd Sieve (2mm)	2mm<D<4mm	1140.70	406.50	734.20	**92.63**
3rd Sieve (1mm)	1mm<D<2mm	387.20	350.80	36.40	**4.59**
4th Sieve (0.5mm)	0.5mm<D<1mm	249.90	243.60	6.30	**0.79**
Remaining	D<0.5mm	0.00	0.00	0.00	**0.00**
			Total:	**792.60**	

4.7.1 Preparation of Test Plate Surfaces

The artificially rough plates were prepared by first applying a tar (Hydro Seal) to the plate on which the grit was to be fixed. Figure 4.21 shows a partially coated plate. An even coat of tar was first applied to a clean surface, with fine or coarse grit then applied and pressed in. When the tar had cured, normally after 12 hours, the surface was screened to make it flat and remove excess grit. Note the photogrammetry camera rig reference point (centre) and three locator bolts in Figure 4.21. These are discussed in Chapter 5.

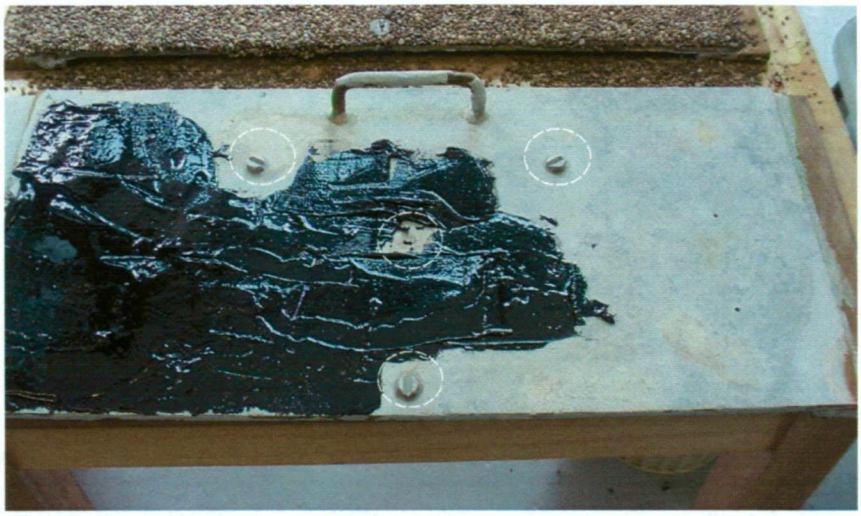

Figure 4.21: A small test plate being prepared for an artificially rough surface.

The Hydro Seal tar is for use on tanks and gutters, and can be used with potable water supplies. To ensure the tar did not unexpectedly retard biofilm growth, a control plate was created (Figure 4.22) and deployed in the field as part of the paint trial studies (see Chapter 3). It was found biofilm growth was not inhibited with a thin layer developing within the first month of deployment.

Figure 4.22: The test plate with tar surface finish deployed in the field.

4.7.1.1 Preparation of Small Test Plates

The small plates used for paint trials had surface coating applied according to manufacturer specifications, and was discussed in Chapter 3. The small plates with the fine and coarse grit applied are shown in Figure 4.23. Note that each of the small test plates (three fine grit and three coarse grit) had the photogrammetry reference points built into the plate. Two fine grit plate and two coarse grit plates were deployed in the field. One of each type at Transition No.

4 and Pond No. 1. The remaining fine and coarse grit plates were used as controls and photogrammetry development by Bendall (2005).

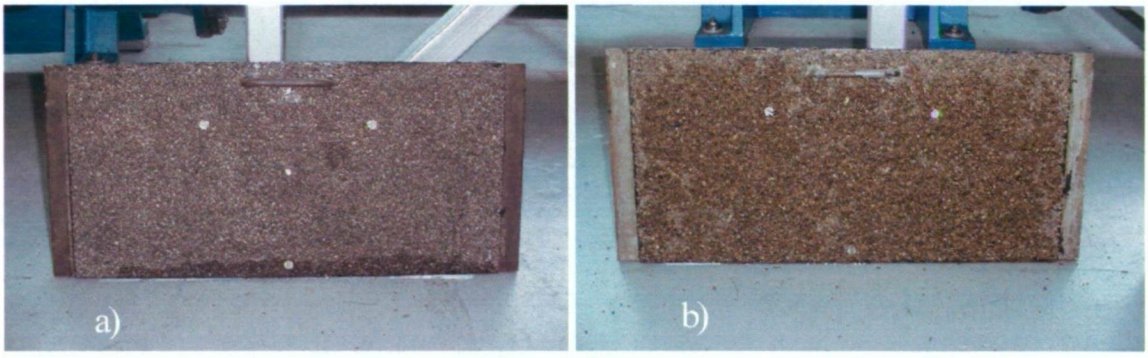

Figure 4.23: The finished product. Photos of one each of the fine grit (a) and coarse grit (b) photogrammetry test plates.

4.7.1.2 Preparation of Large Test Plates

The large test plates had either a fine grit rough surface finish like the fine grit small plate, or a smooth painted surface. The painted plates were spray painted with a Jotun brand (www.jotun.com) Jotamastic 87 two-pack paint. The Jotamastic type was found to be one of the better performing paints in the paint trial studies reported in Chapter 3. Care was taken to spray the paint to create as good a finish as possible. Spray painting was chosen (rather than, say, rolling or brushing), as this would be the most likely form of application if used in the field for relining or refurbishment of a canal. Four coats of the paint were applied to each plate as per manufacturer instructions. Figure 4.24 shows the finished large test plates.

There were six large plates in total, with three smooth painted plates and three fine grit rough plates. One of each type was deployed at Transition No. 4 and Pond No. 1 along with the small test plates. The remaining smooth and rough plates were kept in the laboratory as clean control plates for baseline measurements, and also photogrammetry development for baseline roughness data.

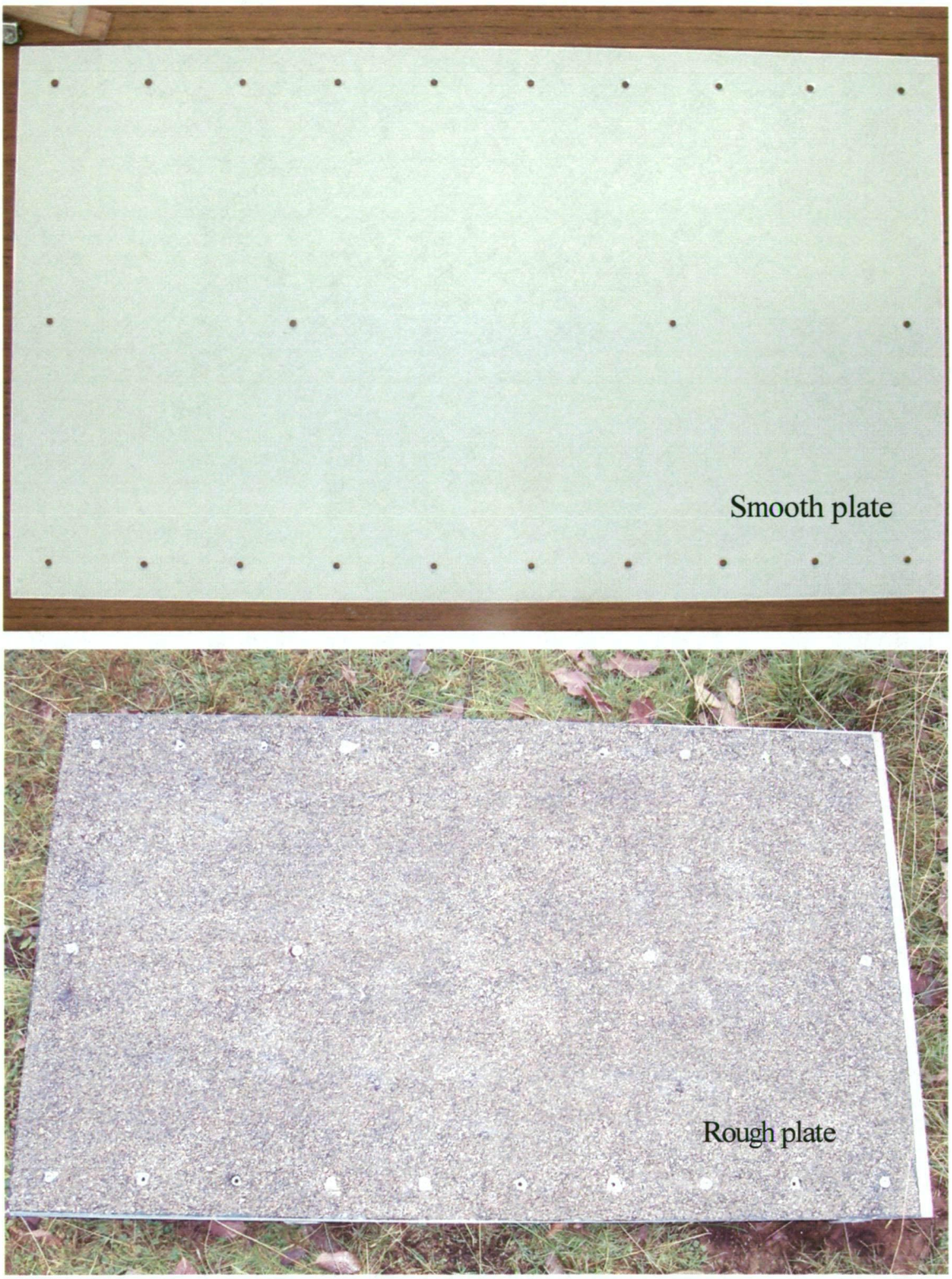

Figure 4.24: Large test plates (clean) looking from above.

4.8 Tarraleah No. 1 Canal Water Quality and Temperatures

4.8.1 Tarraleah Water Quality

Water from Tarraleah No. 1 Canal was sampled at monthly intervals for two 12 month periods to obtain water quality information. presents the data. The water samples were obtained at Bridge No. 9 (first 12 months presented in Table 4.3) and Bridge No. 3 (second 12 months presented in Table 4.4).

Table 4.3: Water quality data for Tarraleah No. 9 Bridge.

		Tarraleah No. Canal @ No. 9 Bridge											
		Date											
Analyte	Units	23-Jun-03	23-Jul-03	22-Aug-03	23-Sep-03	22-Oct-03	24-Nov-03	22-Dec-03	22-Jan-04	24-Feb-04	22-Mar-04	27-Apr-04	26-May-04
Ph													
EC	microS/cm												
Nitrogen total	(mg-N/L)	0.13	0.10	0.13	0.13	0.12	0.16	0.10	0.11	0.12	0.10	0.09	0.11
Phosphorous total	(mg-P/L)	<0.005	<0.005	0.01	<0.005	<0.005	<0.005	0.01	<0.005	<0.005	<0.005	0.01	0.01
Cd total	(µg/L)	<1	<1	<1	<1	<1	<1	<1	<1	<1	<1	<1	-
Co total	(µg/L)	<1	<1	<1	<1	<1	<1	<1	<1	<1	<1	<1	<1
Cr total	(µg/L)	<1	<1	<1	<1	<1	<1	<1	<1	<1	<1	<1	<1
Cu total	(µg/L)	2.00	<1	<1	<1	<1	<1	<1	<1	<1	<1	<1	<1
Fe total	(µg/L)	92.00	84.00	44.00	63.00	50.00	61.00	52.00	90.00	66.00	64.00	90.00	78.00
Mn total	(µg/L)	7.00	<5	<5	<5	<5	<5	<5	9.00	6.00	6.00	6.00	<5
Ni total	(µg/L)	<1	<1	2.00	<1	<1	<1	<1	<1	<1	<1	<1	<1
Pb total	(µg/L)	<5	<5	<5	<5	<5	<5	<5	<5	<5	<5	<5	<5
Zn total	(µg/L)	<1	4.00	<1	1.00	2.00	2.00	<1	<1	<1	2.00	<1	<1
S total	(µg/L)	275.00	347.00	303.00	281.00	275.00	284.00	286.00	270.00	283.00	268.00	247.00	272.00
Ca total	(mg/L)	0.88	0.98	0.85	0.86	0.91	0.91	0.90	0.91	0.81	0.84	0.84	1.54
K total	(mg/L)	0.10	0.13	0.10	0.11	0.13	0.16	0.13	0.14	0.12	0.11	0.10	0.16
Mg total	(mg/L)	0.60	0.63	0.56	0.57	0.58	0.66	0.58	0.64	0.49	0.62	0.60	1.02
Na total	(mg/L)	2.23	2.54	2.22	2.28	2.40	2.55	2.28	2.70	2.71	2.51	2.31	2.95
Organic Carbon total	(mg/L)	4.00	3.00	5.00	2.30	1.90	3.10	2.00	1.90	2.50	1.60	2.20	2.10
Al total	(µg/L)												64.00

Table 4.4: Water quality data for Tarraleah No. 3 Bridge.

		Tarraleah No. Canal @ No. 3 Bridge								
		Date								
Analyte	Units	17/05/05	14/06/05	12/07/05	23/08/05	6.09.05	4/10/05	1.11.05	13.12.05	17.01.06
Ph		6.40	6.30	6.90	6.80	6.60	6.60	6.40	6.50	6.70
EC	microS/cm	25.00	24.00	27.00	26.00	25.00	25.00	25.00	26.00	25.00
Nitrogen total	(mg-N/L)	0.14	0.13	0.14	0.14	0.11	0.11	0.13	0.11	0.12
Phosphorous total	(mg-P/L)	<0.005	0.01	0.01	<0.005	<0.005	<0.005	<0.005	<0.005	<0.005
Cd total	(µg/L)	<1	<1	<1	<1	<1	<1	<1	<1	<1
Co total	(µg/L)	<1	<1	<1	<1	<1	<1	<1	<1	<1
Cr total	(µg/L)	<1	<1	<1	<1	<1	<1	<1	<1	<1
Cu total	(µg/L)	<1	2.00	<1	<1	<1	<1	<1	2.00	<1
Fe total	(µg/L)	102.00	118.00	87.00	102.00	109.00	83.00	109.00	98.00	75.00
Mn total	(µg/L)	6.00	6.00	<5	<5	6.00	<5	<5	9.00	10.00
Ni total	(µg/L)	<1	<2	<2	<2	<2	<2	<2	<2	<2
Pb total	(µg/L)	<5	<5	<5	<5	<5	<5	<5	<5	<5
Zn total	(µg/L)	1.00	<1	<1	<1	<1	2.00	1.00	<1	<1
S total	(µg/L)	235.00	294.00	237.00	315.00	299.00	253.00	271.00	319.00	318.00
Ca total	(mg/L)	0.90	1.01	1.14	0.88	0.96	0.86	0.86	0.96	1.02
K total	(mg/L)	0.10	0.13	0.11	0.11	0.14	0.10	0.09	0.14	0.16
Mg total	(mg/L)	0.61	0.69	0.78	0.62	0.67	0.60	0.63	0.69	0.76
Na total	(mg/L)	2.18	2.38	2.44	2.22	2.83	2.40	2.41	2.65	2.90
Organic Carbon total	(mg/L)	0.90	1.30	1.50	1.10	0.20	2.40	2.60	2.90	2.80
Al total	(µg/L)	74.00	79.00	66.00	98.00	108.00	89.00	79.00	81.00	67.00

From the data recorded in Tables 4.3 and 4.4 it is evident there are no significant variations though the year in water quality which may affect biofilm growth and development such as turnover from a stratified lake. Buia (2006) is further investigating the effect of water quality on biofilm growth in Tarraleah No. 1 Canal.

4.8.2 Tarraleah Water Temperatures

Temperatures were monitored on a continuous basis with the use of eTemperature thermocron temperature loggers (On-Solution, 2004). Three locations were monitored along Tarraleah No. 1 Canal, being Transition No. 4, Bridge No. 3 and Pond No. 1. Figure 4.25 shows the eTemperature logger, and the laptop computer to download the data.

Figure 4.25: The eTemperature data logger used at Tarraleah canal.

Two types of thermocron were used. The first type measured a range of -5 to 25 deg C at 0.5 deg C intervals. The second type measured 0 to 25 deg C at 0.125 deg C intervals. Each was set to log at 30 minute intervals. The second type was used where possible.

Figures 4.26, 4.27 and 4.28 present the temperature over a 12 month period for the three locations monitored. Note that Pond No. 1 also has inflow from Canal No. 2.

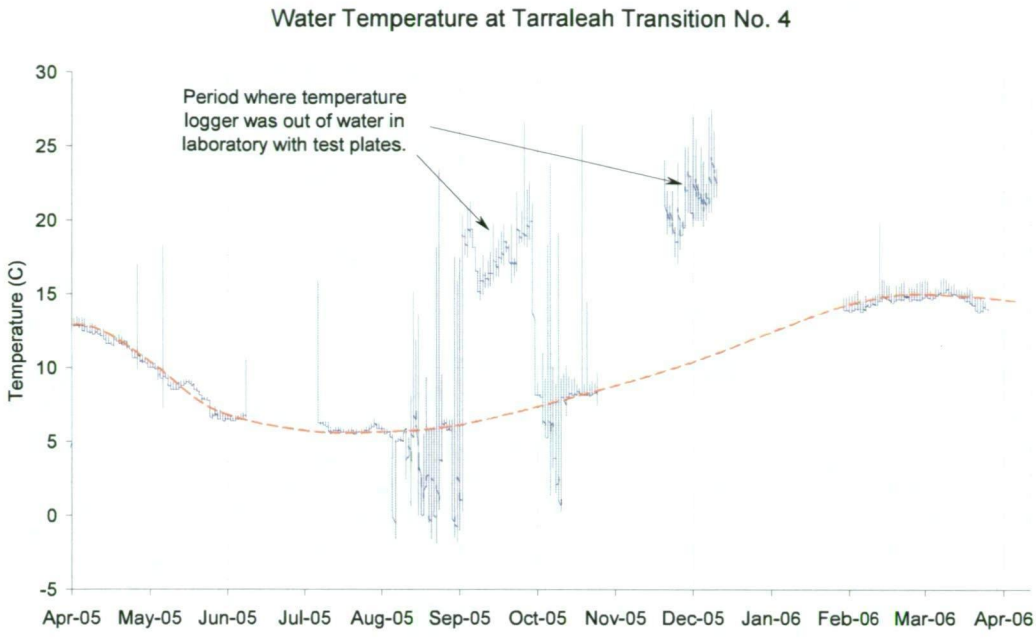

Figure 4.26: Temperature at Transition No. 4.

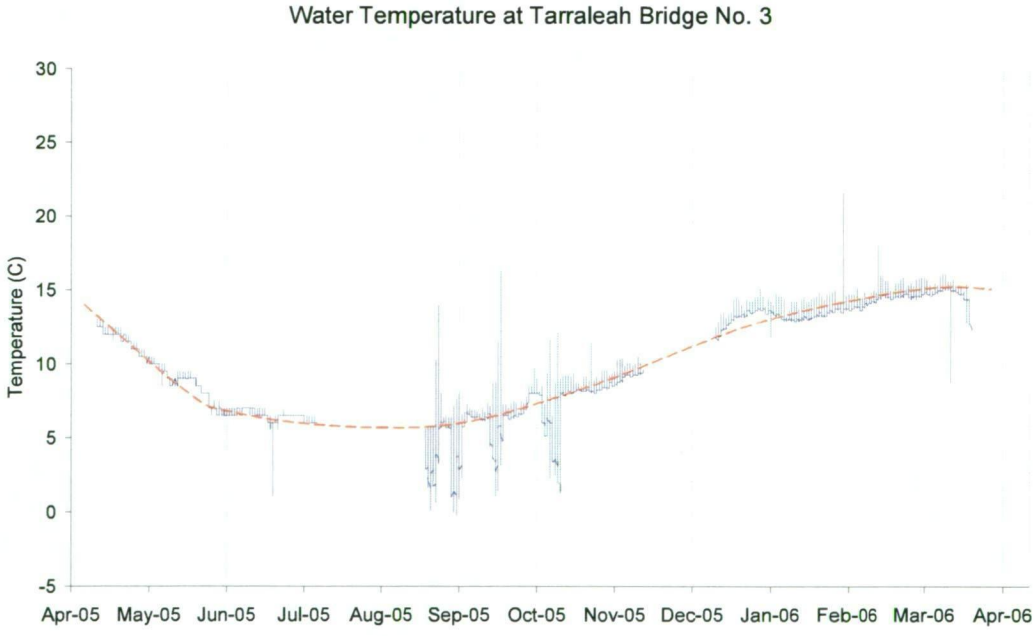

Figure 4.27: Temperature at Bridge No. 3.

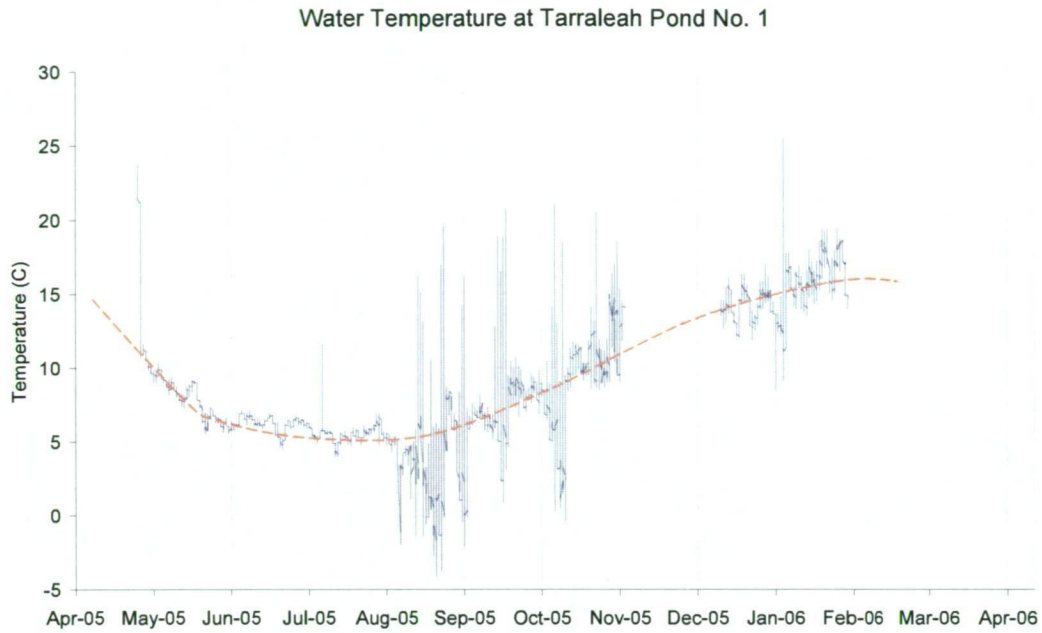

Figure 4.28: Temperature at Pond No. 1.

From Figure 4.26 to 4.28 it is seen that Transition No. 4 generally has lower temperatures than the other sites, with Pond No. 1 having generally higher temperatures.

Daily temperature fluctuations at all sites were mostly less than 2 degrees C.

Hydro Tasmania operated the Tarraleah canal system differently in 2005 than in ordinary years due to low water storage levels. The canal was often switched off and allowed to drain for several days at a time in some cases, to conserve water, and operated in peak power demand periods only. As a result, the test plates (and therefore temperature loggers) were exposed to the ambient air temperatures. This explaines the sometimes sub-zero temperatures, and large fluctuations in the temperature data. Figure 4.29 shows water levels at Bridge No. 9 with the dashed ellipse showing where Figures 4.26 to 4.28 match the temperature fluctuations.

It was observed that most biofouling growth occurred during the warmer months where the temperature was between 10 and 15 degrees C.

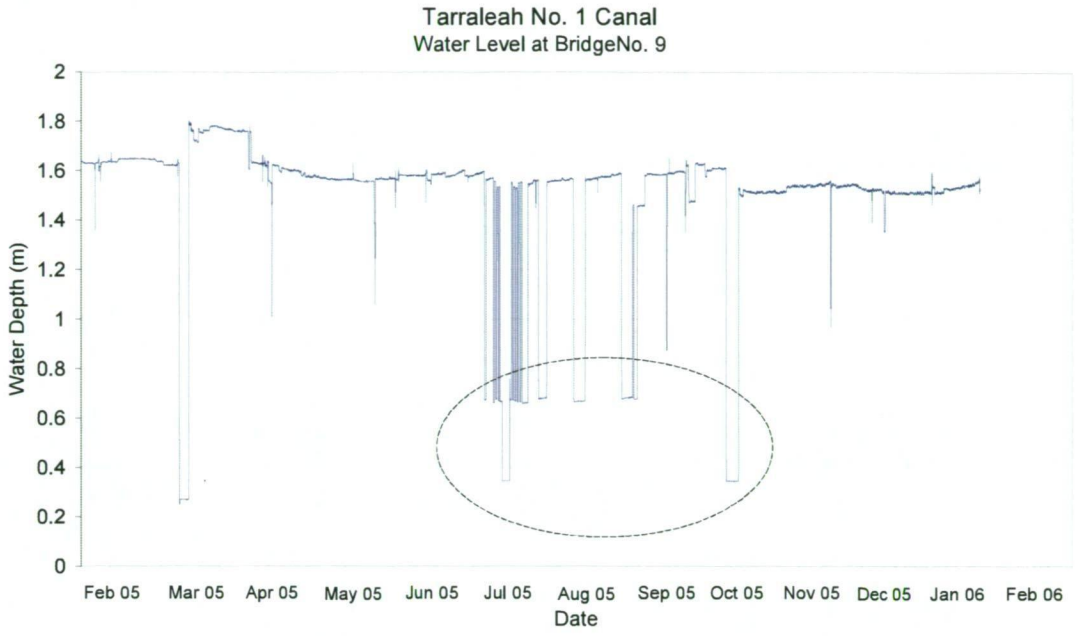

Figure 4.29: Water level at Tarraleah Bridge No. 9.

4.9 Schedule for Test Plate Testing

The small test plates and large test plates were deployed in the field for fouling and brought back to the laboratory for testing as described in Tables 4.5 and 4.6.

Table 4.5: Deployment schedule for small test plates.

Tarraleah Canal No. 1
Small test plate deployment schedule

Transition No. 4			Pond No. 1		
Canal outage (cleaned) 4-8 April					
Deployed	07-Apr-05		Deployed	28-Apr-05	
Brought To Utas	14-Jun-05	(Fouling 1)	Brought To Utas	28-Jun-05	(Fouling 1)
Deployed	28-Jun-05				
Canal outage (maintenance) 2-3 July Canal outage (maintenance) 18-21 August					
Brought To Utas	15-Nov-05	(Fouling 2)	Deployed	04-Oct-05	
			Brought To Utas	15-Nov-05	(Fouling 2)

Note: Fine grit and coarse grit plates from the same location were brough back at the same time.

Table 4.6: Deployment schedule for large test plates.

Tarraleah Canal No. 1 at Pond No. 1 Large test plate deployment schedule				
Paint (Smooth)			Fine Grit (Rough)	
Canal outage (cleaned) 4-8 April				
Deployed	28-Apr-05		7-Apr-05	
Canal outage (maintenance) 2-3 July Canal outage (maintenance) 18-21 August				
Brought To Utas	23-Aug-05	(Fouling 1)	20-Sep-05	(Fouling 1)
Deployed	06-Sep-05		04-Oct-05	
Brought To Utas	7-Feb-06	(Fouling 2)	31-Jan-06	(Fouling 2)

4.10 Chapter Summary

The strategy for the deployment of the test plates, both small for photogrammetry, and large for water tunnel testing and photogrammetry, has been presented. The locations chosen are important because they expose the plates to both high and low flow velocities. This is seen as significant to better understand the biofouling processes and influence on hydraulic conduit performance. Reasonable access to the plates also played a role in the final location of the test plates.

The different surface finishes used on the plates (smooth and rough) were presented and the reason of studying each explained.

The water quality and temperature data from Tarraleah canal system where the plates were deployed were presented. This data is important when viewed in conjunction with the type and extent of biofouling on the test plates.

Chapter 5 Characterising Surface Roughness Using Close Range Photogrammetry

5.1 Introduction

This chapter describes the use of close range photography and the photogrammetric methods used to map the surface of clean and biofouled surfaces.

The purpose of the photogrammetry was to produce accurate three-dimensional measurements of the surface topography. The objective was to achieve sub-millimetre accuracy and to have an arrangement that allowed highly repeatable photography of the same surface over time to monitor biofilm growth and development. This would allow good characterisation of the surface of the biofilm, which in turn can be compared to the experimental measurements of roughness and drag determined from laboratory work.

It should be noted that Dr Jon Osborn (2003) had responsibility for much of the development of the photogrammetry equipment and methods used in the present study. Tim Bendall (2006) also completed significant work, including the development of digital methods, which produced the raw data sets utilised in this thesis. The present author's work was limited to test plate deployment and measurement strategy, leading the design and development of the large plate photogrammetry rig, the co-development of the artificially rough surface, providing some assistance with the photography process, and processing and manipulating all surface data.

The chapter opens with an introduction to close range photogrammetry and the mapping of biofilms. The equipment and methods used to acquire the data are then described. Methods for the analysis of roughness data are presented and examples provided.

The chapter then presents details for the small test plate fouling program. Surface roughness data is shown for clean plate surfaces and subsequently fouled surfaces over time, with the

purpose of investigating the character of biofilms grown on rough surfaces in an applied field situation.

For comparison purposes, results of surface roughness data obtained from different locations along Tarraleah No. 1 Canal is also shown. This considers the typical surface character of an aged concrete lined open channel, which is subject to significant biofouling problems.

The chapter closes with a summary.

5.2 Close Range Photogrammetry and Mapping of Biofilms.

Photogrammetry is the science of obtaining reliable spatial measurements from photographic images. The term close range photogrammetry is normally used when the distance from the cameras to the object is less than about 300 metres (Wolf and Dewitt, 2000).

Consideration of photogrammetry arose from the need for a measurement method that did not interfere with the biological growths. Photogrammetric techniques allow data to be collected very quickly, because they require only that stereophotographs are acquired, and they allow the growths to be measured and mapped without physical contact.

The methods were first trialled on the small plates used for the paint trial study described in Chapter 3, developed from the work of Bae *et al.* (2002) and published in Osborn *et al.* (2005). A method was developed that allowed the photography to be completed in the field, with the test plates out of water for less than approximately 10 minutes and then re-deployed.

Biofilms were observed to be mostly low form gelatinous growths in the paint trials using smooth painted small plates. Most would fit the description of a Type A biofilm in Chapter 2. Some appeared to be quite nodular and robust. For this reason, photogrammetry was thought particularly well suited.

Later in the research program, some filamentous growths were also observed (see Chapters 7 and 8). For the filamentous growths, it was recognised that the photogrammetry may not provide roughness information required to understand some of the unique features of

filamentous growths. However, the qualitative information available with the close range photography was still considered of great value.

5.3 Equipment and Method

This section describes the equipment and methodology. The methods employed for the small plates and the large plates were very similar and so the two are described together.

5.6.1 Leica R5 Semi-Metric Film Camera

The film camera used by Bendall (2006) for the present study was a Leica R5 semi-metric camera (Leica Elcovision; Ernst Leitz Wetzlar GmbH, Germany), with 21mm Leica Super-Angulon-R lens (Ernst Leitz Wetzlar GmbH, Germany) (Figure 5.1). The lens was fitted with a polarising filter.

The 21mm Leica lens was selected due to its close-focus capability and its superior depth of field at close focussing distances when compared to other lenses (Osborn *et al.*, 2005). It has a focal range from 0.2 metres to infinity and a focal length that is appropriate for this research. A calibration of this camera and lens system had previously been undertaken (Bae *et al.*, 2002; Osborn *et al.*, 2005).

Figure 5.1: The Leica R5 camera, 21mm lens and polarising filter (photo from Bendall, 2006).

5.6.2 Adam MPS-2 Analytical Stereoplotter

An ADAM Technology MPS-2 Micro Photogrammetric System (ADAM Technology, Australia) was originally used for the photogrammetric mapping from film images acquired with the Leica camera. The MPS-2 (Figure 5.2) is an analytical stereoplotter used to produce stereo models from small format photography in either 35 mm or 70 mm format. The system has a floating mark of 20 μm diameter and a photographic measurement precision of approximately 4 μm RMS. The system interfaces with a desktop computer running MS-DOS based software. A trained operator is required to set up the stereo photographs in the plotter and the measure three-dimensional coordinates. Some of the earlier results using the MPS-2 are found in Barton *et al.* (2005), Bendall (2005) and Osborn *et al.* (2005). Surface data subsequent to these results were obtained by Bendall (2006) using digital photogrammetric workstation methods described in the next section.

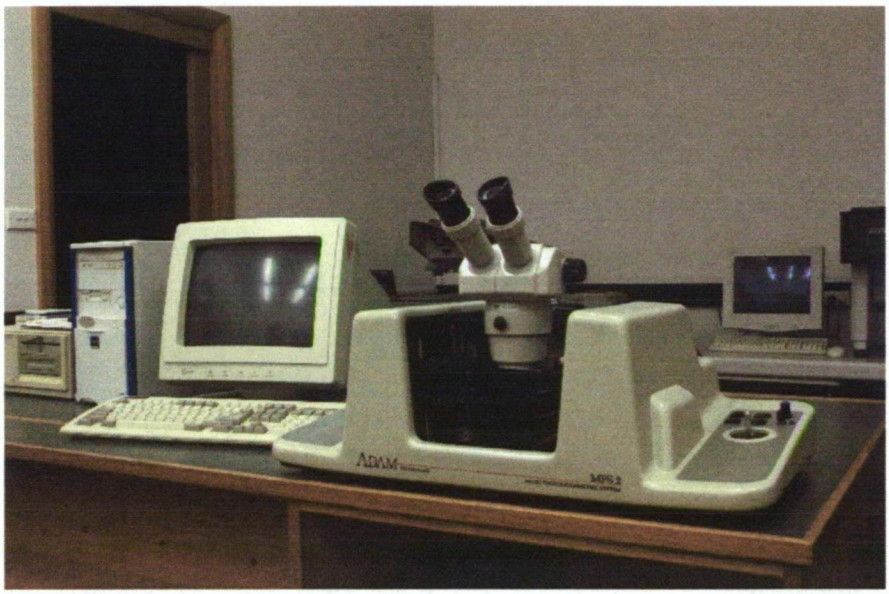

Figure 5.2: The ADAM MPS-2 analytical stereoplotter (photo from Bendall, 2006).

5.6.3 Digital Photogrammetric Workstation

Photogrammetric data were also obtained from scanned film using digital photogrammetric workstation software. The software used was 3DM Analyst (version 2.1, ADAM Technology, Australia). The primary benefit of digital photogrammetric techniques for this application was the greatly reduced time taken to measure a grid of surface height points, since this process is undertaken manually by a human operator on the analytical stereoplotter but automatically on

the digital photogrammetric workstation. The original film photography was scanned into high resolution digital images using commercial available methods. The 3DM Analyst software was then used to digitally plot the surface topography and produce data in the same format as the MPS-2. Because productivity was much higher than analytical methods, many more data points were obtained. All surface data presented in this thesis were acquired by Bendall (2006) using the digital photogrammetric methods. Osborn (2006) suggests there to be no significant differences in expected error using the analytical MPS-2 (reported in Osborn *et al.* (2005)) compared to the digital procedures as they both use the same film photography from the calibrated Leica R5 camera. Any errors from the digital scanning of the film photography are neglected.

Mitchell *et al.* (1999) reported on the successful use of digital photogrammetric methods with the use of VirtuoZo software mapping the surface of concrete. VirtuoZo software (version 3.3, Supersoft Inc., Wuhan, Hubei, China) was used on earlier work relating to the present study by Bendall (2005) and Osborn *et al.* (2005). However, the 3DM Analyst software was deemed more time efficient and superior for the purposes of the present study.

5.6.4 The Camera Support and Associated Equipment

Camera supports were used to mount the camera during photography. Different camera supports were used for the small and large plate photography, although the basic design was the same for both. Figure 5.3 shows the small plate camera support developed by Osborn *et al.* (2005) and Bae *et al.* (2002). Its main function was to hold the camera at a predefined distance from the plate surface. The camera is attached to a sliding cross-beam which can be moved left and right, aligned to special marks, and left and right photos taken. This slide mechanism allows translation of the camera to achieve normal case stereo photographs (Osborn *et al.*, 2005). The width and height of these arms have been designed to provide an object distance of 210 mm and a camera base of 110 mm.

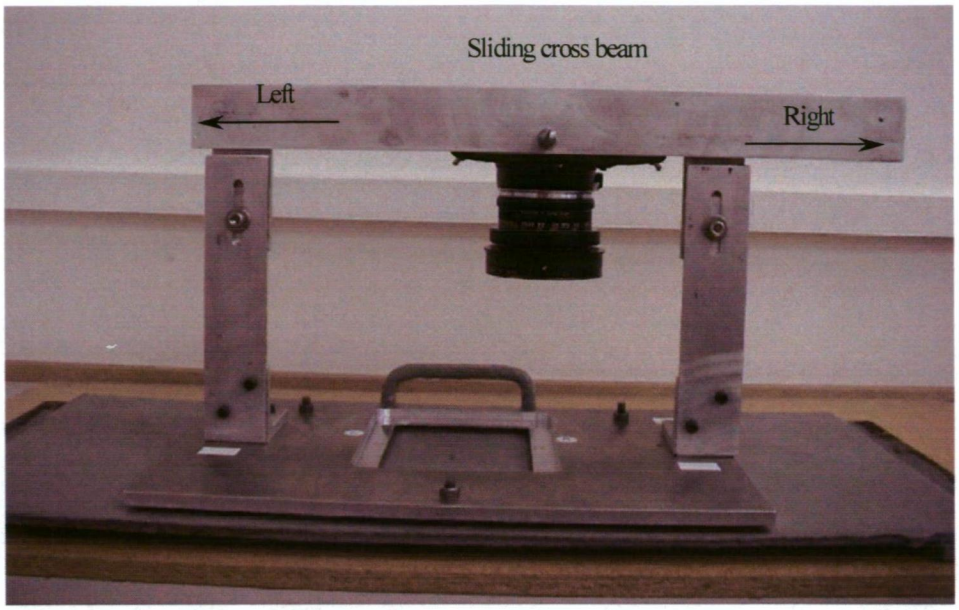

Figure 5.3: Camera support placed on a test plate and with camera attached.

Figure 5.4 shows both types of camera supports used. For the small plates, the camera support was mounted directly onto the plate and located using three pins sitting in bevelled bolt heads (locators) shown in Figure 5.5. Each of the bevels was pointed inwards towards the centre of the plate. The locators ensure a high degree of repeatability for the photography.

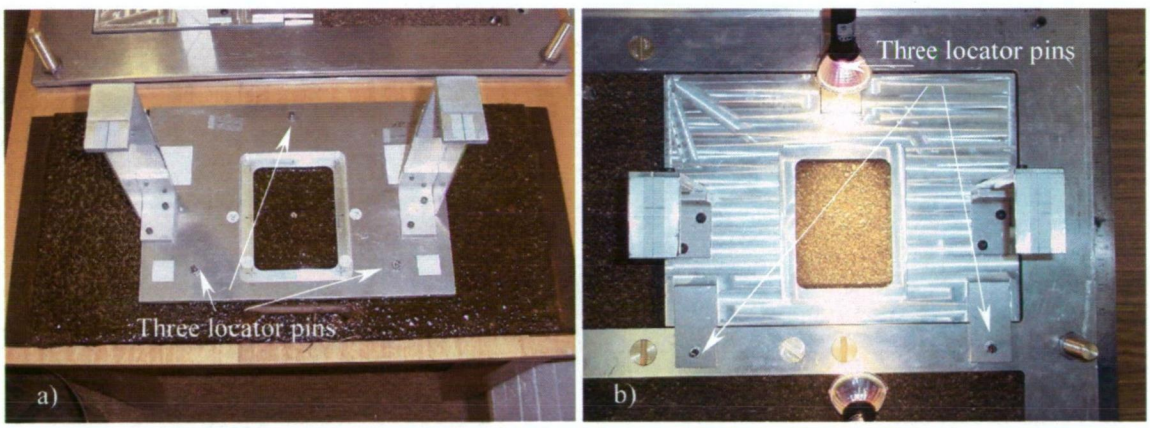

Figure 5.4: Camera support for the small plates (a) and large plates (b).

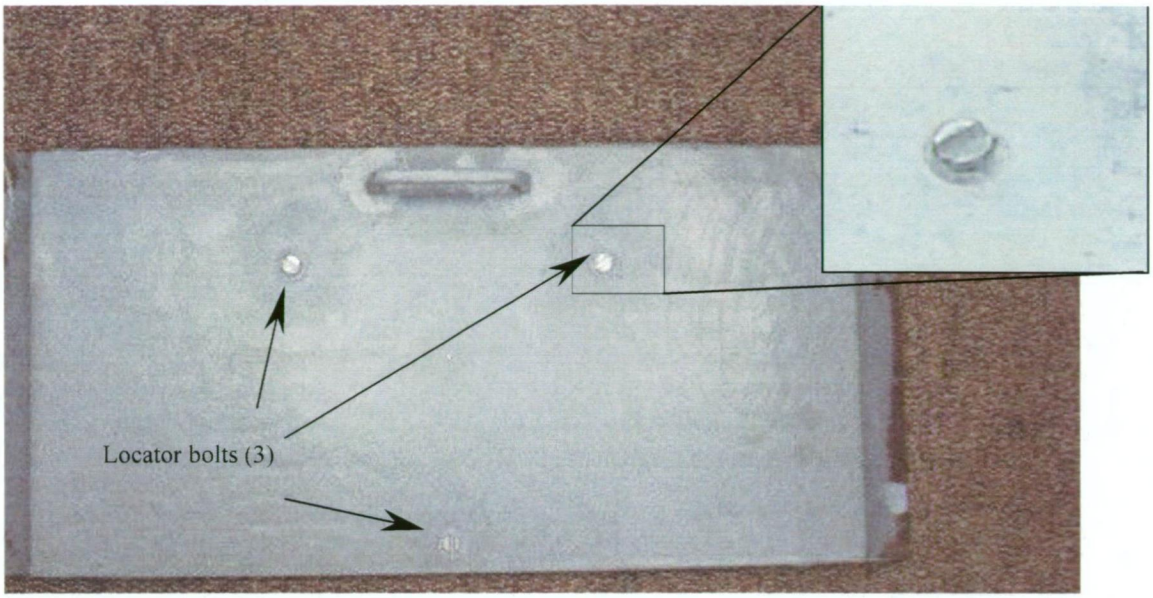

Figure 5.5: Test plate showing the three bolts (with bevelled heads; see inset photo) used to locate the camera support.

The centre of both camera supports contained a window to define the viewing area for the photography. The window measures approximately 100 mm wide by 130 mm tall. Surrounding the window is an array of eight control points for reference during the photogrammetric procedure. Osborn *et al.* (2005) and Bendall (2005) contain more information on this, suffice to say that the eight control points were used by observing them in the left and right photographs to orientate and locate the two photographs in object space.

Figure 5.6 shows the camera support viewing windows for the small plate photography (a), and large plate photography (b). The major difference between the two is the use of a central reference pin for the small plates. This pin provides a repeatable, recognisable reference in all stereo models that was used to detect any gross errors (Osborn *et al.*, 2005). This was not possible on the large test plates, which needed to be free of obstructions for measurements in the water tunnel.

Figure 5.6: Photography window and viewing area for the small plate camera support and large plate support. Note the reference pin in the centre of (a) for the small plates.

The camera support used for large plate photography was essentially the same as for the small plate support except that the three locator pins (Figure 5.4) where designed to project away from the plate to allow placement onto a reference frame described below.

Because the camera support for large plate photography could not be mounted directly onto the plate like the small plates, a photogrammetry rig was specially built. Figure 5.8 shows the different components of the large plate photogrammetry rig.

This reference plate was designed to enable photography at six locations, which would allow a representative area of the plate to be photographed. A large (1100 mm long, 700 mm wide and 12 mm thick) aluminium plate was used as the base plate on which to mount the test plate, photography reference plate, camera support and camera. A thick, large plate was used to minimise any movement from bending or flexing.

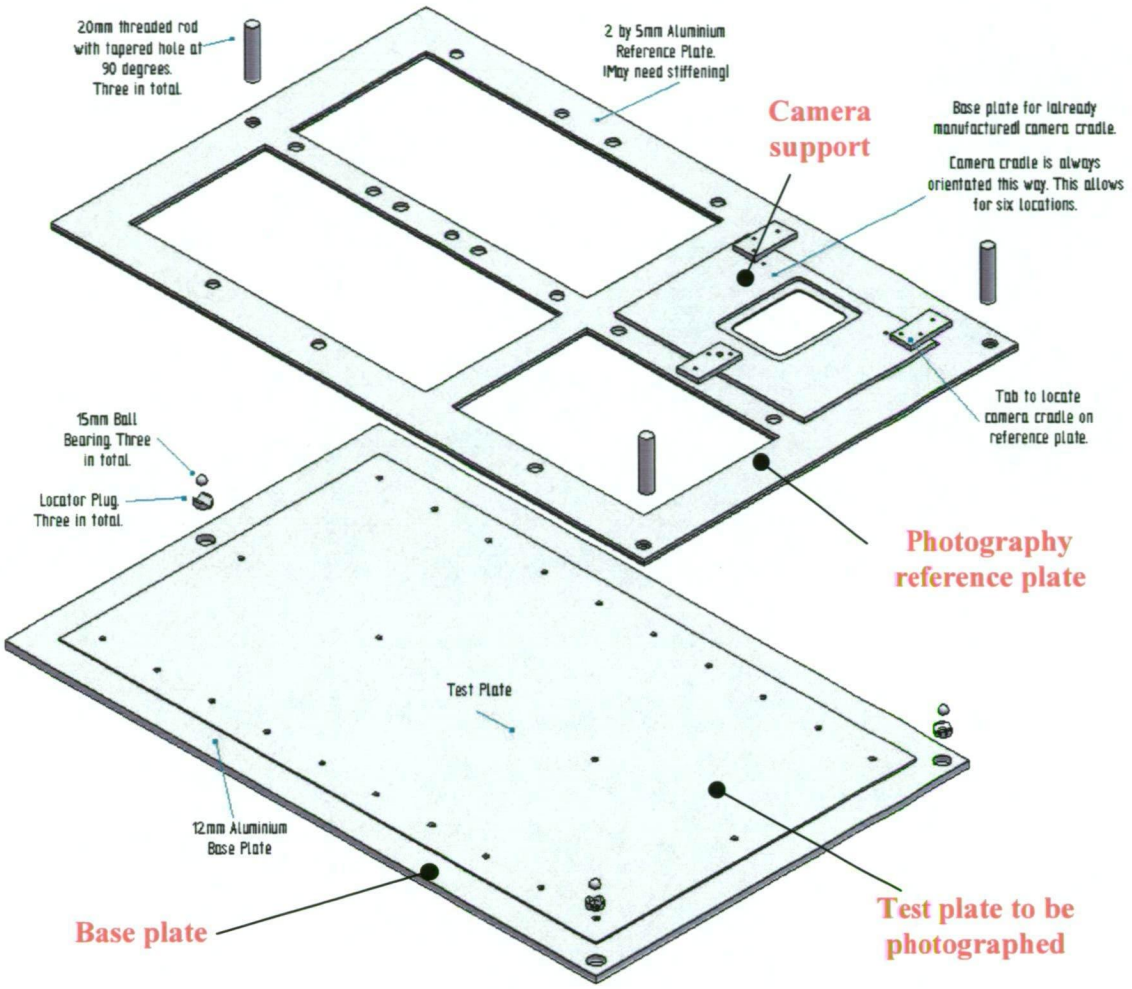

Figure 5.7: General arrangement of large plate photogrammetry rig.

A reference plate (10 mm thick aluminium) is positioned on the base plate, over top of the test plate, and located using a three point arrangement similar to the small plate design. Bevelled brass plugs were fitted into the base plate (Figure 5.9a) with 12 mm diameter ball bearings seated into each of these plugs. These ball bearings allowed machined threaded rods (attached to the reference plate, Figure 5.9b) to sit on top of the base plate. The threaded rods allowed adjustments to be made in height to the reference plate (Figure 5.9c).

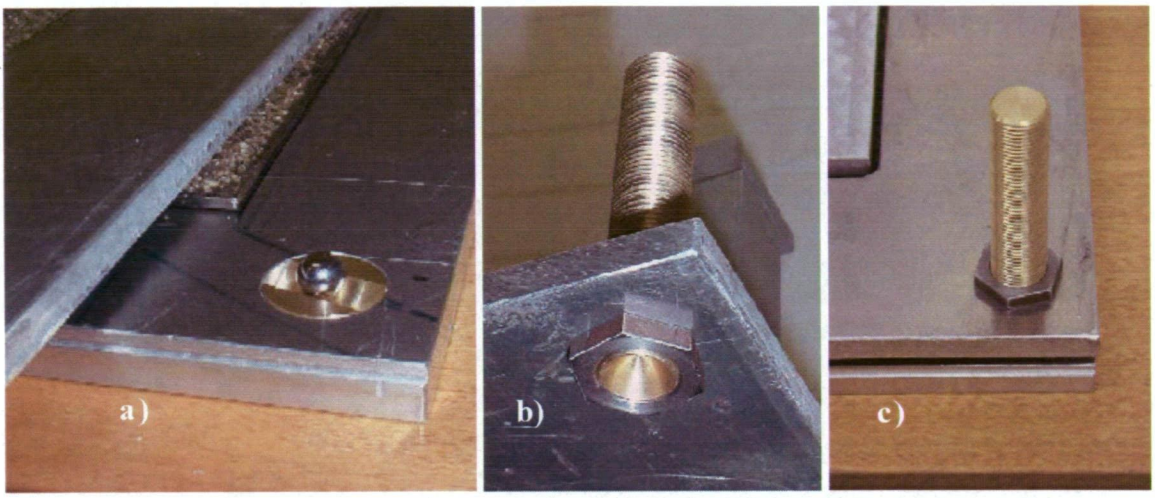

Figure 5.8: Photos showing some features of the large plate photogrammetry rig.

The potential for the reference plate to bend under the weight of the camera support and camera was reduced by the addition of ribbing (to stiffen the frame) and the use of support pins, which could be locked tight once the reference plate was height adjusted. Figure 5.10 shows a pin located in the corner of the plate, and some welded ribbing to stiffen the reference plate.

Figure 5.9: A photo showing some features of the large plate photogrammetry rig.

Bevelled brass locator plugs were also installed into the reference plate to accommodate the three pin arrangement on the camera support. Figure 5.11 shows three of these plugs. Three plugs were installed at each location where the camera support would be positioned onto the

reference plate to acquire photos. There were six photo locations, each with three plugs at each, resulting in a total of 18 bevelled brass plugs installed onto the reference plate. The bevels were each rotated to point inwards to ensure a unique location for the camera support.

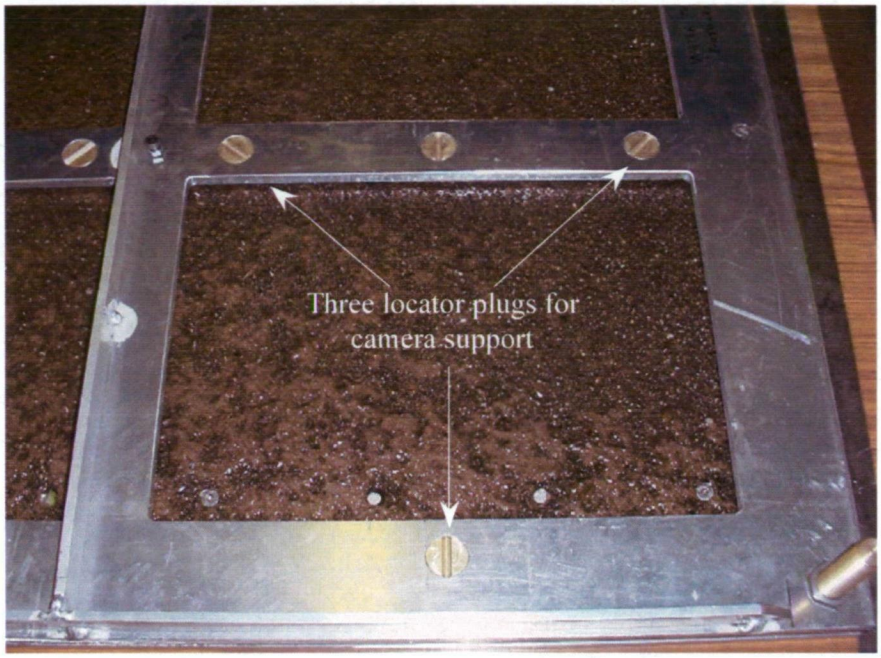

Figure 5.10: Photo showing three locator plugs on reference plate for camera support.

5.6.5 Test Plate Photography

The schedule for test plate photography is provided in Chapter 4. Unlike some of the earlier work described by Osborn *et al.* (2005), it was decided to transport the plates to the laboratory (instead of photographing the plates in the field). This was so that the photography could be completed in more controlled conditions. Special containers were filled with water from Tarraleah canal and plates submerged in these containers for transporting to the laboratory. Transporting the plates in this way was not expected to affect the biofilm so long as they remained wet (Barmuta, 2005; Buia, 2005; Hallegraeff, 2005).

5.6.5.1 Photography for Small Plate

Figures 5.12 to 5.15 show the set up sequence for the small test plate photography. Note that the plate is kept wet at all times. The photos presented here show only one light source. Later photography of the large test plates was conducted in a dark room using two light sources.

Globes used were selected to produce a white light. All photography was completed by Bendall (2006).

Each plate was firstly retrieved from the field and brought back to the laboratory (Figure 5.12). The plate was then placed under the light source (Figure 5.13). The camera support was positioned onto its locators (Figure 5.14) and the camera attached to the sliding cross-beam and laid on top. Left and right images of the stereo pair are then taken (Figure 5.15).

Results from the small test plate biofouling program are presented later in this Chapter.

Figure 5.11: Small plate retrieved from field.

Figure 5.12: Small plate was positioned under light.

Figure 5.13: Camera support rests on three locators on test plate surface.

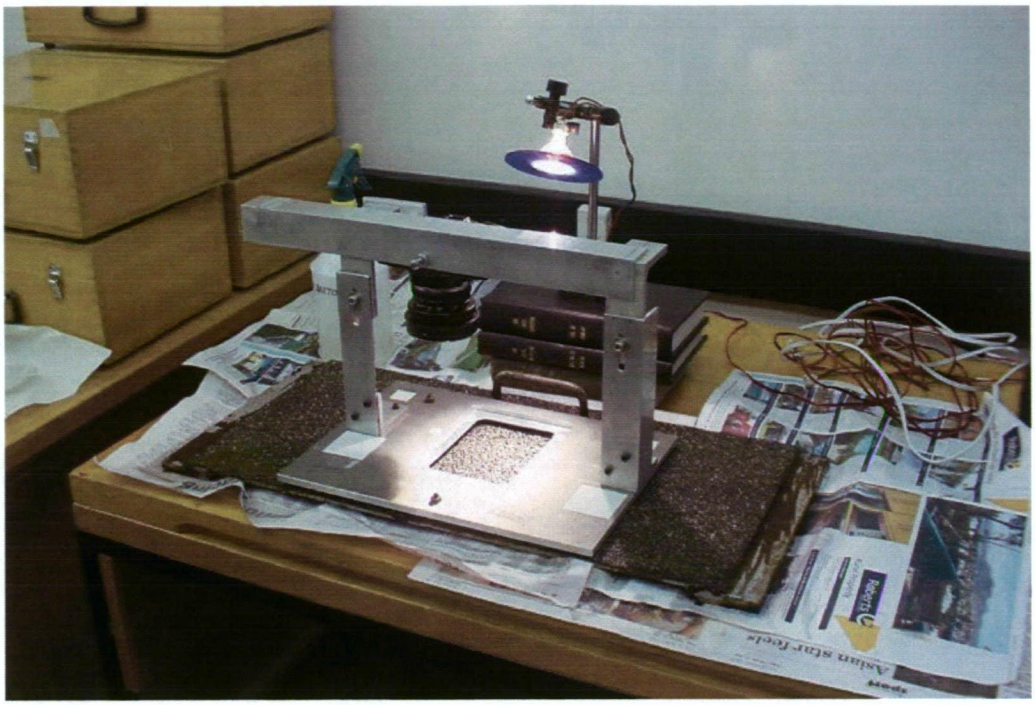

Figure 5.14: Camera attached to a sliding cross-beam and left and right images taken.

5.6.5.2 Photography for Large Plates

The set up sequence for the large test plate photography is shown in Figures 5.16 to 5.24. Note that the plate was kept wet using a spray bottle with Tarraleah No. 1 Canal water. The photography was more involved for the large plates and so efficient use of time was paramount to complete the photography and move the plate as soon as possible to the water tunnel to commence measurements. A period of approximately one to two hours was usual to complete the photography. All photography was completed by Bendall (2006).

First the large test plate was retrieved from the field (Figure 5.16), and transported back to the laboratory (Figure 5.17). The base plate of the photogrammetry rig was cleaned to prevent grit or other material from being stuck beneath the plate (Figure 5.18). The large plate was then screwed firmly down to the base plate (Figure 5.19) and the reference plate mounted over the plate and positioned on the three locators (threaded brass rods protruding from the reference plate) (Figure 5.20). Two lights are clamped to the bench top and adjusted to the correct angle (described below) (Figure 5.21). The camera support was then positioned onto the reference plate at any of the positions A, B, C, D, E or F (described subsequently) (Figure 5.22). The camera was mounted onto the sliding cross-beam (Figure 5.23) and left and right images

taken for the stereo pair. Figure 5.23 shows the dark room with the overhead lights switched off and the photographic lighting switched on.

Figure 5.15: Biofouled test plate in field.

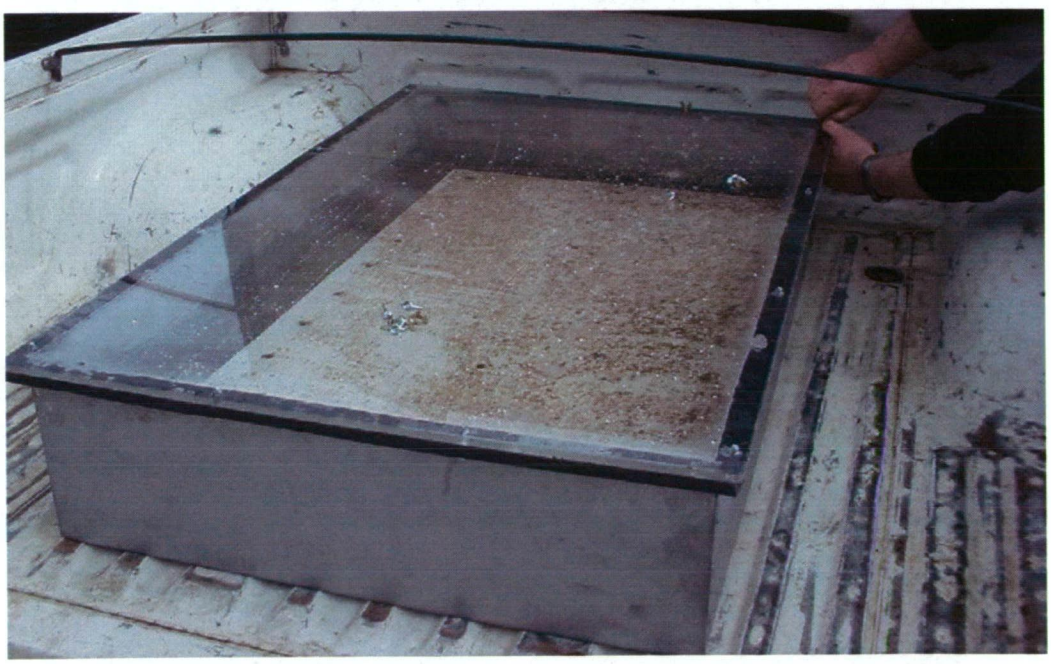

Figure 5.16: Test plate being transported back to laboratory submerged in a container.

Figure 5.17: Base plate cleaned and prepared to accept test plate.

Figure 5.18: Large test plates were screwed down to base plate. Biofouled test plates were kept wet at all times by a water spray bottle.

Figure 5.19: Reference frame was placed over the test plate using the ball bearings, threaded rods and bevelled locators in the base plate.

Figure 5.20: The pair of lights are clamped to the table and angled into position.

Figure 5.21: The camera support was positioned using pins and bevelled locators.

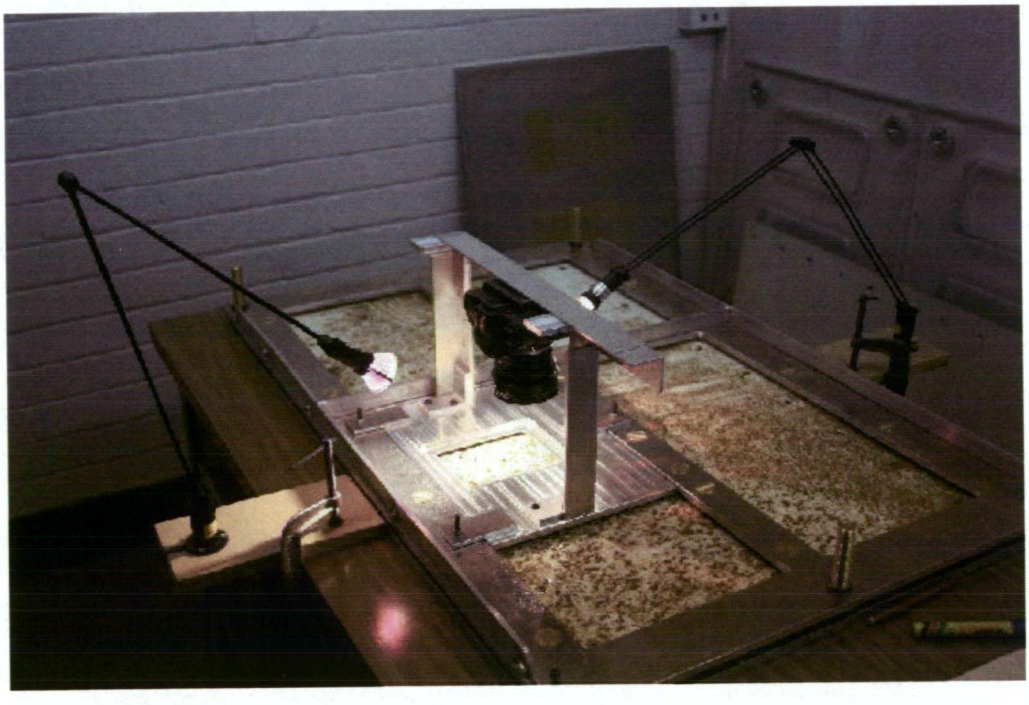

Figure 5.22: The two lights are switched on and camera mounted using the cross-beam.

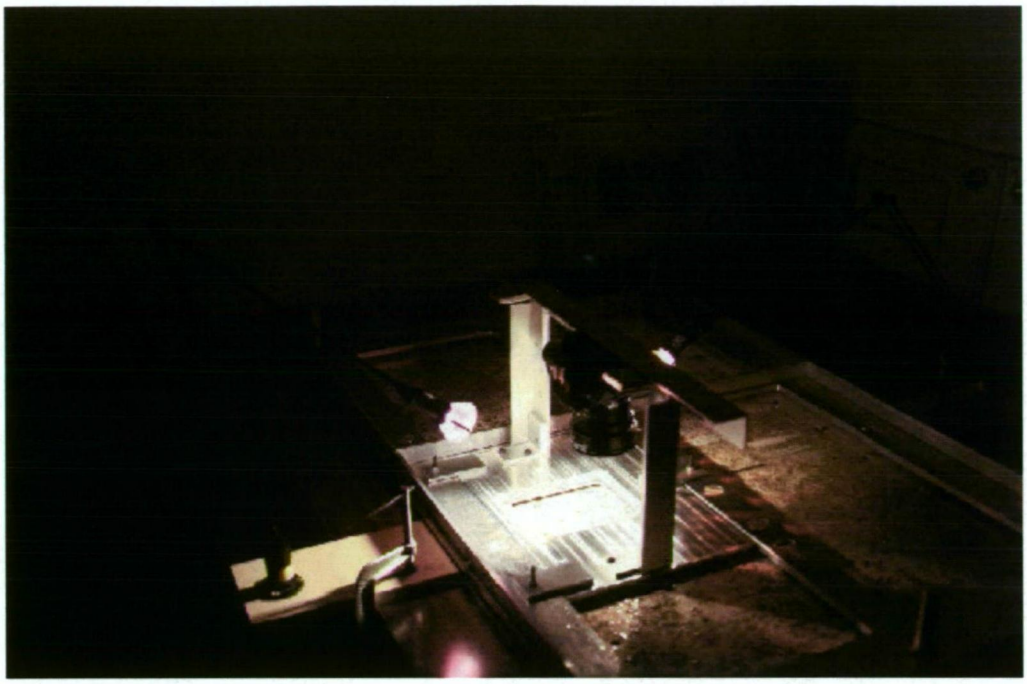

Figure 5.23: Room lights switched ready for photography of plate.

5.6.6 Photographing a Wet Surface

Because the biofilms are wet, and are required to be kept wet to remain in good condition, special arrangements were required to minimise the effects of reflection from the wet surface during photography. Figure 5.24 shows a photo with pooled water and gross reflection problems.

Figure 5.24: Reflections caused by uncontrolled lighting complicating the surface.

Reflections in the photography resulted in poor matching in the both the manual (MPS-2) and automated (3DM Analyst) stereo plotting process and generation of incorrect height data.

Bendall (2006) with the assistance of Osborn (2006) investigated techniques to reduce the problems of reflection. This included the use of a polarising filter, the preparation of a suitable dark room to remove uncontrolled light sources and associated reflections, and the use of two lights adjusted to specific angles to reduce the potential of reflection through the camera lens. Bendall (2006) found illumination angles of between 45 to 55 degrees provided the best distribution of light across the test plate surface and camera support window. It was also found that the fitting of a polarising lens filter reduced the amount of reflected light entering the lens, and was most effective when the light was incident at approximately 55°. This is consistent with expectations, given that the incidence angle of the reflected light will be close to Brewster angle (56°) (Nave, 2000). The polarising lens could be rotated to optimise reduction in reflected light entering the lens. These findings were incorporated into the photogrammetric process of the test plates.

5.4 Data Acquisition, Analysis and Manipulation

When properly analysed, the left and right images will have stereo convergent points that allow the extraction of surface data at a desired resolution. Figure 5.25 shows the typical photos produced for the photography process, a left and right image.

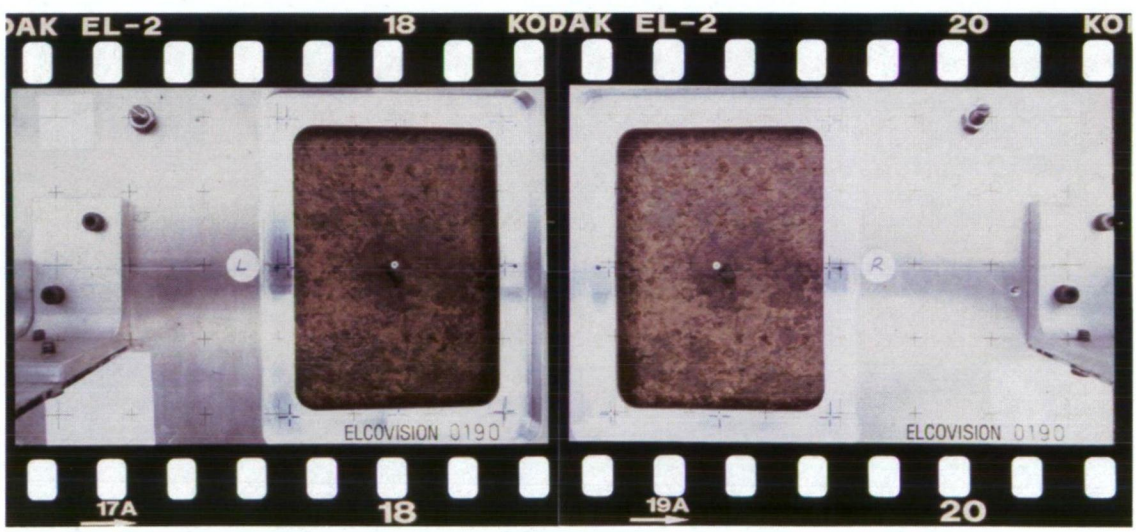

Figure 5.25: Film showing left and right stereo pair.

The small plates had one viewing area for photography as shown in Figure 5.26. The area was in the approximate centre of the plate.

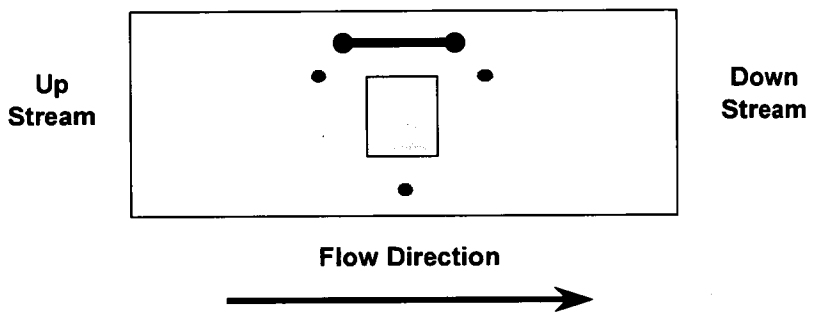

Figure 5.26: Viewing area for photography of small plates shown as the shaded rectangle.

The large plates had six viewing areas for photography as shown in Figure 5.27. Windows A, B, C and D, E, F were respectively each parallel with other, and formed two "lines" down the longitudinal axis of the plate. Windows A, B and C were closer to the plate edge than the centreline, whereas windows D, E and F were closer to the plate centreline than the edge.

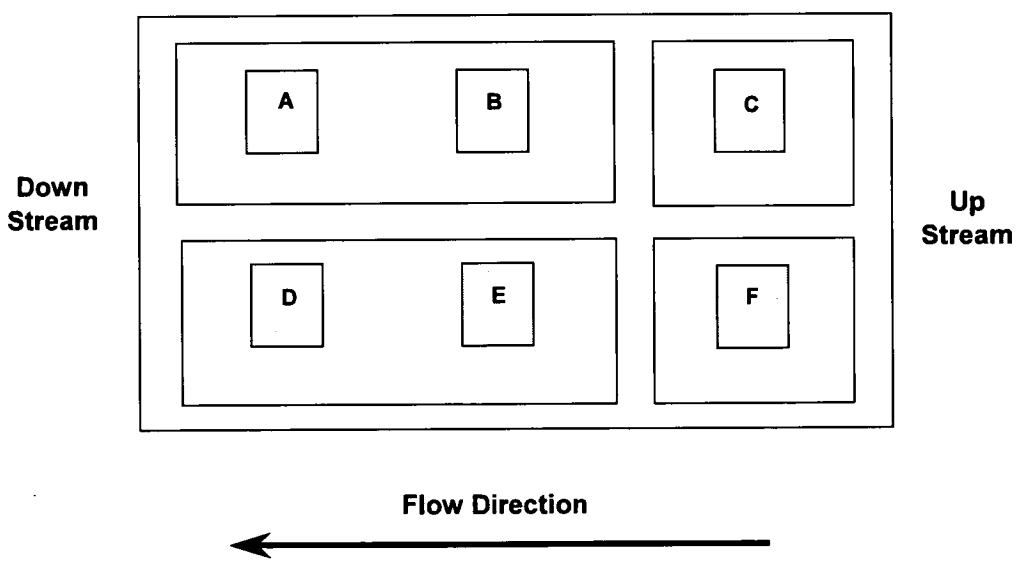

Figure 5.27: Viewing area for photography of large plates shown as the shaded rectangles.

The primary output of the photogrammetric process was X, Y, Z distances of the photographed surfaces. Table 5.1 and Figure 5.28 show, respectively, the typical format of the raw data and the three-dimensional surface reconstructed from the raw data using MatLab.

These data are from the small plate (clean coarse grit) surface (Figure 5.30). All data are in millimetres.

Table 5.1: Sample of raw data produced by the photogrammetric procedure.

X	Y	Z
4.23	20.00	94.08
4.28	20.00	93.99
4.42	20.00	93.67
4.64	20.00	92.67
4.65	20.00	92.71
4.73	20.00	92.65
4.79	20.00	92.64

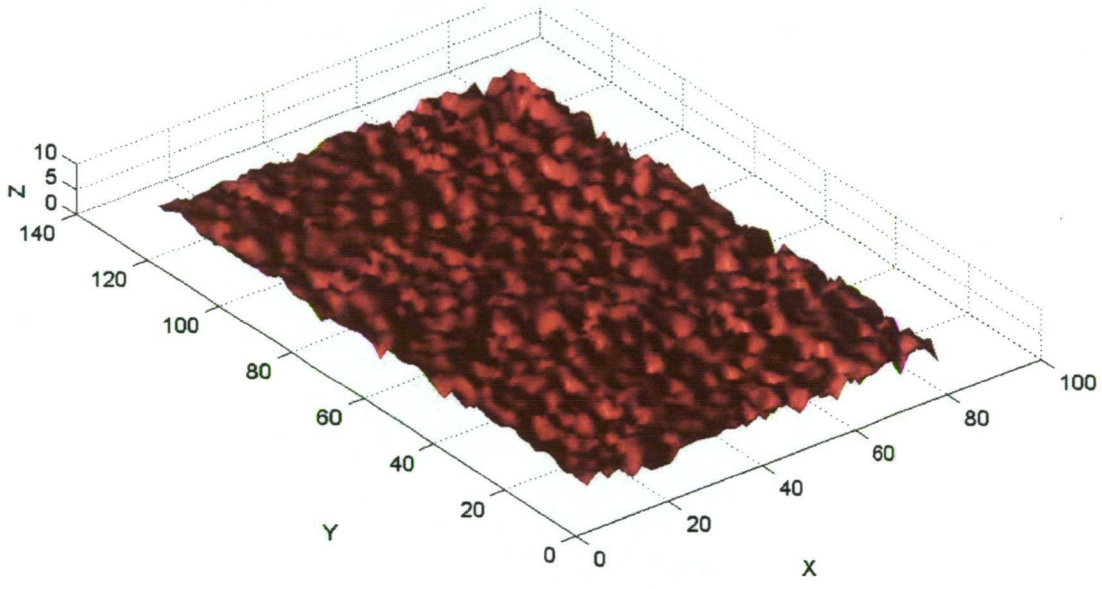

Figure 5.28: Three-dimensional reconstruction of surface for a small plate with coarse grit.

Figure 5.29 shows a digital image of a small plate (clean coarse grit) surface. Overlaid on the image are cross sections at distances of Y = 20, 40, 60, 80 and 100 mm. On the right of the image are the respective plots of the cross section showing the X direction surface profiles at the Y distances. The profile was sampled at intervals, which was determined by the digital photogrammetry software to best describe the profile, and typically varies between 0.1 mm to 0.5 mm.

The surface profiles (Figure 5.30) are plotted about their mean. The plot of the surface profile at Y=100 mm shows additional parameters which are shown in better detail in Figure 5.30.

The parameters used to describe the surface profiles are grouped into two fields: roughness parameters and statistical parameters (or moments). Table 5.2 shows these and provides brief definitions of each. These parameters are commonly used in allied disciplines for roughness analysis. The reason for using these parameters in the present study is to explore how appropriate they are for the adequate description of biofilms, particularly when viewed in conjunction with other data obtained from field or laboratory experiments.

Table 5.2: Parameters used to describe surface profiles.

Roughness Parameter	Description
Ra =	Mean of magnitude of deviation of profile from mean line
Rq =	RMS of surface profile
Rv =	Maximum depth of profile below mean line of sample length
Rp =	Maximum height of profile above mean line of sample length
Rt =	Maximum peak to valley height of profile of sample length
Statistical Moment	Description
1st (mean) =	Arithmetic mean or average
2nd (variance) =	A measure of the spread of a distribution
3rd (skewness) =	A measure of symmetry of the profile about the mean line
4th (kurtosis) =	A measure of sharpness or flatness of profile

It is worth noting the fundamental difference between smooth and rough plates in terms of measuring changes to their initially clean surface. Smooth plates are relatively easy to describe, as any change in surface character can be referenced back to the originally flat surface. For rough surfaces, however, there may be two possibilities of biofouling, forming either on peaks or in valleys, as discussed at the beginning if Chapter 4. It is suggested in subsequent discussions in this thesis that the Rt parameter is the most useful to describe the changes in surface character due to biofouling on rough plates in this regard.

It is in the format presented in Figure 5.29 that the result of Chapters 7 and 8 are presented, and all data are presented in the photogrammetry appendices B, C, D, E, F, G and H in Volume 2 of this thesis.

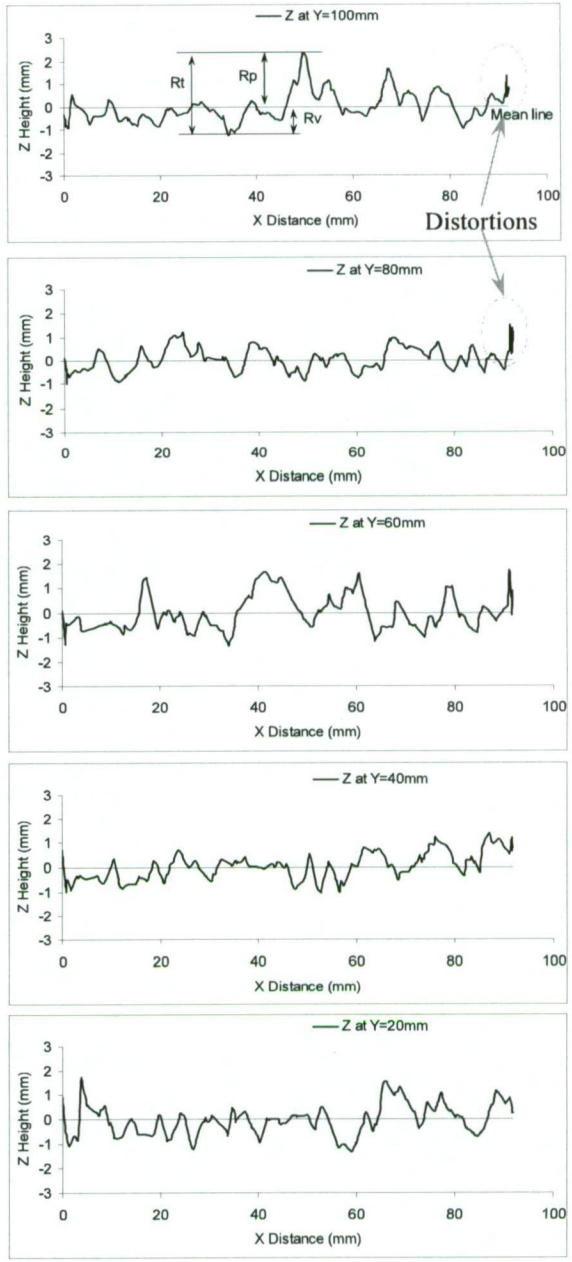

Figure 5.29: Digital image of small plate coarse grit clean surface.

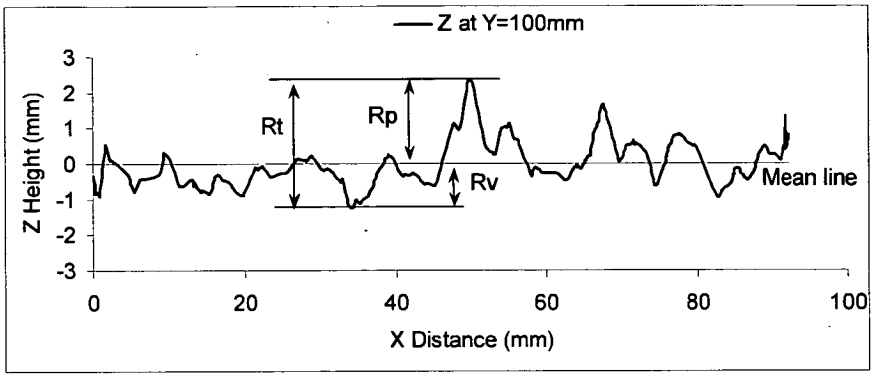

Figure 5.30: Sample surface profile for Y = 100mm.

Typical results using the parameters described in Table 5.2 and surface data from the results presented in Figure 5.30 are shown in Table 5.3.

Table 5.3: Results for analysed data.

Coarse Grit Pond No. 1 - Clean	Roughness Parameters (mm)					Statistical moments				Peak
Surface Profile	Ra	Rq	Rp	Rv	Rt	1st (mean)	2nd (variance)	3rd (skewness)	4th (kurtosis)	Count
Y=20mm	0.52	0.64	1.74	-1.31	3.05	1.31	0.41	0.26	-0.35	12
Y=40mm	0.43	0.54	1.38	-1.02	2.40	1.02	0.29	0.24	-0.37	11
Y=60mm	0.58	0.72	1.73	-1.37	3.10	1.37	0.52	0.65	-0.42	11
Y=80mm	0.44	0.52	1.50	-0.98	2.48	0.98	0.27	0.27	-0.66	14
Y=100mm	0.50	0.65	2.35	-1.25	3.60	1.25	0.42	0.95	1.50	9
Average:	0.50	0.61	1.74	-1.19	2.93	1.19	0.38	0.47	-0.06	11.40

Cross sections at distances of Y = 20, 40, 60, 80 and 100 mm were chosen to obtain good representation of the photographed area, and also to minimise distortions which were sometimes apparent closer to the edges. Distortions are attributed to blurring in the photography near the edges, as can be seen in Figure 5.29. Care was taken when analysing the surface profiles to exclude this data, which usually manifested itself as near-vertical lines as seen in Figure 5.29, profiles Y=100mm and Y=80mm, at approximately X=93mm.

One other parameter used to describe surface roughness was the peak count. A peak count will give an indication of the number roughness elements within the sample profile length. Figure 5.31 shows the surface profile of Y=100m from the data of Figure 5.29 with a peak count. The peaks are found by positively transforming the data, Z(+ve) (or red dashed line); the Rq value (RMS value for the red dashed line sample length) is then plotted, and the peaks that fall above this line are counted off. This is an adaptation of the method described by

Whitehouse (2002). To qualify as a peak, the Z(+ve) profile must begin below the RMS line; the next peak cannot be counted until the profile has again fallen below the RMS line.

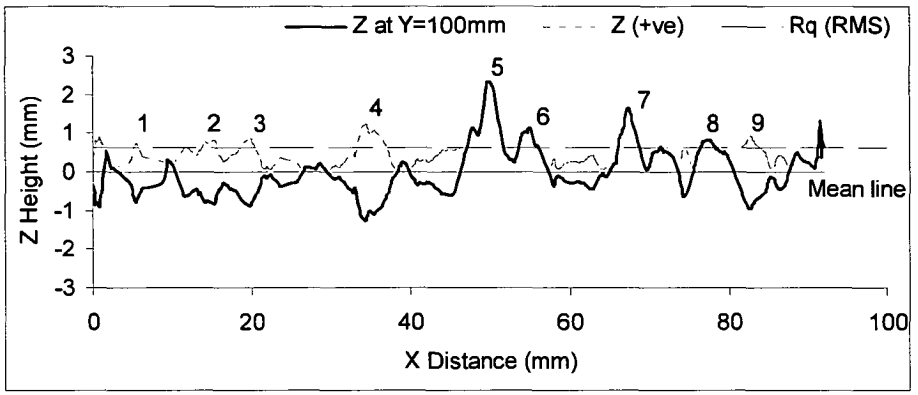

Figure 5.31: Plot showing a peak count.

What data constitutes "roughness," and what data constitutes "waviness" for a surface profile is not well defined and usually subjective. It is dependent on sampling length, and also scale and type of surface roughness that is of interest. Additionally, the scale of roughness of interest to fluid mechanics surface friction studies must be considered. It is generally accepted that long wavelength roughness, or roughness elements of greater longitudinal spacing, is not as critical as short wave length roughness in fluid mechanics problems. This particularly so for small scale laboratory measurements. It is intuitive that increased spacing of roughness elements reduces the generation of vortices and their subsequent spreading and dissipation, in turn reducing the friction loss of flowing water. Morris (1955), Rouse (1965) and Hama (1954) all discuss the effect of roughness density and spacing.

Where large scale undulations were apparent in the surface profiles, a polynomial regression line was fitted. The regression line was then subtracted from the surface profile to remove the "waviness" and leave only the roughness. This method is outlined in Whitehouse (2002) as a type of high pass filter. The order of the polynomial was determined from observation, with a minimum number of inflections intended. Usually a 3rd or 4th order polynomial was sufficient. Figure 5.32 presents an example of surface data pre and post filtering for waviness. Clear differences in the derived roughness parameters were achieved by removing large scale waviness from the surface profile. Filtering to remove large scale waviness was undertaken for the data presented in Chapters 7 and 8.

The removal of waviness had an additional effect of correcting for image distortions from the photography process. This occurred, for example, where a surface was not parallel to the camera due to the three point locators not being exactly equal in height.

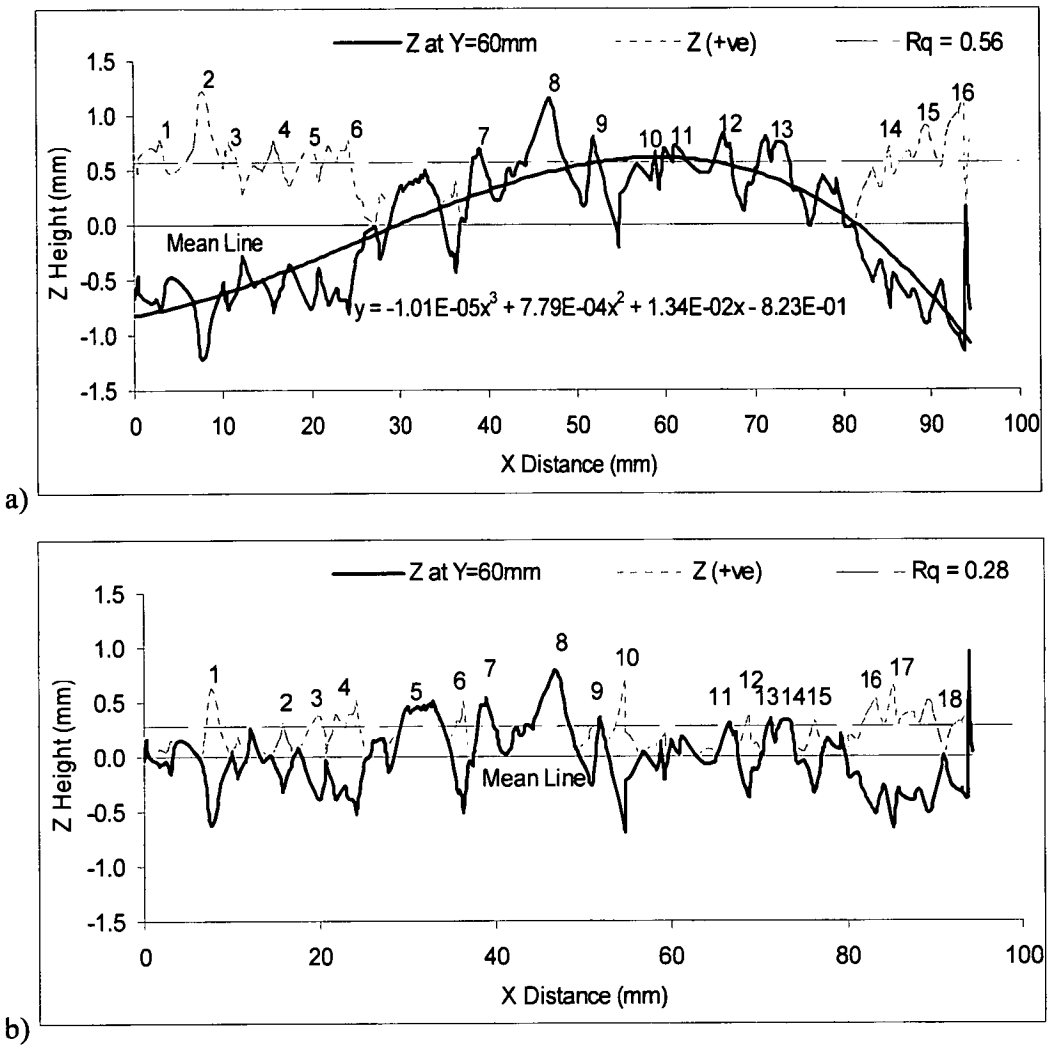

Figure 5.32: Surface profile with large-scale undulation and a polynomial mean line fitted (a). The profile is re-plotted about the polynomial mean line (b).

5.5 Photogrammetry Errors

It should be noted that methods described by Osborn *et al.* (2005) were used to estimate the precision of the photogrammetry data. The resultant predicted precisions were approximately 60 μm in X and Y and 100 μm in Z. Osborn (2006) suggests there to be no significant difference in the estimated accuracy of the data used in the present study (using digital

methods) and the accuracy reported in Osborn *et al.* (2005). However, this error estimate is for a well defined surface with good optical texture. Greater errors can be expected with surfaces of poorer optical texture.

Further details on the photogrammetry development and testing can be found in Bendall (2005) and Osborn *et al.* (2005). Here the investigators also looked at:

- Operator precision on individual well defined points;
- Operator precision on individual poorly defined points;
- Precision of the re-observation of control points;
- Operator precision over an entire cross section; and
- Difference in observing the same cross section with two different orientations.

5.6 Character of Clean and Biofouled Rough Surfaces and Tarraleah No. 1 Canal.

The section presents results for the small test plate biofouling program. This consisted of deploying fine grit and coarse grit artificial surfaces (described in Chapter 4) in Tarraleah No. 1 Canal and allowing them to become fouled. The plates were retrieved at approximately 2 monthly intervals and photographed to monitor biofilm development. Close range photogrammetry was used to obtain surface data, which was analysis and is presented here.

Results are also presented from photographs taken of Tarraleah No. 1 Canal walls. Photos were taken at several representative locations, allowing comparisons to be made with other surfaces used in the present study.

Tables summarising the roughness and statistical data for the surfaces are presented, with plots of the surface profiles then shown.

A discussion and summary of these results is provided at the end of this chapter.

5.6.1 Small Test Plate Biofouling Program

As described in Chapter 4, one fine grit and one coarse grit small test plate was deployed at both Transition No. 4 and Pond No. 1. This was done with the aim of studying the character of biofilms grown on rough surfaces and conditioned to different flow speeds.

There was generally less biofouling at Transition No. 4 (with a higher flow velocity approaching 2m/s) than Pond No. 1 (with a lower flow velocity of approximately 1m/s) for the present study. The plates were never cleaned during the fouling process, just photographed and returned to the field.

A more complete set of photogrammetry results for the small plates, showing peak counts and other data, is included in Appendix B.

5.6.1.1 Fine Grit at Transition No. 4

Photogrammetry was first undertaken on the clean surface of the fine grit small plate. This plate was then deployed at Transition No. 4 and allowed to have biofilms develop. The plate was then brought back in approximately 2 monthly intervals and photographed each time for later analysis.

Table 5.4 presents a summary of the surface roughness analysis for the clean, and subsequently biofouled fine grit plate deployed at Transition No. 4. The different cases are denoted fine grit clean, fouling 1 and fouling 2 or the respective stages of fouling.

The numerical results shown in Table 5.4 show the clean plate with an average Rt value of 1.72mm. This compares well to the particle size distribution of the fine grit in Chapter 4.

A reduced peak count and increased mean is shown for fouling 1, indicating a rougher surface. This is consistent with the observations of a slightly fouled surface, and the small values of mean biofilm thickness. Mean biofilm thickness was determined by subtracting the mean value of the raw clean surface data from the mean value of the raw fouled surface data. By raw data, it is meant the data describing the distance from the camera lens to the test surface. Both fouling 1 and fouling 2 results are relative to the clean plate results.

Fouling 2 was observed to be free from biological grows and is why the results closely resemble the data from the clean plate, with only small measured biofilm thickness.

Table 5.4: Roughness analysis for the fine grit small plates deployed at Transition No. 4.

Transition No. 4 Fine Grit Clean	Roughness Parameters (mm)					Statistical moments				Peak
Surface Profile	Ra	Rq	Rp	Rv	Rt	1st (mean)	2nd (variance)	3rd (skewness)	4th (kurtosis)	Count
Y=20mm	0.31	0.39	1.02	-1.19	2.21	1.19	0.15	0.29	0.08	12
Y=40mm	0.23	0.29	1.03	-0.67	1.70	0.67	0.09	0.96	1.14	13
Y=60mm	0.25	0.31	1.10	-0.53	1.63	0.53	0.10	0.83	0.68	19
Y=80mm	0.21	0.25	0.63	-0.46	1.09	0.46	0.06	0.27	-0.58	13
Y=100mm	0.25	0.37	1.24	-0.74	1.98	0.74	0.14	1.22	1.67	10
Average:	0.25	0.32	1.00	-0.72	1.72	0.72	0.11	0.71	0.60	13.40

Fine Grit Fouling 1	Roughness Parameters (mm)					Statistical moments				Peak	Mean Biofilm
Surface Profile	Ra	Rq	Rp	Rv	Rt	1st (mean)	2nd (variance)	3rd (skewness)	4th (kurtosis)	Count	Thickness (mm)
Y=20mm	0.24	0.31	0.78	-1.08	1.86	1.08	0.10	-0.03	0.47	12	0.18
Y=40mm	0.21	0.27	0.85	-0.64	1.49	0.64	0.07	0.52	0.56	13	0.11
Y=60mm	0.30	0.38	1.34	-0.71	2.06	0.71	0.15	1.03	1.26	15	0.19
Y=80mm	0.28	0.40	1.82	-0.57	2.39	0.57	0.16	2.03	6.21	8	0.24
Y=100mm	0.41	0.51	1.41	-0.97	2.38	1.16	0.23	-0.31	0.52	6	0.04
Average:	0.29	0.38	1.24	-0.79	2.04	0.83	0.14	0.65	1.80	10.80	0.15

Fine Grit Fouling 2	Roughness Parameters (mm)					Statistical moments				Peak	Mean Biofilm
Surface Profile	Ra	Rq	Rp	Rv	Rt	1st (mean)	2nd (variance)	3rd (skewness)	4th (kurtosis)	Count	Thickness (mm)
Y=20mm	0.26	0.34	0.90	-0.74	1.64	0.74	0.11	0.47	0.23	16	0.12
Y=40mm	0.26	0.33	0.96	-0.83	1.57	0.83	0.11	0.32	0.59	9	0.03
Y=60mm	0.26	0.33	1.23	-0.59	1.82	0.59	0.11	0.86	1.13	14	0.08
Y=80mm	0.22	0.28	0.84	-0.66	1.49	0.66	0.08	0.43	0.08	12	0.05
Y=100mm	0.31	0.38	1.11	-0.68	1.80	0.68	0.15	0.60	0.11	11	-0.01
Average:	0.26	0.33	1.01	-0.70	1.66	0.70	0.11	0.54	0.43	12.40	0.05

Figure 5.33 shows a digital image of each analysed surface. The different appearance of each image is from slight differences in lighting and exposure of the film during photography.

Figure 5.34 presents the surface profiles, derived from the photogrammetric process, at cross sections indicated on the images of Figure 5.33 by red lines. The profiles follow very similar patterns, with fouling 1 showing the most discernable increase in height, in most of the profiles.

The Z height (mm) on the vertical axis in Figure 5.34 indicates the total distance from the camera lens, and is not referenced to a zero datum as is the case for data presented later in the thesis. Instead the datum is referenced from the camera support used to locate the camera on the test plates.

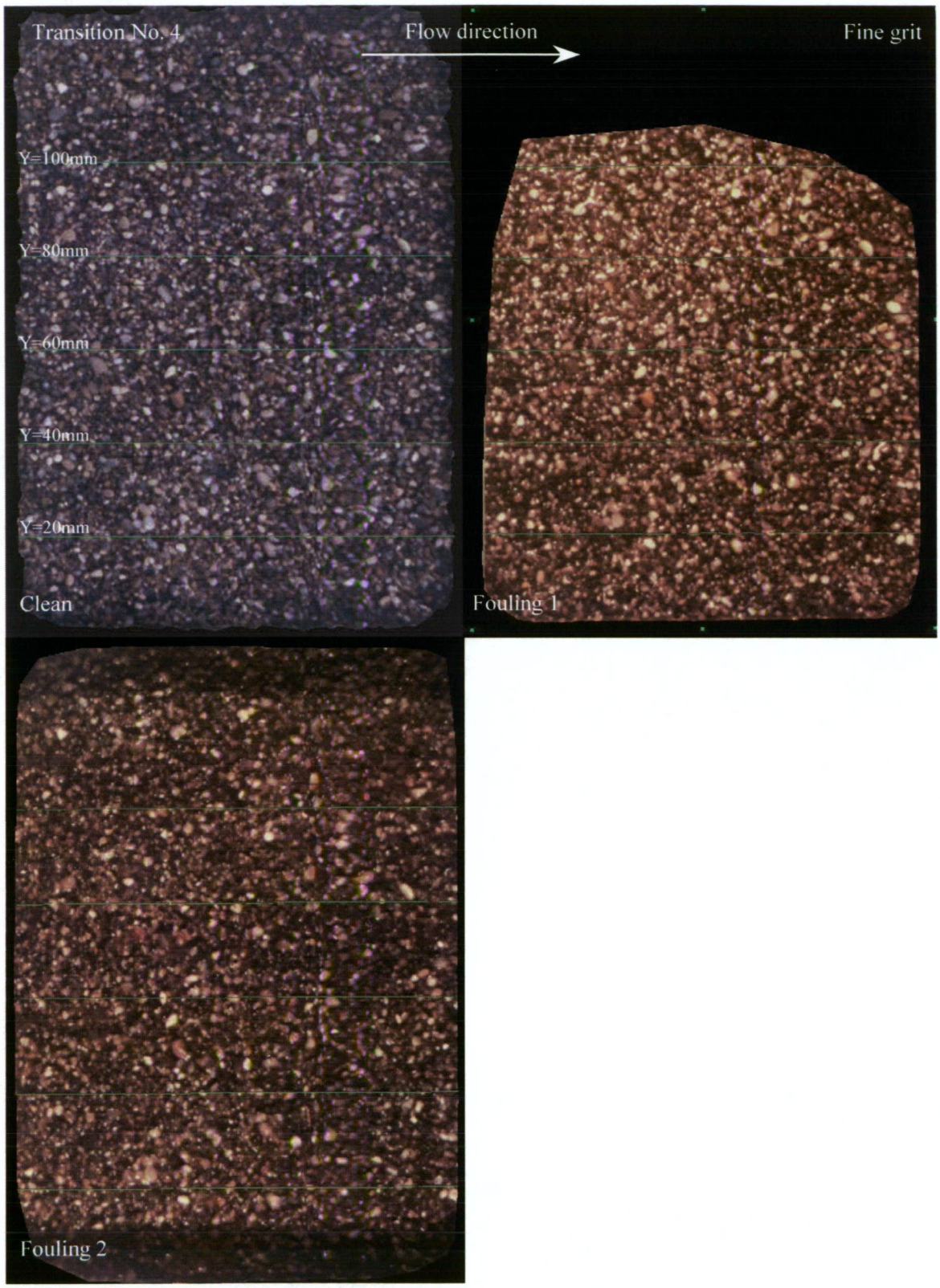

Figure 5.33: Digital images of small plate fine grit clean, fouling 1 and fouling 2 at Transition No. 4.

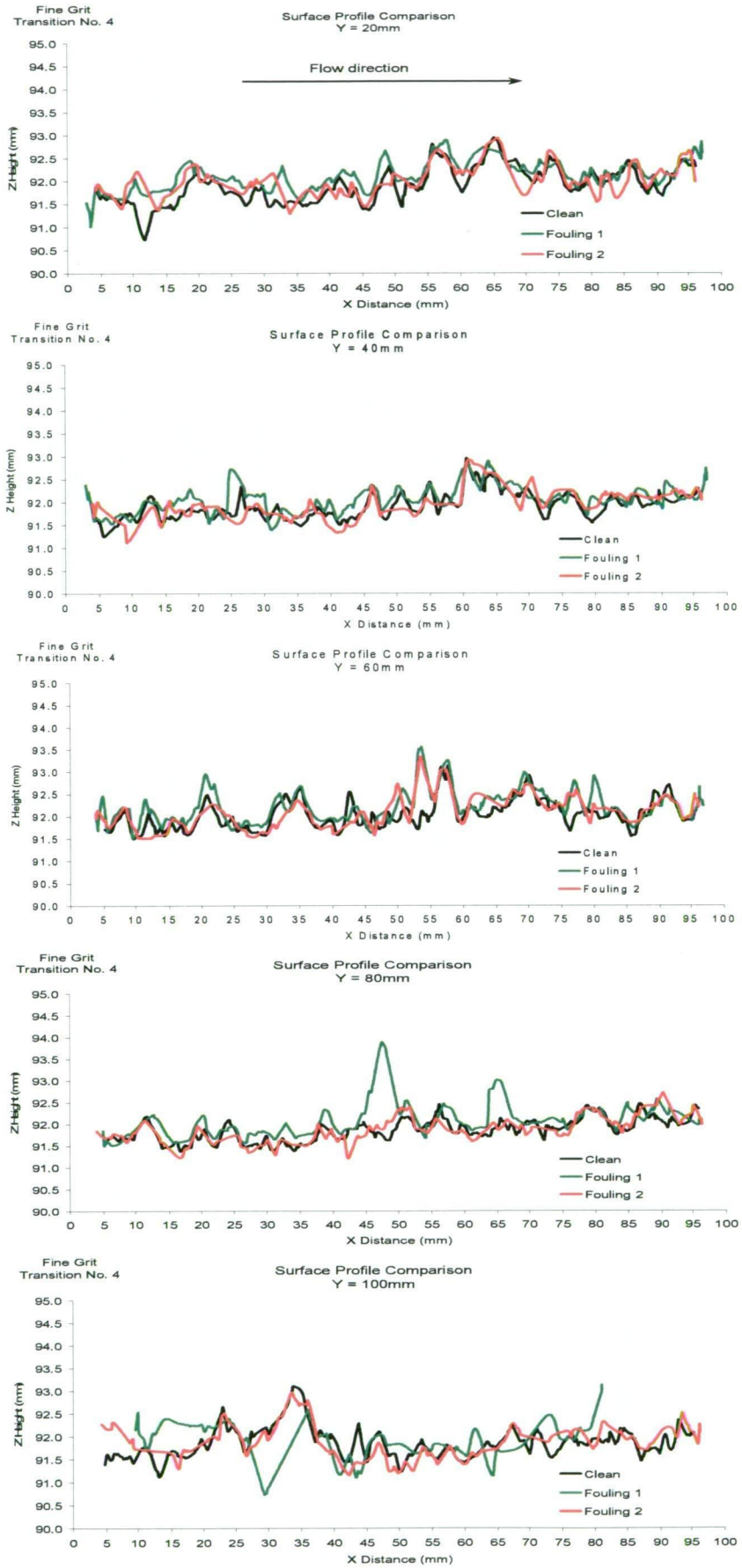

Figure 5.34: Clean and biofouled surface profiles for fine grit at Transition No. 4.

5.6.1.2 Fine Grit at Pond No. 1

The fine grit small plates deployed at Pond No. 1 were examined using the same procedure for the plates at Transition No. 4. A fine grit clean plate was first photographed, then deployed at Pond No. 1 for biofouling. The plate was then retrieved periodically for analysis.

Table 5.5 presents the surface roughness analysis for fine grit clean, fouling 1 and fouling 2. The result for the clean plate displays similar results to other fine grit data.

An important result for fouling 1, is that the mean surface roughness has decreased with the addition of a biofilm layer. The biofilm has filled in the valleys and interstitial spaces of the rough surface, creating a "smoother" surface, corresponding with the middle option put forward in Figure 4.1, Chapter 4. A mean biofilm thickness of 0.5mm was measured. Figure 5.35 shows the considerable amount of biofouling observed on fine grit fouling 1.

Results for fouling 2 show lower values of mean biofilm thickness, although this has been influenced by the removal of some grit. This is shown as a dip on the surface profile in Figure 5.35 at Y=60mm and Y=80mm. Less biofilm was observed for fouling 2 than for fouling 1.

Table 5.5: Roughness analysis for the fine grit small plates deployed at Pond No. 1.

Pond No. 1 Fine Grit Clean	Roughness Parameters (mm)					Statistical moments				Peak	
Surface Profile	Ra	Rq	Rp	Rv	Rt	1st (mean)	2nd (variance)	3rd (skewness)	4th (kurtosis)	Count	
Y=20mm	0.21	0.27	0.77	-0.70	1.47	0.70	0.07	0.12	0.25	12	
Y=40mm	0.45	0.53	1.02	-1.26	2.28	1.26	0.28	-0.09	-0.96	16	
Y=60mm	0.22	0.29	0.74	-1.31	2.05	1.31	0.08	-0.27	2.21	14	
Y=80mm	0.24	0.33	0.82	-1.17	1.99	1.17	0.11	-0.85	2.00	12	
Y=100mm	0.24	0.30	0.78	-0.80	1.58	0.74	0.09	0.06	0.12	13	
Average:	0.27	0.34	0.83	-1.05	1.87	1.04	0.13	-0.21	0.72	13.40	

Fine Grit Fouling 1	Roughness Parameters (mm)					Statistical moments				Peak	Mean Biofilm
Surface Profile	Ra	Rq	Rp	Rv	Rt	1st (mean)	2nd (variance)	3rd (skewness)	4th (kurtosis)	Count	Thickness (mm)
Y=20mm	0.24	0.30	1.03	-0.58	1.61	0.58	0.09	0.61	0.43	12	0.43
Y=40mm	0.43	0.50	0.96	-0.88	1.85	0.88	0.25	0.27	-1.15	12	0.47
Y=60mm	0.23	0.31	1.01	-0.84	1.84	0.84	0.09	0.65	0.98	10	0.53
Y=80mm	0.21	0.26	0.69	-0.67	1.37	0.67	0.07	-0.04	-0.05	16	0.50
Y=100mm	0.29	0.38	1.12	-1.19	2.30	1.19	0.14	0.15	1.30	11	0.55
Average:	0.28	0.35	0.96	-0.83	1.79	0.83	0.13	0.32	0.30	12.20	0.50

Fine Grit Fouling 2	Roughness Parameters (mm)					Statistical moments				Peak	Mean Biofilm
Surface Profile	Ra	Rq	Rp	Rv	Rt	1st (mean)	2nd (variance)	3rd (skewness)	4th (kurtosis)	Count	Thickness (mm)
Y=20mm	0.25	0.32	0.92	-0.63	1.55	0.63	0.10	0.50	0.11	11	0.24
Y=40mm	0.48	0.58	1.27	-1.76	3.03	1.76	0.34	-0.20	-0.29	7	0.16
Y=60mm	0.26	0.43	1.38	-2.29	3.66	2.29	0.18	-1.86	11.38	11	0.12
Y=80mm	0.30	0.43	0.95	-1.97	2.92	1.97	0.18	-0.74	3.35	12	0.16
Y=100mm	0.30	0.36	0.73	-1.15	1.88	1.15	0.13	-0.50	-0.15	11	0.12
Average:	0.32	0.42	1.05	-1.56	2.61	1.56	0.19	-0.56	2.88	10.40	0.16

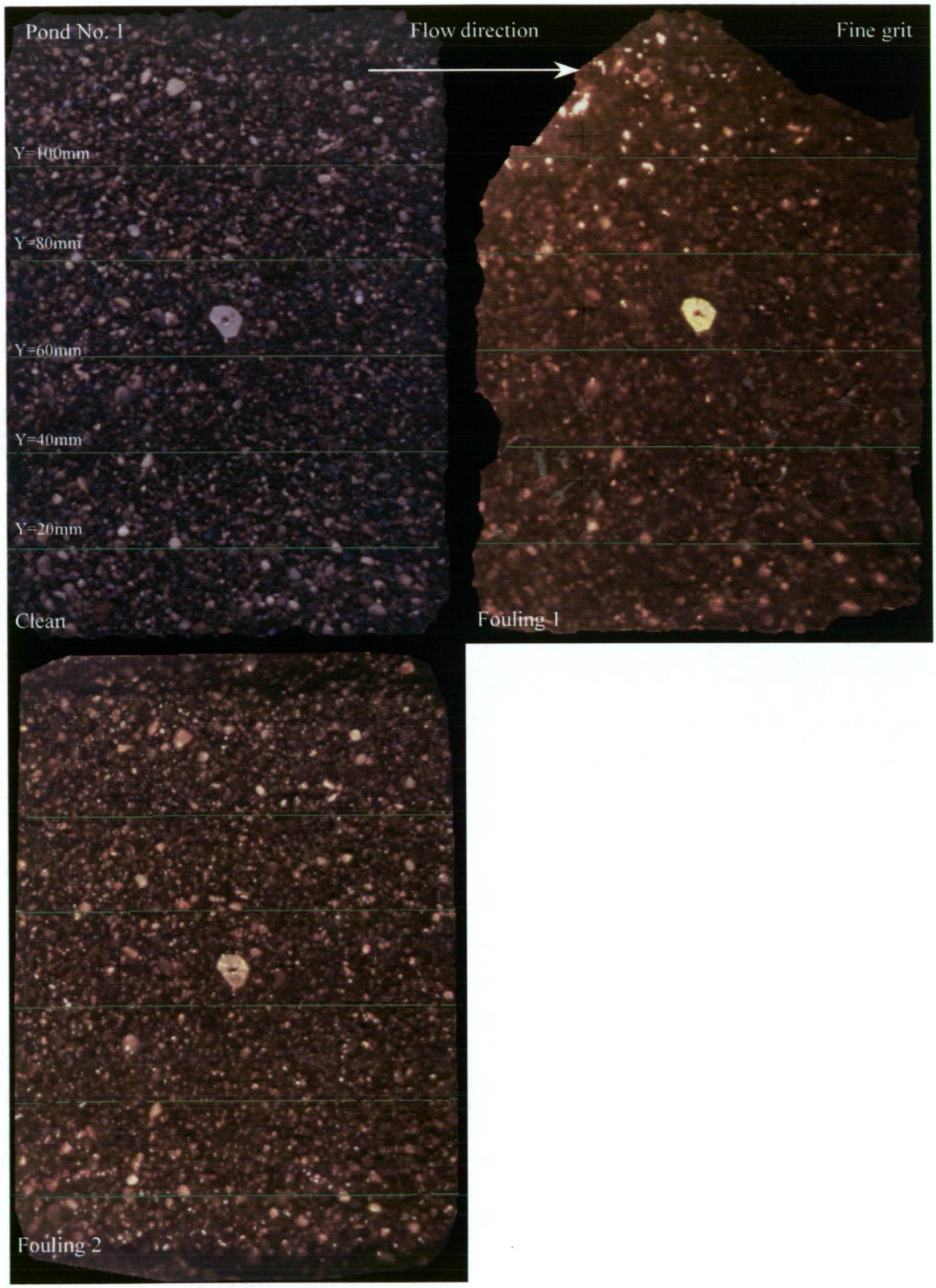

Figure 5.35: Digital images of small plate fine grit clean, fouling 1 and fouling 2 at Pond No. 1.

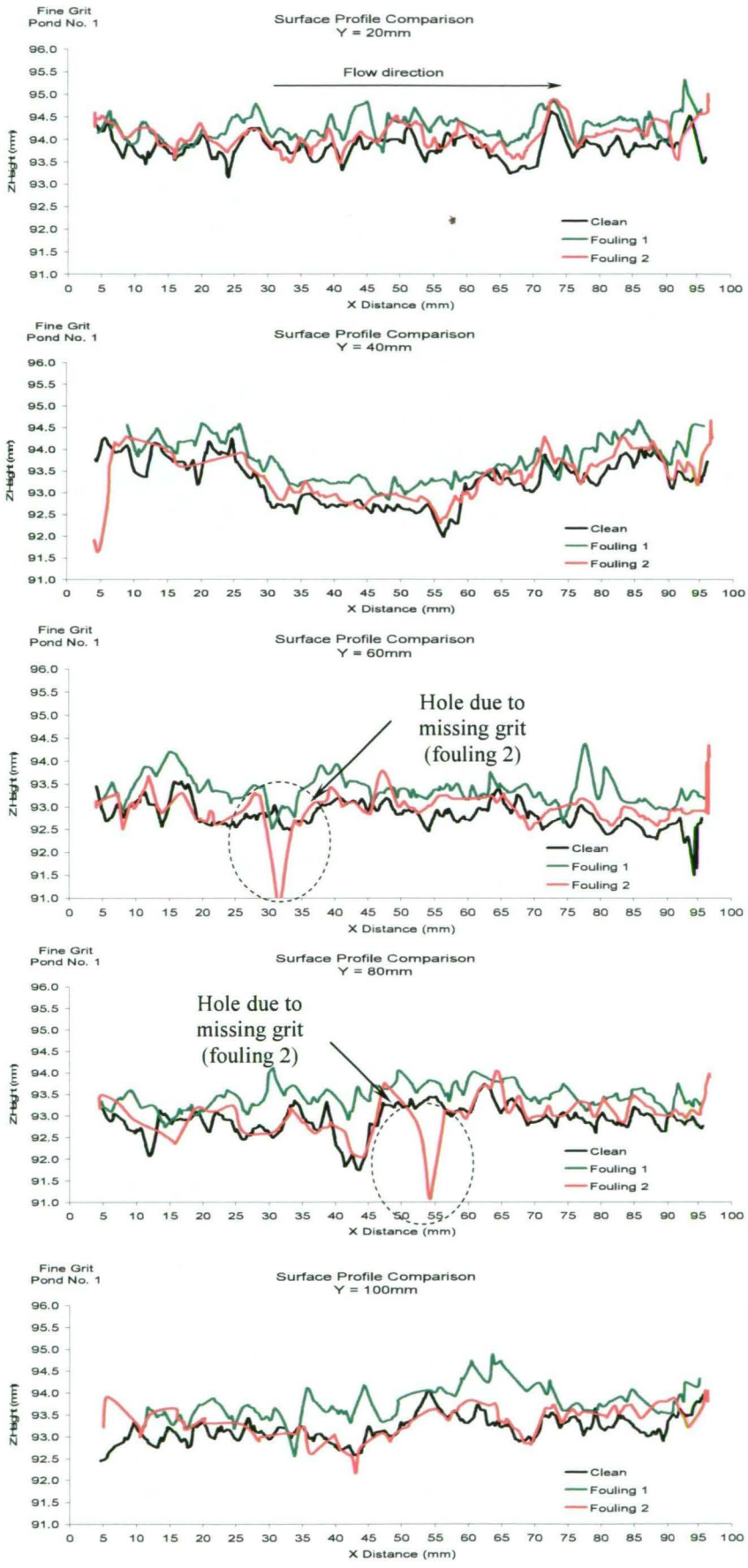

Figure 5.36: Clean and biofouled surface profiles for fine grit at Pond No. 1.

5.6.1.3 Coarse Grit at Transition No. 4

A grit small plate was deployed at Transition No. 4 alongside the fine grit plate. Using the same procedures, photographs were taken of clean and then biofouled plates at regular intervals.

Table 5.6 presents the surface roughness analysis for the coarse grit plate in its clean condition, then fouled conditions, denoted fouling 1 and fouling 2. The Rt values for the clean plate shows similar values to the diameters determined from particle size distribution in Chapter 4.

Fouling 1 shows an increase in mean surface roughness. A biofilm thickness (that is change in mean surface height) was also measured, though it was observed that only some biofilm was present. It is thought that pooling of water on the test plate during photography may have contributed to this mean surface increase.

Fouling 2 shows a significant increase in mean surface roughness, but not due to the presence of a biofilm. Some grit has been washed off resulting in some deeper holes on the surface. The profile at Y=100mm shows this best.

Table 5.6: Roughness analysis for the coarse grit small plate deployed at Transition No. 4.

Transition No. 4 Coarse Grit Clean	Roughness Parameters (mm)					Statistical moments				Peak
Surface Profile	Ra	Rq	Rp	Rv	Rt	1st (mean)	2nd (variance)	3rd (skewness)	4th (kurtosis)	Count
Y=20mm	0.49	0.63	1.00	-1.87	2.87	1.87	0.40	-0.71	0.11	13
Y=40mm	0.41	0.52	1.50	-1.26	2.76	1.26	0.27	0.22	-0.11	12
Y=60mm	0.41	0.49	1.09	-1.20	2.29	1.20	0.24	0.10	-0.60	11
Y=80mm	0.58	0.69	1.65	-1.33	2.98	1.33	0.48	0.44	-0.59	12
Y=100mm	0.52	0.65	1.68	-1.20	2.88	1.20	0.42	0.47	-0.44	12
Average:	0.48	0.59	1.39	-1.37	2.76	1.37	0.36	0.10	-0.32	12.00

Coarse Grit Fouling 1	Roughness Parameters (mm)					Statistical moments				Peak	Mean Biofilm
Surface Profile	Ra	Rq	Rp	Rv	Rt	1st (mean)	2nd (variance)	3rd (skewness)	4th (kurtosis)	Count	Thickness (mm)
Y=20mm	0.47	0.65	2.41	-2.12	4.53	2.12	0.42	-0.64	1.97	6	0.26
Y=40mm	0.48	0.55	0.85	-1.36	2.21	1.36	0.31	-0.41	-1.09	14	0.40
Y=60mm	0.46	0.54	1.20	-1.28	2.48	1.28	0.30	0.15	-0.53	11	0.35
Y=80mm	0.57	0.73	2.06	-1.59	3.65	1.59	0.54	0.58	0.26	8	0.30
Y=100mm	0.49	0.60	1.36	-1.28	2.63	1.28	0.36	0.13	-0.44	10	0.30
Average:	0.49	0.62	1.57	-1.53	3.10	1.53	0.39	-0.04	0.03	9.80	0.32

Coarse Grit Fouling 2	Roughness Parameters (mm)					Statistical moments				Peak	Mean Biofilm
Surface Profile	Ra	Rq	Rp	Rv	Rt	1st (mean)	2nd (variance)	3rd (skewness)	4th (kurtosis)	Count	Thickness (mm)
Y=20mm	0.51	0.63	0.95	-1.75	2.70	1.75	0.40	-0.70	-0.28	13	-0.24
Y=40mm	0.54	0.65	1.54	-1.11	2.65	1.11	0.42	0.46	-0.47	9	0.01
Y=60mm	0.40	0.53	1.73	-1.05	2.78	1.05	0.28	0.88	0.88	9	-0.03
Y=80mm	0.58	0.70	1.94	-1.80	3.74	1.80	0.50	-0.09	-0.50	10	-0.13
Y=100mm	0.58	0.78	1.81	-2.36	4.17	2.36	0.62	-0.13	1.17	6	0.02

Figure 5.37 shows the digital images of the coarse grit test plate in respectively clean and fouled conditions. Figure 5.38 presents the surface data from the photogrammetry analysis. Note the scale difference in the vertical axis from the fine grit plots for the Z height data.

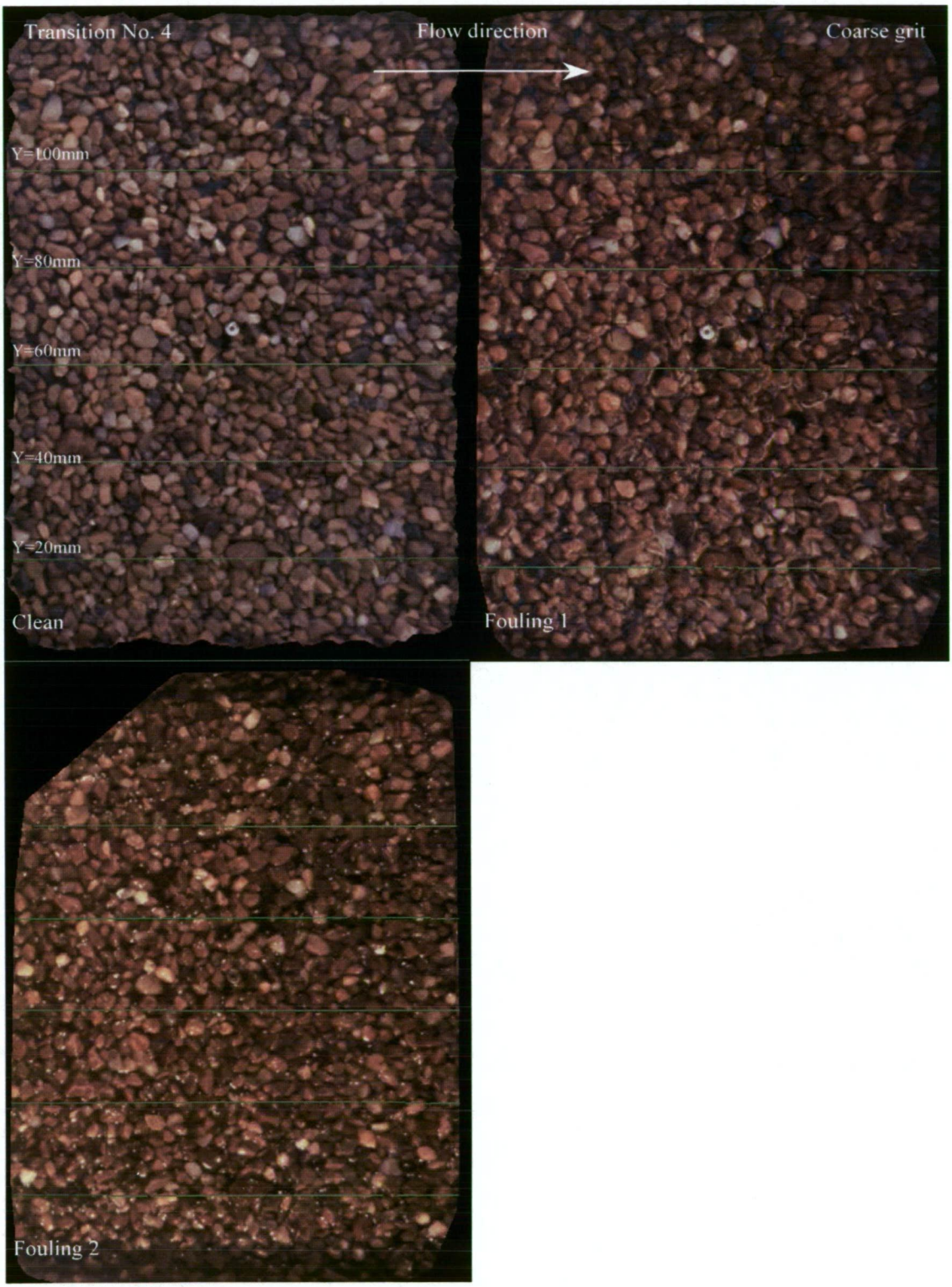

Figure 5.37: Digital images of small plate coarse grit clean, fouling 1 and fouling 2 at Transition No. 4.

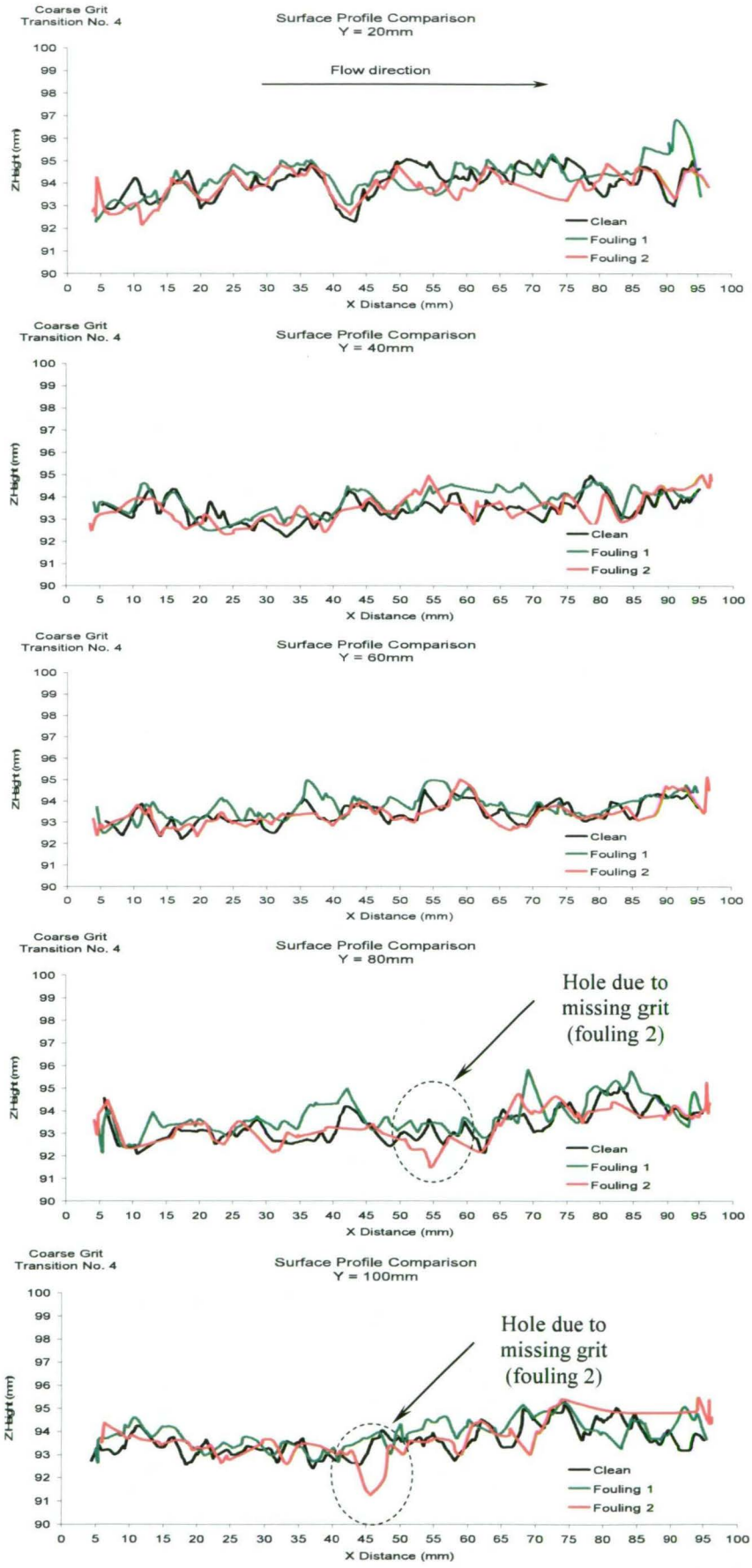

Figure 5.38: Clean and biofouled surface profiles for coarse grit at Transition No. 4.

5.6.1.4 Coarse Grit at Pond No. 1

As with the other plates studied, the coarse grit plate deployed at Pond No. 1 was photographed in its clean state. The plate was then deployed and retrieved, at intervals after fouling, to be re-photographed for photogrammetric analysis.

Table 5.7 presented the numerical results of the surface analysis. Figure 5.39 shows the digital images of the various test plates clean and fouled cases, with Figure 5.40 showing the surface profiles.

The largest amount of fouling observed and measured for any of the small plates was for the coarse grit fouling 1 deployed at Pond No. 1. Approximately 1mm coverage of biofilm was measured across the entire photography window. There was also an associated increase in Rt and mean roughness. Show in Figure 5.40 are periodic clumps of biofilm which were observed running transverse to the flow direction discussed further later in this section. These clumps are the source of the increase in roughness.

Significant amounts of biological growth were present on fouling 2, associated with a small reduction in mean surface roughness. Fouling in this case increased with the plate depth in the water. This supports the "smoothing" action of the physical surface by the biofilm, similar to the observations and measurements for the fine grit plate deployed at Pond No. 1. This is shown particularly well in Figure 5.40 at profiles Y=20 and 40mm. Interestingly, at profiles Y= 60, 80 and 100mm, small "peaks" are seen on some of the larger pieces of grit. This is indicated on Figure 5.40, and corresponds with the bottom option put forward in Figure 4.1, Chapter 4.

Table 5.7: Roughness analysis for the coarse grit small plate deployed at Pond No. 1.

Pond No. 4

Coarse Grit Clean	Roughness Parameters (mm)					Statistical moments				Peak
Surface Profile	Ra	Rq	Rp	Rv	Rt	1st (mean)	2nd (variance)	3rd (skewness)	4th (kurtosis)	Count
Y=20mm	0.52	0.64	1.74	-1.31	3.05	1.31	0.41	0.26	-0.35	12
Y=40mm	0.43	0.54	1.38	-1.02	2.40	1.02	0.29	0.24	-0.37	11
Y=60mm	0.58	0.72	1.73	-1.37	3.10	1.37	0.52	0.65	-0.42	11
Y=80mm	0.44	0.52	1.50	-0.98	2.48	0.98	0.27	0.27	-0.66	14
Y=100mm	0.50	0.65	2.35	-1.25	3.60	1.25	0.42	0.95	1.50	9
Average:	0.50	0.61	1.74	-1.19	2.93	1.19	0.38	0.47	-0.06	11.40

Coarse Grit Fouling 1	Roughness Parameters (mm)					Statistical moments				Peak	Mean Biofilm
Surface Profile	Ra	Rq	Rp	Rv	Rt	1st (mean)	2nd (variance)	3rd (skewness)	4th (kurtosis)	Count	Thickness (mm)
Y=20mm	0.46	0.60	1.59	-1.86	3.46	1.86	0.37	0.16	0.99	6	0.86
Y=40mm	0.45	0.58	1.92	-1.20	3.13	1.20	0.34	0.69	0.85	7	1.22
Y=60mm	0.60	0.70	1.94	-1.34	3.27	1.34	0.49	0.54	-0.57	10	0.97
Y=80mm	0.51	0.66	1.71	-1.29	3.00	1.29	0.44	0.41	-0.17	9	1.10
Y=100mm	0.56	0.67	1.27	-1.20	2.48	1.20	0.45	0.42	-0.88	8	0.96
Average:	0.51	0.64	1.69	-1.38	3.07	1.38	0.42	0.45	0.04	8.00	1.02

Coarse Grit Fouling 2	Roughness Parameters (mm)					Statistical moments				Peak	Mean Biofilm
Surface Profile	Ra	Rq	Rp	Rv	Rt	1st (mean)	2nd (variance)	3rd (skewness)	4th (kurtosis)	Count	Thickness (mm)
Y=20mm	0.33	0.40	1.03	-0.62	1.65	0.62	0.16	0.78	-0.02	8	0.68
Y=40mm	0.41	0.54	1.55	-0.93	2.47	0.93	0.29	0.74	0.42	8	0.75
Y=60mm	0.57	0.72	1.91	-1.21	3.12	1.21	0.52	1.01	0.15	7	0.23
Y=80mm	0.44	0.54	1.25	-1.24	2.49	1.24	0.29	-0.23	-0.57	12	0.22
Y=100mm	0.41	0.50	1.28	-1.07	2.35	1.07	0.26	0.31	-0.32	13	0.06
Average:	0.43	0.54	1.40	-1.01	2.42	1.01	0.30	0.52	-0.07	9.60	0.39

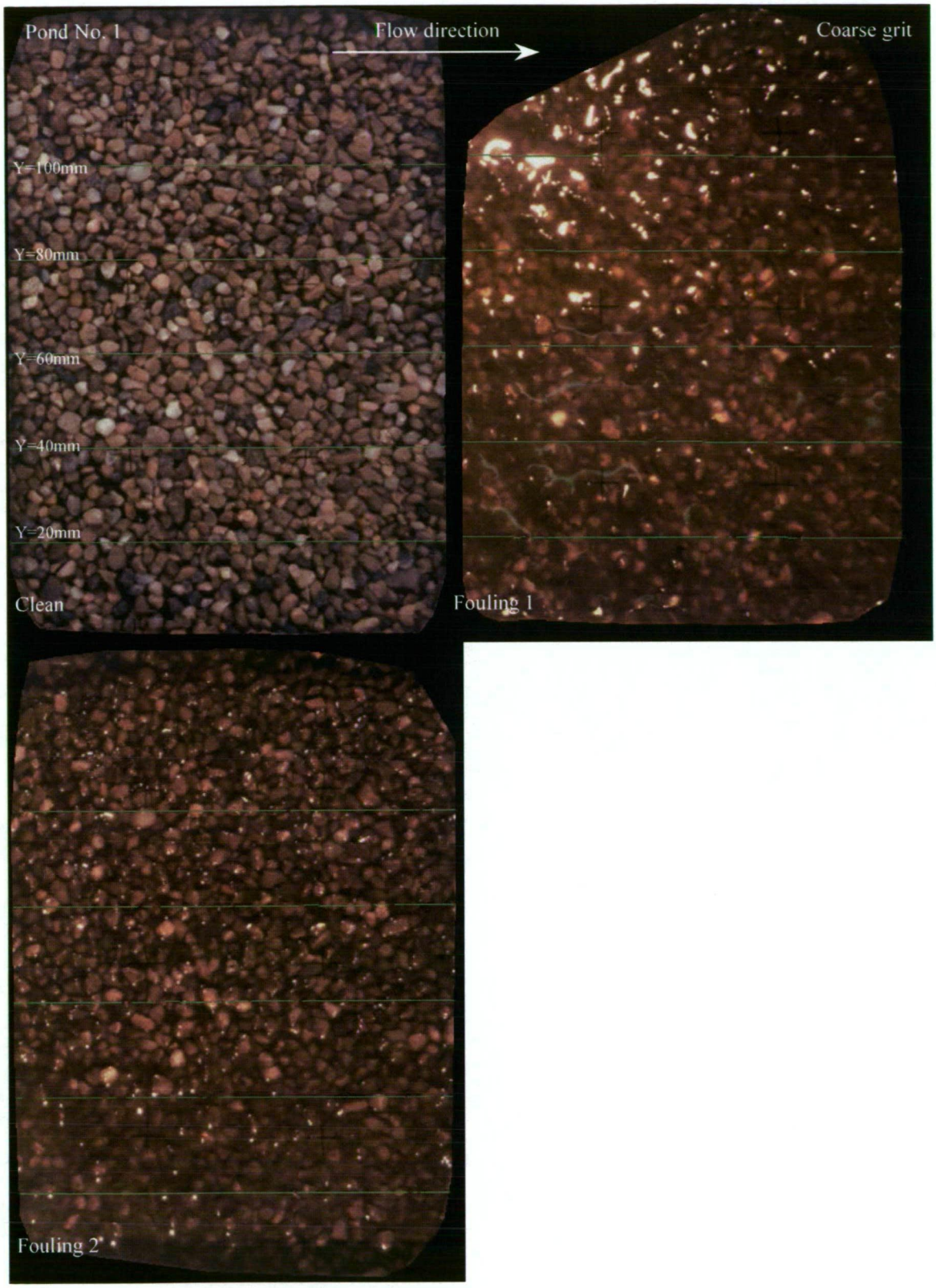

Figure 5.39: Digital images of small plate coarse grit clean, fouling 1 and fouling 2 at Pond No. 1.

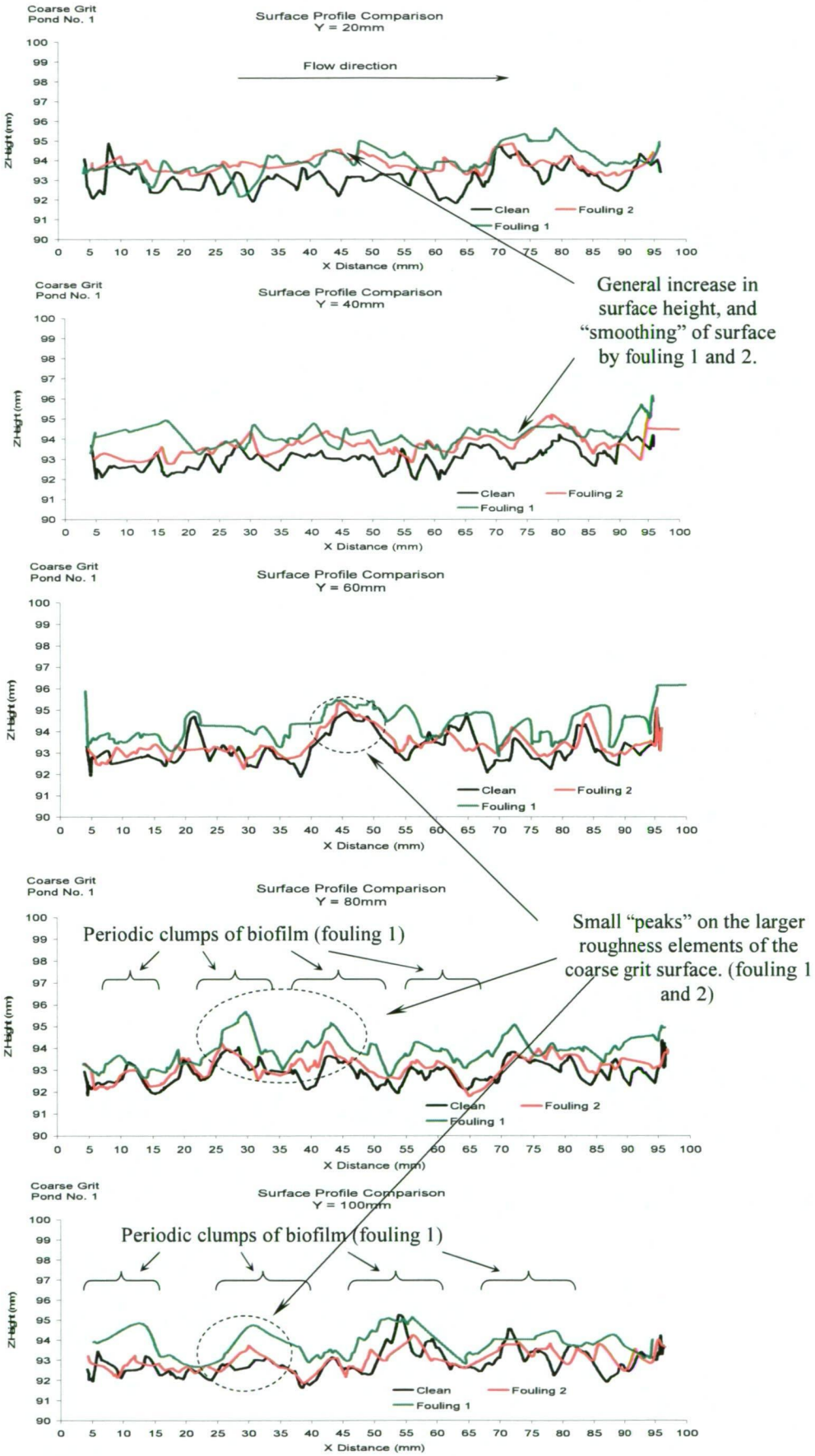

Figure 5.40: Clean and biofouled surface profiles for coarse grit at Pond No. 1.

It was observed on the more densely fouled surfaces, for example, coarse grit fouling 1 from Pond No. 1, the appearance of ripple or dune formations transverse to the flow direction. The biofilm in this case looked particularly vigorous and healthy. Lee *et al.* (1993) presents results for an artificial compliant surface displaying similar transverse ripple behaviour. Kennedy (1963) describes the formation of dunes in some detail on erodible channel beds. Biofilms may be considered erodible, as they have often been described equally so by Stoodley *et al.* (1999; 2001), and so many of the same principles of erodible beds may apply.

Figure 5.41 shows this ripple phenomenon on the test plate. An interesting question is whether or not this is passive behaviour of the biofilm, or if this formation provides a competitive advantage, and so the biofilm somehow actively facilitates this formation. It is known for example that there are generally higher velocities, shear stresses and mass transfer rates near peak regions, and adds to the question raised in Chapter 4 suggested by Nikora *et al.* (2002) on the choice of peaks for biofilm growth. This was also shown earlier in this section from the photogrammetry studies.

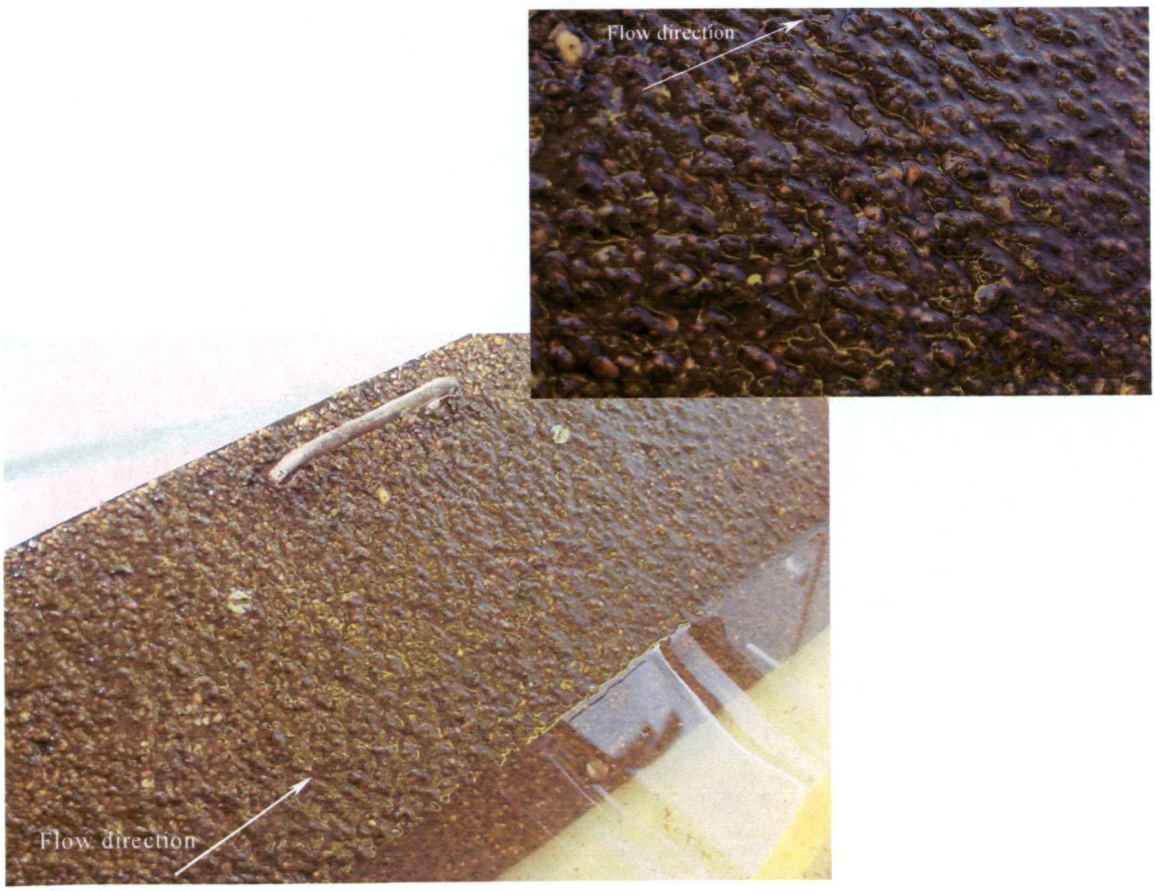

Figure 5.41: Fouling 1 on coarse grit from Pond No. 1 with the inset phot showing a close-up.

Figure 5.42 shows an example of transverse growth behaviour for a filamentous type algae observed in an open channel.

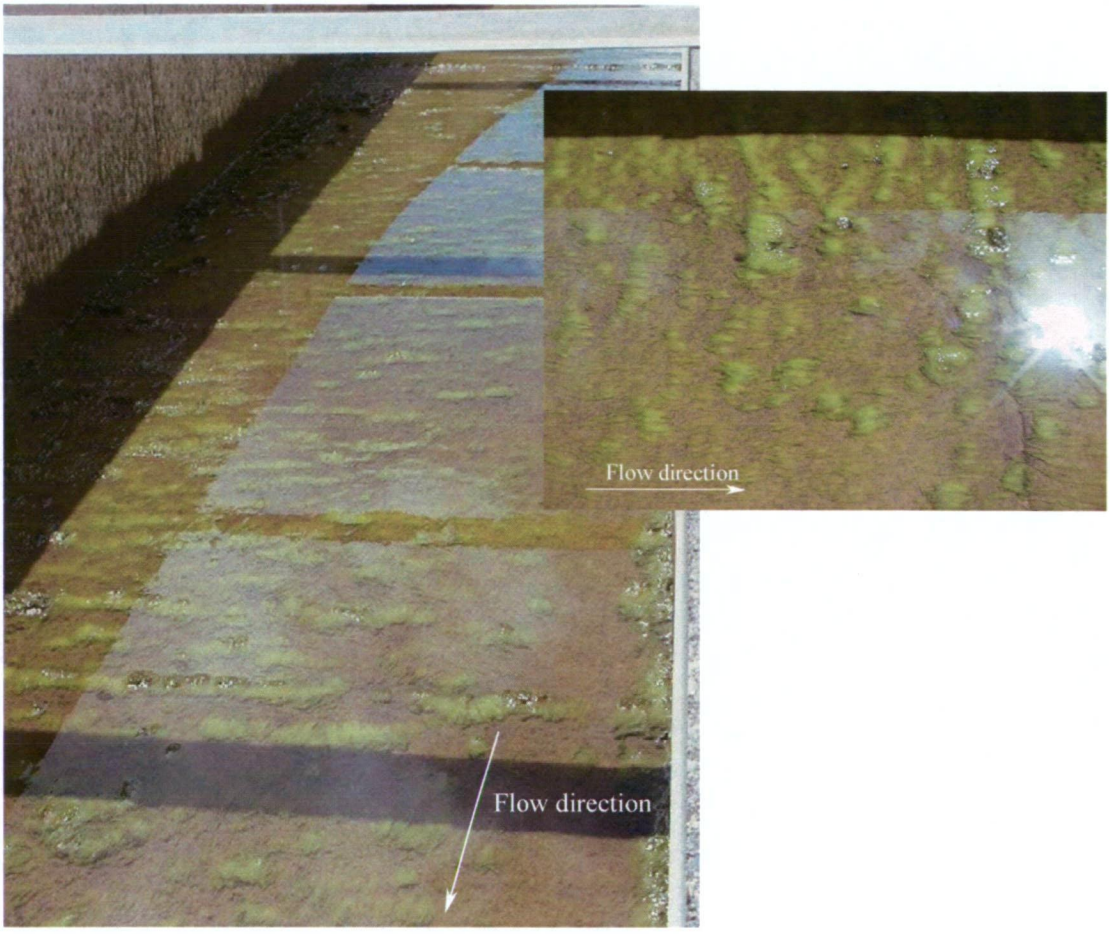

Figure 5.42: Transverse growth pattern of filamentous algae.

5.6.2 Tarraleah No. 1 Canal Wall Roughness

Photographs were taken of Tarraleah No. 1 Canal at various locations. One of the locations was the inverted siphon located approximately halfway between Bridge No. 9 and Transition No. 4 (see Figure 4.9). Photos were taken of the open channel wall, invert (floor) and chamfer (where the floor angles to meet the wall) at both the upstream and downstream ends of this siphon. Photos were also taken at Transition No. 4 where the surface had recently been cleaned with high-pressure water spray, and at a lined section (with a resin type surface coating) where the canal had recently undergone repair work. The lined section in this case

represents the approximate surface condition if the canal were to be re-lined with, for example, a Jotamastic type paint used for the water tunnel measurements (see Chapter 7).

The roughness data (Table 5.8) along with the photographed area and surface profiles (Figures 5.44 and 5.45) are shown only for Transition No. 4, as these data are the most directly comparable to the fine and coarse grits and painted surfaces used in the present study. Figure 5.43 shows the surface of Transition No. 4 where the photos for roughness analysis were taken.

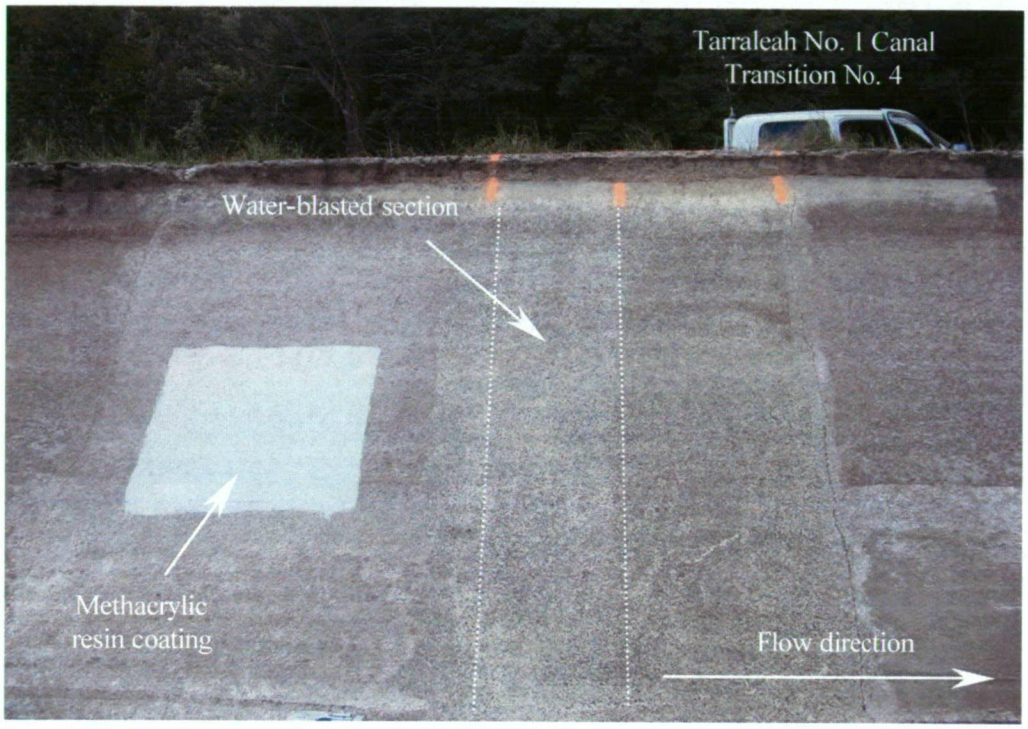

Figure 5.43: Photo showing location at Transition No. 4 where photos where taken for surface roughness analsyis.

The kurtosis of the epoxy coating surface, at Transition No. 4, suggests a very smooth, flat surface profile, confirmed by the low peak count. The large bumps due to bubbles on the surface skew the mean result and significantly change the Rt and other roughness values.

Results for the clean canal wall, at Transition No. 4, show a close resemblance to the artificial grits used for the small plate trials and the large plate water tunnel measurements presented in Chapter 8. The data have had no filtering applied. This validates the use of both the grit types used in the present study.

Table 5.8: Roughness data for Tarraleah No. 1 Canal

Transition No. 4 Clean	Roughness Parameters (mm)					Statistical moments				Peak
Surface Profile	Ra	Rq	Rp	Rv	Rt	1st (mean)	2nd (variance)	3rd (skewness)	4th (kurtosis)	Count
Y=20mm	0.38	0.46	0.97	-1.18	2.15	1.18	0.21	-0.21	-0.35	15
Y=40mm	0.41	0.50	0.79	-1.39	2.19	1.39	0.25	-0.49	-0.21	10
Y=60mm	0.43	0.51	1.27	-1.15	2.42	1.15	0.26	0.09	-0.77	11
Y=80mm	0.47	0.55	1.08	-1.06	2.14	1.06	0.30	0.14	-0.97	12
Y=100mm	0.38	0.46	0.80	-1.16	1.95	1.06	0.21	-0.05	-0.68	14
Average:	0.41	0.50	0.98	-1.19	2.17	1.17	0.25	-0.10	-0.60	12.40

Transition No. 4 Epoxy	Roughness Parameters (mm)					Statistical moments				Peak
Surface Profile	Ra	Rq	Rp	Rv	Rt	1st (mean)	2nd (variance)	3rd (skewness)	4th (kurtosis)	Count
Y=20mm	0.12	0.16	0.72	-0.34	1.07	0.34	0.03	0.74	2.27	5
Y=40mm	0.12	0.16	0.55	-0.59	1.14	0.59	0.03	0.29	1.72	8
Y=60mm	0.19	0.25	0.79	-0.41	1.20	0.41	0.06	0.75	1.06	7
Y=80mm	0.21	0.30	1.07	-0.51	1.58	0.51	0.09	0.91	1.33	3
Y=100mm	0.27	0.41	1.42	-0.67	2.10	0.67	0.02	-0.23	-1.00	2
Average:	0.18	0.26	0.91	-0.51	1.42	0.51	0.05	0.49	1.08	5.00

Data from the other sites display the variability of the surface condition along the canal length with Rt values of between 6.15 and 2.85mm, and are presented in Appendix C of this thesis. Tarraleah No. 1 Canal is also an old structure, and represents aged and weathered concrete. This provides further justification of using the fine grit in the water tunnel measurements in Chapter 8, as this better represents concrete lined channels generally.

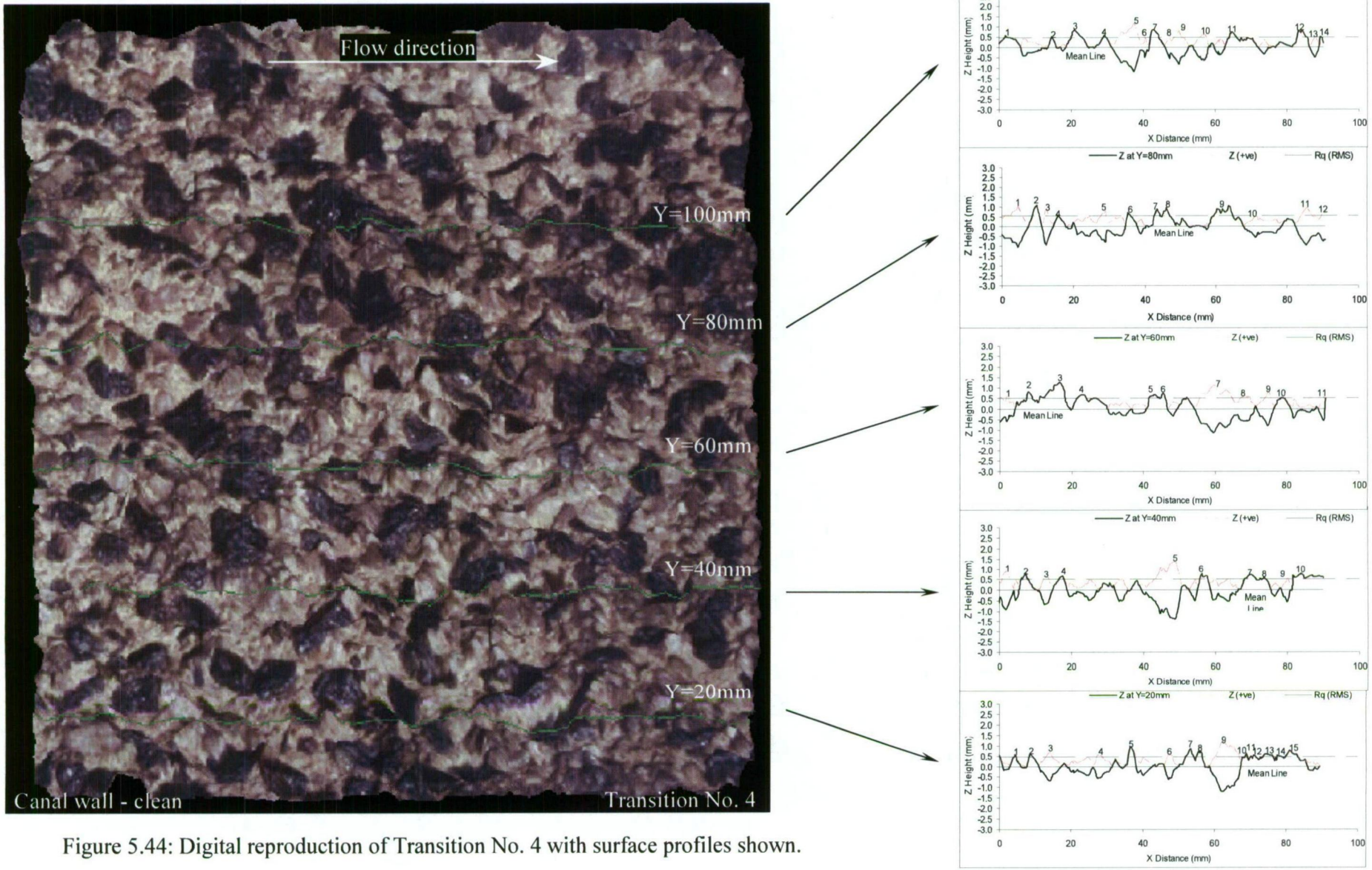

Figure 5.44: Digital reproduction of Transition No. 4 with surface profiles shown.

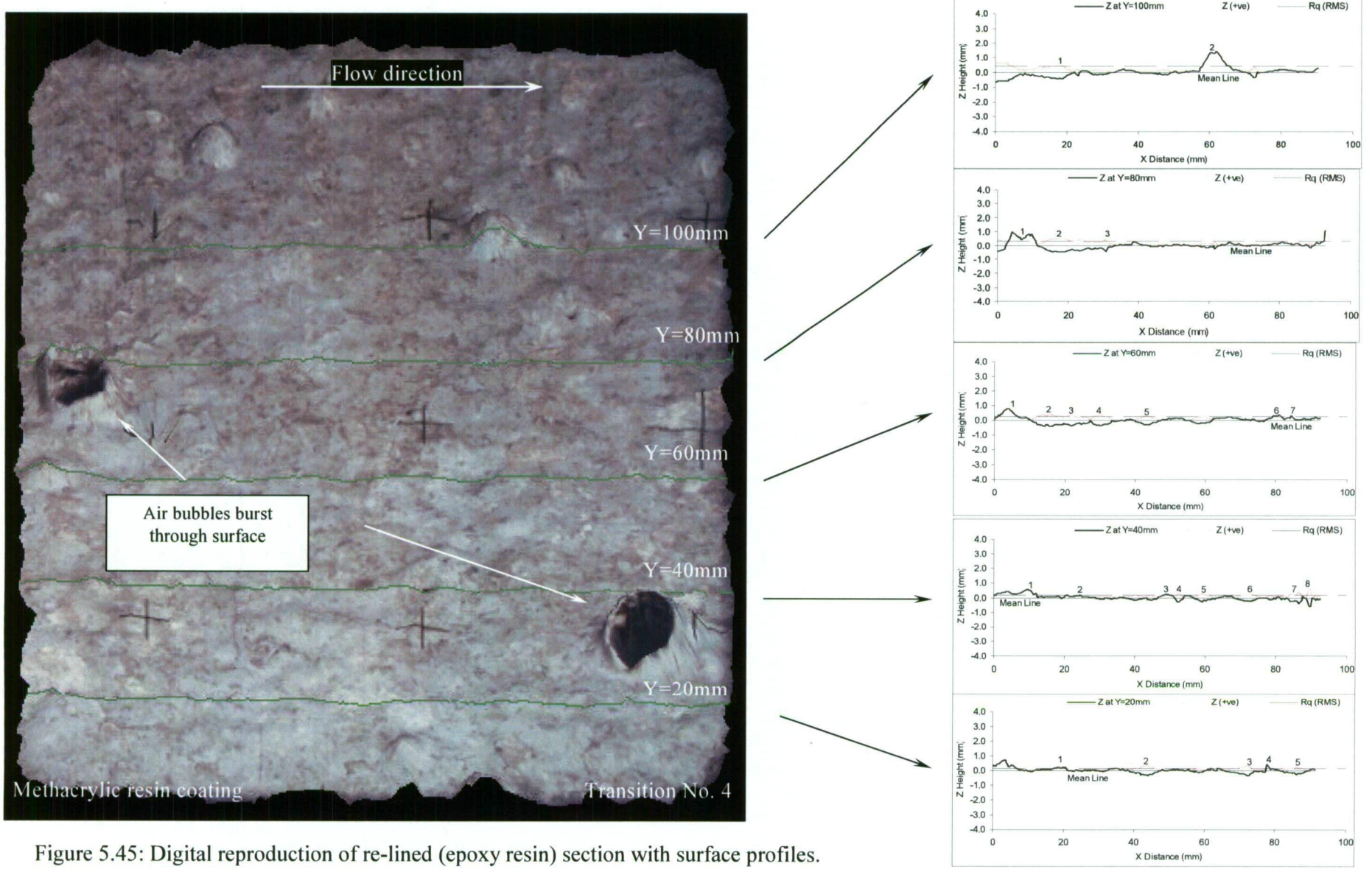

Figure 5.45: Digital reproduction of re-lined (epoxy resin) section with surface profiles.

5.7 Chapter Summary

This chapter has summarised the close range photogrammetric techniques employed to repeatably map the surface of test plates. It was also shown to be successful in being used to map the concrete walls of a canal in a non-repeatable fashion.

Fundamental data reduction to produce recognised roughness parameters and basic statistical information was shown. This information is derived from the X, Y, Z surface data obtained from the photogrammetry. Combinations of quantitative and qualitative methods have been used to describe the biofilm surface character.

The results of the small test plate fouling program show that the fouling characteristics may differ with varying scales of roughness. Observations, supported by the photogrammetry measurements show that fine scale roughness (represented by the fine grit) results in a general increase in mean surface height and even a "smoothing" effect where the biofilm colonises the valleys and gaps between roughness elements. Larger scale roughness (represented by the coarse grit) was also shown to display this behaviour, although some evidence of biofilms growing on peaks of roughness elements was measured. These conclusions are based on the test plates deployed at Pond No. 1 only, since although changes in surface roughness were measured at Transition No. 4, the lack of fouling indicates only changes due to surface wearing.

If an even larger scale roughness was used for investigation, more evidence of this type of growth may be seen. This type of biofouling may be present in parts of Tarraleah No. 1 Canal given the scale of roughness measured. This is recommended as a future area of research, as this may provide additional answers to the problem of reduced flow capacity in biofouled open channels.

Data from different sections of Tarraleah No. 1 Canal show the variability of the concrete surface. The field site at Transition No. 4 shows the surface roughness is similar to the coarse grit used in the small test plate trials. This fine grit is also used in Chapter 8 for water tunnel measurements, and so validates the use of this grit for these studies.

Detailed labelling of each photo was made where possible. The complete set of photos (on film, and digitally scanned in high resolution) have been catalogued and archived at the University of Tasmania, School of Geography and Environmental Studies, and School of Engineering.

Chapter 6 Water Tunnel Details, Instrumentation and Calibration

6.1 Introduction

A large part of the present study was spent on the design, instrumentation, commissioning, and then calibration of the purpose built water tunnel used to do the laboratory measurements presented in this Chapter, and Chapters 7 and 8.

The water tunnel is modelled on wind tunnel boundary layer research facilities such as those used in aeronautical research. It is a closed loop, recirculating design.

This purpose of this chapter is to introduce the water tunnel used, and present the calibration data for its working section where the measurements were made. This is done to show that the facility is suitable for boundary layer measurements and total drag measurements of plates fouled with freshwater biofilms. The water tunnel was designed to also be suitable for marine applications where fresh, brackish or salt water is required.

The chapter starts with an introduction to the water tunnel and its general performance characteristics. Some of the more important components incorporated into the design are introduced before the working section details are given.

The instrumentation used are introduced, methods of use presented, and the various calibrations described. The results for the calibration of the water tunnel are then shown with a running discussion on their meaning.

A short chapter summary is provided.

6.2 Water Tunnel Design and Important Components

The design of the water tunnel is based on the principles of wind tunnel boundary layer research facilities (Bradshaw and Pankhurst, 1964; Mehta and Bradshaw, 1979). It is a closed loop, recirculating design. Figure 6.1 shows a schematic diagram of the arrangement with the various components identified.

It should be noted that Dr Jane Sargison (2004a) designed many of the components of the water tunnel. Dr Paul Brandner (2004) designed much of the working section and force balance arrangement, with input from Prof. Gregory Walker (2004) and the author in the overall design specification.

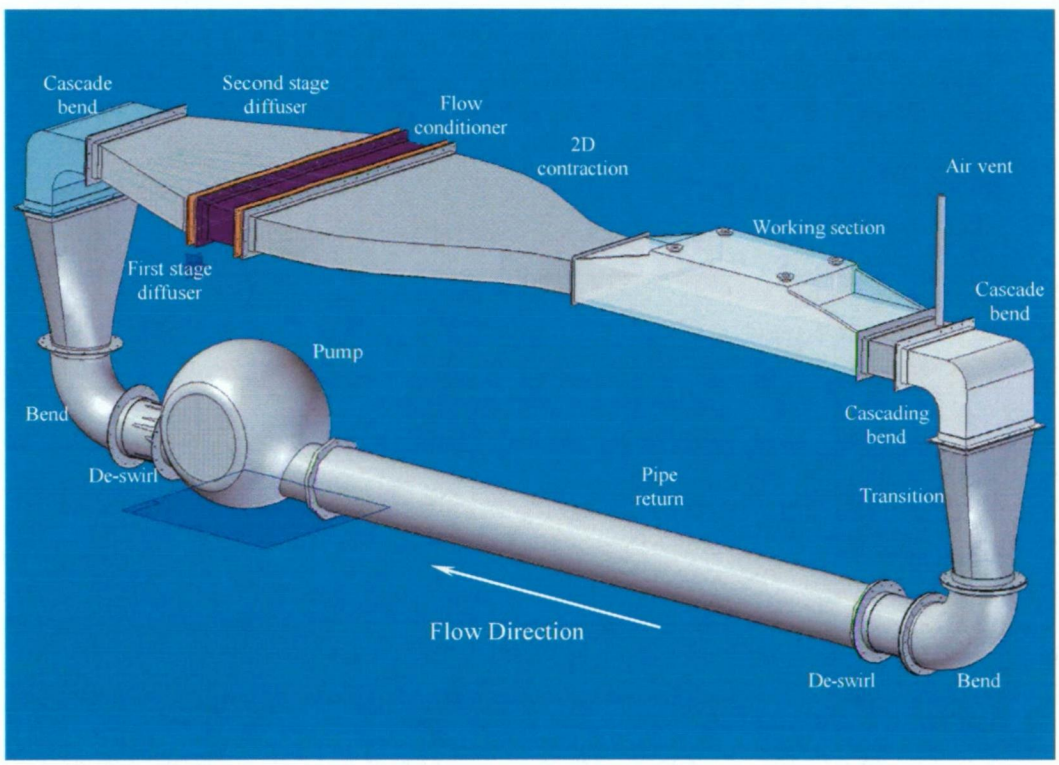

Figure 6.1: A schematic diagram of the closed loop water tunnel.

The flow conditions within the working section were designed to replicate the greatest range of flow conditions typical of field hydraulic conduits. Table 6.1 presents a comparison of hydraulic characteristics of various hydraulic conduits with the water tunnel.

Table 6.1: Typical hydraulic conditions for Hydro Tasmania field conduits and water tunnel working section.

Hydraulic Conduit	Diameter or Hydraulic Radius (m)	Mean Velocity Range (m/s)	Maximum *Re* (at 10°C)	Shear Velocity u^* (m/s)	Relative Roughness (for *ks*=0.2mm)	Roughness Reynolds Number (for *ks*=0.2mm)
Wilmot Penstock	1.98	0-5	7.56×10^6	0.262	0.00101	40
Poatina Penstock	3.05	0-8	1.86×10^7	0.354	0.00066	54
Tarraleah Hilltop Pipeline	2.59	0-4	7.91×10^6	0.190	0.00077	29
Tarraleah No. 1 Canal	1.30	0-2	7.94×10^6	0.098	0.00154	15
Water Tunnel (working section)	0.75	0-2	4.58×10^6 (7.46×10^6 at 30°C)	0.079 (0.131 at 30°C)	0.00267	12 (20 at 30°C)

Based on Moody diagram for friction factor, f, and $u^* = \bar{u}\sqrt{\frac{f}{8}}$, for pipe flow.

$\mathrm{Re}_D = \frac{\bar{u}4(R)\mu}{\rho}$ for the non -circular conduits, where R is the hydraulic radius, $\frac{A}{P}$; where A is the cross section area, P is the wetted perimeter.

$u^* = \sqrt{gRS_f}$ was used for the open channel flow estimation, where S_f is the friction slope, assumed to be the bed slope for uniform flow.

u* for the water tunnel working section was taken from measurements presented later in this Chapter.

When designing the water tunnel, a mean flow speed of no greater than 2m/s was required to obtain wall shear stresses similar to those in hydraulic conduits operated by Hydro Tasmania. This is in contrast to the work of, for example, Candries (2001) and Schultz (1998) who undertook testing at speeds greater than 3m/s or more in water tunnel facilities to study marine biofouling. This may be necessary for maritime type problems where vessel speeds are usually very high, but is not warranted for studying biofouling in hydraulic conduits: it highlights a significant difference in studying freshwater biofilms.

The 10 °C used to determine the values shown in Table 6.1 represent typical field temperatures; 30 °C represent typical maximum water temperatures available in the water tunnel.

6.2.1 Important Water Tunnel Components

Water is circulated around the water tunnel by a split case design, high flow, low head pump, driven by a 7kW 3-phase AC motor. Maximum pump speed was approximately 620 rpm and minimum approximately 100 rpm. This gave a flow range from 0.04 to 0.24 m^3/s, and a mean velocity range of 0.3 to 2.0 m/s in the working section. The pump (Figure 6.2) was manufactured by Regent Pumps, Melbourne, Australia, with a designation of Type 350-S16.

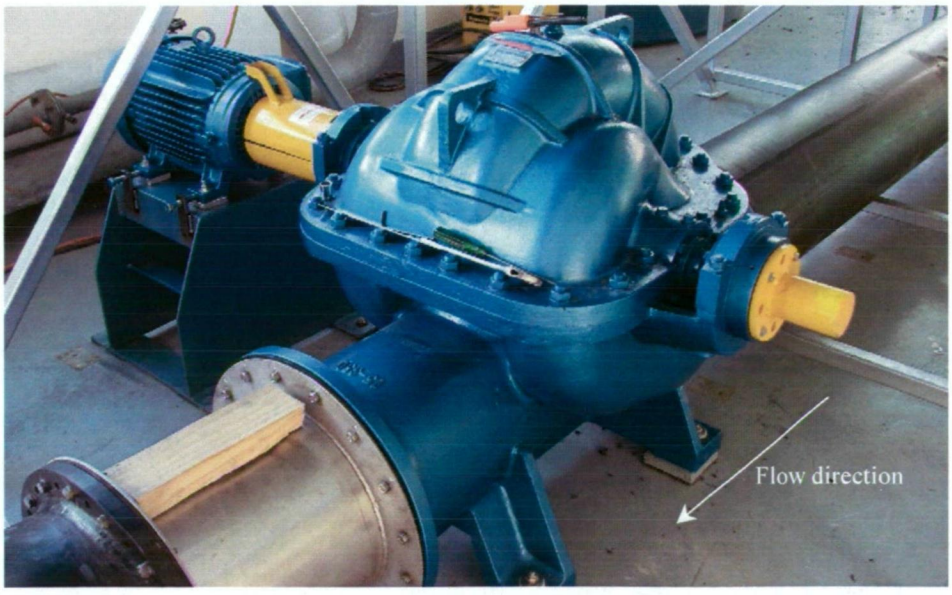

Figure 6.2: The split case pump.

To reduce the level of swirl or secondary flow downstream of the pump, a de-swirl unit is located immediately downstream of the pump, and upstream of the pipe return (see Figure 6.1). The de-swirl is fitted with two mutually perpendicular vanes as shown in Figure 6.3.

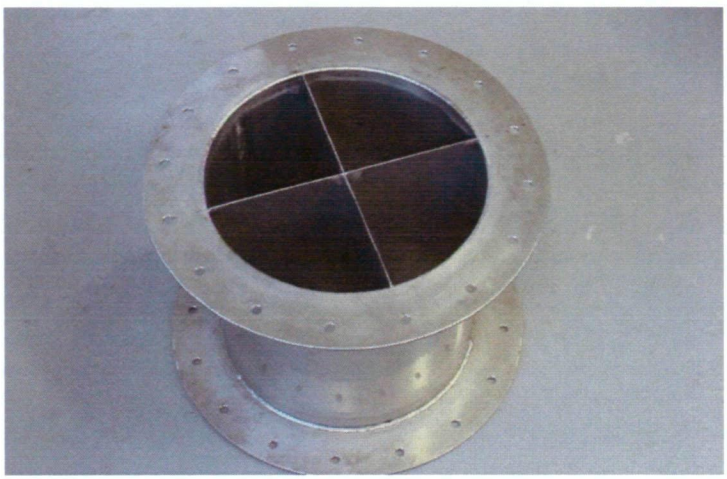

Figure 6.3: One of the two de-swirl units installed on the water tunnel.

Cascade bends are located upstream of the second stage diffuser (see Figure 6.1) and downstream of the working section. The bends are fitted with closely spaced circular arc vanes, which reduce secondary flow as the water travels through the bend. A photo of a cascade bend is shown in Figure 6.4.

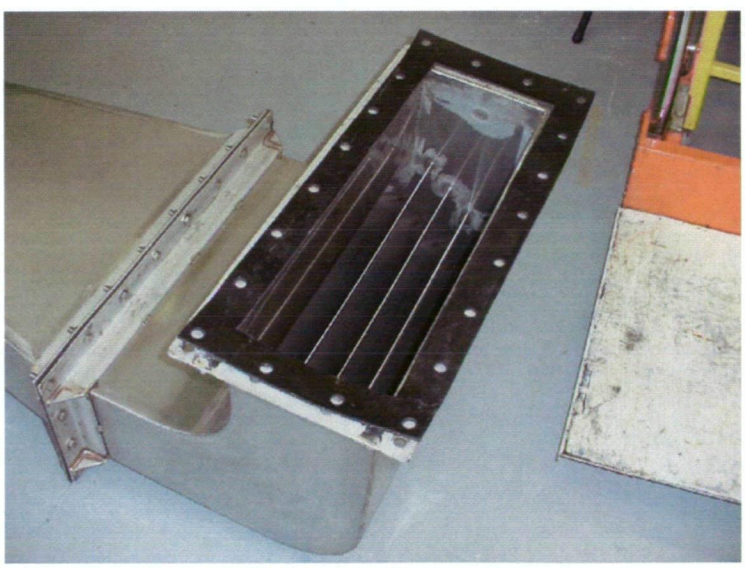

Figure 6.4: One of the two cascade bends. Vanes were inserted in the bends to encourage even flow distribution.

A diffusion ratio of $0.10m^2$:$0.36m^2$ was required downstream of the pump to provide the passage area specified for the flow conditioner and contraction inlet. This was implemented in two stages to reduce the diffuser angles required (Kline *et al.*, 1957; Cochran and Kline, 1958; Bradshaw and Pankhurst, 1964; Mehta, 1977; Mehta and Bradshaw, 1979). The second, larger diffuser (refer to Figure 6.1), was fitted with vanes to spread the flow evenly into the flow conditioner and contraction sections. Sargison *et al.* (2006) contains more information on the design process to ensure the even flow distribution and describes some numerical modelling undertaken to optimise the angle, transition and vane placement. Table 6.2 gives the specifications on the two diffusers.

Table 6.2: Specifications for the two diffusers on the water tunnel.

Diffuser	Upstream End Section	Downstream End Section	Component Length	Number of Vanes	Wall Angle
Stage 1	Diameter = 350mm	200mm×800mm	900mm	nil	7°
Stage 2	200mm×800mm	200mm×1800mm	1100mm	6	49° (equal to 7°)

The flow conditioner contained two sandwiched sections of honeycomb and steel mesh in series separated by 300 mm. The honeycomb was inserted in order to straighten and reduce turbulence in the working section. The honeycomb was a packed arrangement of circular extrusions with a cell diameter of 6 mm. The length of the honeycomb sections was 60 mm. The stainless steel wire screen, with a 3.15 mm square aperture, also had the function of reducing large scale turbulence, and also to hold the honeycomb in place in the tunnel.

The flow conditioner was installed at the traditional location upstream of the contraction to produce the best results, and where the cross sectional area is at its largest to reduce energy losses. Figure 6.5 shows the honeycomb, and stainless steel mesh used.

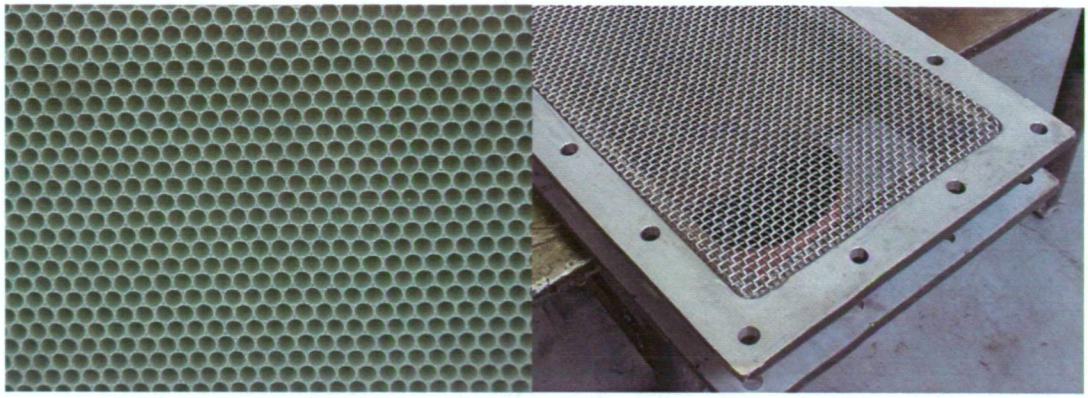

Figure 6.5: Photo showing the honeycomb and stainless steel mesh.

The contraction on the water tunnel is a two-dimensional design. Based on a two-dimensional wind tunnel contraction design (Sargison, 2004b), it provided excellent performance for the purpose of the present study. Figure 6.6 shows a drawing of the contraction located upstream of the working section.

The contraction was 2000 mm in length with end sections of 200 mm by 1800 mm at the upstream end and 200 mm by 600 mm at the downstream end making the contraction ratio of 0.36 m^2 : 0.12 m^2 or 3 : 1. This is lower than typical values used for wind tunnels. The reduced contraction ratio adopted here was dictated by space limitations, structural requirements and cost.

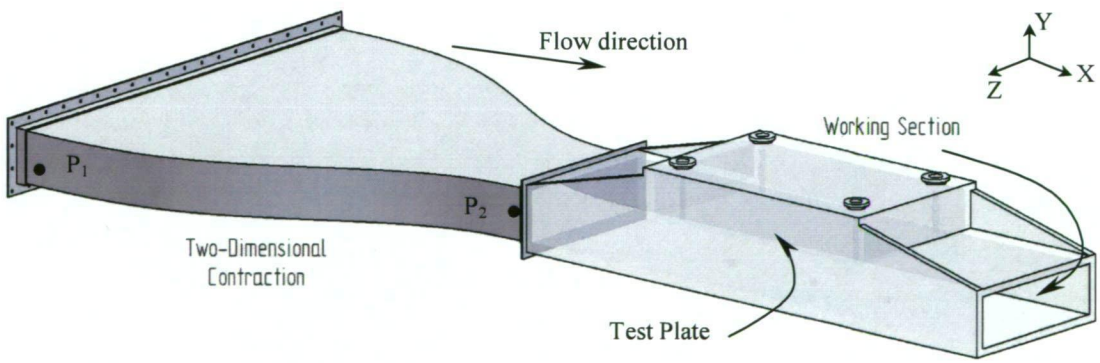

Figure 6.6: The 2D contraction and working section.

Slim-line storage tanks (Figure 6.7) with a capacity of 3.6 m^3 were provided so that water carted from the field where the biofilms were grown could be stored on site. The volume of the tanks was sufficient to enable the water tunnel to be completely filled with some left over. The water tunnel volume is approximately 3.0 m^3.

Figure 6.7: Water tanks for onsite storage of water for the water tunnel.

6.2.2 The Working Section

The working section was constructed entirely of 30mm thick acrylic with dimensions of 2200 mm long, 600 mm wide and 200 mm deep. Figure 6.8 shows a drawing and dimensions of the working section and Figure 6.9 shows a side view.

A lid arrangement was designed to allow for the fitting of large test plates to form the roof for 1m of the working section. While operating, water is allowed to flood the roof cavity between the test plate and the lid.

Plug holes are where probes could be inserted for measurement. These are located at distances (at the centreline) of 115 mm, 515 mm and 885 mm downstream of the leading edge of the test plate, shown in Figure 6.8. The plug upstream is located 85mm upstream of the leading edge of the plate.

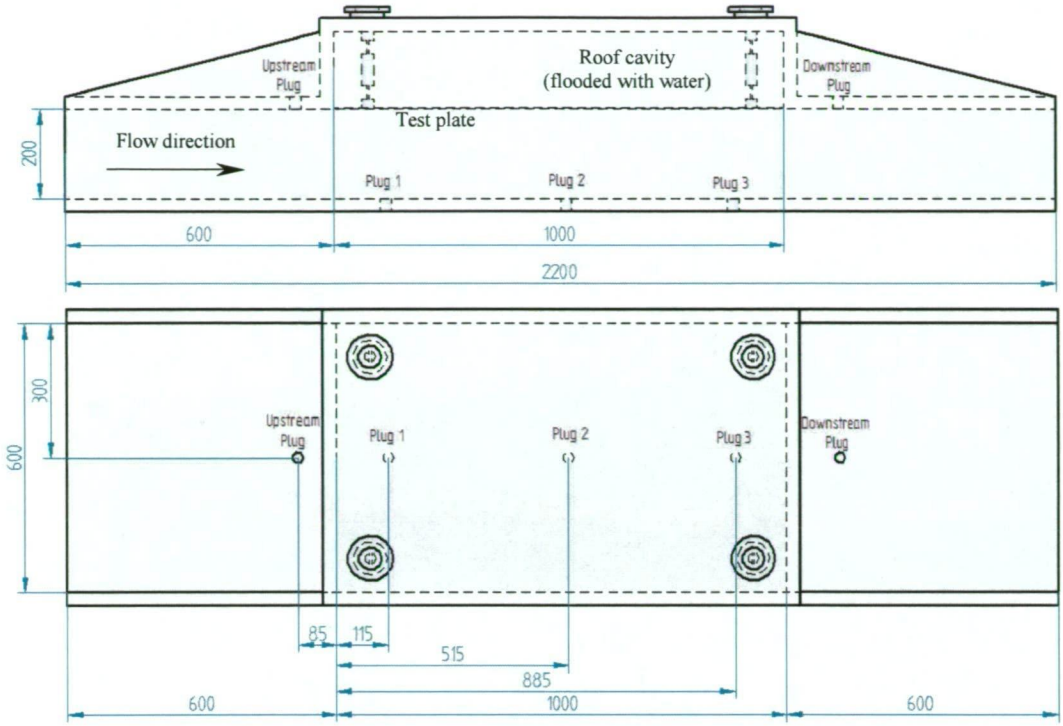

Figure 6.8: Working section of the water tunnel (dimensions in mm).

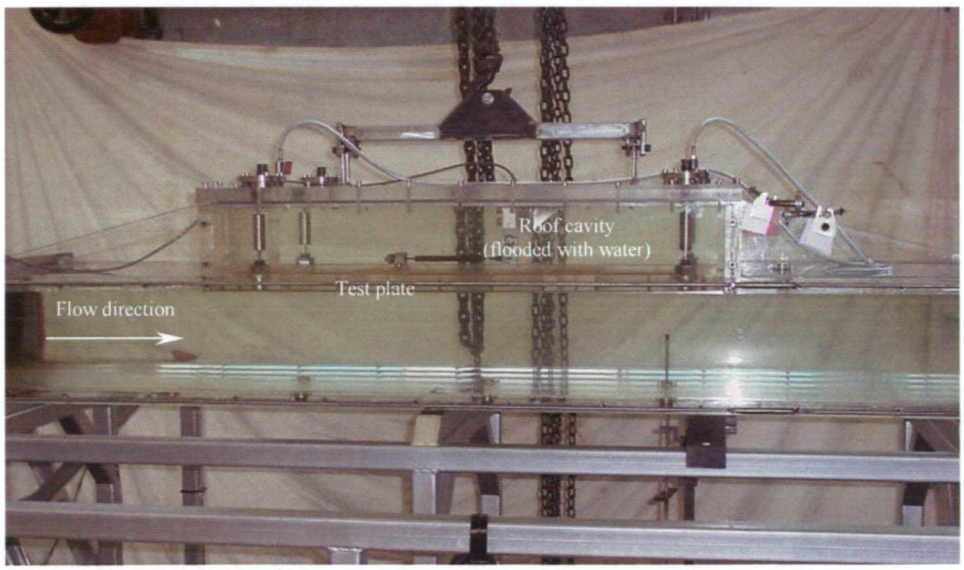

Figure 6.9: Side view of working section showing lid and test plate in place.

Figure 6.10 shows the test plate mounted on an acrylic support plate, which is in turn suspended from the lid proper by 4 flexures and load cell arrangement. The load cell was used for the measurement of total drag of the test plates and is discussed in more detail in section 6.3.2. The whole arrangement could be attached to an overhead gantry for ease in lifting and manoeuvring.

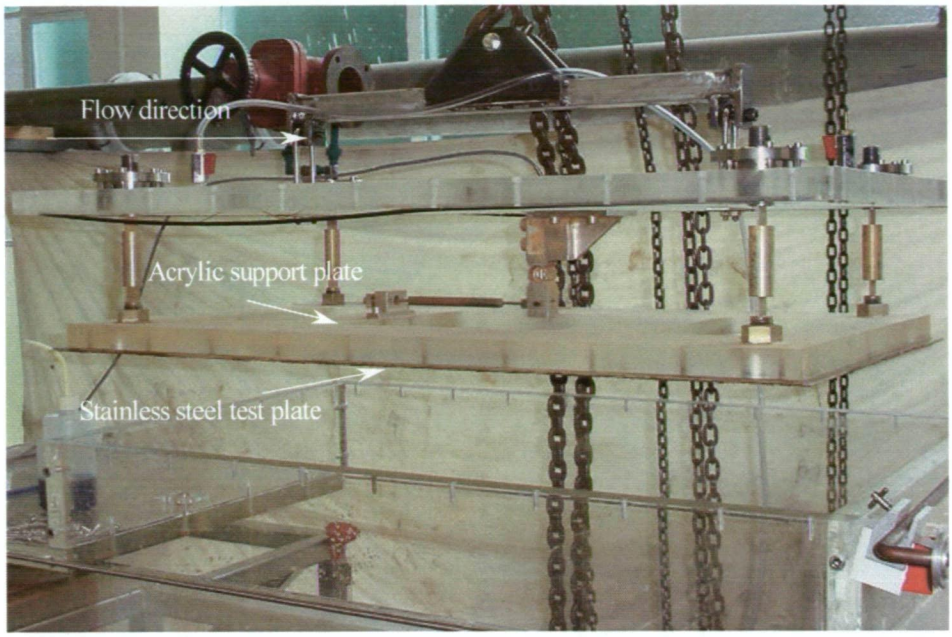

Figure 6.10: The lid and test plate arrangement of the working section.

The stainless steel test plates used in the water tunnel are those introduced in Chapter 4. They were 997 mm long by 597 mm wide by 3 mm thick. They were coated with either an artificially rough surface or a smooth painted surface. The results presented in this chapter for the calibration of the working section, however, are for measurements conducted on an acrylic test plate measuring 997 mm by 597 mm by 5 mm thick.

To ensure a turbulent boundary layer over the test plate length and width, and minimise Reynolds number variations in the working section entrance flow, a boundary layer trip wire was installed 600 mm upstream of the leading edge of the test plate. Figure 6.11 shows the 3 mm brass welding rod attached to the four walls of the working section.

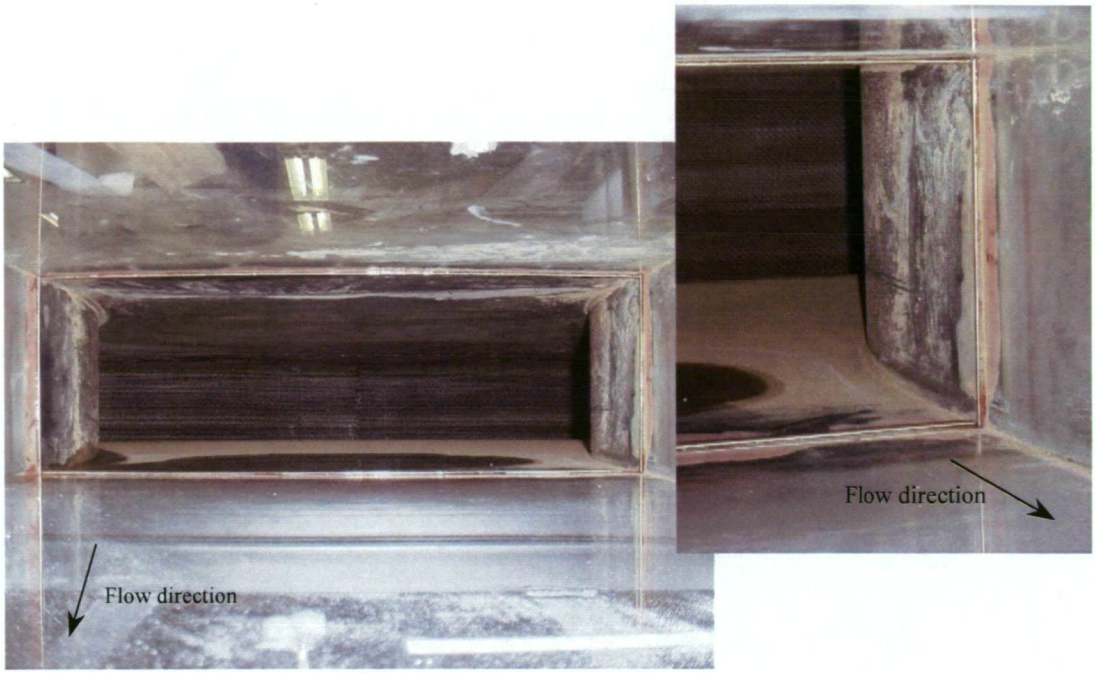

Figure 6.11: Looking upstream from the working section into the contraction, boundary layer trips wires at the entrance to the working section.

Water temperature variation was a significant issue for the water tunnel. The 7kW motor (via the pump) was able to heat up the water by several °C when running at maximum speed over the course of a few hours, depending on the ambient air temperature. The maximum water temperature recorded for the present study was 31 °C, the minimum was 11 °C. Based on these temperatures, the achieved Reynolds number, based on test plate length, varied from a minimum of 2.4×10^5 for a mean flow velocity of 0.3 m/s (at 11 °C) to a maximum of 2.9×10^6 for a mean flow velocity of 2 m/s (31 °C). High costs precluded the installation of a water cooling system to control the water temperature. This is recommended for future development of the facility.

Typical water temperatures were more commonly between 22 °C and 26 °C. It is within this range that the majority of measurements were made for the present study. For comparison, water temperatures where test plates were deployed and allowed to have biofilms develop on them before testing in the water tunnel, were between 10 °C and 15 °C.

Section 6.3.4 describes the use of the pump motor controller, temperature probe and LabView software to control pump speed to maintain constant Reynolds numbers during boundary layer measurements.

6.3 Instrumentation

A variety of measurements were made in the present study including general pressure measurements, boundary layer traverses for mean velocity and turbulence, and total drag measurements.

6.3.1 Pressure Measurements

All pressure measurements were taken using two Validyne Engineering variable reluctance differential pressure transducers (model DP15) shown in Figure 6.12. This particular model is designed for fast response making it suitable for unsteady measurements.

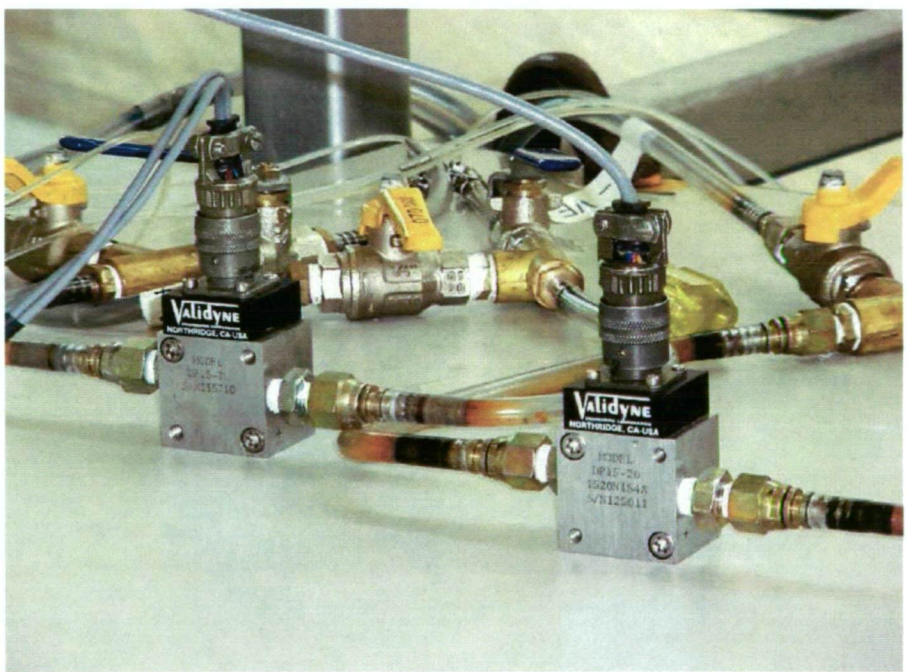

Figure 6.12: Validyne Engineering pressure transducers.

Static wall pressures were measured at upstream and downstream tappings on the contraction, P_1 and P_2 respectively as shown in Figure 6.6. These provided references for all other pressure measurements and were measured concurrently for the majority of results presented in this thesis.

There were many pressures to be measured at any one time during this study. A solenoid switching arrangement with eight channels was used to scan each connected pressure. Figure 6.13 gives a pressure connection schematic diagram.

The various pressure connections (P) were:

s.o. – Solenoid output

P_1 - Upstream contraction

P_2 - Downstream contraction

P_3 - Static at probe (P_{Static})

P_4 - Pitot probe (P_{Pitot})

P_5 - Static at upstream of test plate

P_6 - Static at downstream of test plate

P_7 and P_8 - Other (e.g. used for Preston tube measurements, see section 6.4.3.1)

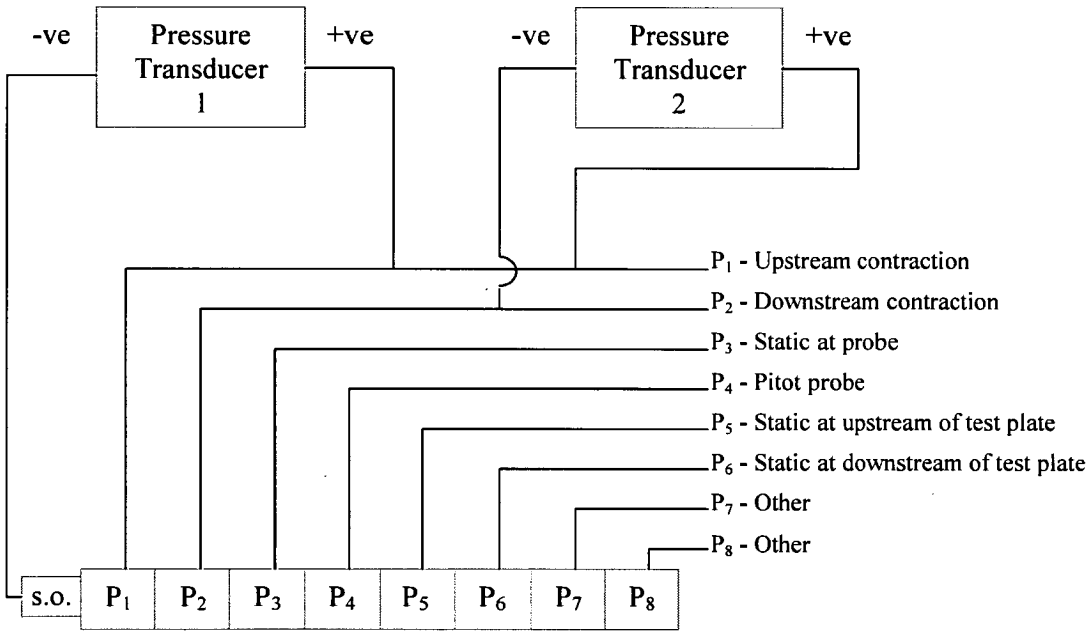

Figure 6.13: Pressure connection schematic diagram.

The solenoid switch was wired to a box that could control which channel was active (Figure 6.14). LabView software was used to change channels and scan for the desired pressure. Section 6.3.5 contains more detail on the LabView data acquisition and control hardware.

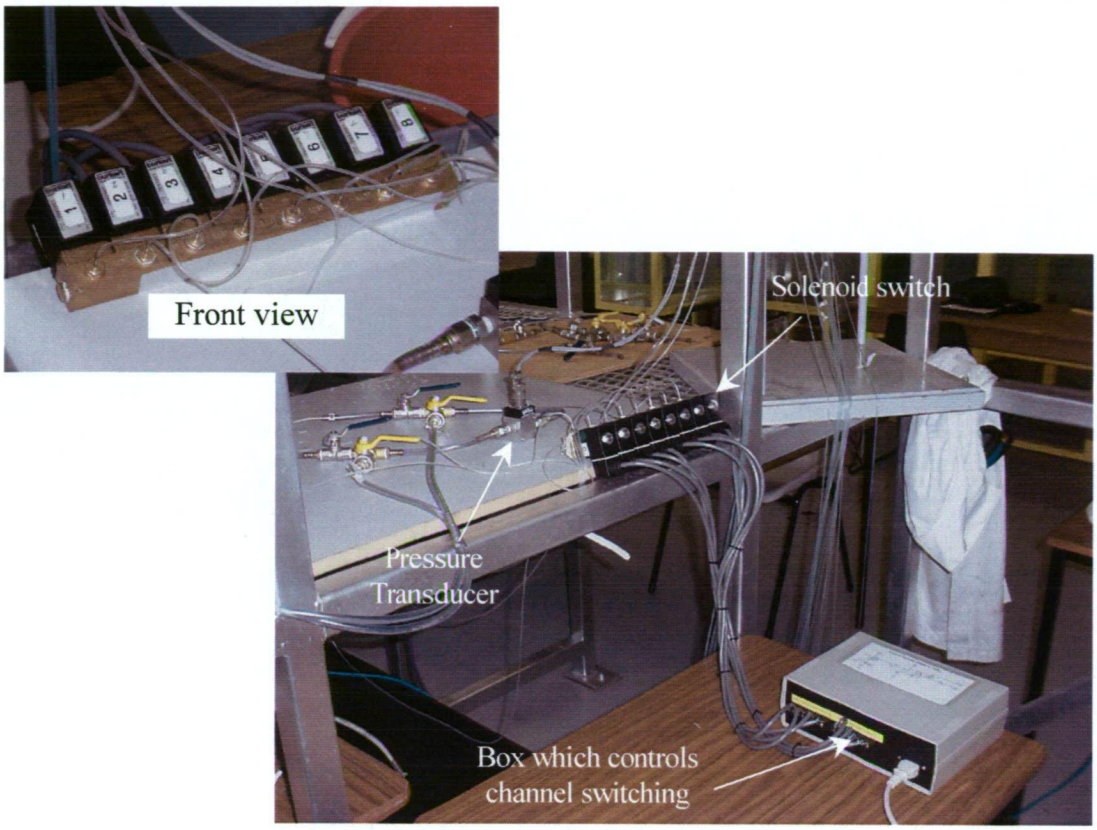

Figure 6.14: The switching arrangement, controlled by LabView software.

The upstream contraction pressure, P_1, was used as the reference pressure on one side of the first differential pressure transducer. The other side of the transducer was connected to the solenoid switching arrangement where each pressure was measured in turn (contraction pressures, static wall tappings and total pressures).

A second, dedicated pressure transducer measured the contraction pressure differential. This independent measurement was used to aid in the removal of any time dependent variation in tunnel operating condition.

The pressure transducers were connected to Validyne signal demodulators (Figure 6.15). One box produced a voltage output, the other a current output. The voltage output was connected directly to the data acquisition card attached to the computer. The current output box was connected to a purpose built current to volt converter, and then a precision volt level shifter to obtain the appropriate output for the data acquisition card (Figure 6.15).

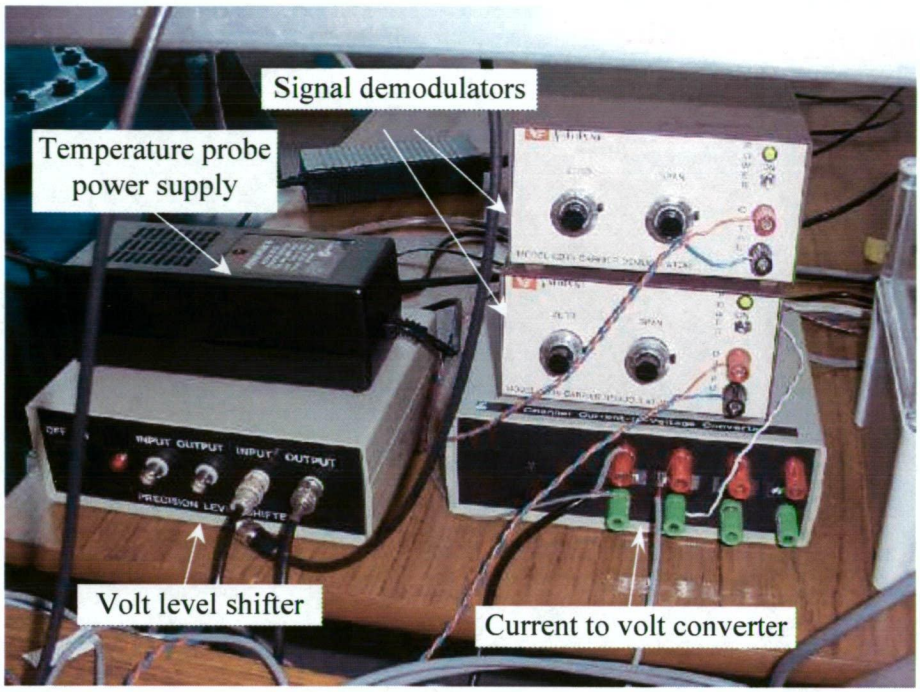

Figure 6.15: Signal demodulators, temperature probe power box, current to volt converter and precision level shifter.

The pressure transducers were regularly calibrated using a purpose built wall mounted water manometer. The voltage output from the two transducers were measured against the differential water level in the manometer. Reading accuracy is estimated to be ± 0.5 mm. Multiple points were taken in the negative and positive pressure range. A linear line of best fit was then plotted on the measured points to find the equation describing the volts versus pressure.

The pressure transducer sensitivity could be adjusted by replacing the internal diaphragm. For the present study, a number 26 and number 24 diaphragm were used. The number 26 and 24 diaphragms were suitable for differential pressures up to 600 mm and 800 mm respectively. These pressure differentials gave the maximum output voltage resolution for the ± 10 volts.

Figure 6.16 shows a typical pressure transducer calibration. Cont. Trans. #26 on the plot denotes the dedicated contraction transducer using a number 26 diaphragm in the transducer. Scan Trans #24 denotes the transducer connected to the scanning solenoid switching arrangement fitted with a number 24 diaphragm.

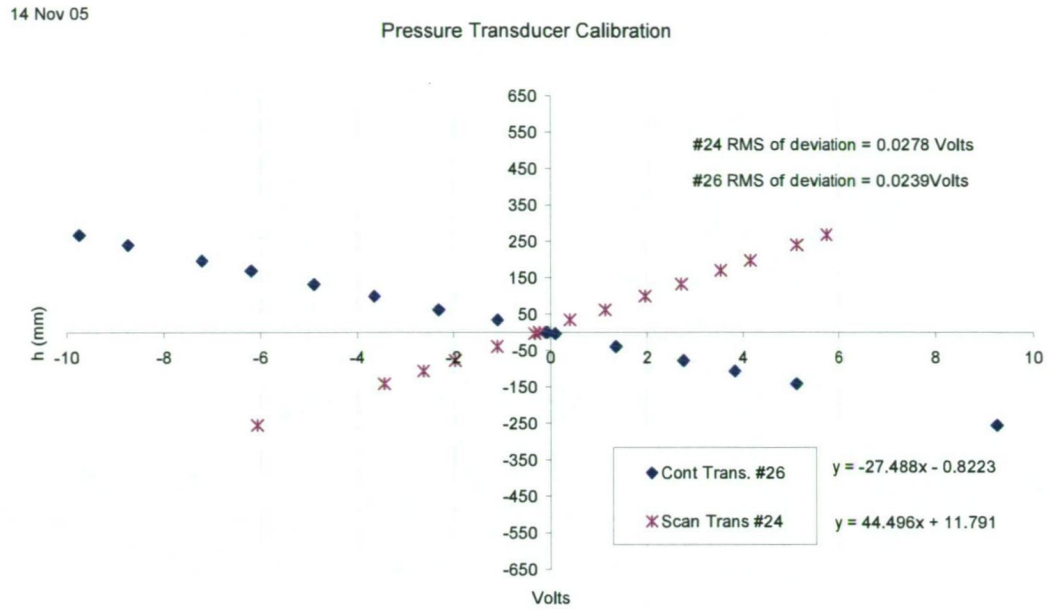

Figure 6.16: A typical pressure transducer calibration.

An analysis of the deviation of the plotted values from the fitted line was undertaken. A plot of the residual (or deviation) data for the #24 diaphragm is shown in Figure 6.17. From these data an RMS value (standard error) was determined to gain an estimate of the uncertainty. This analysis was undertaken for all calibrations (both pressure transducers and drag).

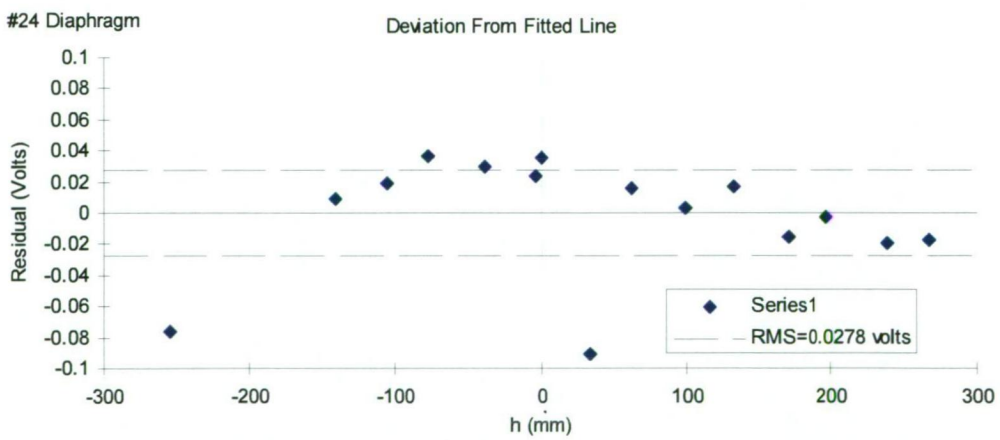

Figure 6.17: Plot of residuals (or deviation) from the fitted line.

6.3.2 Mean Velocity Measurements

Two identical Pitot probes were used to do all boundary layer total pressure traverses. Figure 6.18 shows the probe. The probe tip had a 1mm outside diameter and is square ended. The tip of the probe extends 20 mm from the centreline of the probe stem. The probe support stem is 6mm in diameter.

The velocity at the tip of the Pitot probe was determined by measuring the total (or stagnation) pressure head of the probe and the static pressure head from a wall static tapping located adjacent to the probe. A voltage was recorded from the pressure transducer which was converted to a pressure head (in metres) from a previous calibration. The pressure connection was arranged such that the velocity could then be determined by using Equation 6.1, a manipulation of Bernoulli's equation.

$$u = \sqrt{2g((P_1 - P_{Pitot}) - (P_1 - P_{Static}))} \qquad \text{Equation 6.1}$$

This method removes the zero error from the measurement without the need for precise zero adjustment of the output from the pressure transducers.

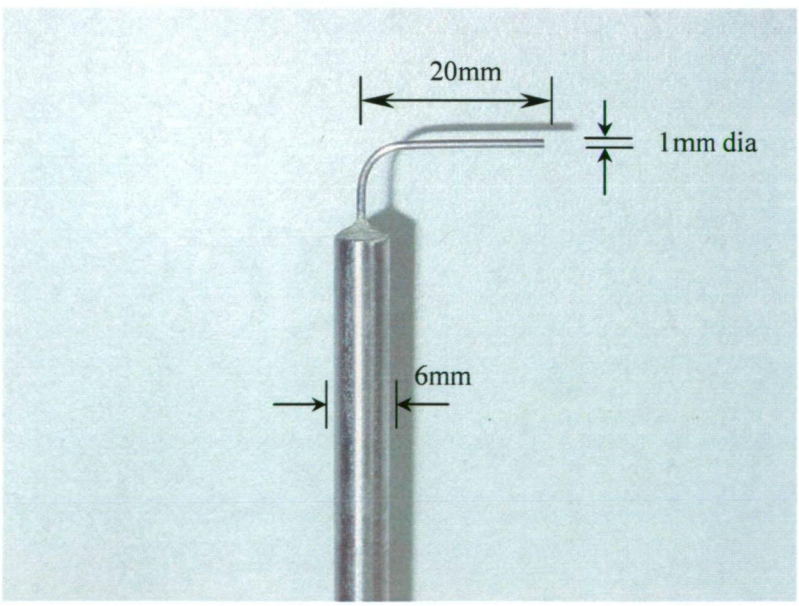

Figure 6.18: Pitot probe used for boundary layer time averaged velocity measurements.

The tip of the Pitot probe is 20 mm upstream of the main stem of the probe support making the probe traverses presented in this chapter 105 mm upstream and 95 mm, 495 mm and 865 mm downstream of the leading edge of the test plate respectively for plugs upstream, 1, 2 and 3 (Figure 6.8 shows these locations).

Static wall tappings were located around the water tunnel. The important locations used in conjunction with test plate measurements were located on the aforementioned contraction, in the working section floor aligned with the upstream and downstream edges of the test plate, and each of the plugs where probes can be inserted. Figure 6.19 shows a photo of the static wall tappings used in conjunction with the Pitot probe to determine mean boundary layer velocities. The tappings were offset 50 mm spanwise from the longitudinal centreline for each of the probe locations to enable the calculation of the local velocity without flow disturbance from the actual probe.

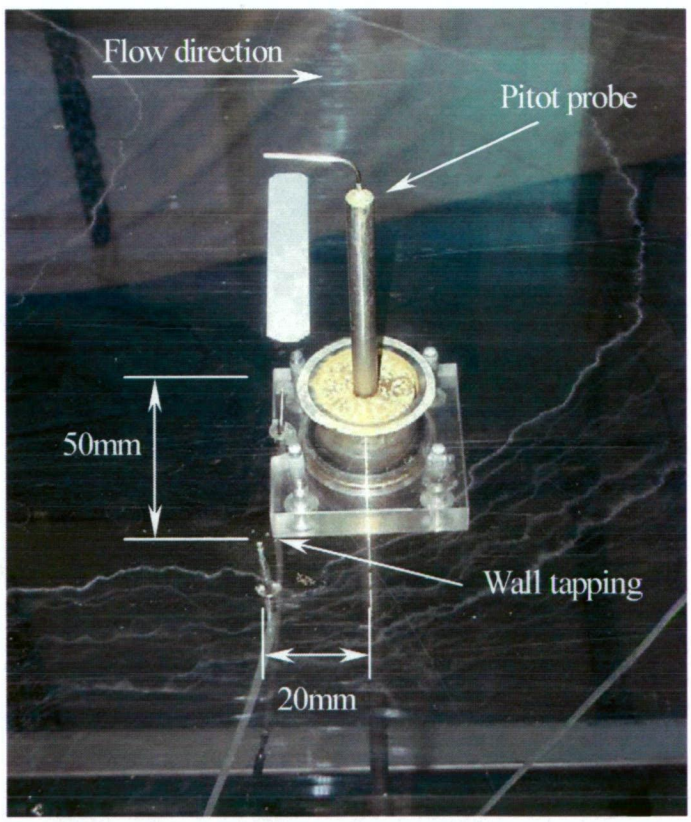

Figure 6.19: Oblique side view of wall static tapping and Pitot probe.

All probes were inserted through plugs with gland seals. Figure 6.19 shows a Pitot probe inserted through the floor of the working section. Plugs with different size holes were used to accommodate different probes.

Probes were attached to a digital precision height gauge (Figure 6.20) for accurate placement in the vertical or wall-normal (y) direction for measurement. The gauge was manually traversed with an accuracy of ± 0.01 mm.

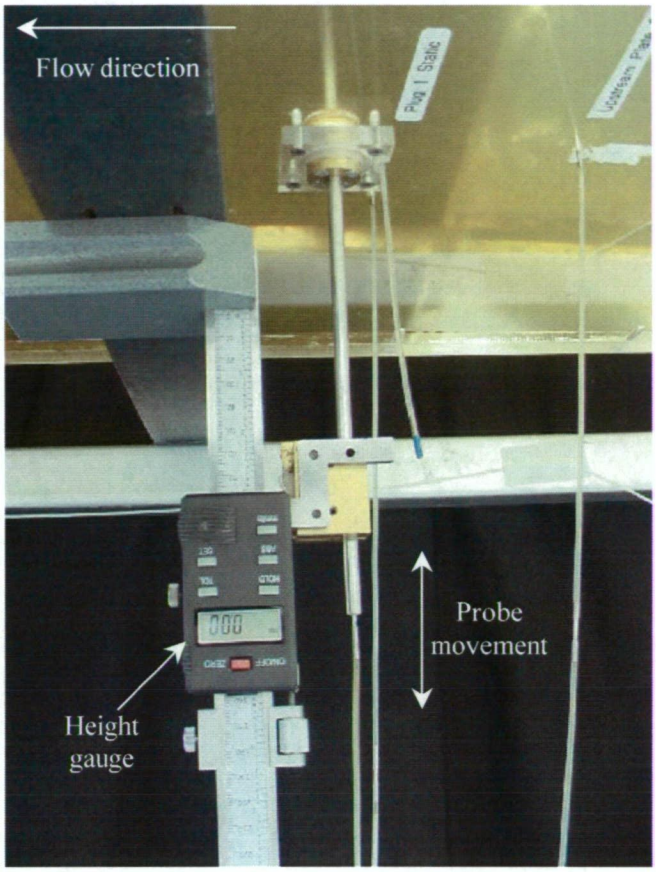

Figure 6.20: Precision height gauge attached to Pitot probe.

6.3.3 Drag Measurements

A force balance arrangement was used for the total drag measurements. The test plate is suspended from the lid of the working section by four precision machined stainless steel flexures shown in Figure 6.21.

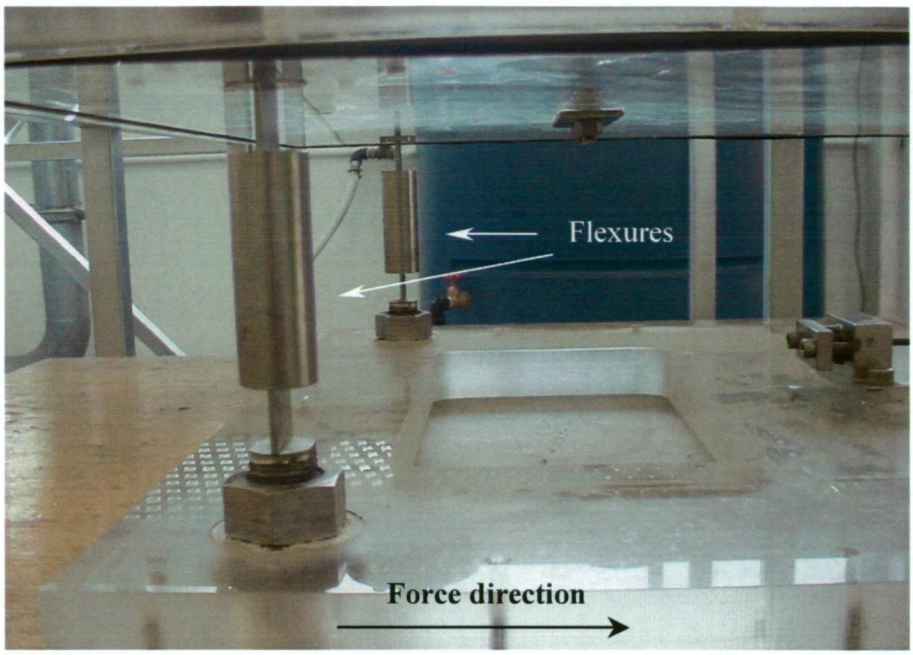

Figure 6.21: Photo showing the flexures suspending the test plate from the lid.

A MTI Weigh Systems single ended shear beam load cell (model MTI-4856-SB) was attached to the lid of the working section and linked by a load transfer rod to the acrylic backing of the test plate (Figure 6.22). The flexures ensure a one-dimensional transfer of force through the load transfer rod to the load cell, which was connected to a Mann Industries strain gauge transmitter and personal computer for data acquisition using LabView software.

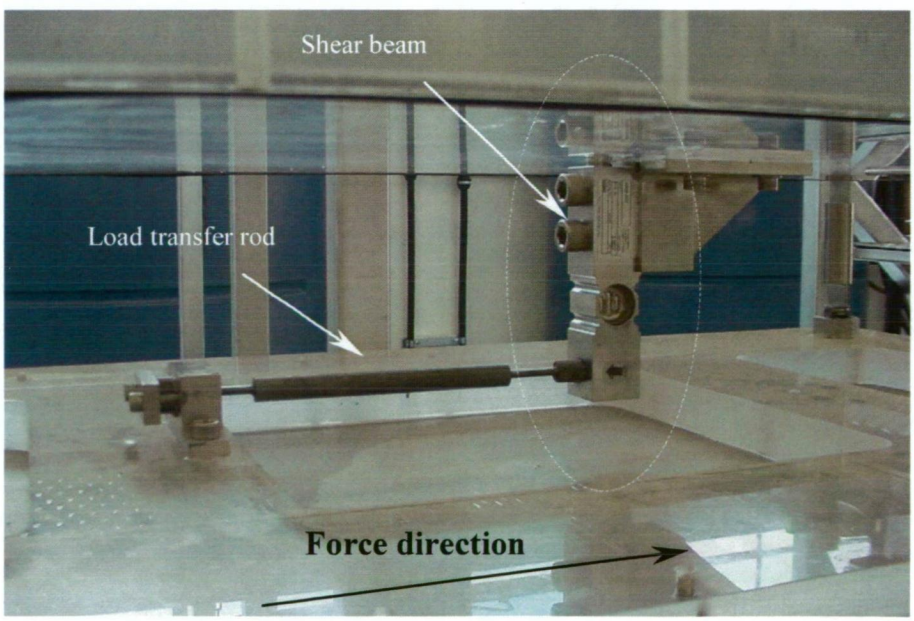

Figure 6.22: The load cell to measure total drag.

To calibrate the load cell for total drag measurements, the whole lid and test plate arrangement was placed on a bench top and clamped down securely (Figure 6.23). The lid and plate were adjusted to be parallel with each other and horizontal using a spirit level. A thin steel cable was attached underneath the plate and ran parallel to the plate over one large low friction pulley. Weights were added to the wire in 50 gram (0.49 Newton) increments and the change in volts recorded.

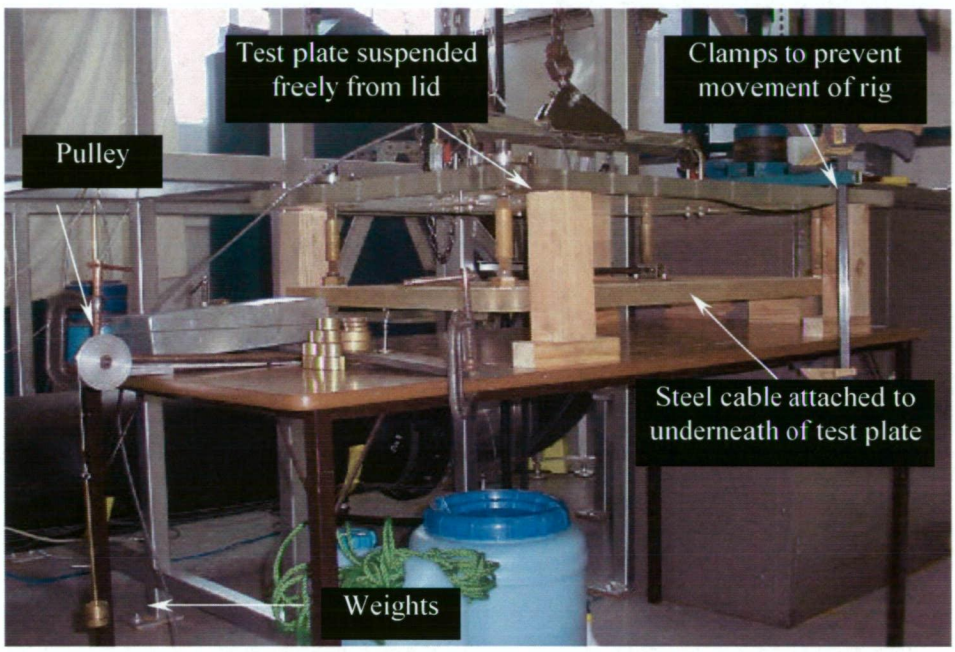

Figure 6.23: Photo showing bench top calibration of drag rig.

Figure 6.24 shows a typical calibration plot for the drag rig. A calibration was repeated every time a plate with different characteristics was attached. For example, the acrylic plate, which was 5mm thick (stainless steel plates were 3mm thick), required a small height adjustment in the flexures to ensure the plate was flat and aligned with the working section roof. This resulted in a slight angle change in the load transfer rod, and thus a re-calibration was required. When the thinner steel plates were subsequently used, the rig was then recalibrated. The load transfer rod was designed to be horizontal, or 90 degrees to the shear beam load cell for the stainless steel plates.

Accuracy for the weights used for calibration were 50g ± 0.2 g. The RMS of the deviation from the fitted line was found from the calibration and is presented in Figure 6.25.

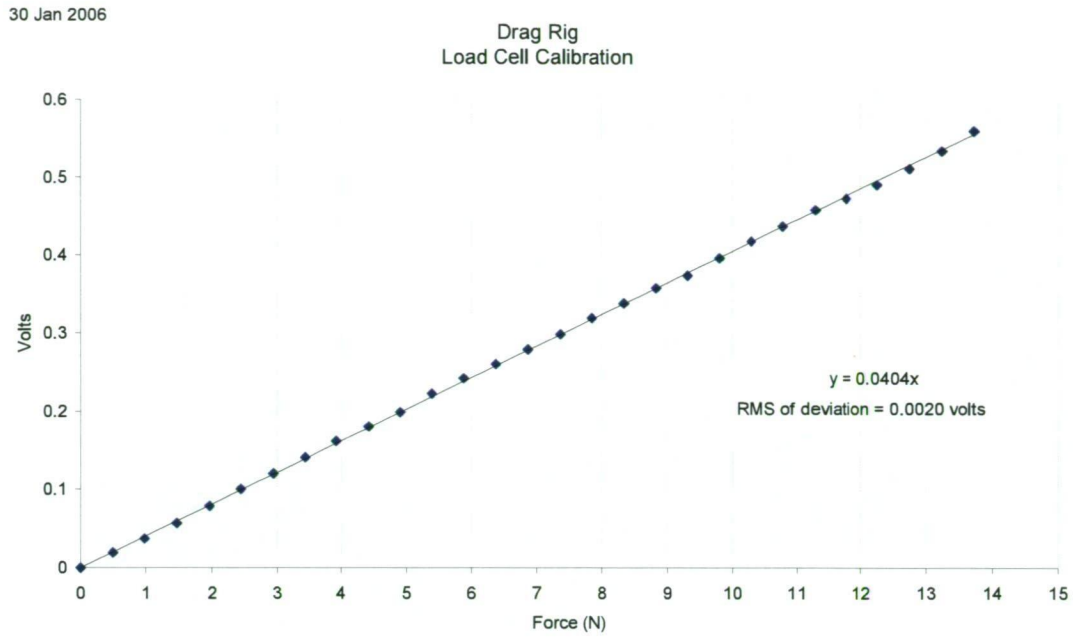

Figure 6.24: Typical drag rig calibration plot.

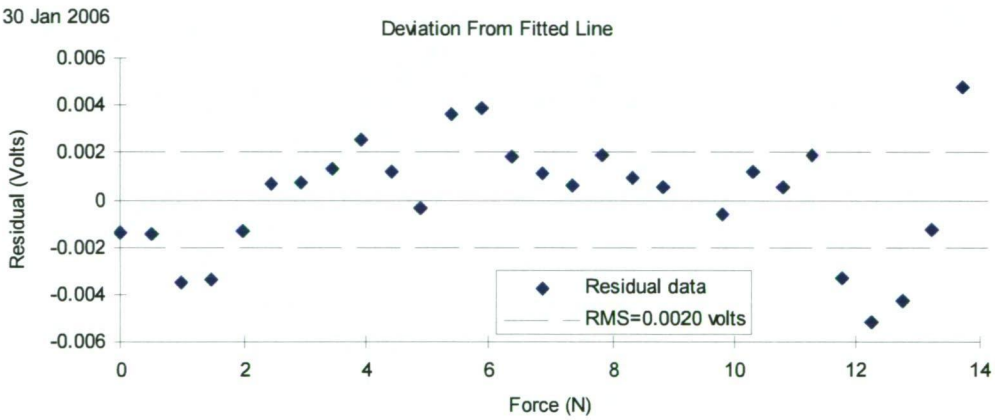

Figure 6.25: Plot of residuals (or deviation) from the fitted line.

Winter (1977) outlines problems associated with direct drag measurement using floating force balances. The problems of particular note for the present study, which have to be considered, are given below:

- Provision of a transducer for measuring small forces, and the compromise between the requirement to measure local properties and the necessity of having an element of sufficient size that the force on it can be measured accurately.
- The effect of the necessary gaps around the test plate.
- The effects of misalignment of the floating element test plate.
- Forces arising from pressure gradients.

- Effects of temperature changes.
- Effects of leaks.

These problems are explored throughout section 6.4 through the study of velocity distributions in the working section, and the comparison of drag measurements with theoretical values.

6.3.4 Turbulence Measurement

A TSI 1218-20W hotfilm probe (Figure 6.26) was used for turbulence measurement in conjunction with a DISA 55M constant temperature anemometer (CTA) (Figure 6.27). This particular model of probe had a pin attached to the main probe stem to prevent over run into the boundary, thereby reducing the risk of damaging the sensor.

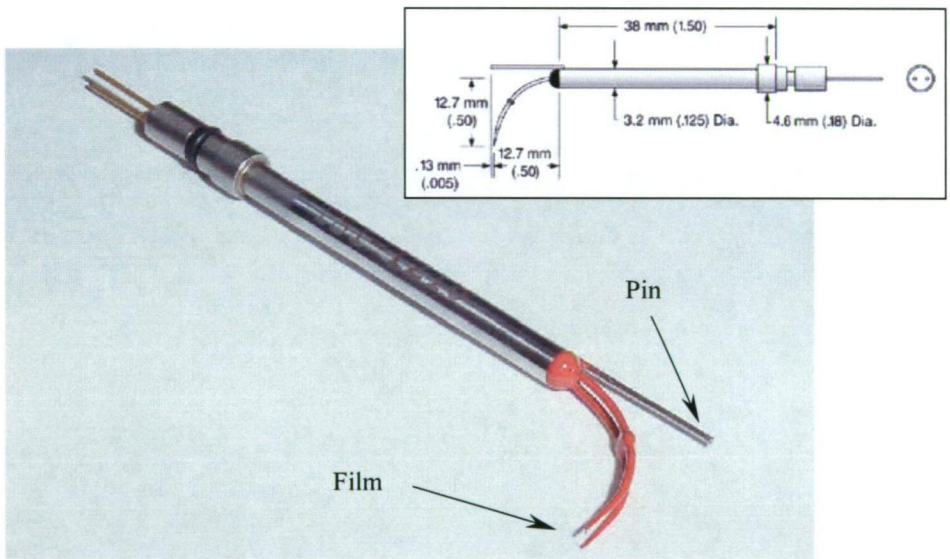

Figure 6.26: TSI 1218-20W hotfilm probe.

A 4.8mm diameter probe support, TSI Model 1159-15, was used with the hotfilm probe which was attached to a 5m cable for direct connect to the anemometer. A 10 mm guide tube (440 mm long), attached to the probe support, was inserted through the plugs in the working section and clamped securely to the precision height gauge for manual traversing. All probes, supports and connections were designed for immersion in water. 5 m cables were used for all turbulence measurements in the present study.

Figure 6.27: DISA 55M CTA used for turbulence measurements.

The mean voltage and RMS of the voltage fluctuations were recorded from the DISA 55M CTA using a LabView program. The water temperature and contraction pressure differential were also recorded concurrent with each turbulence measurement using LabView. This enabled the calculation of turbulence intensities, and the correction of voltage drift both due to water temperature changes and fouling of the probe sensor.

6.3.5 Pump Control for Constant Reynolds Number

Temperature effects during measurements were a concern, as the resulting changes in Reynolds number were significant. To mitigate this problem, each measurement was conducted at a constant Reynolds number, where possible. This was accomplished by using a platinum-resistance temperature probe (Model Pt100 MIR-HPC-TX RTD) with 4-20 mA output to monitor temperature and altering pump speed accordingly via LabView software and the pump speed controller. Figure 6.28 shows a typical water tunnel water temperature increase against water tunnel operating time. This data was taken from the boundary layer measurements of Chapter 7.

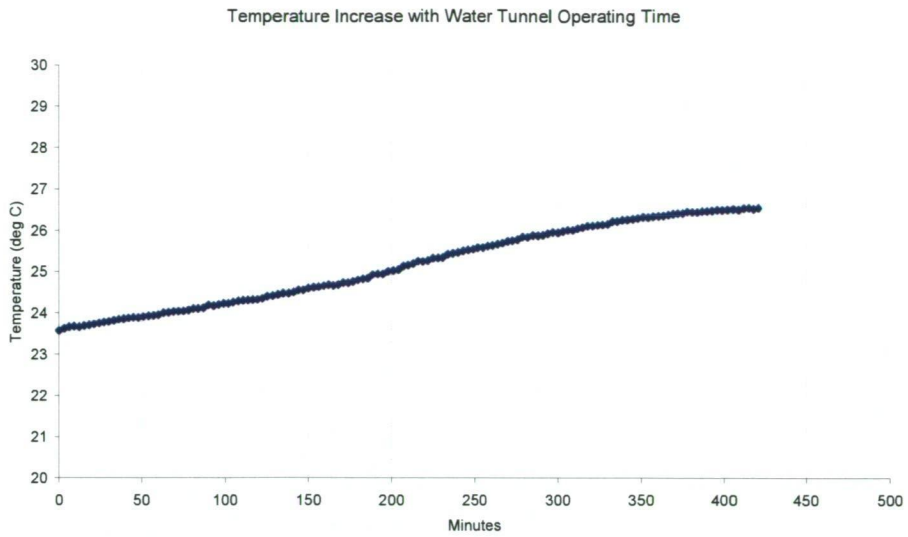

Figure 6.28: Temperature increase with time for water tunnel.

The temperature probe was first temporarily installed just downstream of the test plate but was later permanently installed in the flow conditioning section of the water tunnel where the flow velocity is at its lowest to avoid unnecessary energy losses.

An Xtravert pump controller (model number X716) was connected to the data acquisition terminal block. The procedure programmed into LabView to control pump speed, to maintain an approximate Reynolds number was as follows:

- The water temperature of the bulk flow is monitored using the temperature probe.
- Using the calibration curve of Figure 6.29, a relationship between pump speed and mean working section velocity was found.
- The required Reynolds number is input into LabView
- Based on the measured temperature and the contraction reference velocity versus pump speed relation, the pump speed is determined.

Equation 6.2 was used to determine the required contraction reference velocity, and the associated pump speed.

$$\mathrm{Re}_{Plate} = \frac{\rho U_{Contraction} x_{plate}}{\mu} \qquad \text{Equation 6.2}$$

Here, Re_{Plate} is the Reynolds number based on plate length, μ is the water dynamic viscosity, ρ is the water density, $U_{Contraction}$ is the contraction reference velocity, x_{plate} is the plate length (997 mm).

Temperature measurements are input into Equations 6.3 and 6.4, where T is the water temperature in °C.

$$\mu = -\left(\frac{(T-15)}{5}(0.00014)\right) + 0.00114 \qquad \text{Equation 6.3}$$

$$\rho = -\left(\frac{(T-15)}{5}\right) + 999 \qquad \text{Equation 6.4}$$

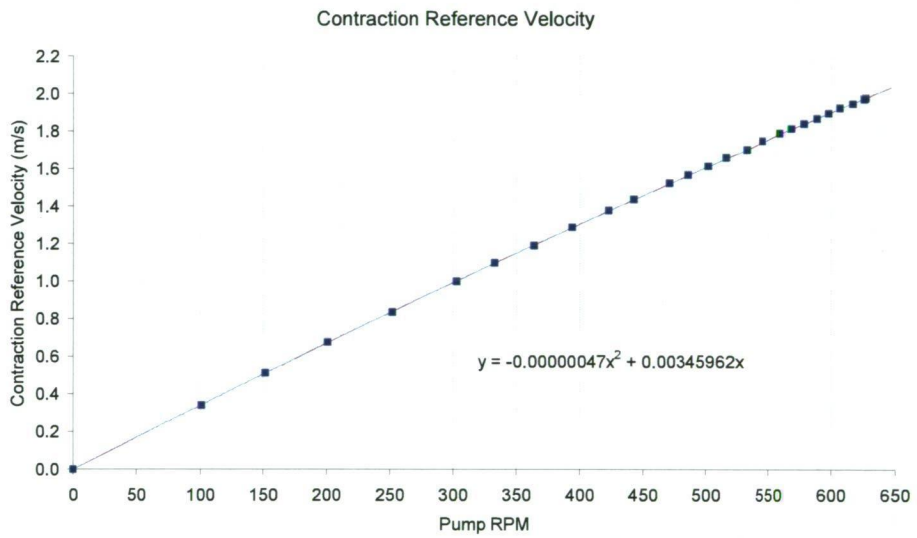

Figure 6.29: Contraction differential (as a reference velocity) versus pump speed.

The method outlined to control pump speed provides only a general control of the Reynolds number, as the contraction reference velocity used in Figure 6.28 is still subject to slight change with temperature. Figure 6.30 presents a plot using the temperature data of Figure 6.28 showing the effect on Reynolds number with and without the described pump speed control to maintain constant Reynolds number.

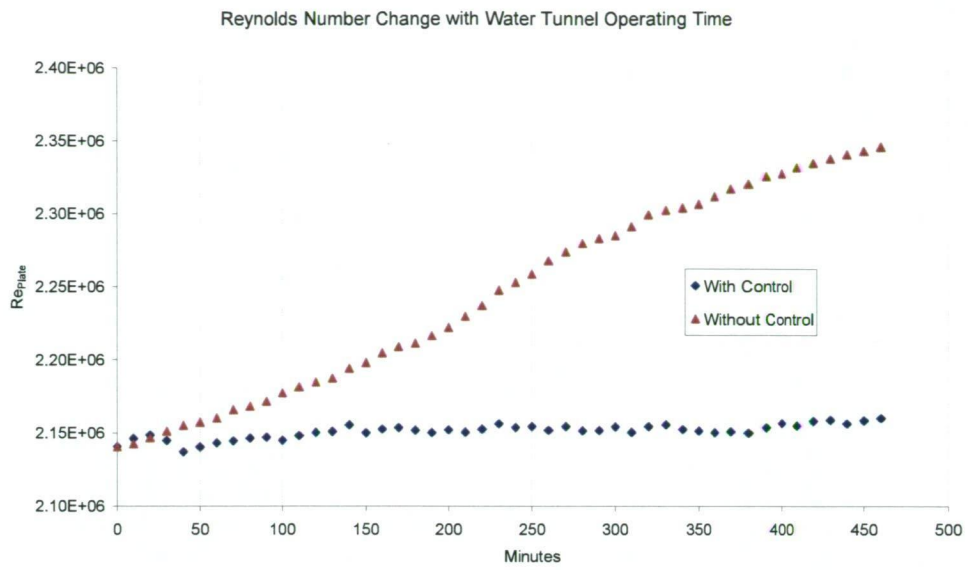

Figure 6.30: Reynolds number with and without controlling pump speed.

6.3.6 Data Acquisition

LabView software was used to acquire all data for the present study. A National Instruments 12 bit PCI 6025E acquisition card was installed on a personal computer, and all instrumentation electrical outputs were connected to a National Instuments SBC100 100 pin shielded connector block in the correct format (i.e. ± 10 volt range). Low-pass R-C filters (or Pi filters) were used on some inputs to aid in the removal differential noise for the electrical signals. Induced current fields were found to affect some of the signals due to cables being draped across the steel frame of the water tunnel. Earth loops were also carefully removed.

To determine the appropriate sample time for all measurements, cumulative time averaged pressures were plotted, and the optimal sample length determined. In Figure 6.31 it is shown that a minimum sample length of 7 seconds is required for total pressure measurements with the Pitot probe. 12 seconds was used for all scanned pressures for the present study, with 10 seconds used as the settling time (between adjustments in flow speed to allow a steady flow) before the actual sample was taken.

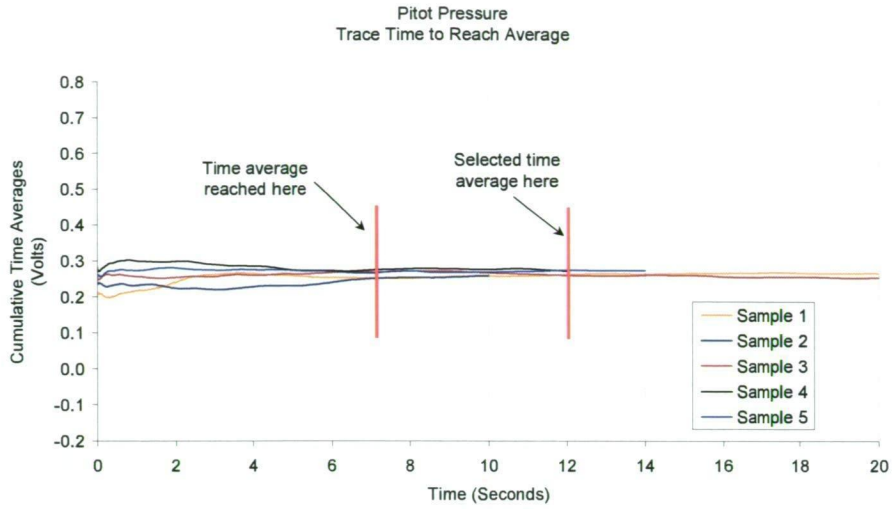

Figure 6.31: Plot of cumulative time averaged pressures.

A 20 second sampling period was used for all total drag measurements, with a 10 second settling time following pump speed adjustments.

A 35 second sampling period was used for hot film turbulence measurements to obtain mean bridge and RMS voltages with an approximate 30 second settling time preceding the sampling period to allow for pump speed adjustments.

6.4 Calibration of Water Tunnel

As the water tunnel used for this study was newly constructed and unique in design, a comprehensive calibration was required to demonstrate that the facility was suitable.

This section provides an overview of the bulk flow properties through the water tunnel and working section, and then looks at detailed measurements in the working section including boundary layer development and total drag measurements.

6.4.1 Tunnel Headloss Characteristics

Wall tappings were installed on the water tunnel on each component shown in Figure 6.1. These were attached via 2 mm (outside diameter) tubing to a vertical manometer

board where pressure readings could be recorded. Figure 6.32 shows a photo of the manometer board in operation.

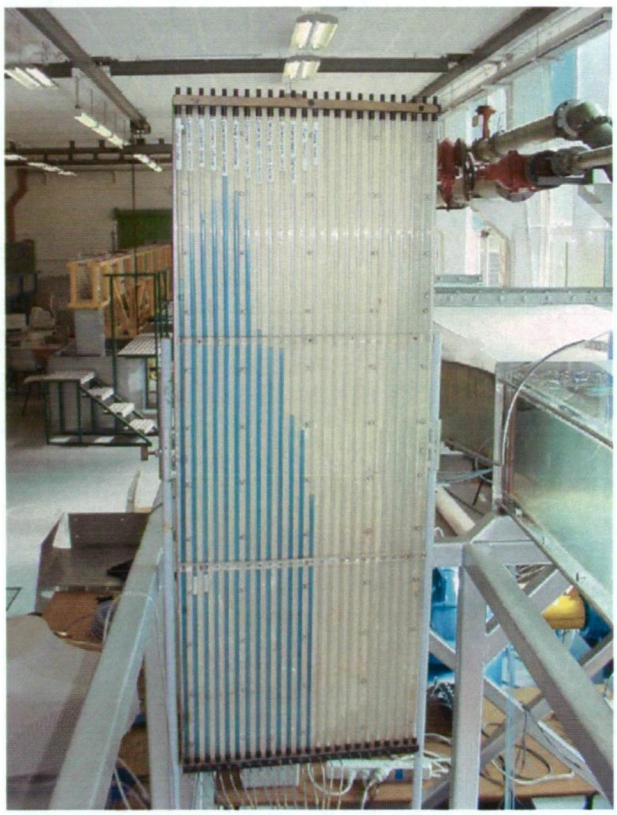

Figure 6.32: The manometer board used to record the pressure levels.

Readings of the manometer board were taken for three different pump speeds of 300, 450 and 600 RPM which approximates a mean flow velocity of 1 m/s, 1.5 m/s and 2 m/s in the working section.

Results for the measurements are plotted in Figure 6.33 as the Hydraulic Grade Line (HGL), and Figure 6.33 as the Total Energy Line (TEL). Both sets of results have been non-dimensionalised using the working section velocity head. The working section was used as the datum level for the results.

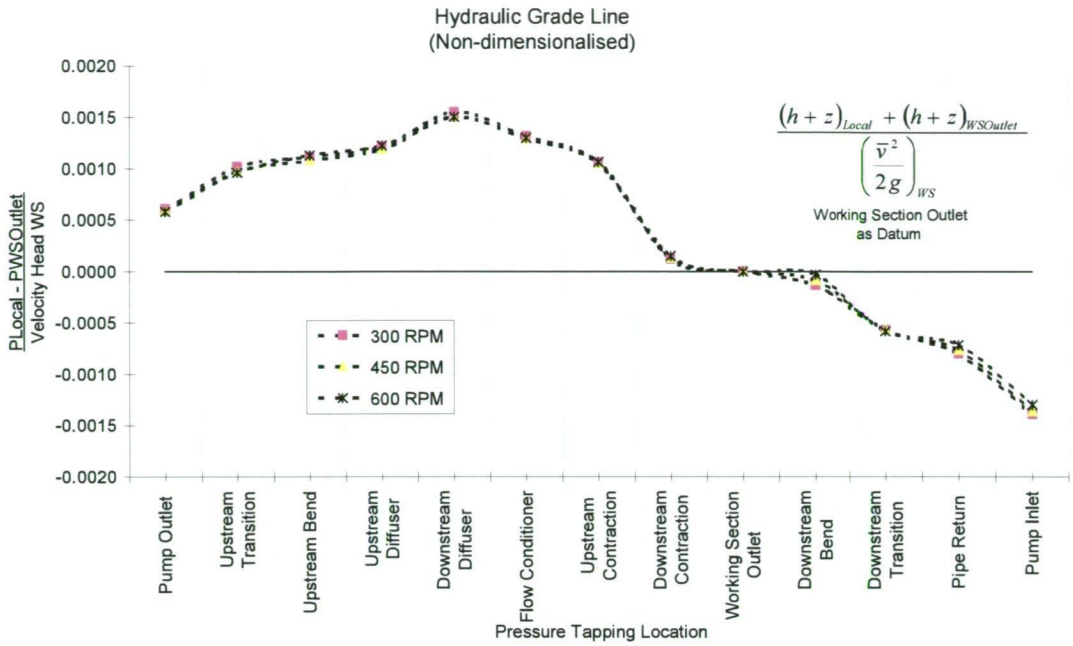

Figure 6.33: Measured HGL for the water tunnel.

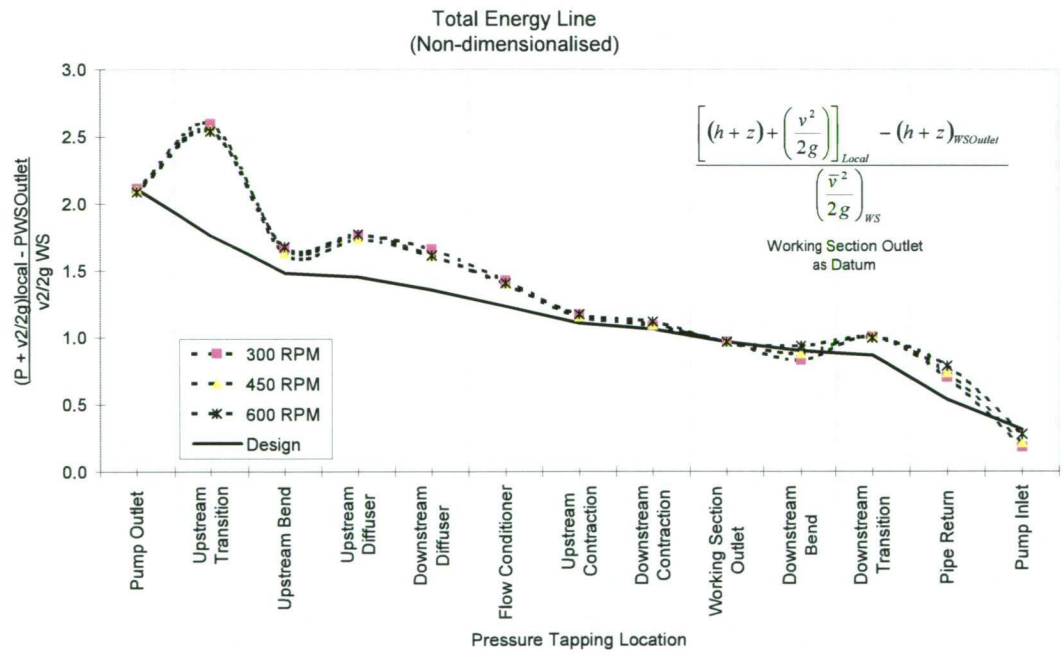

Figure 6.34: Measured TEL for the water tunnel and the design TEL values.

The values of some wall pressures would have been influenced by local flow curvature associated with bends or sudden changes in wall angle. This explains the significant deviations between measured and design values for the upstream transition (first stage diffuser) and the second stage diffuser in Figure 6.34. The total energy loss between pump outlet and pump inlet agrees well with the overall design loss value.

Further details of the design values for the TEL can be found in Sargison *et al.* (2006).

6.4.2 Longitudinal Flow Acceleration in the Working Section

Longitudinal flow acceleration occurs due to wall boundary layer growth through the working section. To measure the flow acceleration, static wall tappings were installed at the upstream and downstream ends of the test plate and contraction. Figure 6.35 presents the measured flow acceleration over the length of the test plate as a percentage (expressed as $\left(\frac{u_{trailing} - u_{leading}}{u_{leading}}\right) \times 100$) against the mean velocity at the entrance to the working section. Here, $u_{trailing}$ is the velocity at the trailing edge of test plate and $u_{leading}$ is the velocity at the leading edge of plate.

Flow acceleration was an approximately constant value of 2.7 % over the length of the 1m long acrylic test plate for a range of flow rates through the working section.

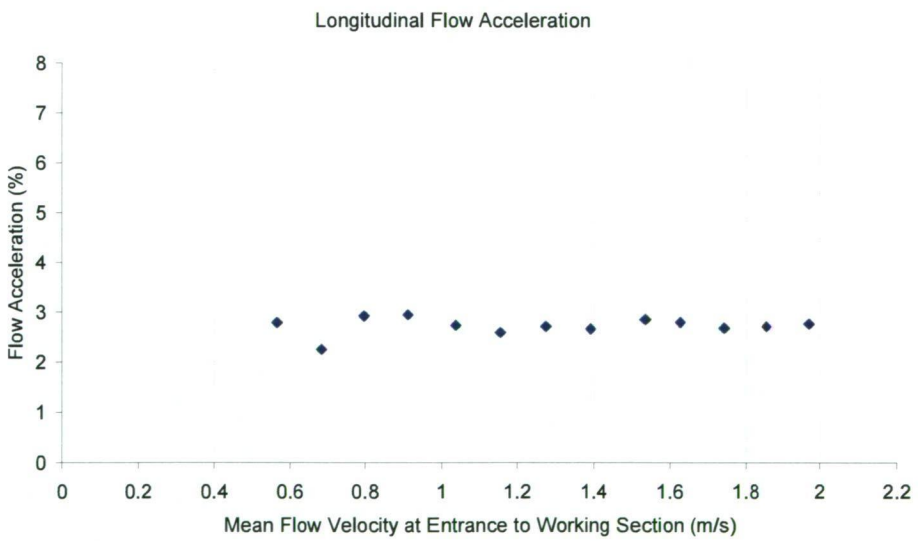

Figure 6.35: Longitudinal flow acceleration over test plate.

Longitudinal flow acceleration was important when measuring total drag, as corrections were required to remove the drag contribution from the resulting force applied to the plate. This is discussed further in section 6.4.6.

6.4.3 Horizontal Flow Distributions

Two methods were used to determine the horizontal (transverse) flow distribution in the working section. The first was to measure the pressure coefficients across the test plate surface, the second was to measure the velocity distribution across the working section at the vertical centreline.

6.4.3.1 Plate Pressure Coefficients

A series of Preston tubes of 1.58 mm ($1/16^{th}$ inch) outside diameter were installed in a transverse array at the mid-section and end-section of the acrylic plate to measure the wall skin friction variation (as pressure coefficients) as a check for flow uniformity in lieu of a continuous probe traverse. The measurements at both the mid-section and end-section also gave an indication of the flow development along the plate. Figure 6.36 illustrates how the tubes were located on the plate. The probes (a total of 21) were located at distances of 5, 12.5, 25, 37.5, 50, 75, 100, 150, 200, 250 and 298.5 mm from the edge of the plate (plate width = 597 mm). The probe locations were symmetric about the plate longitudinal centreline.

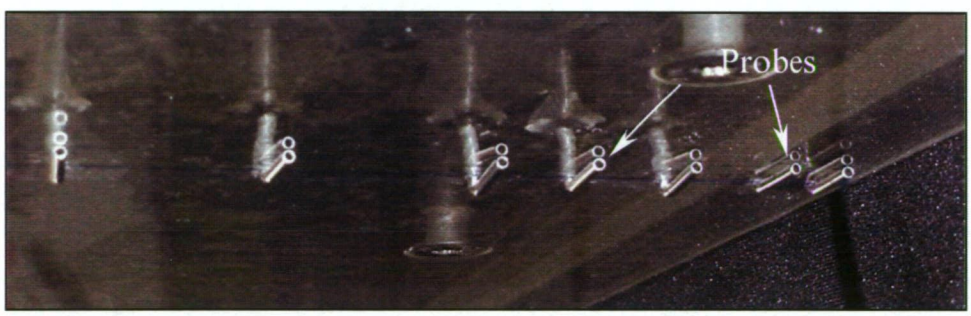

Figure 6.36: A series of Preston tubes temporarily installed on the acrylic test plate showing a close-up of the tubes with their tips hard against the plate surface.

All pressures were measured by the Validyne pressure transducers and scanned via the solenoid switch arrangement. Only six wall pressures could be measured at any one time as two of the eight channels were used to monitor the contraction pressure differential. Therefore, several passes were made to measure all the required pressures.

Results for the mid-section and end-section of the plate are shown in Figures 6.37 and 6.38 respectively. The mid-section measurements were 20 mm upstream of the middle centreline of the plate. The end-section measurements were 30 mm upstream of the trailing edge of the plate.

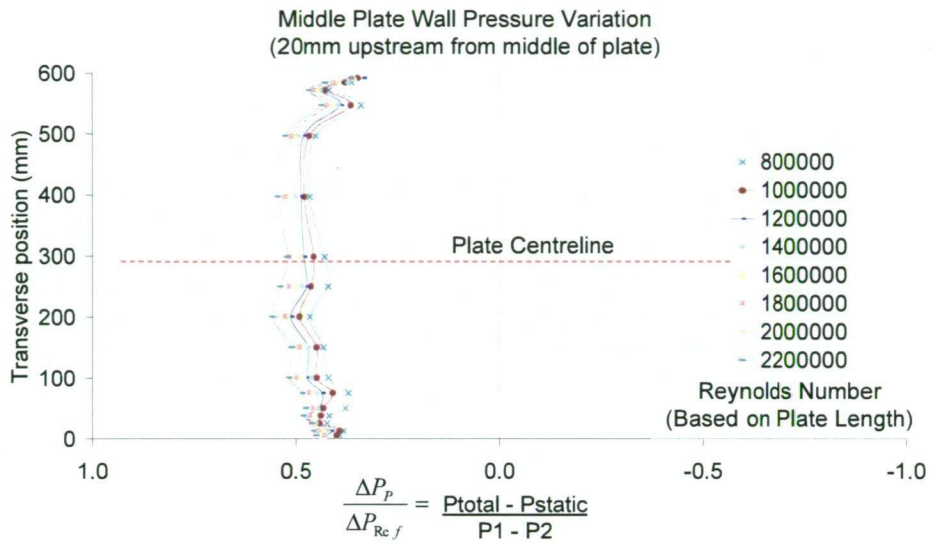

Figure 6.37: Pressure coefficients for the mid-section of the plate.

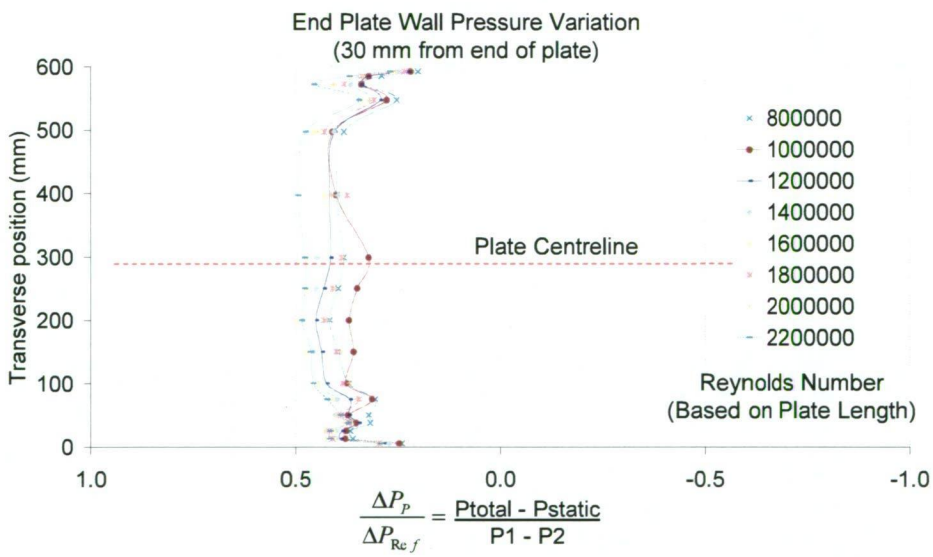

Figure 6.38: Pressure coefficients for the end-section of the plate.

A higher density of measurement points were clustered near the plate longitudinal edge to better ascertain edge effects due to secondary corner and leakage flows. The flow was found to be essentially symmetrical about the plate longitudinal centreline.

Figures 6.37 and 6.38 show that the flow is evenly distributed across the central 400mm of the working section width. The results at the edge of the plate clearly show some corner phenomena, due to leakage flow in or out of the roof cavity, and indicate secondary flows becoming more developed with increasing distance downstream. Longitudinal vortices in tunnel facilities are discussed by Mokhtari and Bradshaw (1983) and Kim and Patel (1994). They are not considered very significant in the present study.

6.4.3.2 Transverse Velocity Distribution on Centre-Plane of Working Section

Whereas the pressures presented in Figures 6.37 and 6.38 are across the plate surface, measurements were also made of the velocity distribution using a Pitot-Static probe at the vertical centreline across the working section width. A temporary arrangement was used where the probe was used and positioned at 50 mm intervals along the end-section of the plate. Figure 6.39 shows a photo of how the probe was positioned in the gap between the test plate and wall.

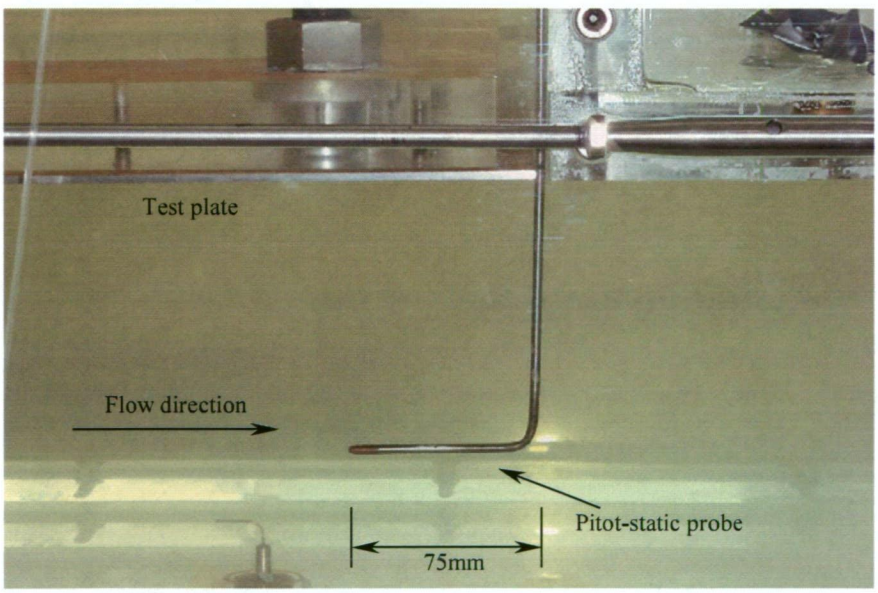

Figure 6.39: A Pitot-static probe used to measure the transverse velocity distribution.

Figures 6.40 and 6.41 show the results for the measurements where probe positions are plotted against the measured velocity. Velocities were taken at intervals in pump speed

rather than Reynolds number in this case. The tip of the probe (for total pressure measurement) is 75 mm upstream from the downstream edge of the plate.

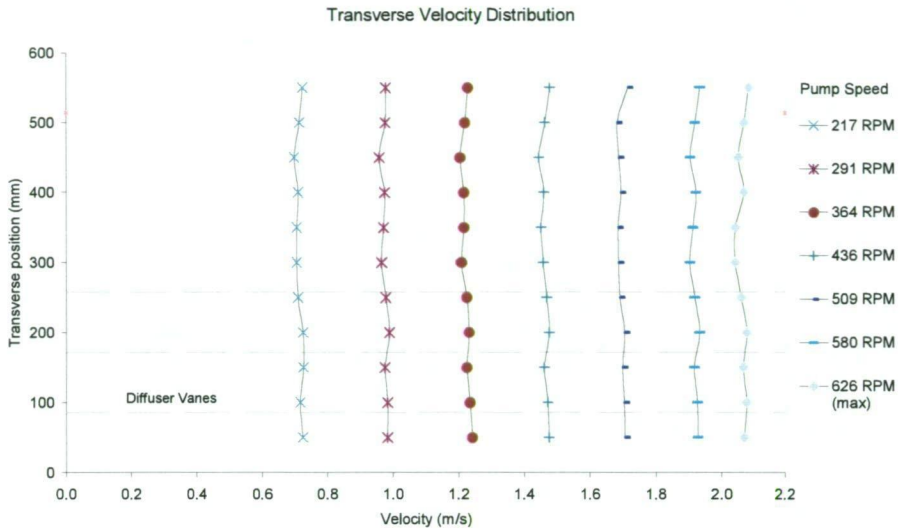

Figure 6.40: Transverse velocity distribution.

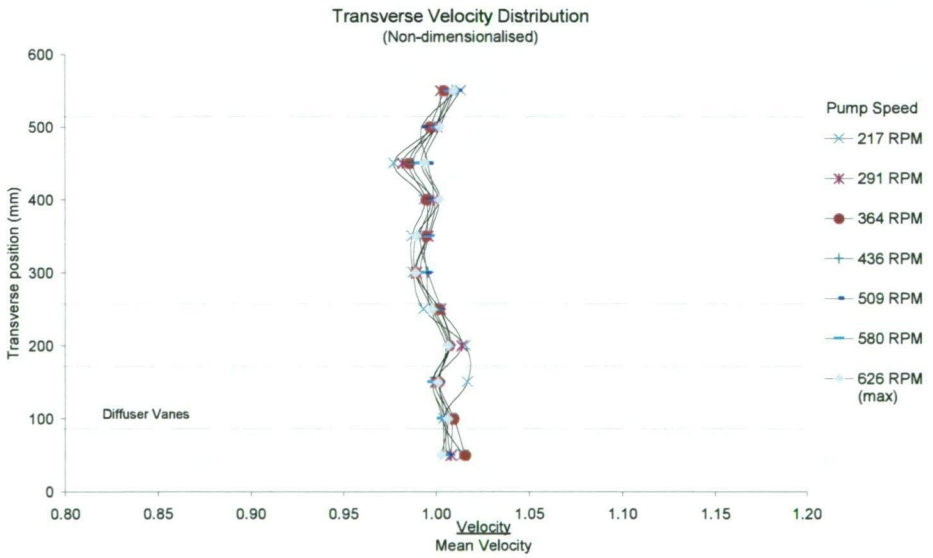

Figure 6.41: Non-dimensionalised transverse velocity distribution.

Results show that the flow is uniform within ± 2 % across the central 500 mm of the working section. Also plotted on Figures 6.40 and 6.41 are the locations of the vanes in the second diffuser immediately upstream of the flow conditioner and contraction. The perturbations in mean velocity across the working section do not appear to correlate with these positions.

6.4.4 Vertical Velocity Distributions

Velocity profiles were measured 105 mm upstream, and 95 mm, 495 mm and 865 mm downstream of the leading edge of the test plate respectively for plugs upstream, 1, 2 and 3.

The velocity profiles (Figure 6.42) do not show symmetry in the vertical direction, and this becomes more pronounced further downstream. This is thought to be due to lower energy fluids attracted to the inside circumference of the water tunnel loop.

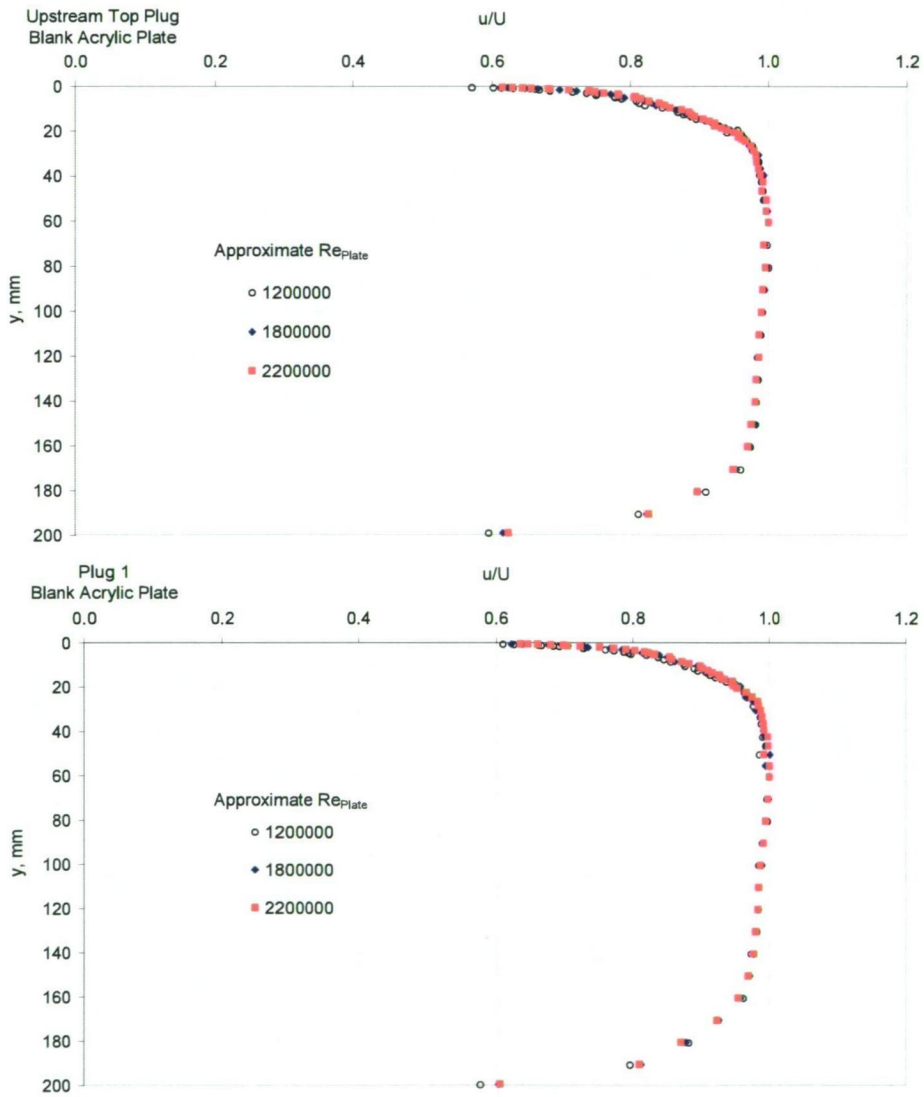

Figure 6.42: Velocity profiles at upstream plug, plug 1, plug 2 and plug 3.

(Continued next page)

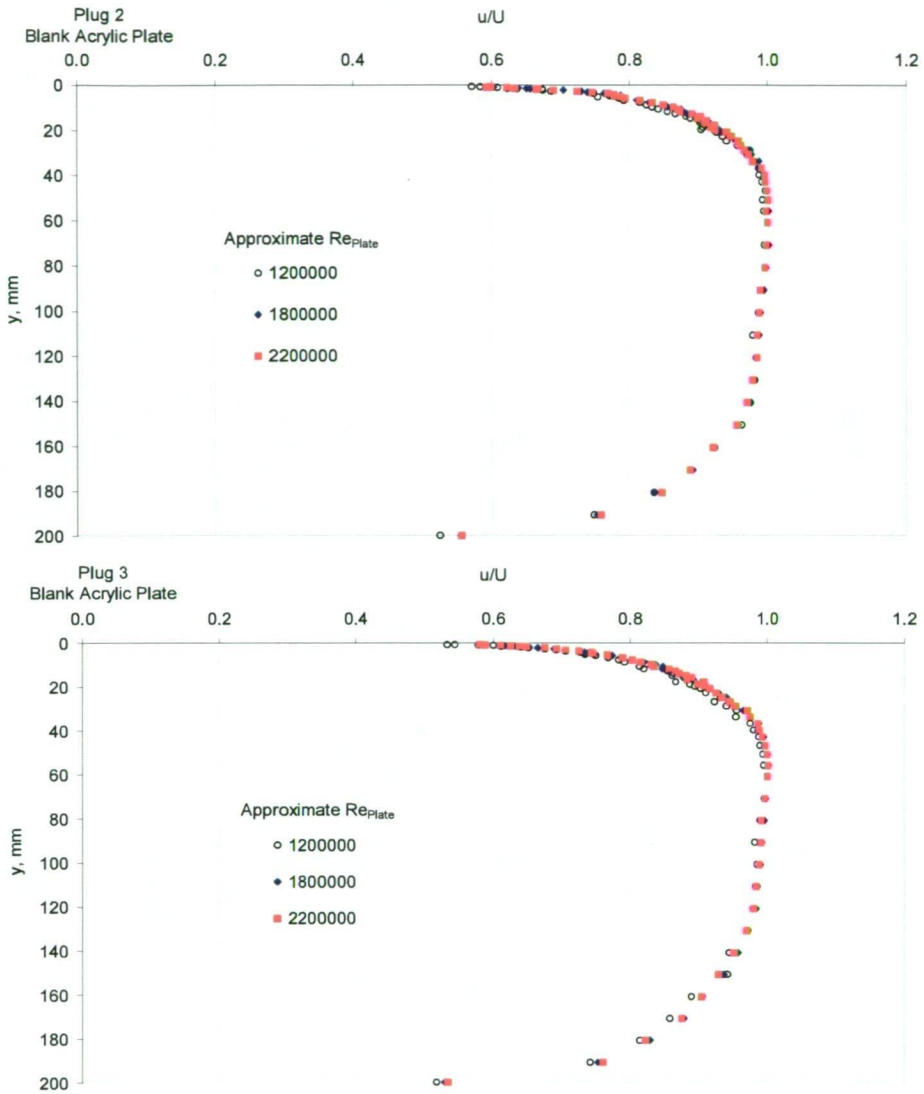

Figure 6.42 (continued): Velocity profiles at upstream plug, plug 1, plug 2 and plug 3.

Blockage effects (and associated flow acceleration) caused by the probe stem as the Pitot probe was traversed through the working section were checked. Figure 6.43 shows the various pressure variations measured at plug 1 (x = 95mm), with the static pressure remaining constant.

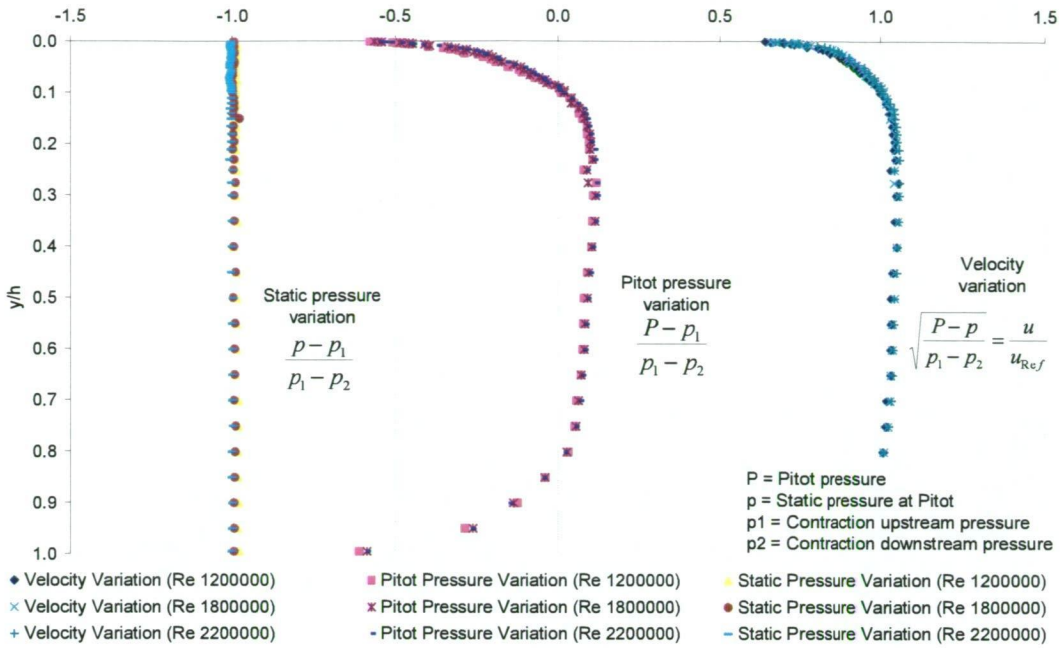

Figure 6.43: Pressure variations for the acrylic plate at plug 1 (x=95mm).

Probe flexure from the force of the moving water was observed not to be significant. If flexing of the probe was apparent, this would have warranted corrections to the probe position.

6.4.5 Boundary Layer Measurements in Working Section

6.4.5.1 Thermal Boundary Layer

A boundary layer traverse was undertaken at the upstream (plug 1) and downstream (plug 3) ends of the acrylic test plate to measure for any temperature gradient (or thermal boundary layer). This was done using a thermo-couple attached to a support stem mounted on the traversing rig.

The water tunnel water was heated to 26 °C to achieve a difference between the ambient air (at 16 °C) and water of 10 °C. No gradient was measured. This is thought to be due to both the turbulent boundary layer ensuring good mixing, and the fact that water is able to circulate above and around the test plate in the working section roof cavity, therefore making there no temperature difference between the two sides of the test plate.

6.4.5.2 Velocity Profiles

Table 6.3 presents a summary of the boundary layer parameters derived from the mean velocity profiles shown in Figure 6.44. U was taken as the point of maximum velocity in the measured velocity profile. The boundary layer thickness, δ (mm), was derived from the momentum thickness using $\theta = \frac{7}{72}\delta$ as given by the $\frac{1}{7}^{\text{th}}$ power law. The boundary layer momentum thickness is a more reliable parameter as it is less sensitive to error in determining the wall position, particularly so due to the slightly non-uniform vertical velocity distribution in the working section. The displacement thickness, δ^* (mm), is given by $\delta^* = \int_0^\infty \left(1 - \frac{u}{U}\right) dy$. The momentum thickness, θ (mm), is given by $\theta = \int_0^\infty \frac{u}{U}\left(1 - \frac{u}{U}\right) dy$. The velocity profile shape factor, H, is found from $H = \frac{\delta^*}{\theta}$. $u*$ is the wall shear (or friction) velocity and c_f is the local skin friction coefficient.

Re_{Plug} is the Reynolds number based on the distance from the plate leading edge to the plug being used for measurement. Re_{Plate} is the Reynolds number based on the length of plate (997 mm) and was used as a reference to maintain an approximate Reynolds number while operating the water tunnel. Three Re_{Plate} values are used for the boundary layer traverses (1.2×10^6, 1.8×10^6, and 2.2×10^6), representing both the widest useful range of the water tunnel, and typical near wall conditions for field assets.

Re_δ, Re_{δ^*} and Re_θ are the boundary layer thickness, displacement thickness and momentum thickness Reynolds numbers respectively.

Repeatability tests were conducted with the Pitot probe against the wall and also with the probe in the bulk flow. Figures 6.44 and 6.45 show the results of these tests where the uncertainty in u, represented as $\frac{u}{u_{\mathrm{Re}f}} = \sqrt{\frac{P-p}{p_1 - p_2}}$, was measured to be ± 1.56 % at the wall and ± 0.29 % in the bulk flow. This uncertainty is applicable to all velocity measurements in the present study.

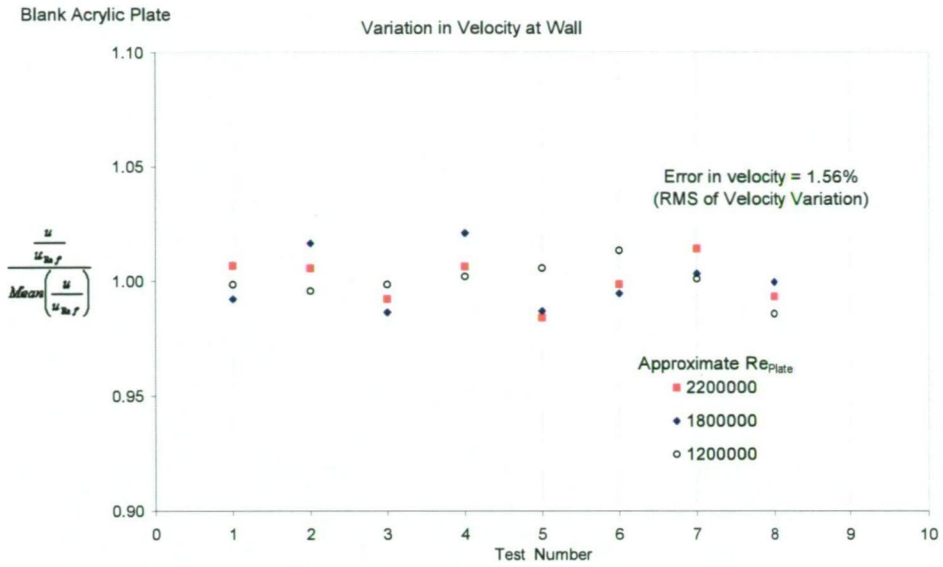

Figure 6.44: Error in measured velocity, u, at the wall.

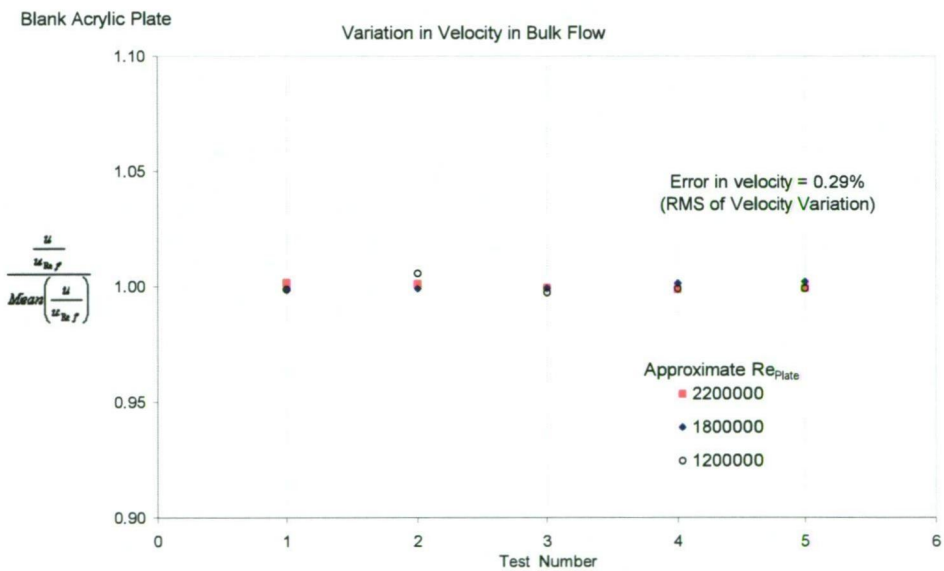

Figure 6.44: Error in measured velocity, u, in bulk flow

Table 6.3: Summary of boundary layer parameters for acrylic test plate.

Acrylic Plate												
Measurement Station	U (m/s)	δ (mm)	δ* (mm)	θ (mm)	u* (m/s)	c_f	H	Re_{Plug}	Re_{Plate}	Re_{δ}	Re_{δ^*}	Re_{θ}
x = -105mm (Upstream Plug)	1.03	33.04	3.89	3.21	0.0450	0.0038	1.21	-1.29E+05	1.23E+06	4.07E+04	4.79E+03	3.96E+03
	1.59	31.00	3.60	3.01	0.0676	0.0036	1.19	-1.99E+05	1.89E+06	5.88E+04	6.83E+03	5.71E+03
	1.93	30.94	3.55	3.01	0.0799	0.0034	1.18	-2.42E+05	2.30E+06	7.13E+04	8.18E+03	6.93E+03
x = 95mm (Plug 1)	1.02	29.83	3.43	2.90	0.0473	0.0043	1.18	1.14E+05	1.20E+06	3.58E+04	4.12E+03	3.48E+03
	1.57	27.10	3.09	2.63	0.0680	0.0038	1.17	1.75E+05	1.83E+06	4.99E+04	5.68E+03	4.85E+03
	1.91	26.03	2.96	2.53	0.0815	0.0036	1.17	2.13E+05	2.23E+06	5.83E+04	6.62E+03	5.66E+03
x = 495mm (Plug 2)	1.07	36.69	4.33	3.57	0.0466	0.0038	1.22	6.18E+05	1.24E+06	4.58E+04	5.41E+03	4.45E+03
	1.64	31.54	3.72	3.07	0.0683	0.0035	1.21	9.47E+05	1.91E+06	6.03E+04	7.11E+03	5.87E+03
	1.99	32.12	3.77	3.12	0.0805	0.0033	1.21	1.15E+06	2.32E+06	7.46E+04	8.75E+03	7.25E+03
x = 865mm (Plug 3)	1.03	43.89	5.27	4.27	0.0434	0.0035	1.24	1.06E+06	1.22E+06	5.37E+04	6.45E+03	5.22E+03
	1.59	37.64	4.51	3.66	0.0645	0.0033	1.23	1.63E+06	1.88E+06	7.09E+04	8.50E+03	6.90E+03
	1.93	37.62	4.49	3.66	0.0759	0.0031	1.23	1.98E+06	2.28E+06	8.60E+04	1.03E+04	8.36E+03

The law of the wall was fitted to the velocity profile plots using Equation 6.5.

$$\frac{u}{u^*} = \frac{1}{0.41} \ln \frac{yu^*}{\upsilon} + 5.0 \qquad \text{Equation 6.5}$$

The power law was fitted using Equation 6.6.

$$\frac{u}{U} = \left(\frac{y}{\delta}\right)^{\frac{1}{n}} \qquad \text{Equation 6.6}$$

Here, u = the local velocity, y = the distance from the wall and υ is the water kinematic viscosity. n was taken at 7 for the $1/7^{th}$ power law for smooth walls.

The traversing procedure for the boundary layer measurements began with the probe tip against the wall, determined from observation. The probe was then incrementally stepped from the wall into the mainstream flow at distances approximating a log distribution. Measurements were recorded at approximate Reynolds numbers (based on plate length) of 1.2×10^6, 1.8×10^6, and 2.2×10^6.

Figure 6.44 presents the mean velocity turbulent boundary layer profiles measured from the acrylic test plate. Results are presented as $\frac{u}{u^*}$ (or u+) versus $\frac{yu^*}{\nu}$ (or y+).

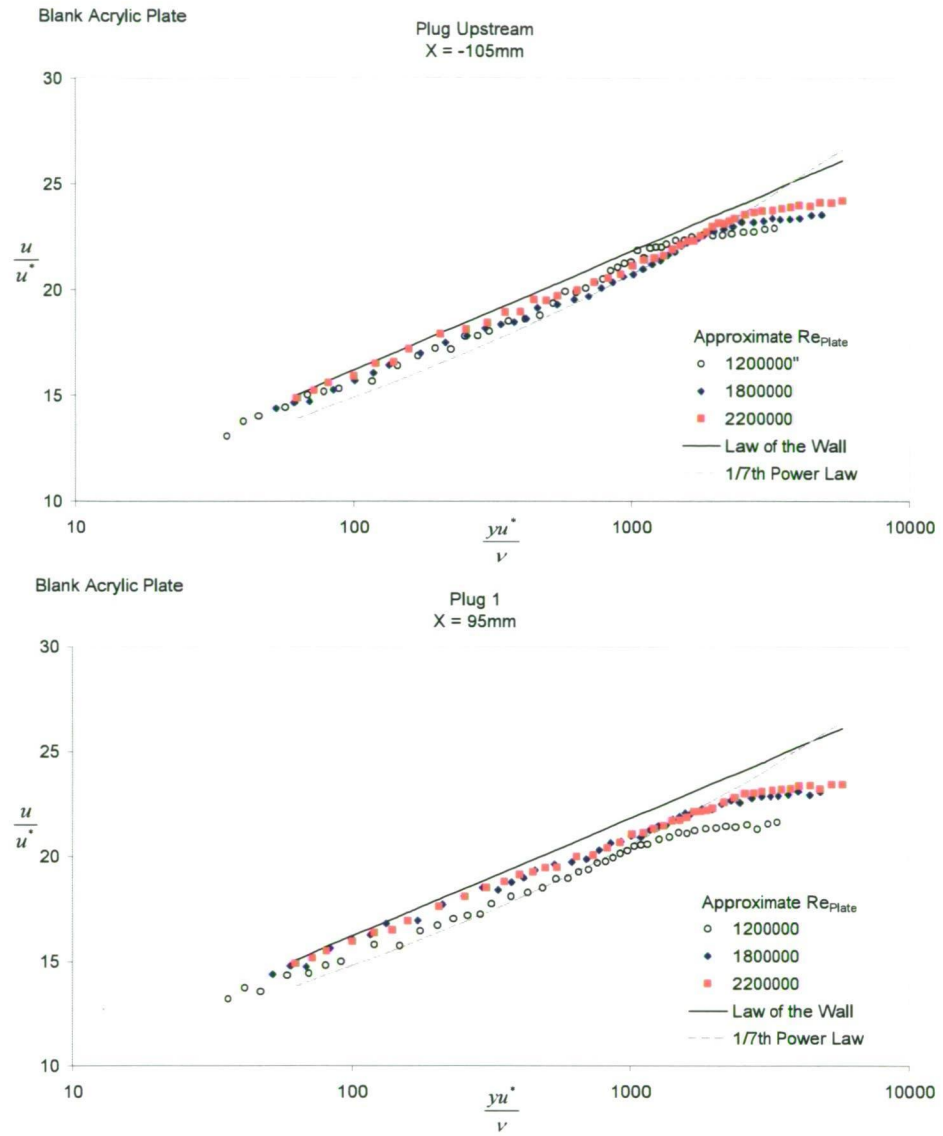

Figure 6.44: Boundary layer velocity profiles.

(Continued next page)

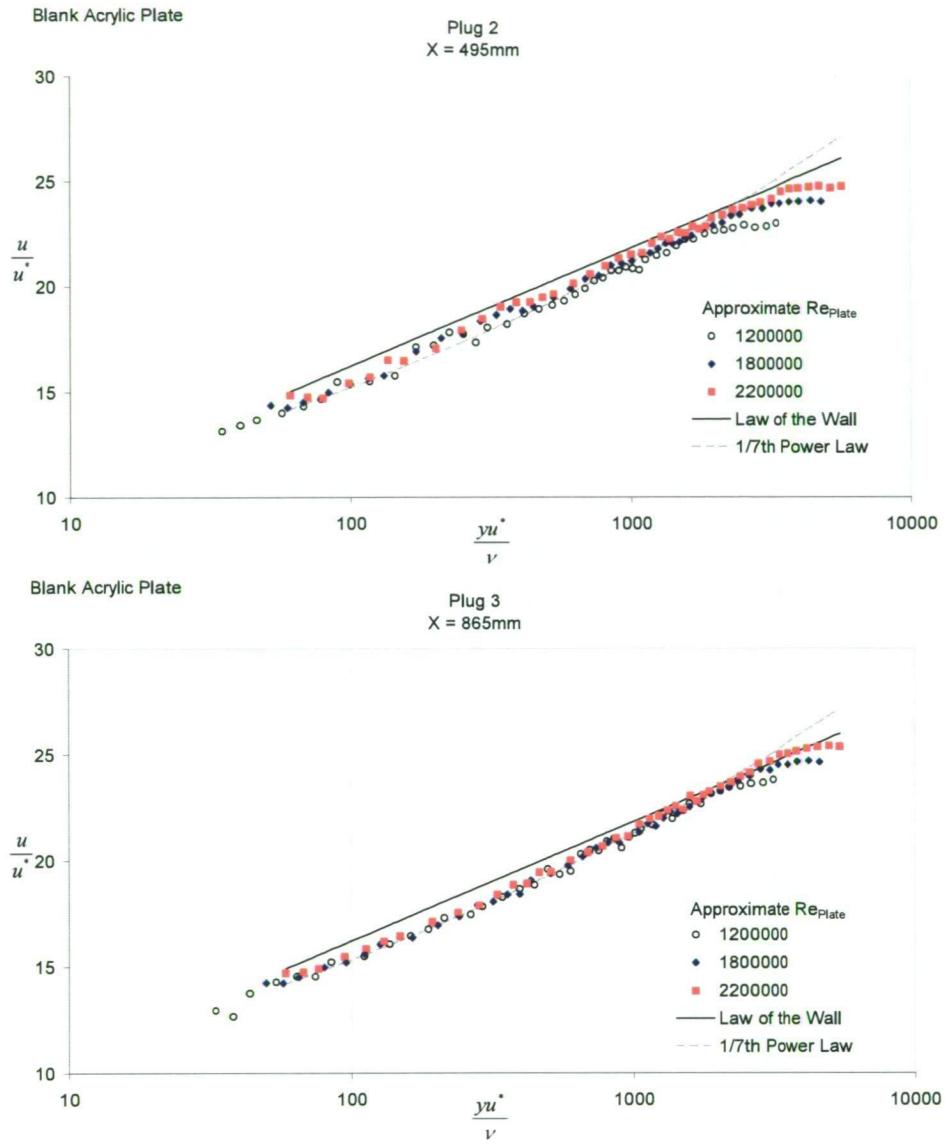

Figure 6.44 (continued): Boundary layer velocity profiles.

Figure 6.44 shows a developing boundary layer over the length of the test plate. The velocity profile is generally well approximated by both the law of the wall and $\frac{1}{7}^{\text{th}}$ power law at the upstream plug and plug 1, with the $\frac{1}{7}^{\text{th}}$ power law better approximating the velocity distribution at the two downstream plugs.

A plot of the shape factors (Figure 6.45) at each measurement location at each Reynolds number shows a turbulent boundary layer tending towards equilibrium. The local equilibrium values of H for Re_{Plate} are shown in as a comparison. The theoretical

equilibrium values were determined from the Nash equilibrium relation (Equation 6.7) and are for $\mathrm{Re}_{Plate} = 2.2 \times 10^6$ only.

$$G = 6.1(\Pi + 1.81)^{\frac{1}{2}} - 1.7 \qquad \text{Equation 6.7}$$

The Nash-Macdonald skin friction law (Equation 6.8) was use to plot the local skin friction equilibrium values and wall shear velocities for Figure 6.47 and 6.48

$$\left(\frac{2}{c_f}\right)^{\frac{1}{2}} = 2.4711\ln(\mathrm{Re}_\theta) + 1.5G + \frac{1725}{(G^2 + 200)} - 12.12 \qquad \text{Equation 6.8}$$

The velocity defect parameter, G, can be found from $G = \left(\frac{2}{c_f}\right)^{\frac{1}{2}}\left(1 - \frac{1}{H}\right)$, and the pressure gradient parameter, Π, from $\Pi = -\left(\frac{2H}{c_f}\right)\left(\frac{\theta}{U}\right)\left(\frac{dU}{dx}\right)$. The streamwise distance, x, was determined from the virtual origin of the boundary layer described in section 6.4.6 to create the boundary layer thickness measured from the velocity profiles in Figure 6.44.

A discontinuity (Figure 6.45) is observed between the upstream plug and plug 1 due to leakage into the small gap of about 1.5 mm between the working section roof and the leading edge of the acrylic test plate. Some of the boundary layer fluid moves into the roof cavity of the working section. This was observed using the flow visualisation technique of injecting dye into the flow. This leakage flow is driven by the pressure differential between the upstream and downstream ends of the test plate resulting from flow acceleration due to wall boundary layer growth in the working section.

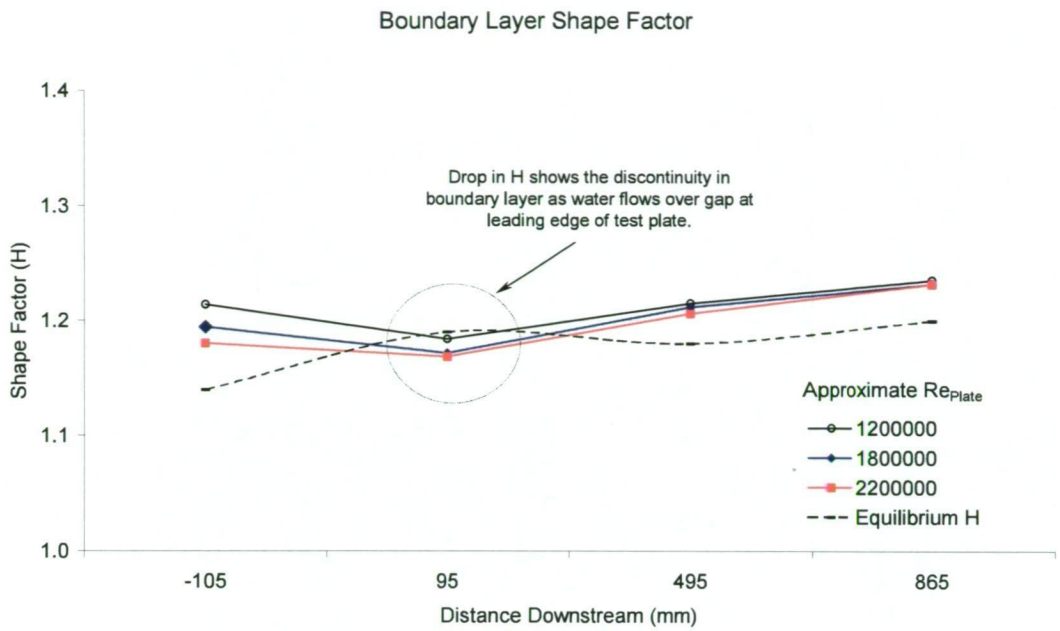

Figure 6.45: Shape factor variation along the test plate.

A plot of the boundary layer thicknesses at each measurement location (Figure 6.46) also shows this phenomenon of boundary layer thinning due to leakage into the roof cavity at the leading edge of the plate. The boundary layer thinning increases the skin friction at plug 1, as indicated in Figure 6.47.

The data in Figure 6.47 show the boundary layer determined from the $\delta = \frac{72\theta}{7}$ relation and the more usually definition of $\delta = y$ at $0.99U$. Results show the large differences at the forward measuring stations, and better comparison at x = 865 mm.

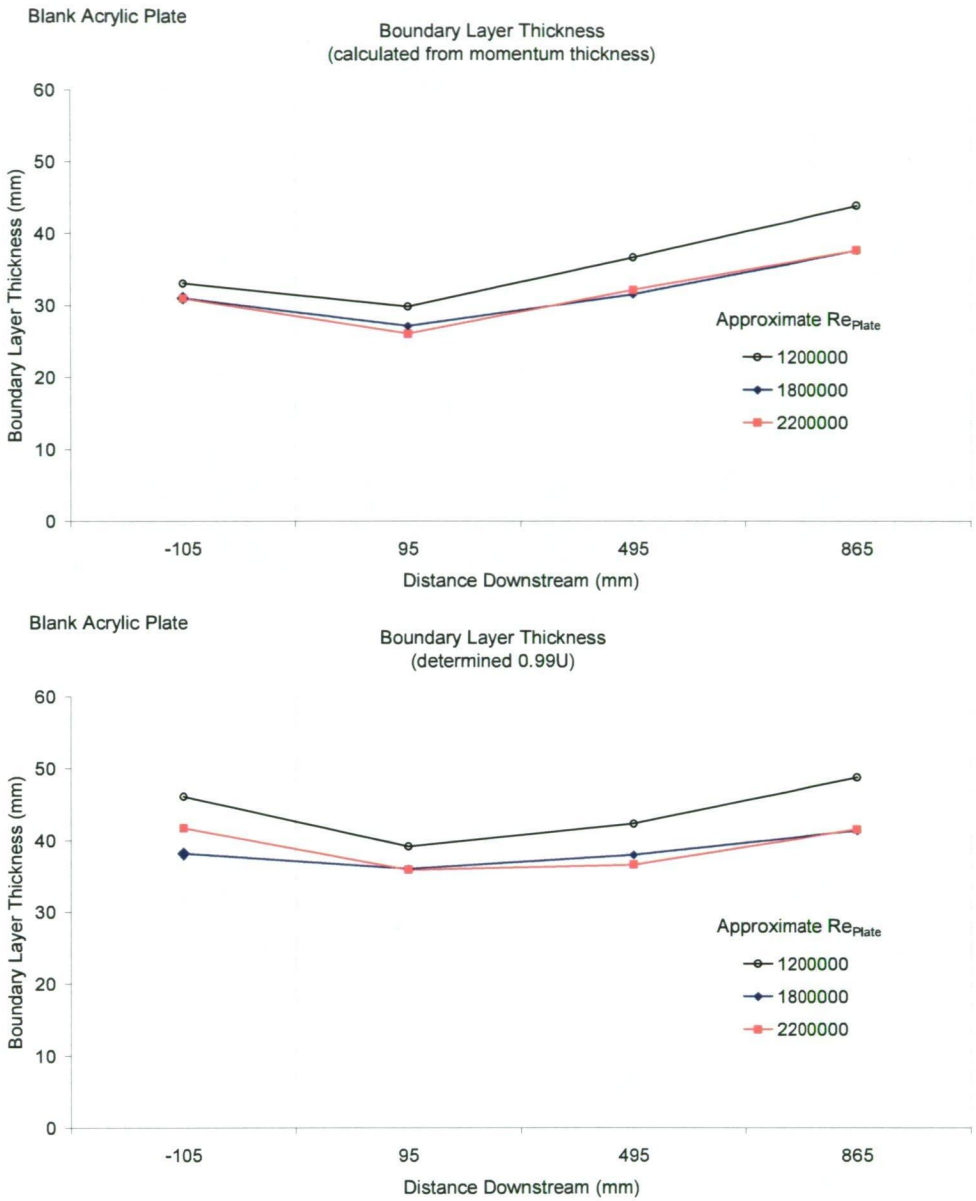

Figure 6.46: Plot of boundary layer thickness for the acrylic calibration plate.

To determine the wall local skin friction coefficients (Figure 6.47), the wall friction velocity was determined using the Preston tube correlation of the form described by Equation 6.9, from Patel (1965) using the apparent dynamic pressure ΔP_p indicated with the Pitot probe against the wall.

$$\frac{\tau_0 d^2}{4\rho\upsilon^2} = F\left(\frac{\Delta p_p d^2}{4\rho\upsilon^2}\right) \qquad \text{Equation 6.9}$$

The local skin friction coefficient was calculated by using Equation 6.10 (see Schlichting, 1979) where c_f is the local skin friction coefficient, and τ_0 is the wall shear stress.

$$c_f = \frac{\tau_0}{\frac{1}{2}\rho U^2} \qquad \text{Equation 6.10}$$

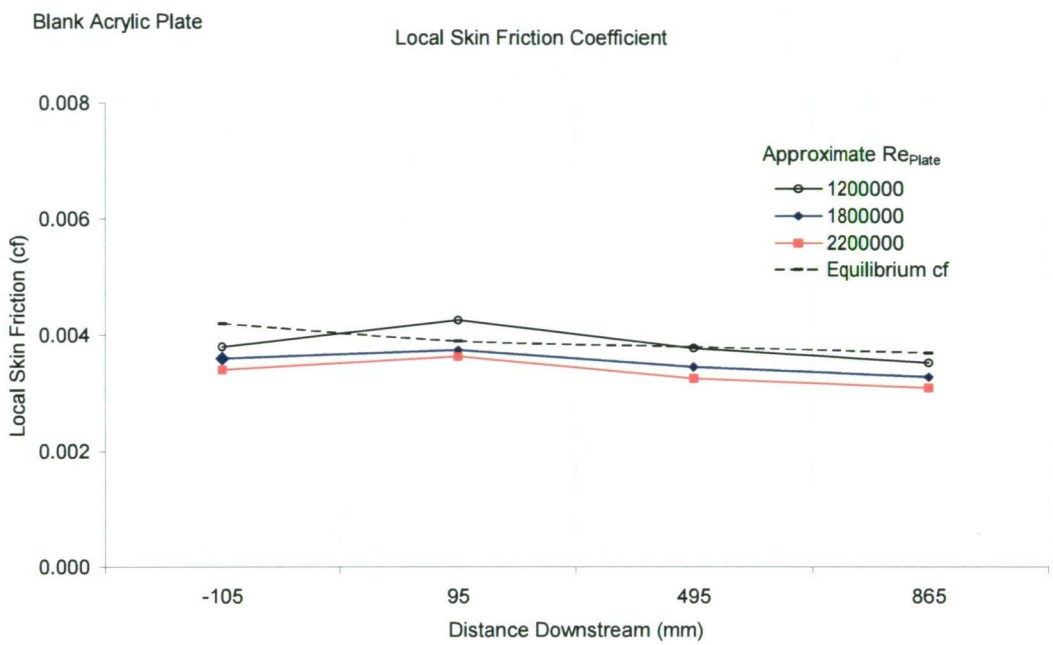

Figure 6.47: Plot of local skin friction values for the acrylic calibration plate.

Wall shear velocity was determined from Equation 6.11.

$$u^* = \sqrt{\frac{\tau_0}{\rho}} \qquad \text{Equation 6.11}$$

Figure 6.48 shows the wall shear velocity at a distance upstream, and distances downstream from the leading edge of the test plate. For comparison, wall shear velocities of Hydro Tasmania assets from Table 6.1 are are also shown. Values for equilibrium conditions are presented for comparison based on the skin friction values in Figure 6.47 for $\mathrm{Re}_{Plate} = 2.2 \times 10^6$.

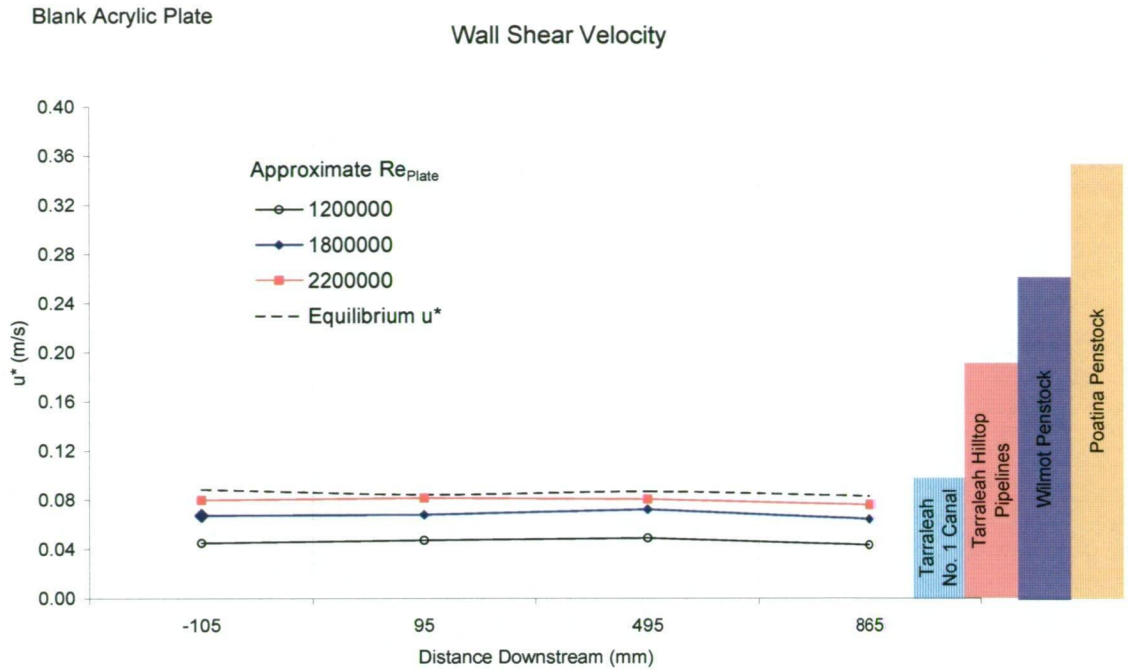

Figure 6.48: Plot of wall shear velocity measured for the acrylic calibration plate.

The wall shear velocities shown in Figure 6.48 are in a useful region when compared to the Hydro Tasmania conduits. It was established in Chapter 3 that the transitional hydraulic roughness regime is of particular interest. This is where the wall shear velocities for the smooth acrylic plate lay in comparison to the field assets. Rough plate measurements presented in Chapter 8 show wall shear velocities at higher levels.

To give an indication of the size of the Pitot tube used in relation to the boundary layer measured, $\frac{d}{\delta} = 0.027$ and , $\frac{u^* d}{\nu} = 0.185$ where d is the Pitot tube outside diameter of 1 mm. δ and u^* are taken from x = 865mm measurements at $\mathrm{Re}_{Plate} = 2.2 \times 10^6$ (U = 1.93 m/s) from Table 6.3.

6.4.5.3 Turbulence Profiles

Turbulence measurements were made in the water tunnel using a hotfilm probe. The correlation of Collis and Williams (1959) was used to relate the Nusselt number, Nu, to the probe film Reynolds number, $\mathrm{Re}_{film} = \frac{ud}{\nu}$ (film diameter for the 1218-20W probe is

$d = 50.8\mu m$). A correlation of this type was necessary to account for the water temperature variations in the water tunnel.

The Nusselt number is described by Equation 6.12, where h is the heat transfer coefficient (Equation 6.13), and k_{water} is the thermal conductivity (W/m.K) of the water at temperature T_m. The film length, l, for the 1218-20W probe used was 1.02 mm. $\Delta T = T_m - T_a$, where it is assumed that $T_m = \frac{T_{film} - T_a}{2}$. T_{film} is the probe film operating temperature nominally around 60-65 °C. T_a is the ambient water temperature.

$$Nu = \frac{hd}{k_{water}} \qquad \text{Equation 6.12}$$

$$h = \frac{Q}{\pi l d \Delta T} \qquad \text{Equation 6.13}$$

Q in Equation 6.13 is the heat input to the film (Watts) and can be described by Equation 6.14.

$$Q = \frac{E^2 R_P}{R_P + R_{ca}} \qquad \text{Equation 6.14}$$

E is the bridge voltage, R_P is the probe operating resistance and R_{ca} is the cable resistance, 0.28 Ω in this case.

Ultimately, Nu can be expressed as Equation 6.15.

$$Nu = \frac{Q}{\pi l \Delta T k_{water}} \qquad \text{Equation 6.15}$$

A typical calibration plot is given in Figure 6.49, with the regression equation described by Equation 6.16 where the exponent, *n*, was taken as 0.51. The calibration was completed by positioning the probe at the working section vertical centreline, and measuring the probe voltage at steps in flow speed. The working section contraction

was used as the reference velocity. Collis and Williams (1959) provides a correlation for Re_{film} up to 140. Re_{film} values for the present study typically ranged from approximately 100 to over 300. A two stage curve of best fit was used to provide a more accurate correlation above $\mathrm{Re}_{film} = 140$ (Figure 6.49).

$$Nu\left(\frac{T_m}{T_a}\right)^{-0.17} = A + B\,\mathrm{Re}_{film}^{n} \qquad \text{Equation 6.16}$$

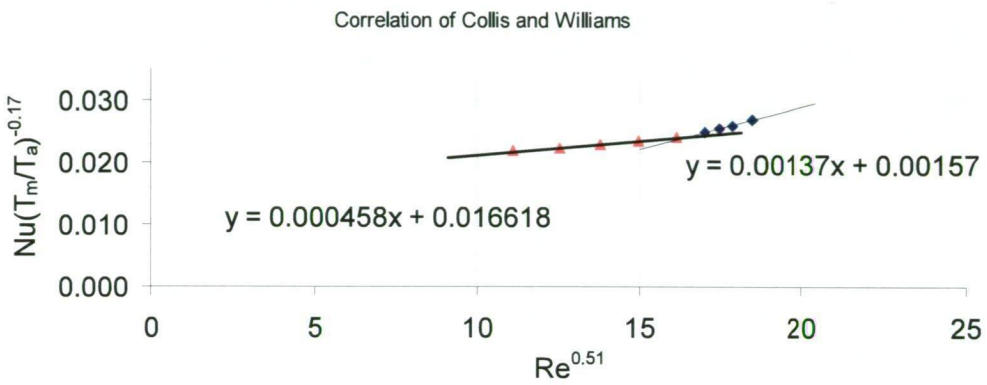

Figure 6.49: Correlation of hotfilm probe.

Because u_{RMS} sensitivity is relatively constant over a range of bridge voltages, the slope of curve, $\frac{dE}{du}$, fitted to the data in Figure 6.49 allows the determination of the RMS velocity, described as $u_{RMS} = \frac{V'_{RMS}}{\frac{dE}{du}}$. Electrical noise is subtracted from the measured values, which is described by $V'_{RMS} = \sqrt{V_{RMS}^2 - V_{RMS0}^2}$, where V_{RMS0} is the measured RMS volts at zero flow.

Turbulence intensity was determined using Equation 6.18. Here, $U_{Contraction}$ is the mean flow velocity at the entrance to the working section, derived from the contraction pressure differential.

$$Tu(\%) = \left(\frac{u_{RMS}}{U_{Contraction}}\right) \times 100 \qquad \text{Equation 6.18}$$

Figure 6.50 show the turbulence intensities for the acrylic plate. To compare results, the turbulence data of Klebanoff (1955) for smooth plates are also plotted on the Figures.

Boundary layer traverses were completed whereby the probe was positioned at the working section vertical centreline, and then traversed toward the boundary. At the end of the traverse, the hotfilm probe was brought back to the centreline and remeasured to check for voltage drift due to changes in water temperature and also the state of probe fouling.

The probe film sensor is 12.7 mm upstream of the probe stem centreline, making the measurements 102.3, 502.3, and 872.3 mm downstream of the leading edge of the test plate at plugs 1, 2 and 3 respectively.

Probe dimensions and support arrangement precluded turbulence measurements at the upstream plug to check the state of boundary layer turbulence before flowing over the leading edge gap of the test plate. Figure 6.50 presents the turbulence intensities measured at plugs 1, 2 and 3 downstream of the leading edge of the test plate. Data were acquired using LabView software at 10,000 Hz, for a 35 second sample time.

Results from the hot film measurements are inconclusive, as Figure 6.50 show a much higher bulk flow turbulence intensity compared with typical smooth plate turbulence data of Klelanoff (1955). The edge of the boundary layer is not clear from these measurements.

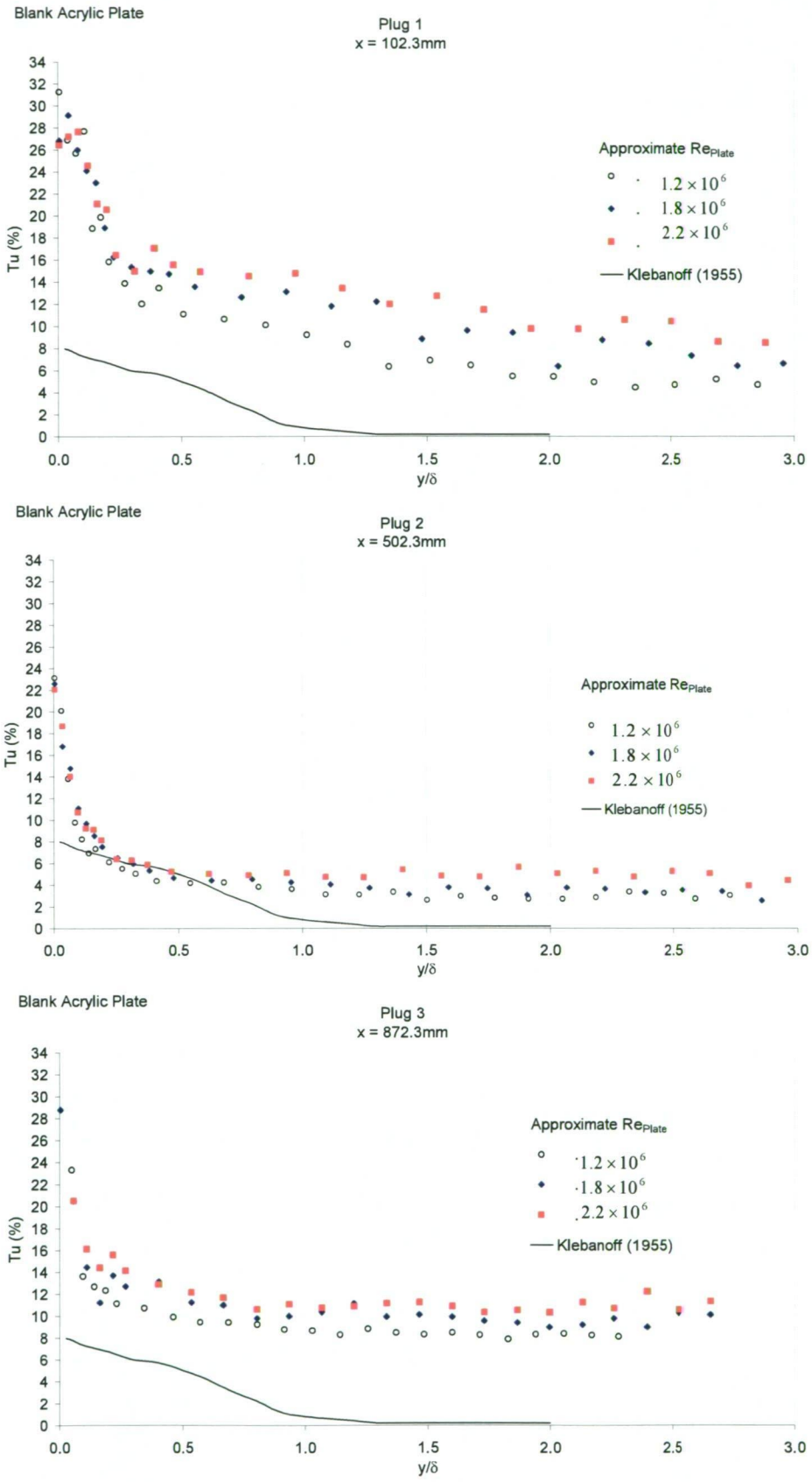

Figure 6.50: Turbulence intensities along the acrylic test plate using hotfilm probe.

There were significant drift problems encountered with the hot film probe and uncertainty in *Tu* (%) is estimated to be large due to probe fouling which could not be adequately corrected for. Richardson and McQuivey (1968) and Bradshaw (1971) both discuss the considerable difficulties with turbulence measurements in water using hotfilm probes, both stating that only demineralised and de-aerated water can be seriously considered as suitable for hotfilm anemometry. Others advise not using hotfilm probes and CTA for turbulence measurements (Chanson, 2006), given the availability of other technologies such as acoustic doppler or laser doppler velocimetry, and particle image velocimetry.

An alternative was sought to the hotfilm anemometry which was more robust and less prone to fouling problems. The Validyne transducers (described in section 6.3.1) have a frequency response of up to 1000 Hz, and so one was used to complete unsteady pressure measurements in the boundary layer to see if turbulence information could be obtained more reliably than the hotfilm probe.

Figure 6.51 shows the turbulence intensities measured at plugs 1, 2 and 3 using the Pitot probe shown in Figure 6.18. It was recognised that the frequency response from such a probe is far less than CTA methods, and so to improve measurements response special steps were taken. The most important was to reduce the viscous damping effects as much as possible by connecting the pressure probe as close as possible to the transducer. A 50mm piece of tubing was used to provide a distance from the probe tip to transducer diaphragm of approximately 470mm. This was the minimum distance achievable. The other side of the transducer was connected directly to the static pressure wall tapping, but the tubing was several times longer to maintain high levels of viscous damping to provide a relatively constant reference pressure.

Turbulence intensities were derived in the same manner as outlined above for the hotfilm probe, using the RMS of the velocity fluctuations, where the electrical noise (measurement at zero flow) was subtracted from the measured values. The contraction velocity was taken as the reference velocity in the same way as described above.

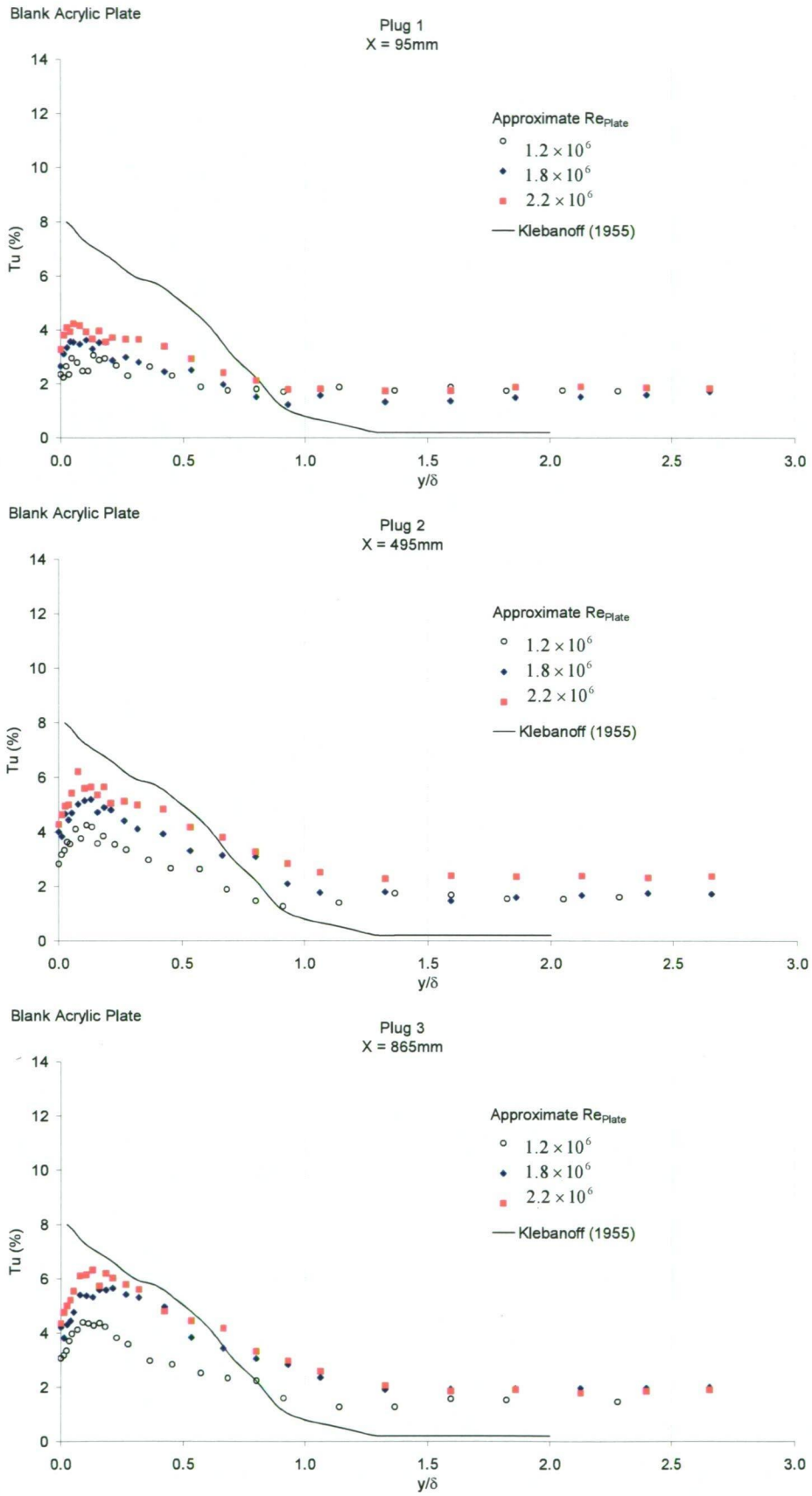

Figure 6.51: Turbulence intensities along the acrylic test plate using Pitot probe.

Results shown in Figure 6.51 indicate a bulk flow free stream turbulence of between 1.5% and 2.5 %. This is much more reasonable than that indicated in Figure 6.50, and is more in line with what could be expected from the character of the flow conditioner, and a contraction ratio of 3:1.

Turbulence intensities near the wall region are least upstream near the leading edge of the test plate, and increase with distance downstream. This is consistent with the thickening of the turbulent boundary layer resulting in a reduction in the frequency of the velocity fluctuations. The edge of the boundary layer is also much more distinguishable.

Figure 6.52 shows sample data traces for 10 second of data taken at 1000 Hz, with the probe tip against the wall (0 mm from the wall), at 5mm from the wall (within boundary layer) and at 100 mm from wall (within the bulk flow). These data are from plug 3, measured at approximately $\mathrm{Re}_{Plate} = 2.2\times10^{6}$.

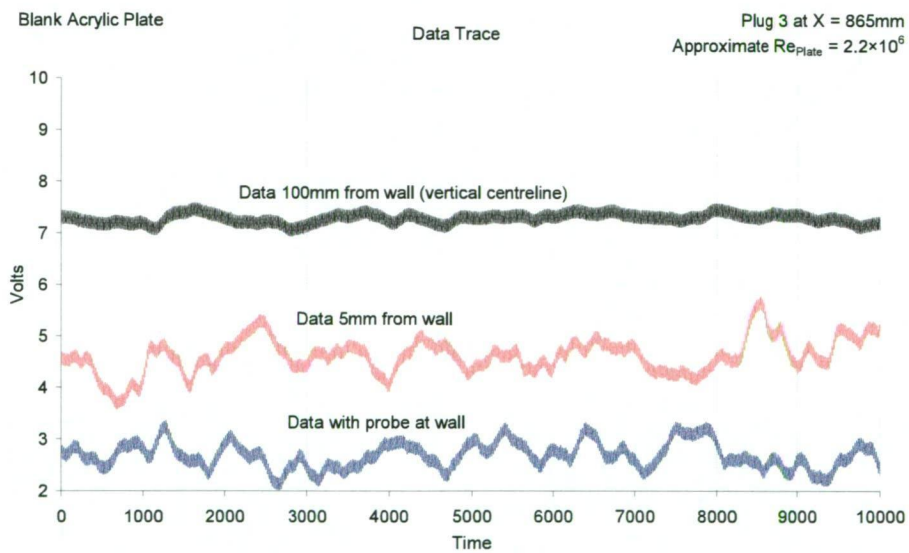

Figure 6.52: 10 seconds data traces of unsteady pressures.

Fast Fourier Transforms were used to determine the frequency response characteristics of the Pitot probe and pressure transducer combination. Figure 6.53 shows a plot of the signal spectra. The spike in signal frequency at 50 Hz indicates electrical interference from the power supply. It is important to note no other spikes in the signal, indicating

for example, no probe vibration, particularly when the probe is most exposed in the flow when measuring in the boundary layer region.

A useful frequency response of up to 30 Hz is shown in Figure 6.53, with no sudden reductions or drop-offs. This makes the use of the Pitot probe and pressure transducer acceptable for basic one dimensional streamwise turbulence measurements, of low frequency, in the working section.

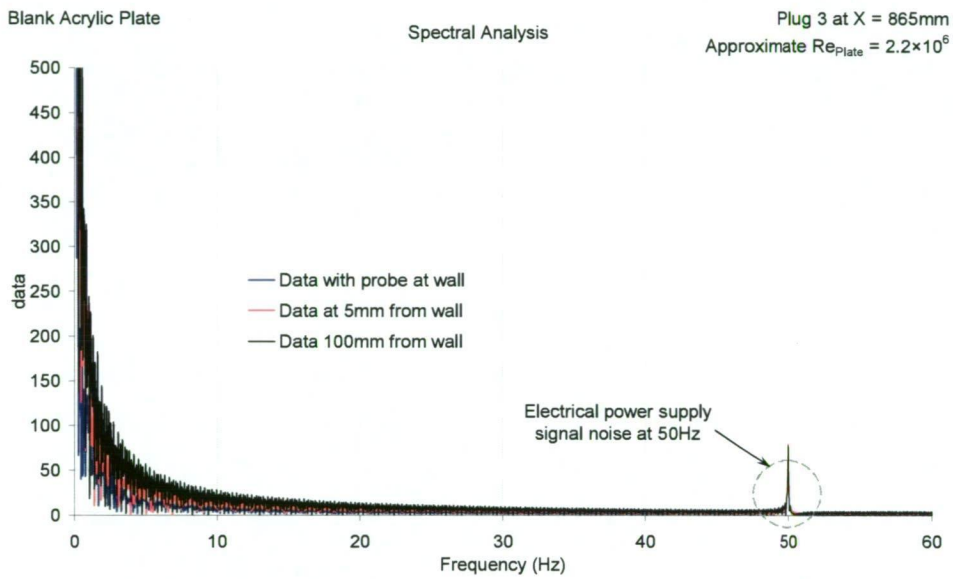

Figure 6.53: Spectral analysis of data trace showing distribution of frequencies.

A further improvement to what has been used in this study would be an adaptation of the relatively low cost fast response pressure probe, successfully developed by Brandner, Clarke *et al.* (2004) for use in a cavitation tunnel. This probe has an outside diameter of 1mm and useful frequency response up to 2.5 kHz. This type of probe is more robust, and less sensitive to fouling than hotfilm probes, and is considered a more appropriate technology for unsteady pressure measurements in a water tunnel where large amount of fouling material are contained in the recirculating water.

6.4.6 Total Drag Measurements

6.4.6.1 Drag Measurement Corrections

Total drag measurements on the test plate were conducted at intervals in pump speed and associated plate Reynolds numbers. The total drag force on the plate was measured as a voltage output from the strain gauge signal conditioner and acquired by computer using the LabView software as described in section 6.3.2. The voltage was then converted to a force (N) using bench top calibration data.

In order to determine an accurate total drag coefficient (due to friction), C_D, on the plate, and to satisfy the problems listed by Winter (1977), it was important in the first instance to correctly align the plate in the water tunnel. The test plate dimensions allowed for a design gap of 1.5 mm on each side of the plate in the working section. The actual gap varied from 1 mm to 2 mm on the various edges of the plate.

Temperature effects were found to significant influence drag measurements. Zero drift occurred due to the different rates of thermal expansion and contraction of the test plate (stainless steel or acrylic), test plate support (acrylic) and working section lid (acrylic) as the ambient air and water temperatures varied over the course of measurements. This was overcome by simply measuring zero drag (i.e. no flow) with each drag measurement. The zero drag was then subtracted from the measured drag to remove any drift problem.

Various corrections were applied to the raw data. The first correction subtracted the net pressure force on the ends of the plate arising from the longitudinal flow acceleration due to wall boundary layer growth through the working section. This was accomplished by measuring the pressure difference between the ends of the plate (using static wall tappings) and multiplying this pressure across the end cross sectional area. For the acrylic test plate used in this chapter these dimensions were 597 mm by 5 mm (0.002985 m^2). For the stainless steel plates the end section was 597 mm by 3 mm (0.001791 m^2). The typical force correction was around 0.3 N, contributing a maximum of approximately 10% of measured drag for low-drag smooth plates and approximately 2.5% of measured drag for biofouled rough plates.

The drag coefficients of a flat plate of width b and length l in a stream of velocity U and density ρ is defined by Equation 6.19 (Schlichting, 1979).

$$Drag_{(Plate)} = C_{D_{Plate}} \rho b l_{Plate} \frac{U^2}{2}$$ Equation 6.19

To compare the present results for plate drag with theoretical models for an isolated plate it is first necessary to allow for the initial non-zero boundary layer thickness at the leading edge of that test plate.

This is done by estimating a virtual origin at distance l_1 upstream from which a continuously turbulent boundary layer on an isolated plate would produce the same initial boundary layer thickness. Figure 6.54 shows the concept of the virtual origin of the turbulent boundary layer, and the definitions for Equations 6.19, 620 and 6.21.

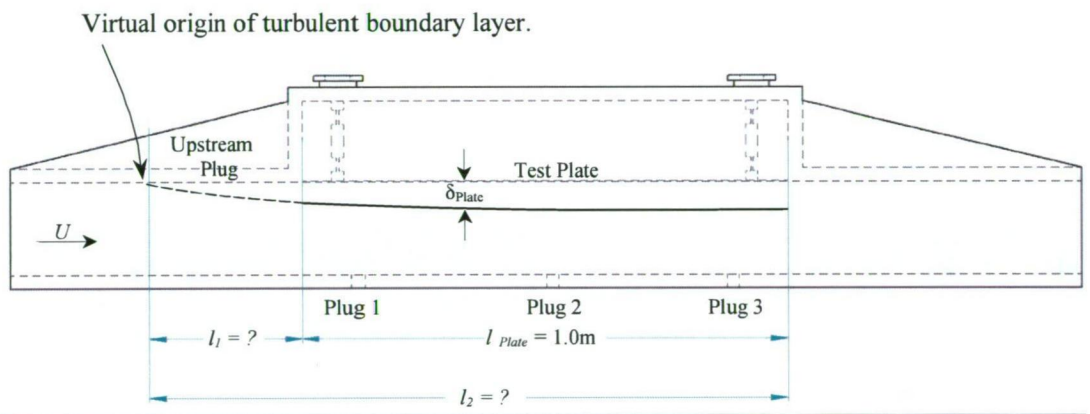

Figure 6.54: Assumed boundary layer development over the test plate.

For a smooth flat plate, with the known boundary layer thickness at plug 1, 2 and 3, the value of l_1 was found by using Equations 6.20 and 6.21 (Schlichting, 1979) based on the $\frac{1}{7}^{th}$ power law for the turbulent boundary layer velocity distribution.

$$l_1 = \frac{\delta \mathrm{Re}_{l_1}^{0.167}}{0.22}$$ Equation 6.20

Note that δ was derived from the momentum thickness. Equation 6.21 can be applied for hydraulically smooth conditions.

$$C_D = \frac{0.074}{\mathrm{Re}_l^{\frac{1}{5}}}$$ Equation 6.21

$\mathrm{Re}_l = \frac{\rho U l}{\mu}$ is the Reynolds number based on the length of l. Typical values of Re_{l_1} for the acrylic plates used for this chapter ranged from 8.3×10^5 to 3.2×10^6 for $l_1 = 1.39m$.

The theoretical drag for the test plate is then obtained from Equation 6.22.

$$Drag_{(Plate)} = C_{D(l_2)}\rho b l_2 \frac{U^2}{2} - C_{D(l_1)}\rho b l_1 \frac{U^2}{2}$$ Equation 6.22

6.4.6.2 Drag Measurements for Smooth Acrylic Plates

Two acrylic plates were used, one with bolts and one with no bolts. This was to check on the influence (if any) on the drag from flow perturbations caused by the bolts, which attached the various test plates to the acrylic support plate. Figure 6.55 shows the bolt arrangement used on every test plate used in the water tunnel. Bolts were counter sunk to create a flush finish. However, the bolts had hexagonal indentations for hex key (Allen key) tightening. The bolt head diameter was 12mm.

The acrylic plate with no bolts (shown in this chapter only) simply had the acrylic plate permanently glued onto a spare acrylic support plate rather than bolted, resulting in a continuously smooth surface.

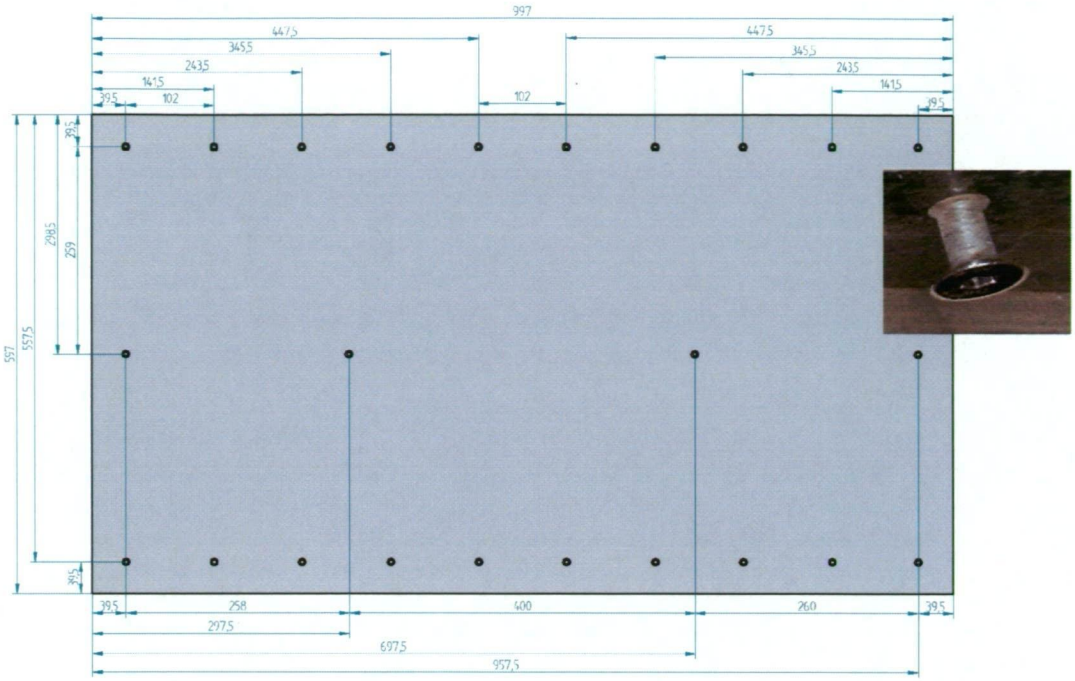

Figure 6.55: Bolt layout for the test plates used on the water tunnel. Distances are shown in mm. Inset is a photo of the bolt heads used.

Results of the drag measurements are shown in Figure 6.56. The theoretical drag calculated using the principles outlined in section 6.4.6.1 is also shown in this Figure.

The results from Figure 6.56 show the test data displaying a similar trend of decreasing drag coefficients with increasing Reynolds number. However, the measured drag is approximately 16% greater than that predicted by the above theoretical model. The difference may be partly explained by the increase in skin friction due to the boundary layer bleed through the clearance at the upstream end of the test plate.

A comparison of c_f values from Figure 6.47 with the drag coefficients show similar values, with the same trend of decreasing friction with distance downstream. Local c_f values from Figure 6.47 show an increase at x=95mm as suggested above due to the flow leakage into the roof cavity and subsequent thinning of the boundary layer at the leading edge.

The bolts do not seem to make a significant contribution to the drag compared to the plate with no bolts.

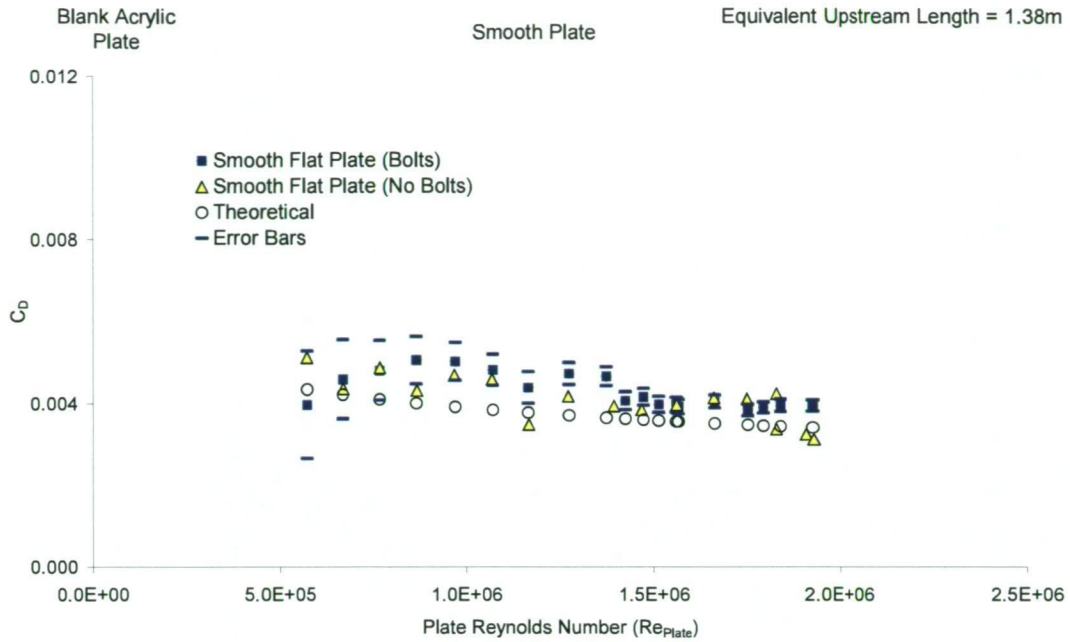

Figure 6.56: Plot showing coefficients of drag versus plate Reynolds number.

An estimate of error in the measured drag was made using the RMS of the deviations of the calibration curves in Figure 6.17 and 6.25 for pressure and drag respectively. An error in voltage at these RMS values was propagated though the data reduction procedure, and an uncertainty of ±2.7% in C_D was found. However, more realistically, errors in plate alignment and the spacing of gaps around the plate affected the measured drag greater than the accuracy of the instrumentation used.

A repeatability test was performed using the acrylic test plate to better find the typical deviation of measured drag from the mean. To do this, drag measurements were made 10 times at three flow Reynolds numbers (30 drag measurements in total). Small changes in the plate alignment were made by randomly varying the gap widths around the edge of the plate. The RMS of the deviations was found to be ±0.0108 volts (Figure 6.57), which is considerably larger than the ±0.0020 volts of the calibration curve in Figure 6.25. This implies greater uncertainty with reducing flow velocity and Reynolds numbers. This also explains the greater variability in C_D at lower Reynolds numbers for drag measurements presented throughout this thesis. Error bars are displayed for Smooth Flat Plate (Bolts) on Figure 6.56 showing the uncertainty in C_D.

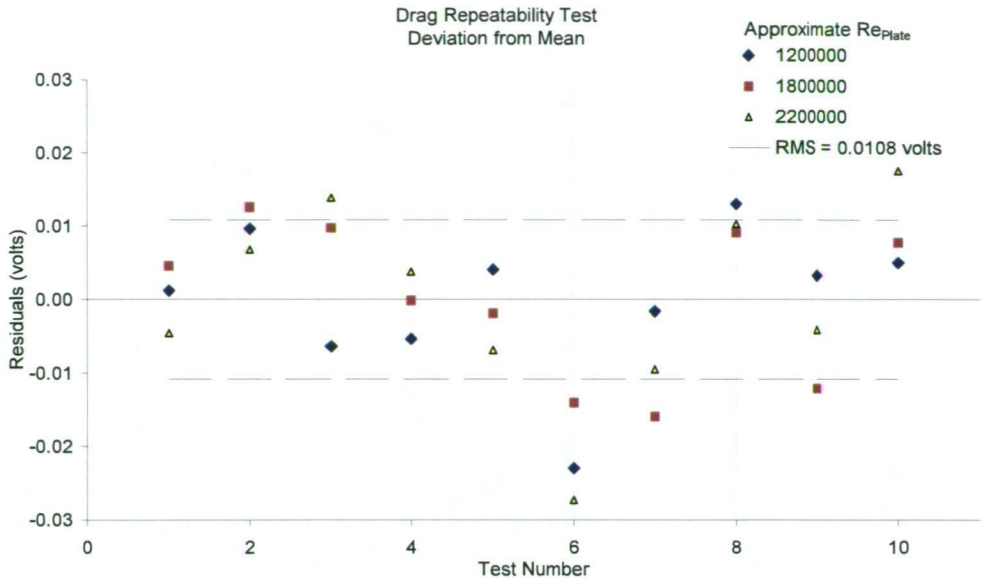

Figure 6.57: Results for the repeatability test for the drag rig.

6.5 Chapter Summary

Baseline conditions have been established for the water tunnel, setting the scene for subsequent results presented in Chapters 7 and 8.

Flow conditions within the working section and water tunnel generally are matching the design aims, and display good flow distribution characteristics.

It is noted that secondary flows in the water tunnel may be producing a slightly non-uniform velocity distribution in the vertical direction.

Edge effects were found to be present due to longitudinal corner vortices and the movement of water between the edges of the test plate and the roof cavity in the working section. However, these are confined to regions within 50mm of the sidewall and a good understanding of these effects has allowed appropriate consideration to be made with regard to the treatment of results.

Boundary layer measurements clearly show a developing mean velocity profile, which is interrupted at the leading edge of the test plate due to the gap required for total drag

measurements. Both the log law and the $1/7^{th}$ power law approximate the velocity distribution.

Results show that equilibrium conditions are not reached in the working section, though results are tending toward this condition.

The wall shear velocities are within a useful range for results to be directly applicable to field hydraulic conduits such as those in the Hydro Tasmania hydro power system. This is important for the application of results from biofouled test plates presented later in this thesis.

Due to problems with probe fouling and significant temperature drift, hotfilm anemometry was abandoned in favour of unsteady pressure measurements using a Pitot probe. These measurements proved more reliable and consistent than the hotfilm probe. A bulk flow turbulence intensity of between 1.5% and 2.5% was recorded for the working section.

Total drag measurements, while not exactly replicating theoretical values, are displaying the general characteristics required to gain useful information. The drag measurements are affected by the leakage of flow into the roof cavity at the leading edge of the test plate, which reduces the boundary layer thickness, and increases the skin friction at the front section of the plate.

This chapter has shown that the purpose built water tunnel is a useful instrument for measuring the boundary layer characteristics, drag and roughness of biofilms found in hydraulic conduits. Chapters 7 and 8 present results conducted in the water tunnel for biofouled smooth and rough test plates.

Chapter 7 Boundary Layer, Drag and Roughness Measurements for Clean and Fouled Smooth Plates

7.1 Introduction

This chapter provides results of boundary layer and drag measurements for smooth painted plates conducted in the water tunnel described in Chapter 6. The plates were smooth, coated with Jotun brand Jotamastic 87 two-pack paint. This surface coating was discussed previously in Chapter 4. Roughness information is also presented from close range photogrammetry of the fouled test plates. These data are compared to examine the relationship between measured and physical roughness.

A description of the fouled plates is given first. Because biofouling is so variable, it is important to show the general character of the biofilm.

Boundary layer measurements are then shown with data from the mean velocity profiles presented. Finally total drag characteristics of each plate are presented.

Results of roughness characterisation for the fouled surface are presented using the photogrammetric techniques outlined in Chapter 5. Roughness characterisation of biofilms in the past has not been overly sophisticated due to the complex nature and variability of biofilms. This results presented in this chapter are significant development over past efforts. Standard roughness and statistical information is provided along with mean biofilm thicknesses, and qualitative information.

A summary then completes the chapter..

7.2 Description of Fouled Plates

All smooth painted plates used the same spray painting method. A clean plate was used as a control and kept in the laboratory. Clean plate results are from this plate. The other two plates were deployed in the field for biofouling. The first plate studied is denoted smooth plate fouling 1 and was deployed for approximately 4 months in Tarraleah Pond No. 1. Figure 7.1 shows a photo of this biofouled plate.

Growth of the biofilm (Figure 7.1) was very uneven. The growth was skewed toward the downstream and bottom half of the plate. Much of the growth seemed to be in poor condition, much of it dead or dying, confirmed from microscopic analysis by Perkins and Hallegraeff (2006). The condition of the biofilm is a reflection of the operating conditions of the canal during plate deployment, where Pond No.1 was often emptied exposing the plate to ambient air temperatures (discussed in chapter 4). Air temperature ranges were far greater than typical water temperatures, ranging from below 0°C to above 20°C in some instances. Chapter 4 showed that daily water temperature fluctuations were typically about 2°C. The biofilm was probably also dried out when exposed to air for extended periods.

The smooth plate was deployed upstream of the rough plate in the field installation (see Figure 4.6 in Chapter 4), which made the upstream edge a leading edge. The biofilm growth pattern suggests thicker growth proportionate with the distance downstream of the leading edge, most likely a consequence of boundary layer development over the plate. This is investigated further in section 7.5.

Figure 7.2 shows a side oblique view (with an approximate scale shown) of the plate submerged in the water tunnel working section with water flowing. Filaments were apparent on the downstream section of the plate to a length of 5mm to 20mm, though these laid flat against the plate when water was flowing. Some filaments were seen to lengthen over the course of testing. A line is drawn on Figure 7.1, which identifies the filamentous growth.

Figure 7.1: Smooth plate fouling 1 before testing in the water tunnel.

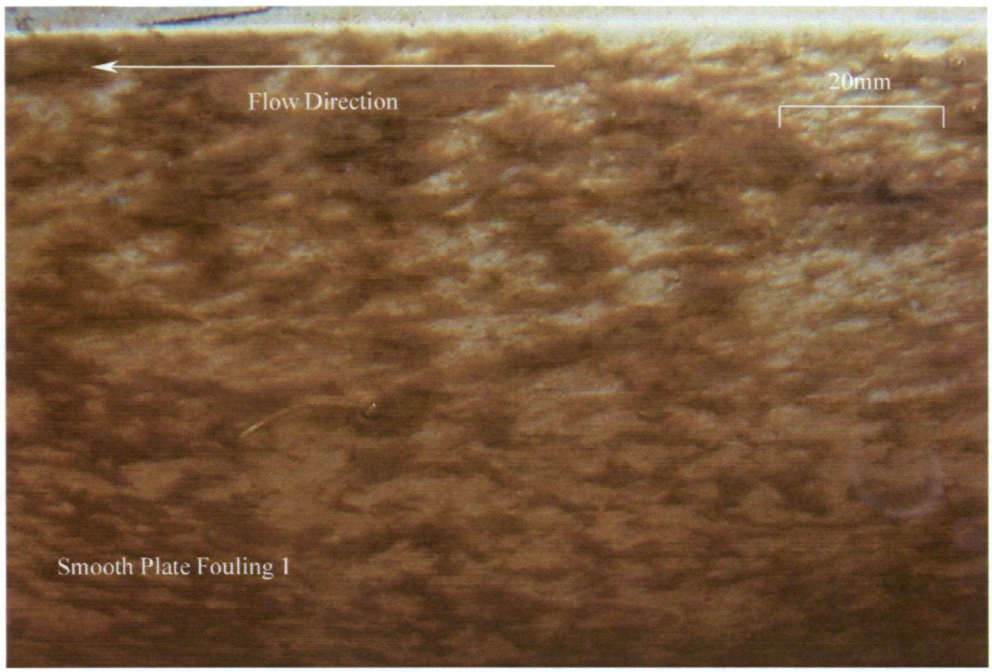

Figure 7.2: Photo showing the biofilm laying flat against the plate.

Figure 7.3 shows a view from underneath with water flowing in the water tunnel. Discrete patches of growth can be seen. Filament tails were attached to some of these patches.

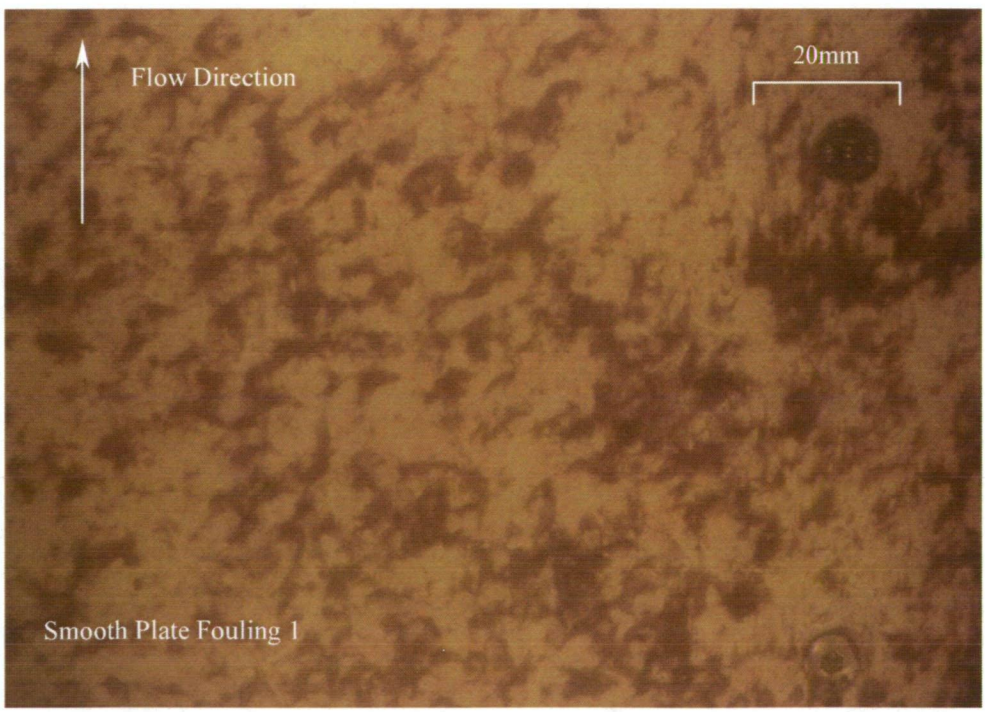

Figure 7.3: Photo from underneath.

The smooth plate fouling 1 was re-deployed to Pond No. 1 for a further 5 months. The plate was not cleaned after testing, simply reattached to its support plate and re-deployed to the canal wall. The existing growth on the plate changed over time, with some washed off, and new growth taking the place of the older growth as part of natural processes. This new biofilm growth after the additional 5 months of deployment was designated smooth plate fouling 2. The operation of Tarraleah No. 1 Canal returned to normal during this period, with the canal flowing full or near full, ensuring the plate was fully submerged at all times.

The smooth plate fouling 2 had an even coverage of growth, though there were still some areas near the leading edge corners with little growth. The biofouling was also different in texture compared to fouling 1, as it had more gelatinous growth than filamentous. Figure 7.4 shows the plate after being taken from the canal at Pond No. 1.

Section 7.5 looks at measuring the physical thickness of the biofouling on the smooth plates.

Figure 7.4: Photo of smooth plate fouling 2 prior to testing in the water tunnel.

Many small nodules of biofilm were observed, as shown in Figure 7.5. These ranged in size from approximately 2mm to 5mm in diameter, as shown by the scale rule in the Figure.

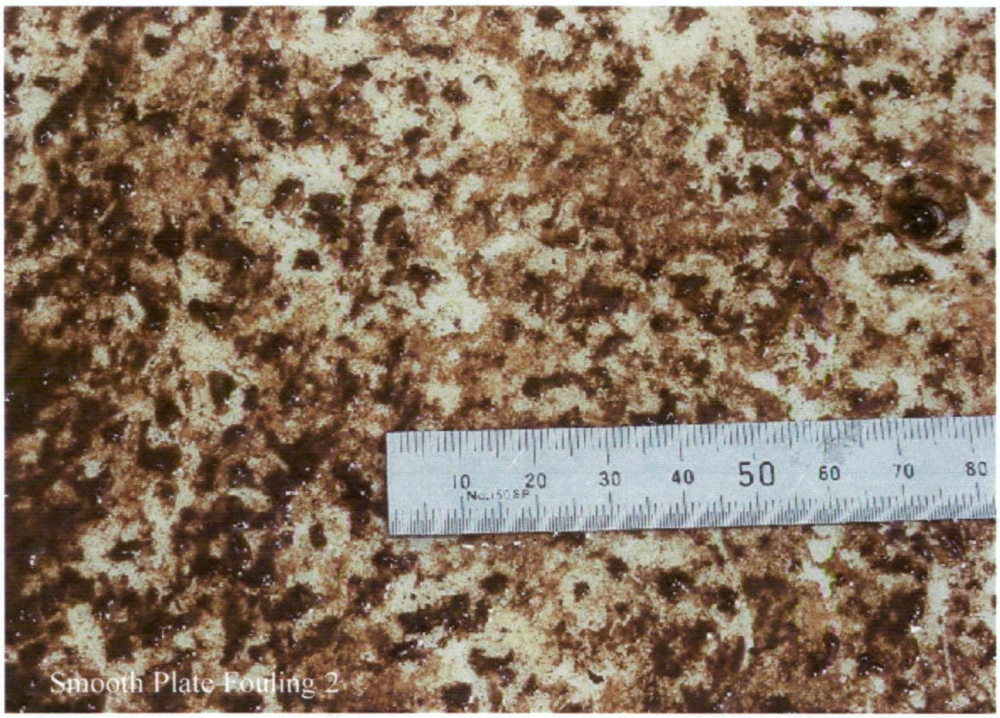

Figure 7.5: Close up of the gelatinous growths showing scale.

Small patches of translucent gelatinous biofilms were also observed (Figure 7.6). These growths were low form, compact and more rigid than the other type of growth depicted in Figure 7.5.

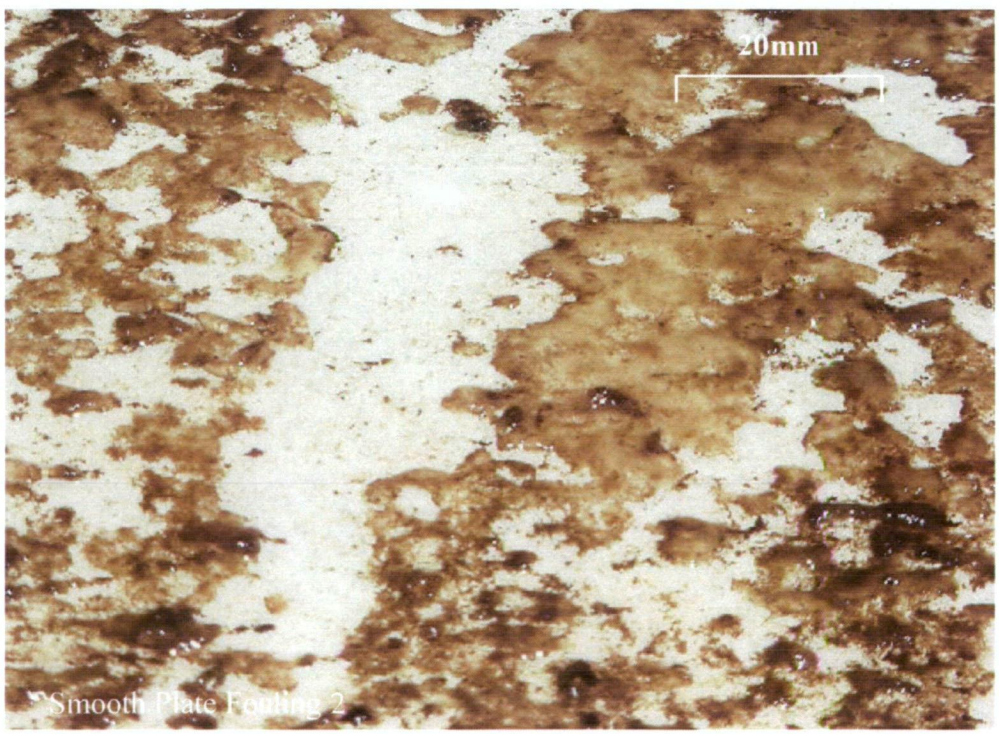

Figure 7.6: Close up of low form gelatinous growths.

Once smooth plate fouling 2 was submerged in the water tunnel, filaments were observed. The filaments were typically much shorter (approximately 2 – 5mm) than fouling 1. It is thought many of the filaments were "streamers," formed from Extra Polymeric Substances (EPS) or slime material. Figure 7.7 shows a section of biofouling in still water in the water tunnel. These filaments laid flat against the wall and fluttered about (in three dimensions) when water was flowing.

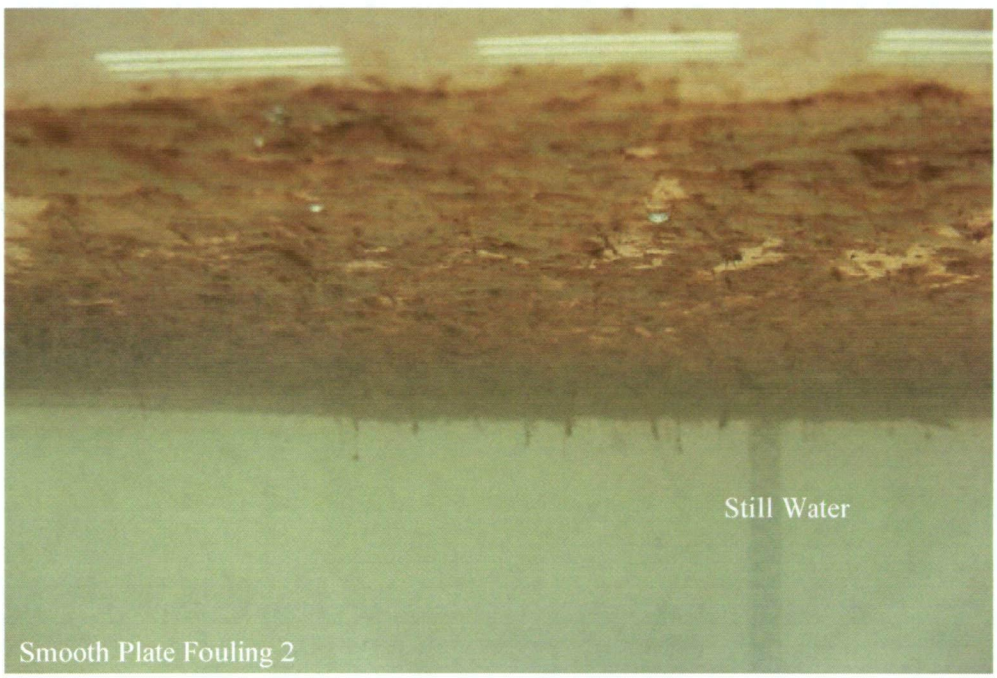

Figure 7.7: Photo of smooth plate filamentous growth in still water.

Invertebrates were abundant on smooth plate fouling 2 and could be seen wriggling vigorously for the first two days of testing in the water tunnel. Species were identified as Black fly larva, nymphs and mudeye (Barmuta, 2005). They were later either washed off or dead from environmental shock (e.g. temperature variations). It is a common defence mechanism of freshwater invertebrates to simply release themselves from the boundary surface and be washed away in the flow as an escape method. In nature, they would then reattach themselves at another more favourable location downstream. Figure 7.8 shows the most numerous invertebrate, black fly larvae. These are filter feeders, and attach by their head to the surface. They weave mucus threads across their tails, which they wave about in the flow in the hope of catching what passes by. In high flow velocities, their bodies lay flat, aligned with the flow, and there was little fluttering movement. They measured between 5mm and 10mm in length. These invertebrates

would have been present during the photogrammetry work, but not for the entire duration of water tunnel measurements.

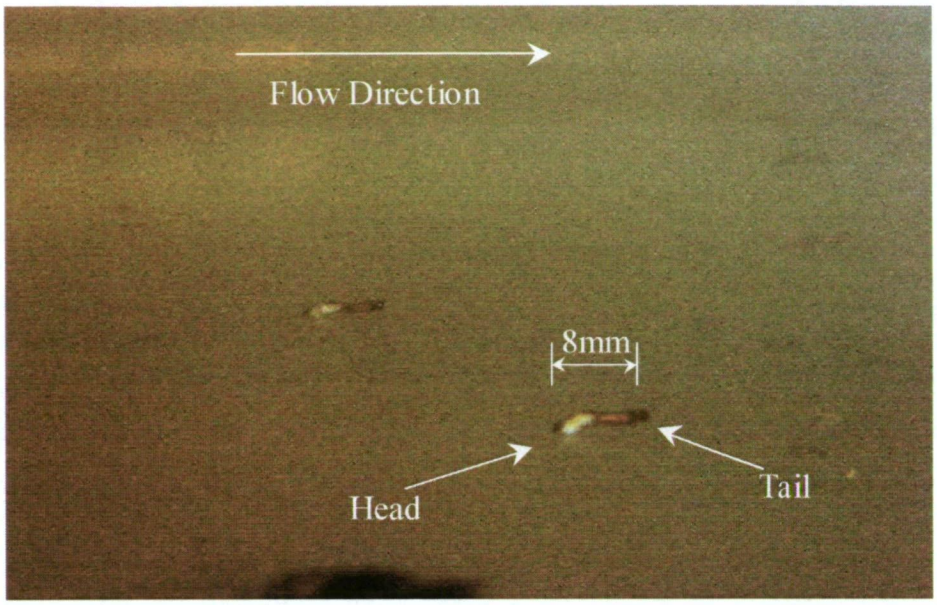

Figure 7.8: Black Fly Larvae attached to the wall in the water tunnel.

A general identification of the biofilm on the smooth plates fouling 1 and 2 was undertaken by Perkins and Hallegraeff (2006). Two types of diatom dominated the growths. They are Tabellaria type diatom and a Gomphonema stalked diatom shown in Figures 7.9 and 7.10 respectively. Figure 7.11 shows both types together.

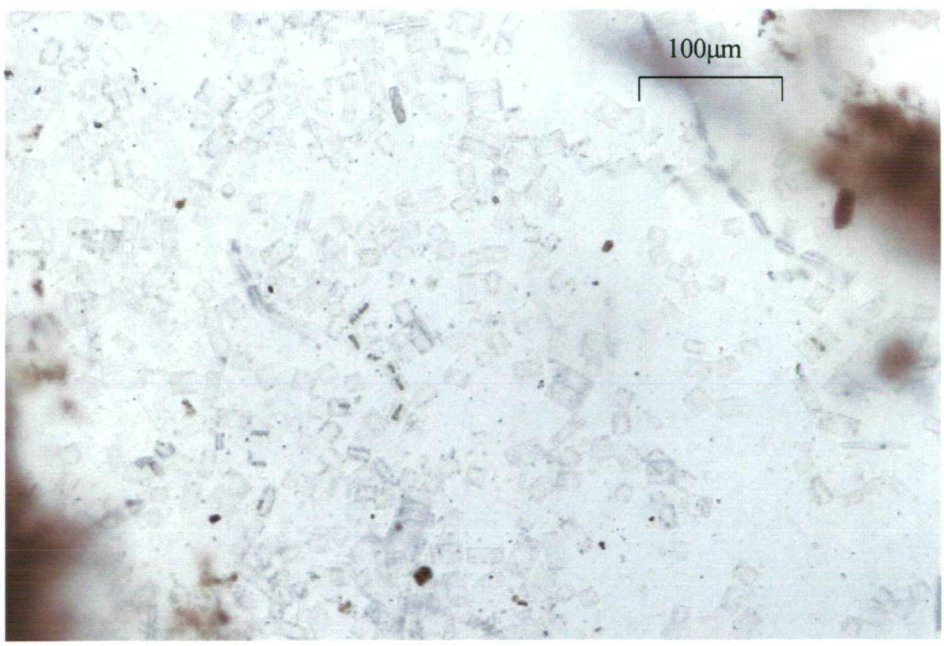

Figure 7.9: Tabellaria type diatom (photo by Perkins, 2006).

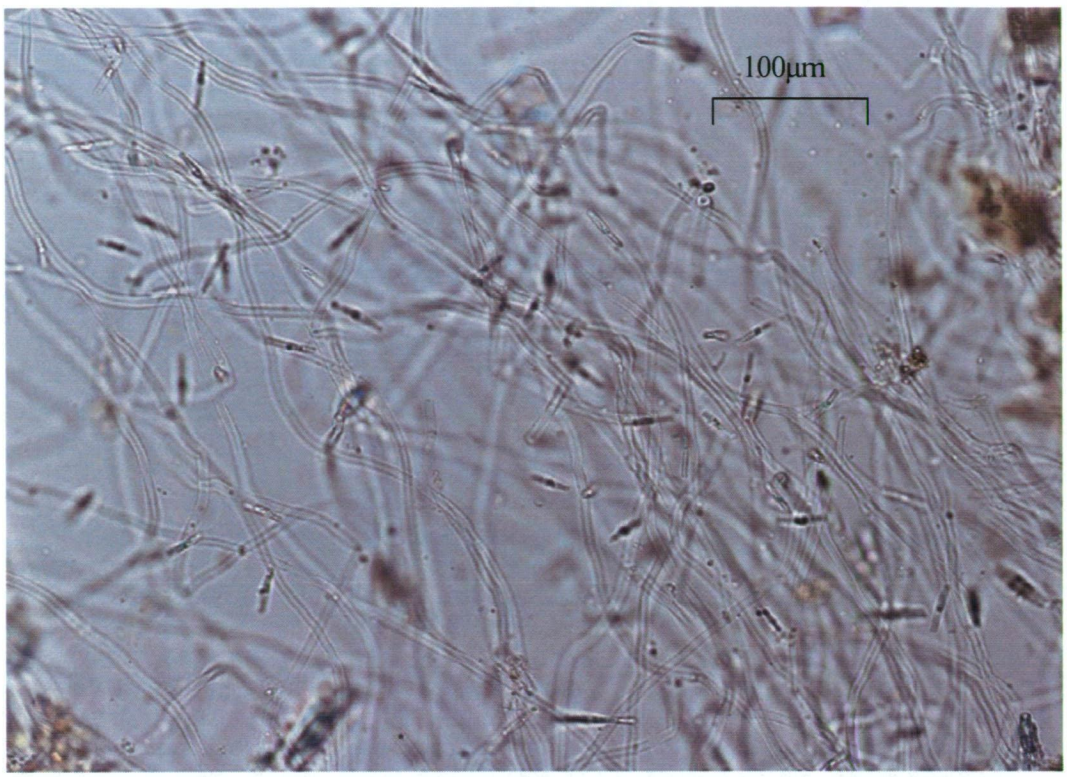

Figure 7.10: Gomphonema stalked diatoms (photo by Perkins, 2006).

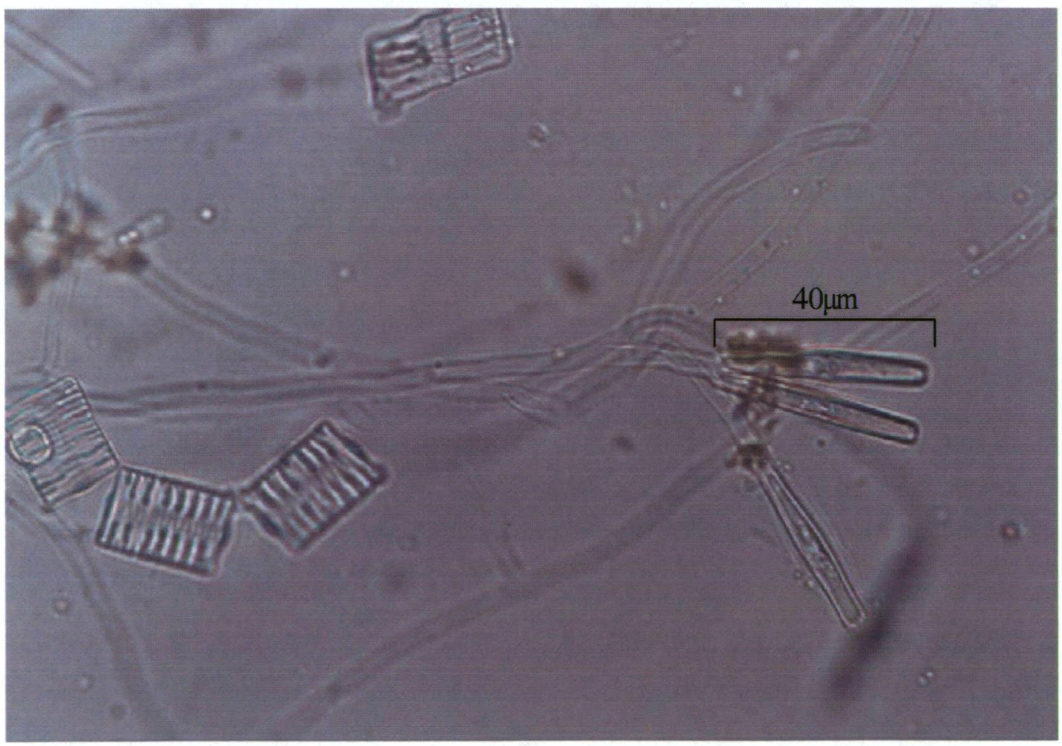

Figure 7.11: Tabellaria and Gomphonema type diatoms (photo by Perkins, 2006).

The Tabellaria type algae were more prevalent on smooth plate fouling 1. Both Gomphonema and Tabellaria were present on smooth plate fouling 2.

Tabellaria has weaker connections or bonds to the substrate than the Gomphonema and thus can survive only in the lower velocity conditions of Pond No. 1 (Perkins, 2006). The cells shown in Figure 7.9 (from smooth plate fouling 1) are all dead (no longer photosynthesising) and appear to have been so for some time (Perkins, 2006). This means that the nature of the mucous 'glue' (EPS) that bonds them to the plate may also have changed. It is therefore quite possible that water tunnel observations for smooth plate fouling 1 differ significantly from the typical behaviour in the field. Smooth plate fouling 2 is thought to be a better representation of what normally occurs.

7.3 Boundary Layer Characteristics

Measurements were taken from smooth plate clean, fouling 1 and fouling 2 in the water tunnel described in Chaper 6. Boundary layer traverses were made 95, 495, and 865mm downstream of the leading edge on the test plates, at three approximate Reynolds numbers of 1.2×10^6, 1.8×10^6, and 2.2×10^6 (based on the test plate length of 997mm).

The same methods used for the measurement of the acrylic plate in Chapter 6 were used for the measurement of the smooth plate clean, including the Preston tube method for the determination of u^*.

The fouled plate cases were treated as rough wall measurements, and a variation of Clauser's method (Clauser, 1954) called the log-law slope method was adopted to determine the wall shear stress. This method, used by Schultz (1998), and Candries (2001), involves plotting experimentally measured points of $\frac{u}{U}$ versus $\ln\left(\frac{yU}{\nu}\right)$ and fitting a linear curve of best fit. The slope of this regression line is then used to find the local skin friction coefficient, c_f, by using Equation 7.1

$$c_f = 2\kappa^2 (slope)^2 \qquad \text{Equation 7.1}$$

Here, κ is the von Karman constant (taken as 0.41), and "*slope*" is the slope of the regression line.

Using this method to find c_f allowed the determination of u^* by Equation 7.2, which is derived from Equations 6.10 and 6.11 in Chapter 6. U is the free stream velocity taken as the maximum measured velocity in the profile.

$$u^* = \frac{U}{\sqrt{\frac{2}{c_f}}} \qquad \text{Equation 7.2}$$

An issue with rough walls however, is the wall origin, $y = 0$. A wall origin error, ε, was therefore introduced to create a virtual origin, $y + \varepsilon = 0$, to better determine wall shear velocity, as the true wall origin is not known beforehand. In the present study, an adaptation of the method of Perry *et al.* (1963; 1969) and Schultz (1998) was used to determine ε.

The steps used to find ε were:

1. Plot data for $\frac{u}{u^*}$ versus $\ln\left(\frac{(y+\varepsilon)u^*}{\nu}\right)$.
2. Select inner and outer y cut-off values to ensure only log-law values are used.
3. Fit a linear curve to the log-law data region of the plot.
4. Adjust ε in small increments forcing a linear log-law region until a linear curve of best fit is reached.
5. Re-calculate u^*, using $\frac{u}{U}$ versus $\ln\left(\frac{(y+\varepsilon)U}{\nu}\right)$ and Equation 7.1 described above.
6. Adjust inner and outer cutoff values based on new $y + \varepsilon$.
7. Begin process again starting from step 4.

For the present study, a Microsoft Excel spreadsheet was used to iteratively find ε. Figure 7.12 shows an example of a log-law fit. The log-law data is shown and the y cut-off data indicated.

Inner and outer cut-off values were taken as $\frac{1.5\nu}{U}$ (inner cut-off) and between 10% and 15% of the boundary layer thickness, δ, (outer cut-off) as suggested by Schultz (1998) and commonly used elsewhere.

When the final ε value is found, the full range of boundary layer parameters are calculated.

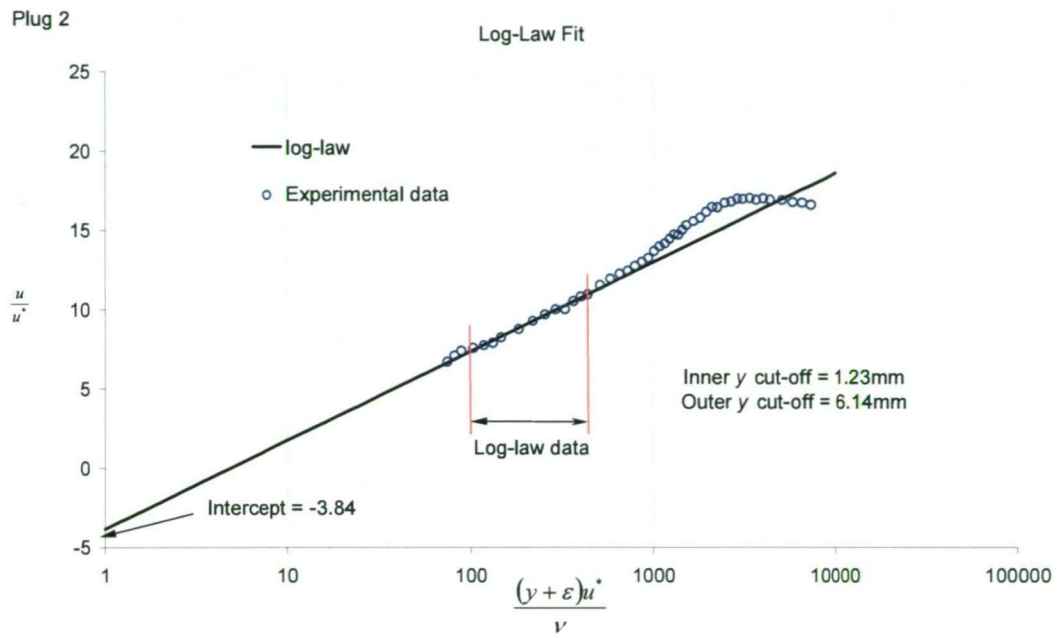

Figure 7.12: Example of log-law curve fit for the determination of ε.

Table 7.1 presents the results for mean velocity boundary layer profiles measured from the smooth clean plate, fouled plate 1 and fouled plate 2 respectively. The tables are spread over two pages.

The momentum thickness was used for the definition of boundary layer thickness, rather than the typical definition of $\delta = y$ at $0.99U$. This was due to both the non-uniform vertical flow distribution (shown in Chapter 6), and because θ is less sensitive to an accurate wall origin, particularly important for the rough wall measurements. Both θ and δ^* were determined from numerical integration using the trapezoidal rule.

For the smooth plate clean (as for the acrylic plate in Chapter 6), δ was defined by the relation $\theta = \frac{7}{72}\delta$ based on the $1/7^{th}$ power law. For the rough plates, δ was defined as $\theta = \frac{5}{42}\delta$ based on a $1/5^{th}$ power law. The relationship between δ and θ was taken as $\frac{\theta}{\delta} = \frac{n}{(1+n)(2+n)}$ (Schlichting, 1979), where n is found from Equation 6.6. Using this method resulted in a much more conservative values of δ, which is acceptable, as δ is only used as a relative measure to define the inner and out cut-off values in this case.

Results are shown for the smooth clean plate using both the Preston tube method and log-law slope method to determine u^*. For smooth plates it is usual to take the effective centreline of the Pitot probe at 65% of the outside diameter. For this study, this meant the zero position was 0.65mm from the wall using the 1mm (outside diameter) probe. This compares to a minimum of 0.28 mm to 1.15mm in ε determined from the log-law slope method. This variance about the approximate wall zero position is due to the normally encountered scatter in experimental measurements of velocity. The small differences for the respective boundary layer parameters can also be attributed to the scatter in the in wall zero position.

Error in u is the same for both smooth and rough plate measurements, and is the same as that present in Chapter 6, section 6.4.5.2. However error in u^* for rough walls is generally greater than for smooth wall measurements due to the introduction of the variables ε and Δu^* into the analysis procedure. Schultz (1998) reports that this may give an average error in c_f of 12%. This is not thought an unreasonable approximation for the present study.

Table 7.1: Boundary layer parameters for clean and fouled smooth painted plates. (Continued next page)

Smooth Painted Plate - Clean (Preston tube method)

Measurement Station	U (m/s)	δ (mm)	δ* (mm)	θ (mm)	u* (m/s)	c_f	H	Re_{Plug}	Re_{Plate}	Re_{δ}	Re_{δ^*}	Re_{θ}
x = 95mm (Plug 1)	1.01	20.20	2.39	1.96	0.0475	0.0045	1.22	1.12E+05	1.17E+06	2.37E+04	2.81E+03	2.31E+03
	1.54	18.48	2.18	1.80	0.0680	0.0039	1.21	1.71E+05	1.79E+06	3.32E+04	3.92E+03	3.23E+03
	1.87	17.35	2.05	1.69	0.0799	0.0036	1.21	2.07E+05	2.18E+06	3.79E+04	4.47E+03	3.68E+03
x = 495mm (Plug 2)	1.01	25.43	3.05	2.47	0.0441	0.0038	1.23	1.13E+05	1.18E+06	3.02E+04	3.62E+03	2.94E+03
	1.54	24.68	2.93	2.40	0.0656	0.0036	1.22	1.73E+05	1.82E+06	4.50E+04	5.34E+03	4.37E+03
	1.87	21.68	2.59	2.11	0.0763	0.0033	1.23	2.10E+05	2.20E+06	4.78E+04	5.72E+03	4.65E+03
x = 865mm (Plug 3)	1.03	34.29	4.07	3.33	0.0465	0.0040	1.22	1.15E+05	1.20E+06	4.14E+04	4.91E+03	4.03E+03
	1.57	28.97	3.41	2.82	0.0664	0.0036	1.21	1.74E+05	1.82E+06	5.30E+04	6.24E+03	5.15E+03
	1.91	28.52	3.37	2.77	0.0791	0.0034	1.22	2.12E+05	2.22E+06	6.36E+04	7.52E+03	6.19E+03

Smooth Painted Plate - Clean (log-law slope method)

Measurement Station	U (m/s)	δ (mm)	δ* (mm)	θ (mm)	u* (m/s)	c_f	H	Re_{Plug}	Re_{Plate}	Re_{δ}	Re_{δ^*}	Re_{θ}	k_s (mm)	Re_k	ε (mm)	Δu+
x = 95mm (Plug 1)	1.01	19.04	2.39	1.85	0.0453	0.0041	1.29	1.12E+05	1.17E+06	2.24E+04	2.81E+03	2.18E+03	0.11	5.74	0.85	0.76
	1.54	17.58	2.18	1.71	0.0640	0.0035	1.28	1.71E+05	1.79E+06	3.16E+04	3.92E+03	3.07E+03	0.06	4.46	0.73	0.15
	1.87	16.34	2.05	1.59	0.0734	0.0031	1.29	2.07E+05	2.18E+06	3.57E+04	4.47E+03	3.47E+03	0.04	3.78	0.95	-0.25
x = 495mm (Plug 2)	1.01	24.04	3.05	2.34	0.0467	0.0043	1.30	5.88E+05	1.18E+06	2.86E+04	3.62E+03	2.78E+03	0.16	8.63	0.47	1.76
	1.54	23.29	2.93	2.26	0.0663	0.0037	1.29	9.02E+05	1.82E+06	4.24E+04	5.34E+03	4.13E+03	0.08	6.31	0.32	0.99
	1.87	20.51	2.59	1.99	0.0790	0.0036	1.30	1.09E+06	2.20E+06	4.53E+04	5.72E+03	4.40E+03	0.06	5.98	0.28	0.86
x = 865mm (Plug 3)	1.03	32.54	4.07	3.16	0.0491	0.0045	1.29	1.04E+06	1.20E+06	3.93E+04	4.91E+03	3.82E+03	0.25	14.58	1.15	3.03
	1.57	27.43	3.41	2.67	0.0685	0.0038	1.28	1.58E+06	1.82E+06	5.02E+04	6.24E+03	4.88E+03	0.13	10.63	1.10	2.27
	1.91	26.97	3.37	2.62	0.0816	0.0037	1.29	1.93E+06	2.22E+06	6.02E+04	7.52E+03	5.85E+03	0.10	9.11	0.87	1.89

Table 7.1 (continued): Boundary layer parameters for clean and fouled smooth painted plates.

Smooth Painted Plate - Fouling 1 (Filamentous Biofilm)

Measurement Station	U (m/s)	δ (mm)	δ* (mm)	θ (mm)	u* (m/s)	c_f	H	Re_{XPlug}	Re_{XPlate}	Re_δ	Re_{δ^*}	Re_θ	k_s (mm)	Re_k	ε (mm)	Δu+
x = 95mm (Plug 1)	1.05	18.76	2.77	2.23	0.0684	0.0086	1.24	1.13E+05	1.19E+06	2.24E+04	3.31E+03	2.66E+03	0.68	53	0.81	6.16
	1.61	19.22	2.82	2.29	0.0945	0.0069	1.23	1.74E+05	1.83E+06	3.52E+04	5.17E+03	4.19E+03	0.39	42	0.71	5.54
	1.95	17.44	2.57	2.08	0.1141	0.0069	1.24	2.11E+05	2.22E+06	3.88E+04	5.72E+03	4.61E+03	0.37	48	0.69	5.95
x = 495mm (Plug 2)	1.05	23.75	3.66	2.83	0.0698	0.0088	1.29	5.96E+05	1.20E+06	2.86E+04	4.40E+03	3.41E+03	1.72	138	2.00	8.45
	1.61	22.78	3.51	2.71	0.1028	0.0081	1.30	9.12E+05	1.84E+06	4.20E+04	6.47E+03	5.00E+03	1.39	164	1.91	8.87
	1.96	21.96	3.37	2.61	0.1284	0.0086	1.29	1.11E+06	2.23E+06	4.91E+04	7.55E+03	5.85E+03	1.42	209	1.74	9.46
x = 865mm (Plug 3)	1.03	26.74	4.36	3.18	0.0667	0.0085	1.37	1.03E+06	1.19E+06	3.20E+04	5.21E+03	3.81E+03	2.06	160	1.51	8.77
	1.58	28.45	4.60	3.39	0.0980	0.0077	1.36	1.60E+06	1.84E+06	5.25E+04	8.48E+03	6.25E+03	1.55	177	1.26	9.03
	1.91	26.06	4.21	3.10	0.1188	0.0077	1.36	1.93E+06	2.22E+06	5.81E+04	9.39E+03	6.92E+03	1.50	208	1.25	9.40

Smooth Painted Plate - Fouling 2 (Low-Form Gelatinous Biofilm)

Measurement Station	U (m/s)	δ (mm)	δ* (mm)	θ (mm)	u* (m/s)	c_f	H	Re_{XPlug}	Re_{XPlate}	Re_δ	Re_{δ^*}	Re_θ	k_s (mm)	Re_k	ε (mm)	Δu+
x = 95mm (Plug 1)	1.07	14.35	2.39	1.71	0.0696	0.0085	1.40	1.13E+05	1.18E+06	1.70E+04	2.83E+03	2.03E+03	1.35	105	0.86	7.89
	1.64	14.13	2.32	1.68	0.0920	0.0063	1.38	1.73E+05	1.81E+06	2.57E+04	4.22E+03	3.06E+03	0.84	85	1.11	7.32
	1.99	13.37	2.23	1.59	0.1056	0.0056	1.40	2.10E+05	2.20E+06	2.95E+04	4.93E+03	3.52E+03	0.78	91	1.27	7.50
x = 495mm (Plug 2)	1.05	29.39	5.35	3.50	0.0582	0.0061	1.53	5.88E+05	1.18E+06	3.49E+04	6.35E+03	4.15E+03	1.79	117	0.86	8.03
	1.63	28.83	5.30	3.43	0.0856	0.0055	1.54	9.09E+05	1.83E+06	5.29E+04	9.72E+03	6.30E+03	1.37	132	0.52	8.14
	1.98	27.56	4.99	3.28	0.0979	0.0049	1.52	1.10E+06	2.22E+06	6.14E+04	1.11E+04	7.31E+03	0.82	90	0.27	7.34
x = 865mm (Plug 3)	1.10	33.43	5.96	3.98	0.0626	0.0065	1.50	1.05E+06	1.21E+06	4.07E+04	7.25E+03	4.85E+03	1.89	131	1.03	8.45
	1.69	34.60	6.15	4.12	0.0867	0.0052	1.49	1.62E+06	1.87E+06	6.49E+04	1.15E+04	7.73E+03	1.05	101	0.69	7.78
	2.05	33.22	5.90	3.95	0.1008	0.0048	1.49	1.97E+06	2.27E+06	7.57E+04	1.34E+04	9.01E+03	0.84	94	0.65	7.59

Boundary layer velocity profiles are presented in Figures 7.13, 7.14 and 7.15. Results are presented for the smooth plate clean, fouling 1 and fouling 2 respectively in each Figure. The law of the wall plotted in these Figures are based on the $Re_{Plate} = 2200000$ data. The $1/7^{th}$ power law is also fitted to the smooth plate clean results for comparison.

The boundary layer development for the clean plate is much like the acrylic plate from Chapter 6. However, a difference in the leading edge gap has resulted in less boundary layer thickness at the leading edge, and the downstream measurement stations.

The velocity profiles for smooth plate fouling 1 show a very depressed form, with the boundary layer quickly developing.

The velocity profiles for smooth plate fouling 2 also show a quickly developing boundary layer, though displaying a more clearly defined wake in the outer region.

The results for both smooth plate fouling 1 and 2 show a clear shift downward, which is indicated by the roughness functions, Δu^+, in Table 7.1. The roughness function for the fouled plates are investigated further in Chapter 9.

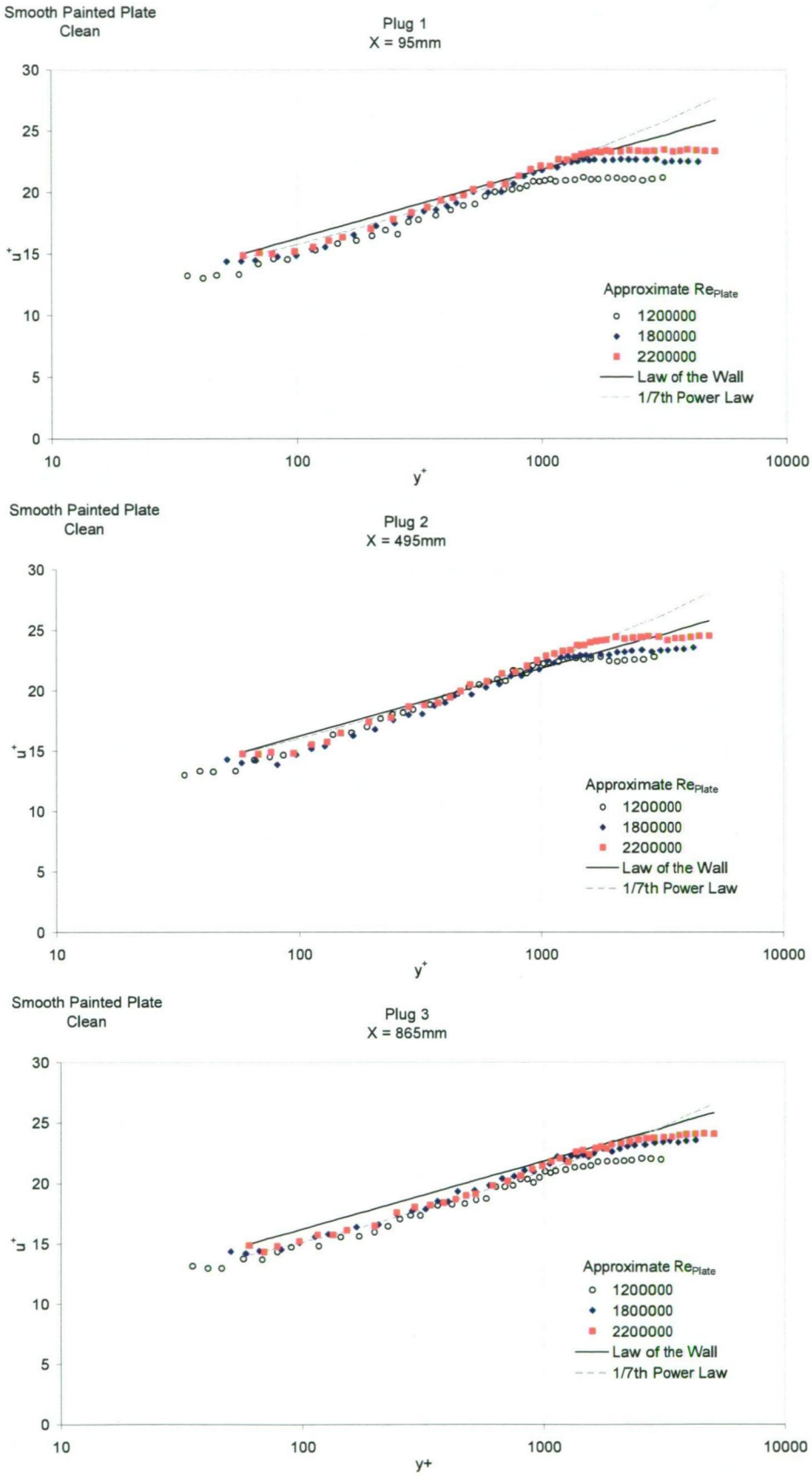

Figure 7.13: Velocity profiles for smooth clean plate (painted).

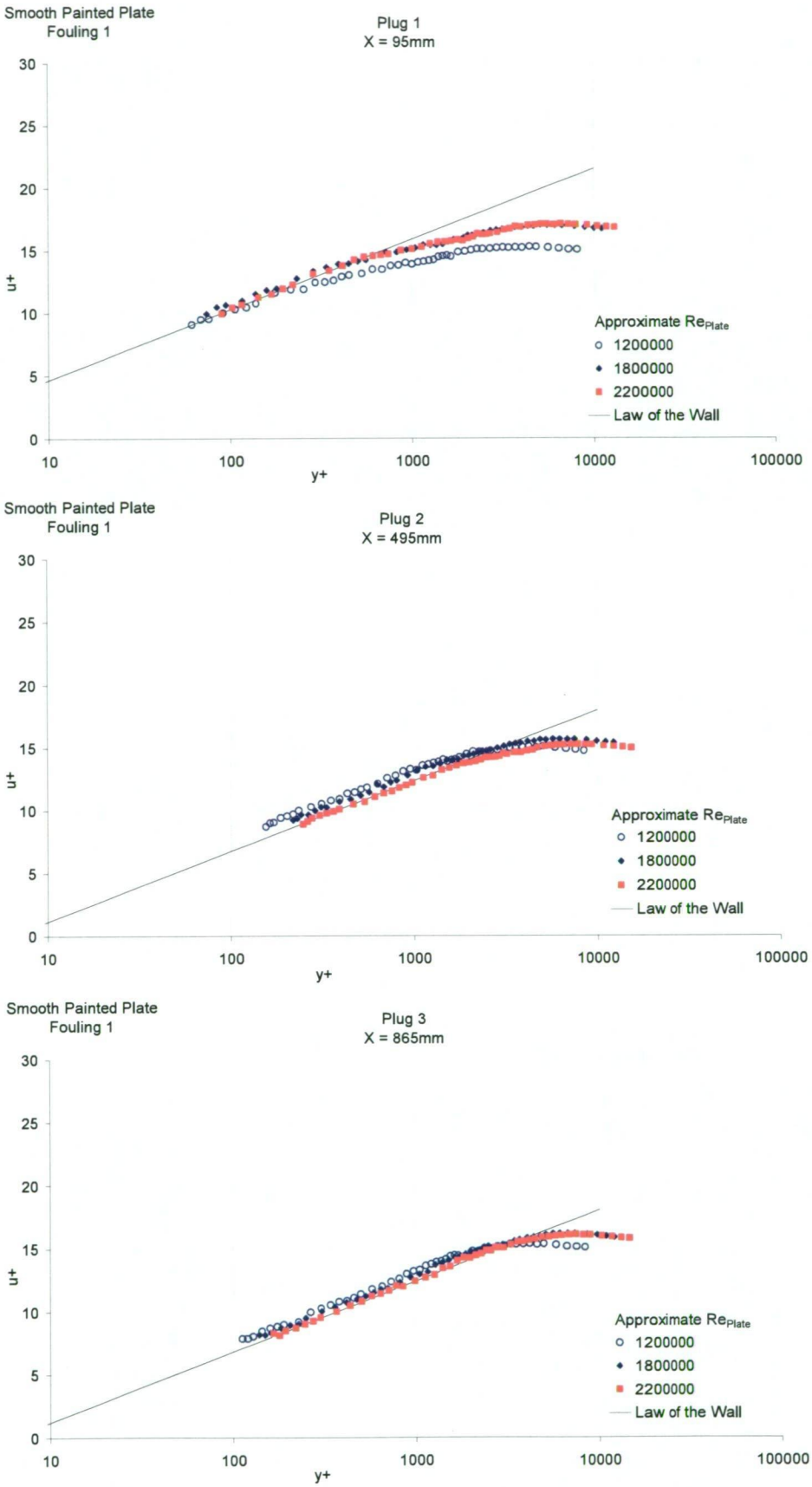

Figure 7.14: Velocity profiles for painted plate fouling 1 (filamentous biofilm).

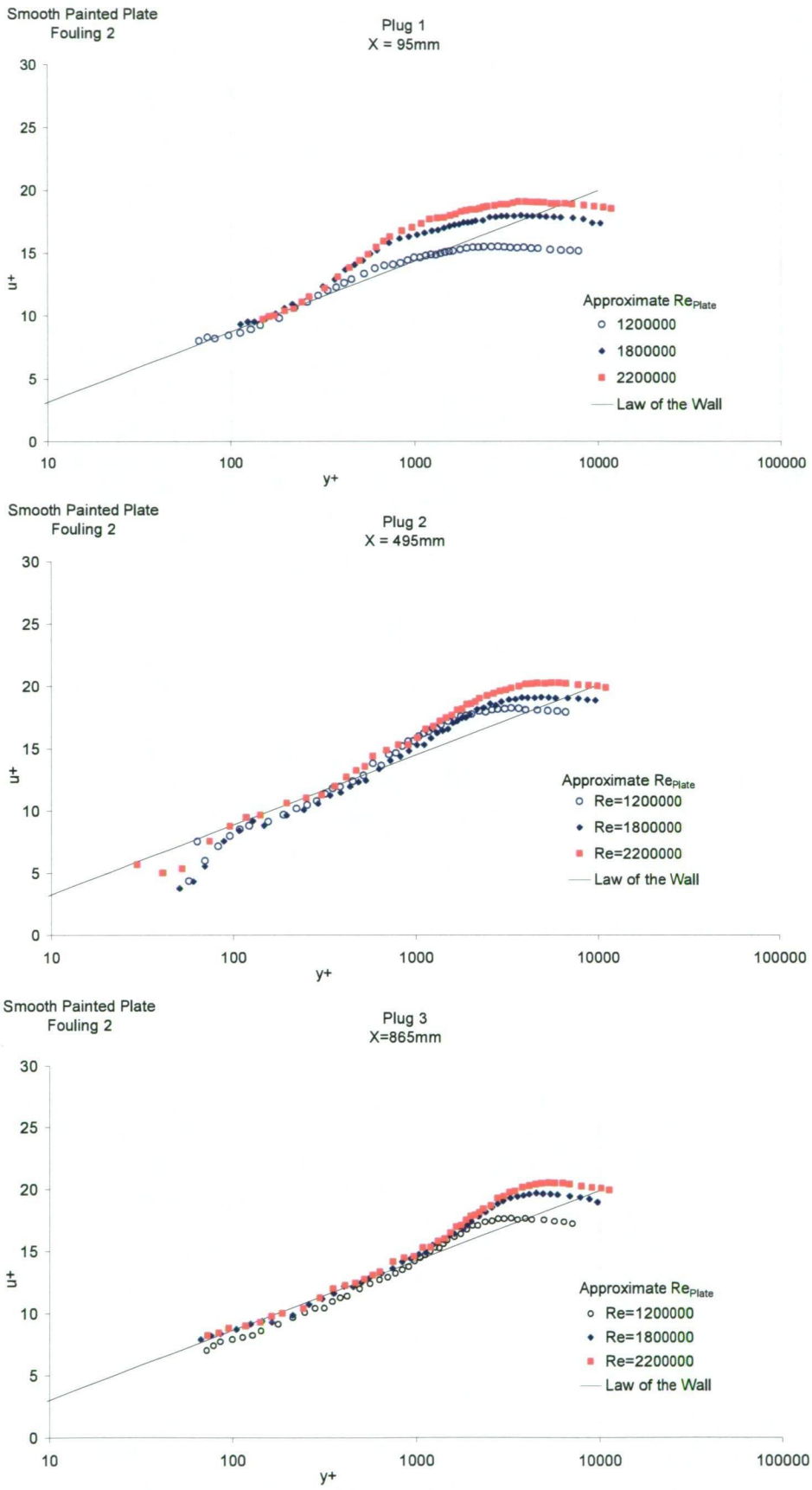

Figure 7.15: Velocity profiles for painted plate fouling 2 (low-form gelatinous biofilm).

Boundary layer shape factors shown in Figure 7.16 show the clean smooth plate with relatively constant H values. Smooth plate fouling 1 shows increasing H values due to the changing biofilm character with distance downstream. Smooth plate fouling 2 shows an increasing H only to the midway point at x=495mm (plug 2), then a small decrease in H at the downstream measurement station at at x=865mm (plug 3).

The alignment and position of the test plate in the water tunnel affected the state of the boundary layer at the leading edge. Calibration of the water tunnel in Chapter 6 showed that the gap between the working section roof and leading edge of the test plate caused a discontinuity in the boundary layer due to a portion of the flow moving into the roof cavity. Although care was taken to ensure alignment of the plate with the working section, the size of the leading edge gap varied slightly with each plate, and in turn varied the amount of boundary layer flow moving into the roof cavity.

Momentum thicknesses (Figure 7.17) increased by 64%, 49% and 148% for smooth plate clean, fouling 1 and fouling 2 respectively from x=95mm to x=865mm at a plate Reynolds number of 2.2×10^6. This shows that the filamentous biofilm on smooth plate fouling 1 may have actively reduced the growth of momentum thickness, whereas the gelatinous biofilm of smooth plate fouling 2 accelerated momentum thickness compared to clean plate conditions.

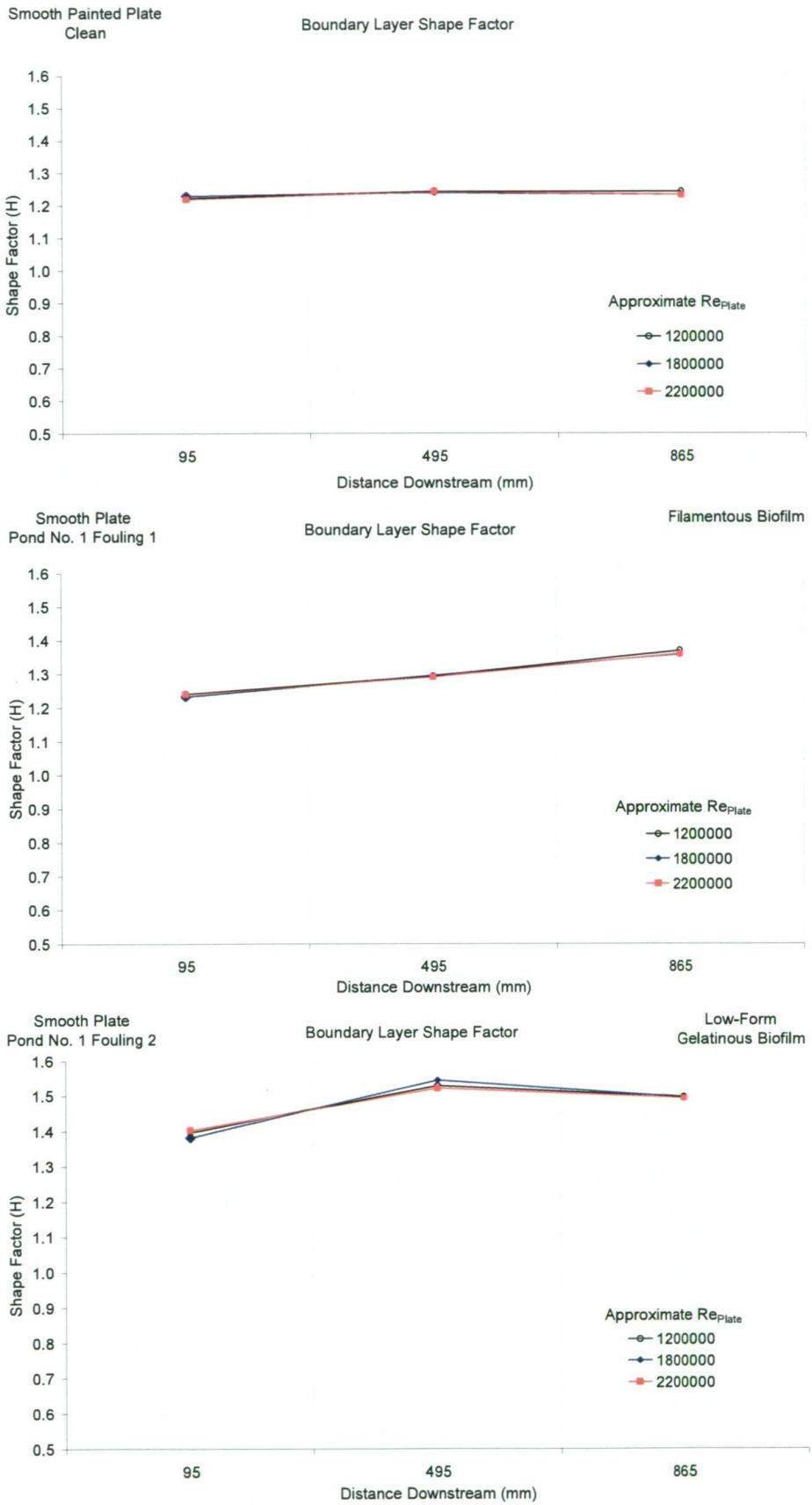

Figure 7.16: Boundary layer shape factor for the measured plates.

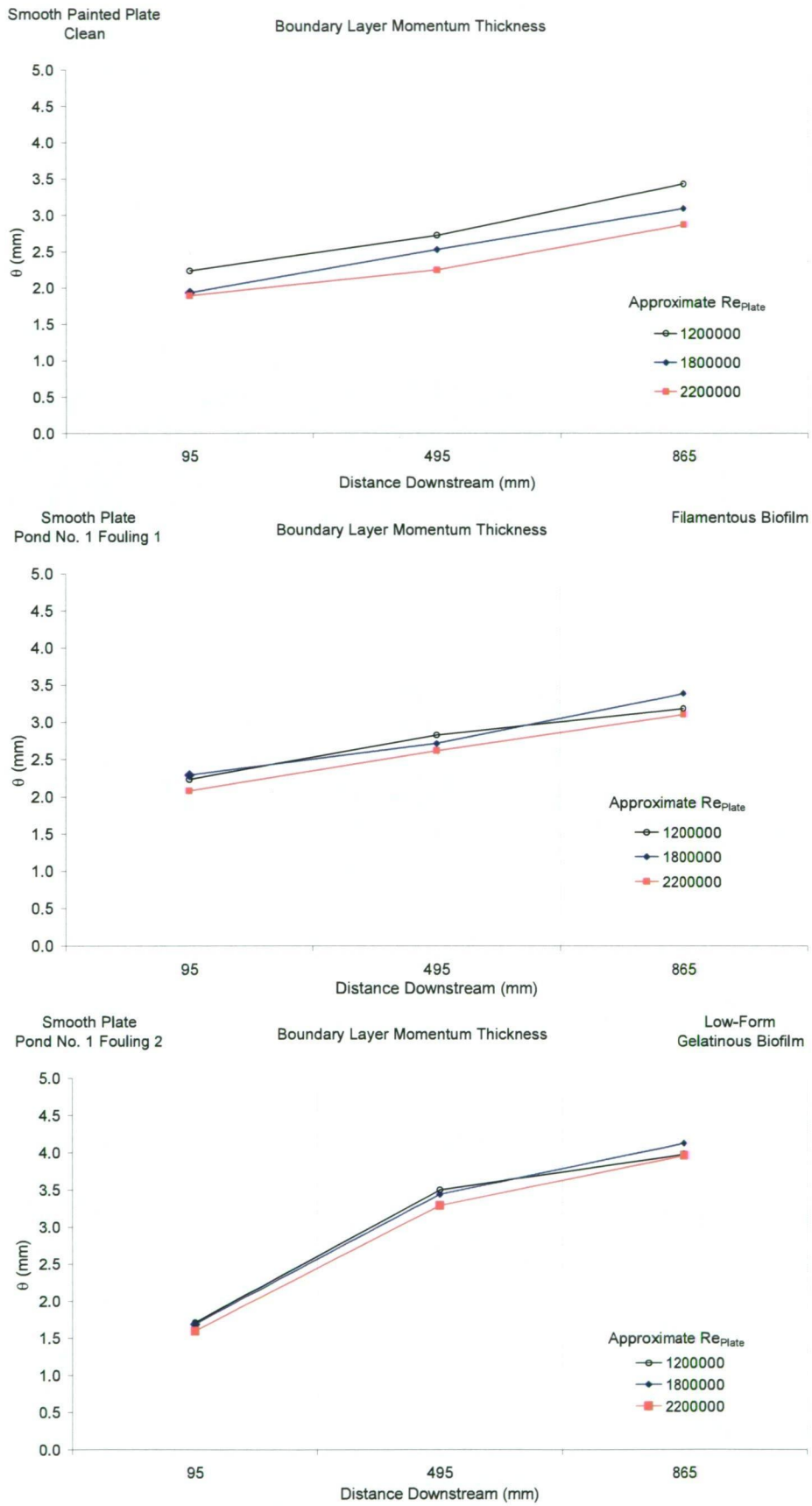

Figure 7.17: Boundary layer momentum thickness.

Figure 7.18 shows the local skin friction coefficient, c_f, reducing with distance downstream on in accordance with boundary layer growth for the clean plate and fouling 2 plate. These two plates had a relatively constant surface condition along the plate centreline, shown in Figure 7.4 for fouling 2.

The smooth plate fouling 1 measurements show generally higher c_f values than the other plates. Smooth plate fouling 1 had increasing amounts of biofilm with distance downstream, shown in Figure 7.1, which is thought to explain this.

Wall shear velocities shown in Figure 7.19 are not to indicate friction behaviour, because c_f values do this in a more meaningful way. Rather, as u^* is likely to influence biofilm attachment and interaction with the near wall flow, it is useful to compare measured values against the range of typical u^* values found in Hydro Tasmania hydraulic conduits. Figure 6.48 in Chapter 6 shows the range of wall shear velocities for a range of Hydro Tasmania conduits. Direct comparison with the Tarraleah No. 1 Canal deployment conditions are also made by estimating the local skin friction by using Equation 7.3 (White, 2006), for a smooth plate. It is assumed in using this equation that there is no initial laminar boundary layer region at the forward section of the plate. x was taken as 95, 495 and 865mm representing the same locations along the plate where boundary layer measurements were taken in the water tunnel. Mean flow velocity at Pond No. 1 was taken as 1m/s and water temperature was taken as 10 deg C.

$$c_f = \frac{0.027}{\mathrm{Re}_x^{\frac{1}{7}}} \qquad \text{Equation 7.3}$$

A comparison of the theoretical friction and wall shear velocities (Figure 7.15) for the smooth clean plate (representing the initial state the plate was deployed in) show that the deployment conditions closely match the measured values at $\mathrm{Re}_{Plate} = 1.2 \times 10^6$. This validates the use of the field installation.

Chapter 9 further investigates the biofilm behaviour in relation to u^*, and looks at this result in the context of field conduits.

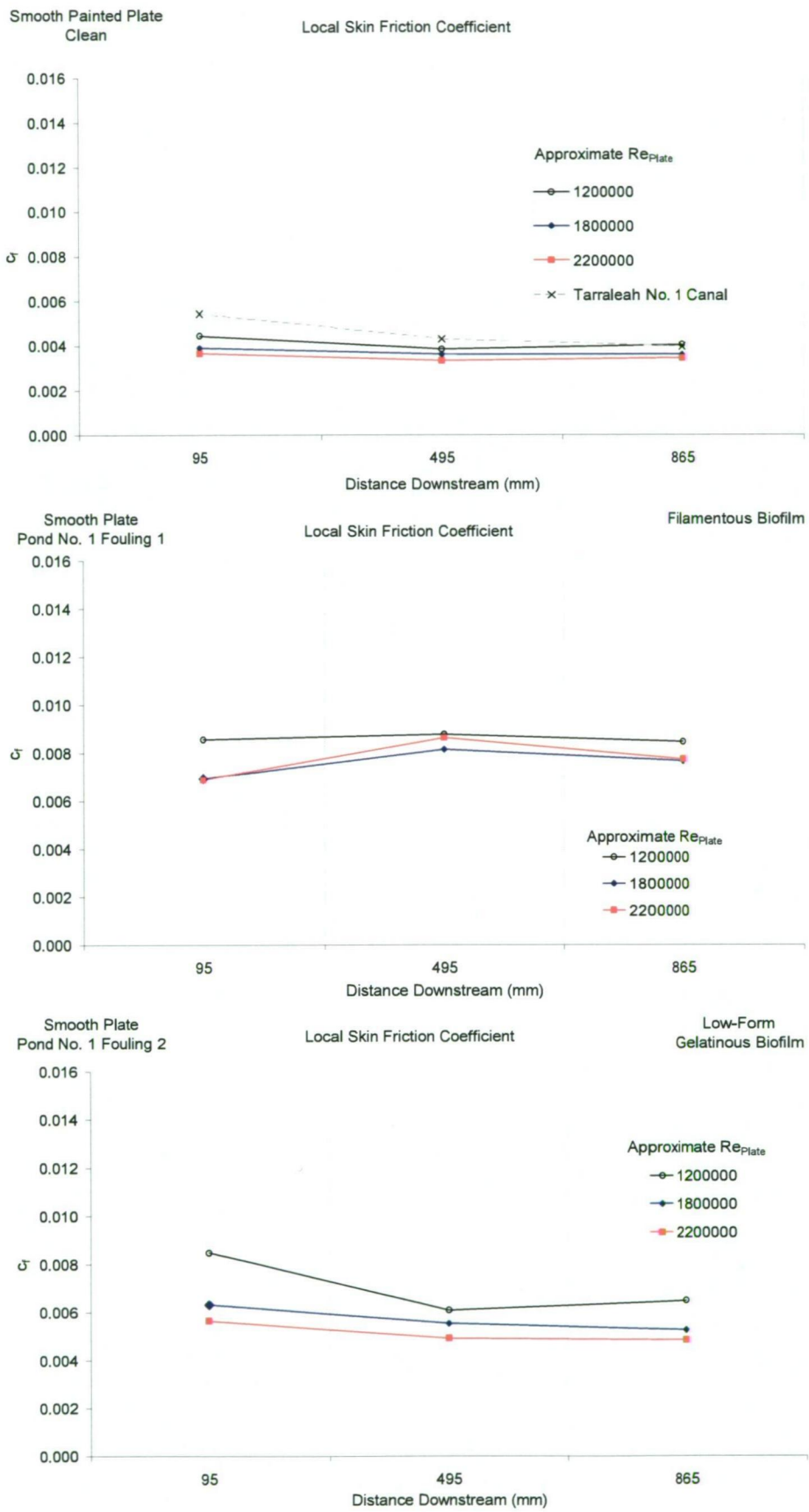

Figure 7.18: Local skin friction coefficient.

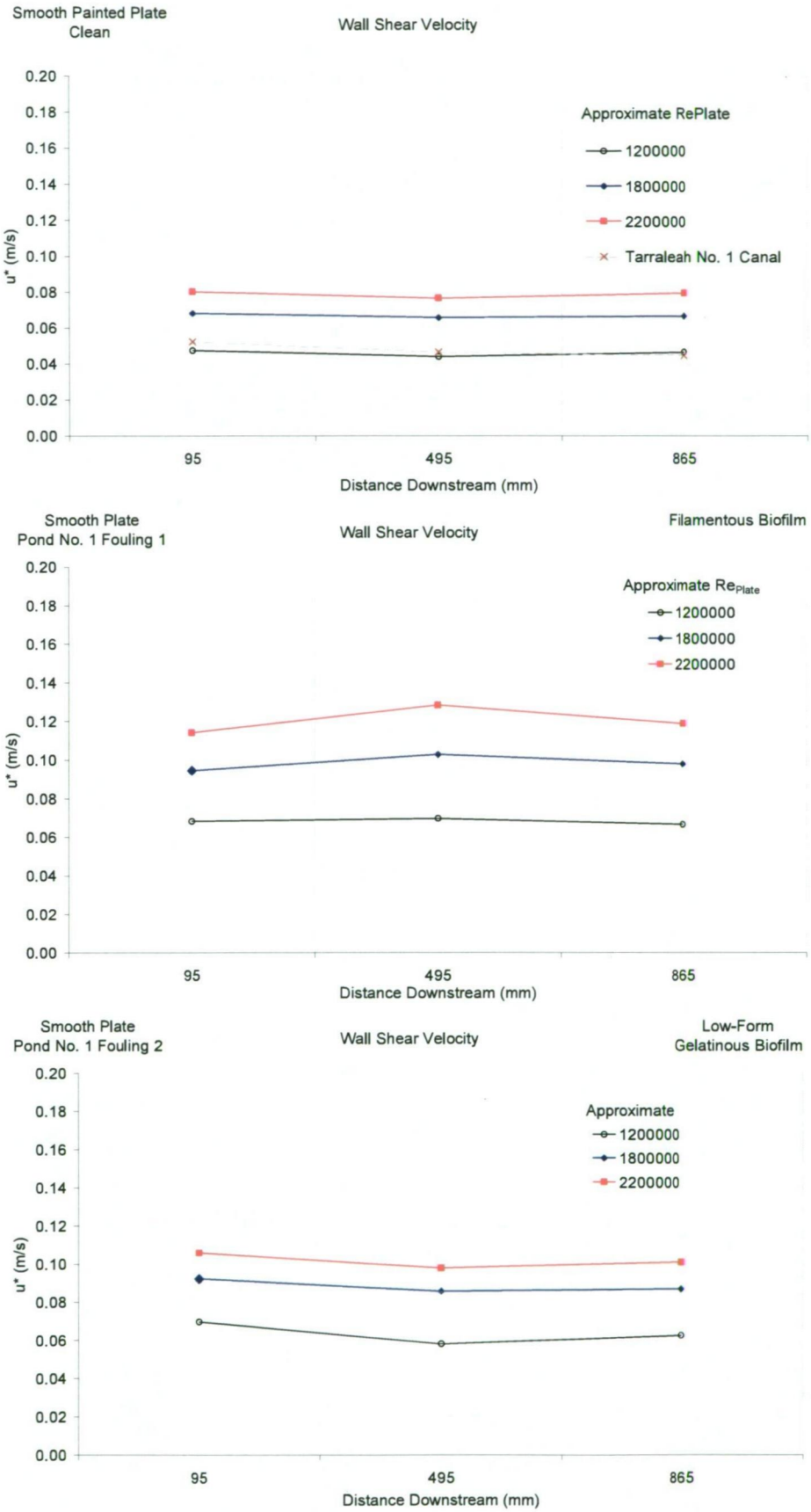

Figure 7.19: Wall shear velocity for clean and fouled plates.

Local roughness values of k_s, shown in Figure 7.20, displayed interesting behaviour of the biofilms. Equation 2.4 was used to find k_s, assuming hydraulically rough conditions. The most obvious property is the clear separation of measured roughness values at different Reynolds numbers. This may be due to the visco-elastic property of the biofilm creating different roughness effects at the different Reynolds numbers.

The roughness was measured to be greatest for smooth plate fouling 1 at plug 3, 865mm downstream of the leading edge. This is consistent with the observed biofilm abundance in Figure 7.1. The least amount of biofilm was observed on the forward 1/3rd of the plate, also consistent with observations.

Smooth plate fouling 2 also showed generally increased roughness with distance downstream.

Table 7.1 shows the roughness of the plate was in the fully hydraulically rough regime except at plug for smooth plate fouling 1.

The general decrease in origin error, ε, with increasing flow speed and associated Reynolds number is thought to be related to the "thinning" of the biofilm on the test plate. As the biofilm is forced harder against the wall, the virtual origin decreases, as the roughness elements reduce in size and expose the probe. This fits with the concept of biofilm canopy thinning by Nikora (2004) described in Chapter 2.

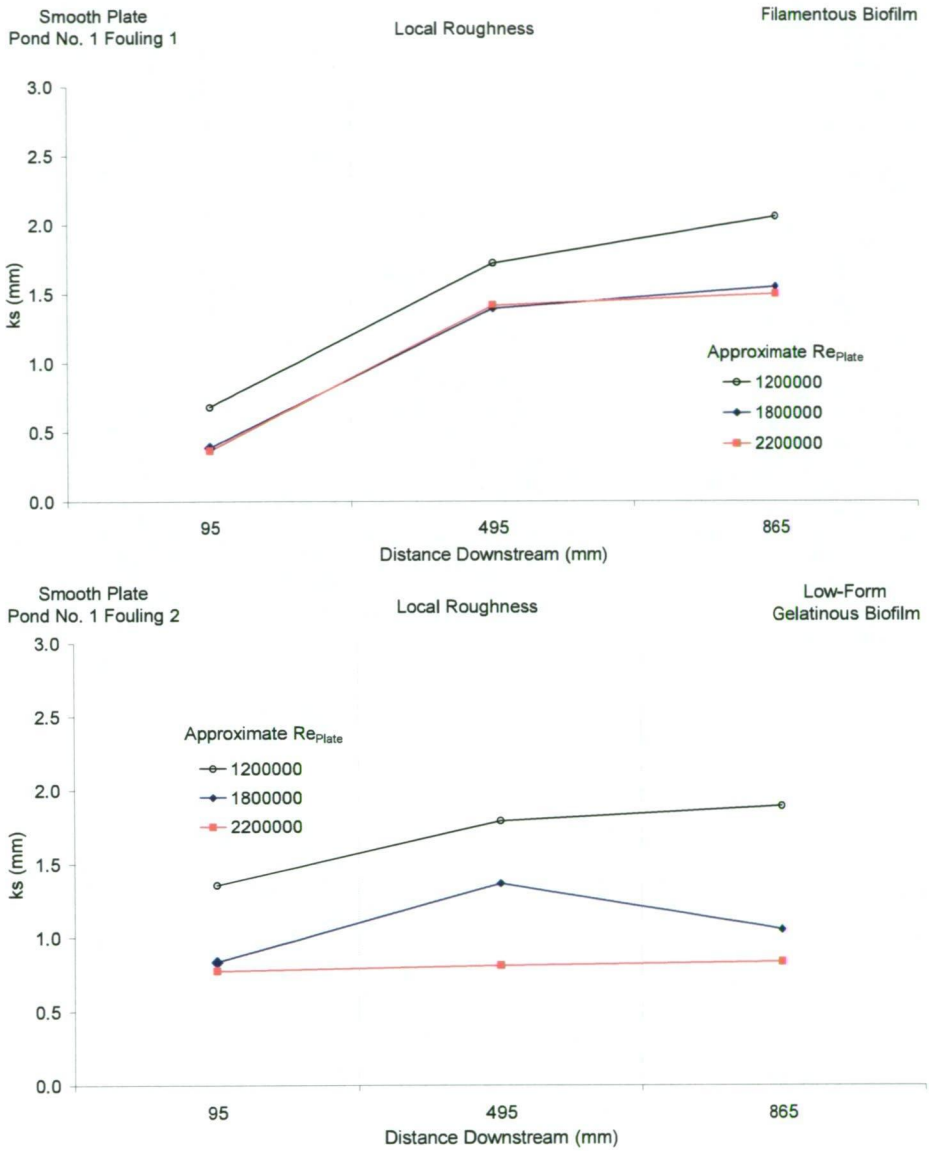

Figure 7.20: Local roughness values determined from velocity profiles.

The mean velocity profiles measured for the smooth plates clean, fouling 1 and fouling 2 are respectively presented in Figure 7.21 at the three Reynolds numbers for comparison. Results are presented as $\frac{y}{\delta}$ versus $\frac{u}{U}$ for the clean smooth plate, and $\left(\frac{y+\varepsilon}{\delta}\right)$ versus $\frac{u}{U}$ for the fouled plates. For these plots, δ was defined using the more traditional method, taken as y at $0.99U$.

The velocity deficit for the fouled plate measurements clearly exceeds that for the clean plate.

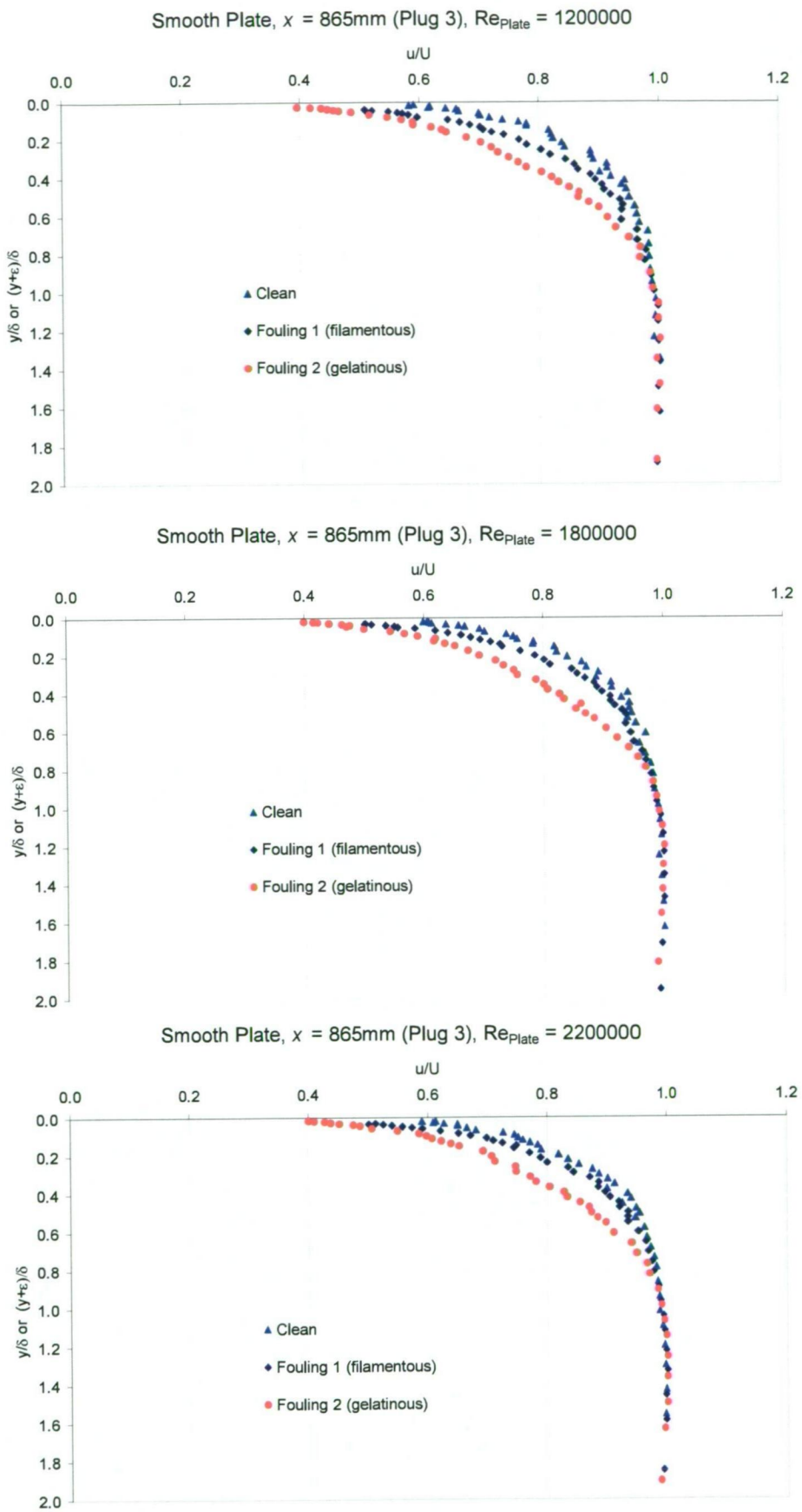

Figure 7.21: Comparison of velocity profiles at plug 3.

7.4 Total Drag Characteristics

Total drag measurements were undertaken on smooth plate clean and smooth plate fouling 1 and fouling 2.

Figure 7.22 shows a comparison of the results of the total drag measurements for the smooth plate clean with theoretical values. The theoretical values were found using the methods described in Chapter 6, section 6.4.6. Errors were determined from repeatability tests described in Chapter 6, and shows that uncertainty is greater at lower Reynolds numbers.

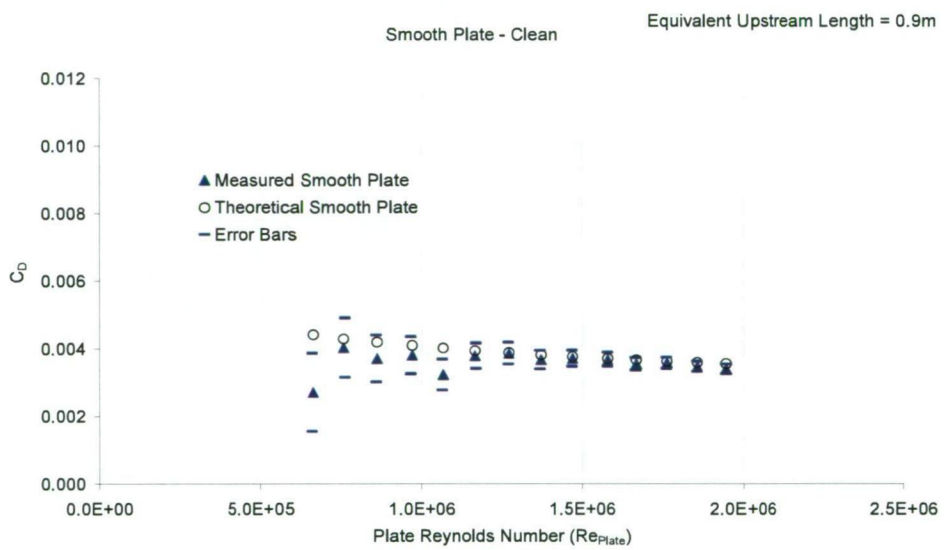

Figure 7.22: Comparison of measurement and theory for smooth plate clean.

Corrections were made to the data presented in Figures 7.22 and 7.23 including the removal of pressure forces on the plate ends. These methods are described in Chapter 6.

Equation 6.21, from Chapter 6, was used to find C_D for the smooth plate clean. However, smooth plate fouling 1 and fouling 2, were considered rough plates, verified from Table 7.1 where the majority of Re_k were greater than 60 (hydraulically rough). Accordingly, Equation 7.4 was used to find C_D as suggested by Schlichting (1979). The distance, l, was either the equivalent upstream length, the plate length, or both.

$$C_D = \left(1.89 + 1.62 \log \frac{l}{k_s}\right)^{-2.5} \qquad \text{Equation 7.4}$$

An iterative method was used to find k_s, which was incrementally adjusted until values matched for both $C_{D(l_1)}$ and $C_{D(l_2)}$. $k_s \pm$ the standard deviation (SD) are shown in the figures.

Figure 7.23 shows a comparison of the results of the total drag measurements for smooth plate fouling 1 and fouling 2. On this Figure, "Measured Drag 1" denotes drag measurements completed at the start of water tunnel testing. "Measured Drag 2" denotes drag measurements completed at the completion of all water tunnel testing. This was used as a general check that the nature of the biofilm did not change significantly over the test period. For clarity of the figure, error bars are shown for Measured Drag 1 only.

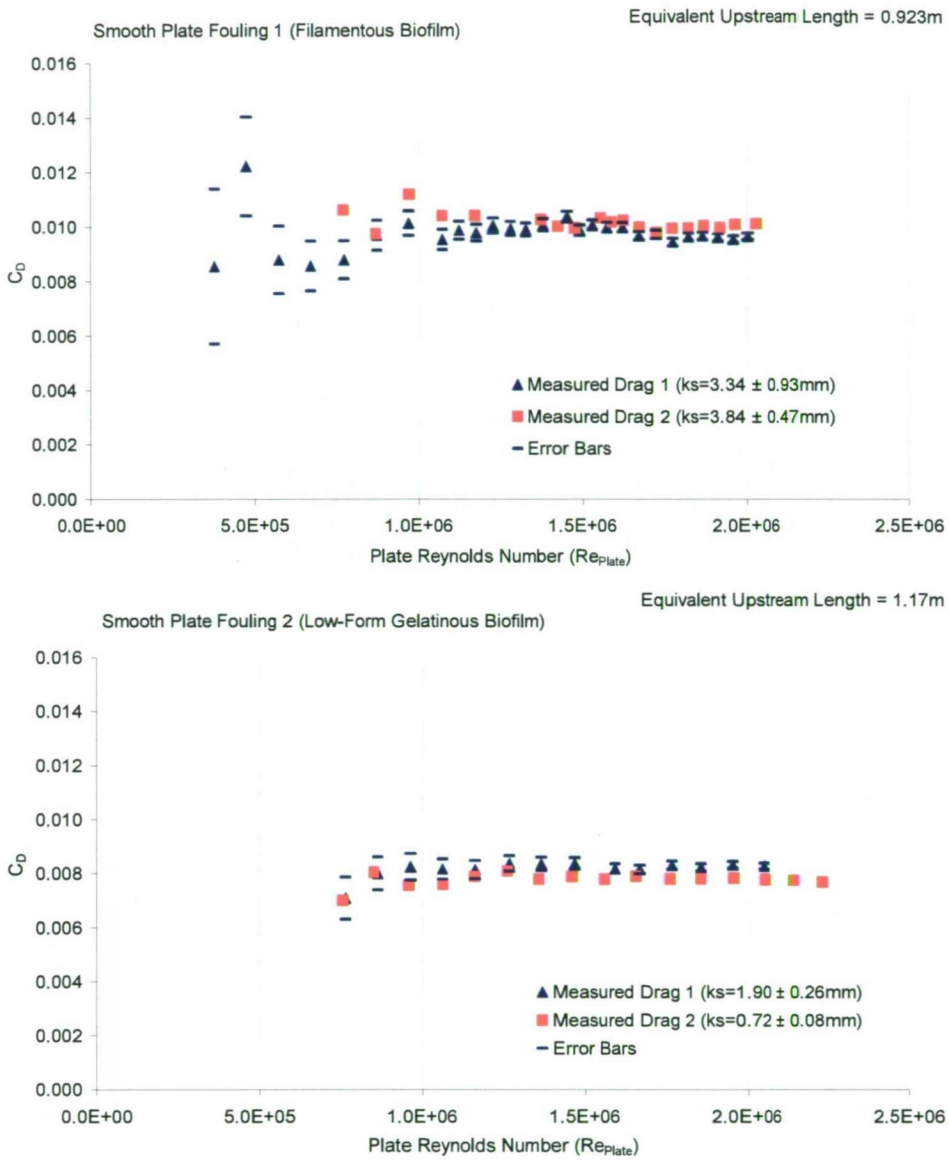

Figure 7.23: Comparison of measurements before and after testing.

The high C_D and k_s values for smooth plate fouling 1 total drag measurements can be explained by the large filaments which were not on the plate centreline flow path that is measured by the velocity profiles in section 7.3. This is seen in Figure 7.1.

A 172.6% increase in total drag was measured for fouling 1 (from Measured Drag 1) from the smooth plate clean condition. An increase of 127.8% in total drag was recorded for fouling 2.

There was a slight increase in measured drag for smooth plate fouling 1 over the course of testing as shown in Figure 7.23. The filamentous biofilm was observed to deteriorate

from its initial condition at the commencement of testing and become stiff and less flexible over the course of testing which may explain the increase in drag.

Smooth plate fouling 2 showed a decrease in total drag over the course of testing due to a loss of biofilm on the plate over the course of testing. Schultz (1998) observed the same thing after testing with his plates. There was usually a visible loss of biofilm, due to the shear force of the flow removing it over time. Loss of biofilm also occurred with the rough plates over the course of water tunnel testing, shown in Chapter 8.

This loss of biofilm raises the question of whether laboratory conditions are typical of those in the field. One of the reasons the biofilms were grown in the field were to condition them. This would permit stronger bonds between the biofilm and the plate substrate that would not occur if biofilms were grown in static water tanks like those in Schultz (1998). Smooth plate fouling 1 and fouling 2 are both from Tarraleah Pond No. 1, where flow velocities are approximately 1m/s. However, some of the water tunnel measurements were conducted at wall shear velocities much higher than Pond No. 1 to replicate the wall shear of other hydraulic conduits.

Cloeta *et al.* (2003) measured quite specific detachment velocities for biofilms attached to various pipe materials. The general conclusion was that increased velocity resulted in increased detachment, although the maximum velocities used in the experiment did not necessarily results in the highest rate of detachment. This complicated type of biofilm behaviour supports the involvement of microbiologists in the investigation of biofouling problems.

7.5 Surface Character from Photogrammetry

Immediately after smooth plate fouling 1 and fouling 2 were retrieved from the field, and before the plates were placed in the water tunnel for testing, stereo photographs were taken of the plates at locations or "windows" shown in Figure 7.24. These locations are the same as described in Chapter 5, and were located to provide a representative area of the plate. These locations importantly also provided two series of three windows in the same longitudinal direction at distances downstream of the test plate. This allowed for the measurement of physical biofilm surface character with

distance downstream of the leading edge, and also some ability to check for biofilm character across the plate width.

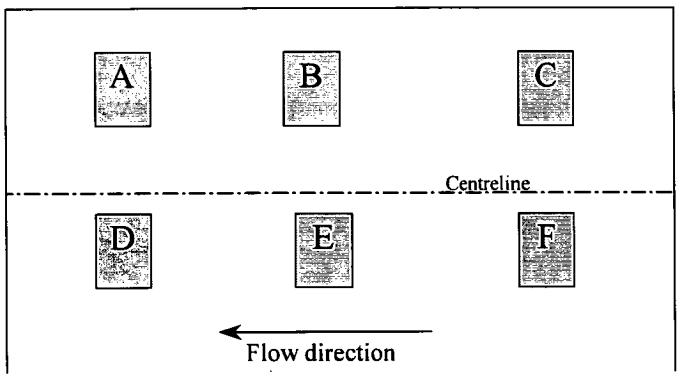

Figure 7.24: Layout of the photography windows for the large test plates.

Photogrammetry for the smooth painted plate was not undertaken, as the accuracy required to map a smooth surface was not available using the photogrammetric methods outlined in Chapter 5. In addition, the smooth painted surface did not have the required optical texture for accurate stereo imaging. For the purpose of characterising biofilm roughness, it was not important in the present study to find the roughness character of the clean painted plate.

All surface profiles used to derive the roughness information for smooth plate fouling 1 and 2 are included in the Appendix. Tables 7.2 and 7.3 summarise the roughness and statistical information taken from each of the photography windows. Ra and Rq are non-dimensionalised in these tables with the statistical mean.

Roughness and statistical parameters have previously been explained in Chapter 5. Sample lengths are taken at Y=20, 40, 60, 80 and 100mm. The surface data was filtered using the method described in Chapter 5.

Table 7.2: Photogrammetry results for smooth plate fouling 1.

Photographed	Roughness Parameters (mm)					Statistical moments				Peak
Area	Ra/mean	Rq/mean	Rp	Rv	Rt	Mean	Variance	Skewness	Kurtosis	Count
Window A	0.23	0.32	0.48	-0.33	0.81	0.33	0.01	0.76	5.50	13.20
Window B	0.27	0.35	0.46	-0.36	0.81	0.36	0.02	0.34	1.50	13.20
Window C	0.26	0.34	0.43	-0.32	0.75	0.32	0.01	0.62	1.80	13.00
Window D	0.10	0.13	0.22	-0.29	0.51	0.62	0.01	-0.86	4.51	11.80
Window E	0.26	0.33	0.24	-0.28	0.51	0.28	0.01	-0.36	0.49	15.20
Window F	0.27	0.34	0.20	-0.28	0.48	0.28	0.01	-0.42	0.16	9.80

Table 7.3: Photogrammetry results for smooth plate fouling 2.

Photographed Area	Roughness Parameters (mm)					Statistical moments				Peak Count
	Ra/mean	Rq/mean	Rp	Rv	Rt	Mean	Variance	Skewness	Kurtosis	
Window A	0.33	0.44	0.65	-0.37	1.01	0.37	0.03	1.16	2.54	12.60
Window B	0.19	0.28	0.95	-0.35	1.30	0.66	0.04	1.82	6.53	9.60
Window C	0.38	0.48	0.84	-0.48	1.32	0.48	0.06	0.87	1.39	10.80
Window D	0.39	0.53	0.82	-0.46	1.29	0.42	0.06	1.25	2.35	9.20
Window E	0.36	0.49	0.64	-0.30	0.93	0.30	0.02	1.33	4.11	12.80
Window F	no data									

The results from Tables 7.2 and 7.3 quantitatively demonstrate the earlier observation that the biofilm character changes over the plate area. In the case of smooth plate fouling 1, biofilm character changed both along the length of the plate and across the plate width. There was generally thicker biofilm measured along the bottom half of the plate (windows A, B, and C) consistent with observations from Figure 7.1. There was also a general increase in biofilm thickness with distance downstream.

Mean biofilm thickness is represented by the statistical mean of the measured surface. That is, the height of the biofouled surface above the clean surface. This is possible as the lowest point on the surface profile indicates the minimum amount of biofilm growth, which for the photographed windows presented in this section, was equivalent to the clean surface within the measurement uncertainty of this technique. Windows B and D were measured to have the greatest biofilm thickness for smooth plate fouling 1. Windows B and C were measured to have the greatest biofilm thickness for smooth plate fouling 2.

Smooth plate fouling 2 showed a more consistent biofilm character. The biofilm was measured to be thicker for fouling 2 than fouling 1. This is because the biofilm of fouling 2 was gelatinous and clumpy. Fouling 1 was more filamentous, especially windows A and B, and so the biofilm laid flat against the plate during photography.

The maximum peak to valley height is often many times greater than mean thickness showing the unevenness and variability of growth. Some of the larger observed clumps in fouling 2 approached 3mm in height.

Kurtosis values show a generally increasing sharper surface profile with distance downstream, being related to increased presence of biofilm for both fouling 1 and fouling 2.

Data from Tables 7.2 and 7.3 show a generally higher peak count for smooth plate fouling 1 and generally higher skewness for smooth plate fouling 2. The higher skewness values were mostly present where there were clumps of biofilms.

The limit of the photogrammetry is evident where, on the surface profiles (see Figures 7.25 ad 7.24), there is "noise" on what should be a flat surfaces, between the clearly shown biofilm patches. It is estimated that this shows an accuracy nearer 200μm in the Z direction, rather that the 100μm stated in Osborn *et al.* (2005), although this may be explained by the poor optical texture of the paint surface, resulting in poor stereo matching of the image.

Figures 7.25 and 7.26 show sample photos and respective surface profiles for areas on the respective test plates where much biofouling was present.

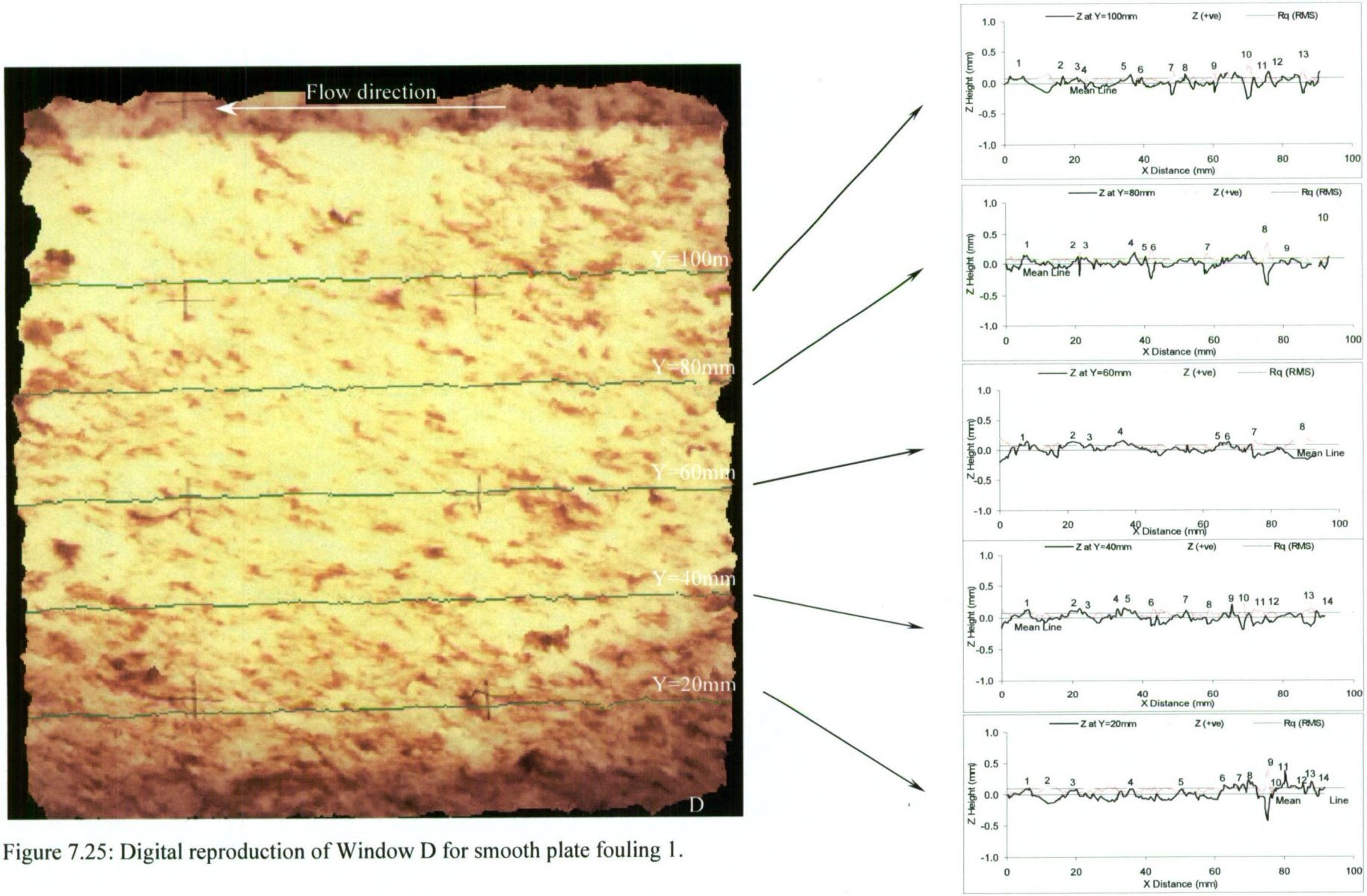

Figure 7.25: Digital reproduction of Window D for smooth plate fouling 1.

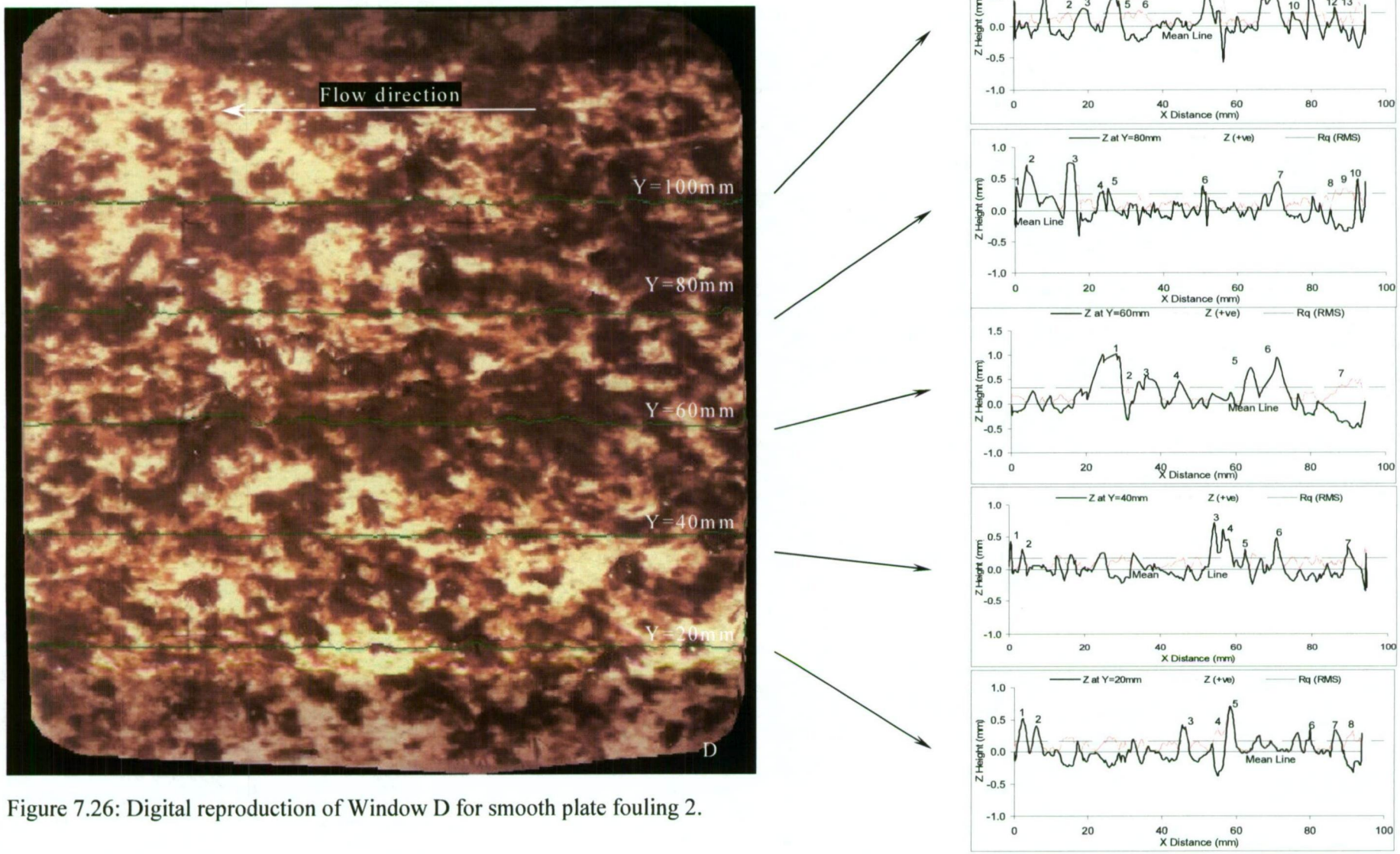

Figure 7.26: Digital reproduction of Window D for smooth plate fouling 2.

7.6 Chapter Summary

Results from water tunnel measurements and photogrammetry for a clean and two fouled smooth, spray painted, test plates have been presented in this Chapter. A comprehensive approach has been used to understand the roughness characteristics of freshwater biofilms. The roughness information obtained in goes well beyond that previously available from such studies as Schultz (1998) and Picologlou *et al.* (1980).

Results show that biofilms in general create roughness effects beyond what their physical surface character and simple average thickness may otherwise suggest using sandgrain type roughness comparisons.

An increase in roughness effects and associated friction due to biofilms was measured on both the fouled smooth plates compared the smooth plate in its clean condition.

Boundary layer measurements showed that biofilms might become thinner under increased flow speeds. This was shown as a change in wall origin using rough wall data analysis methods. This behaviour is consistent with the concept put forward by Nikora (2004), and with visco-elastic observed by others.

Although it was measured that filamentous biofilms create more drag than purely gelatinous types of biofilm, the physical surface could not be genuinely characterised while out of water using the photogrammetric methods of the present study. It was observed that filaments display three-dimensional behaviour, and this is an area that deserves particular attention in future research. A CD containing video footage of biofilms observed during this study are attached as Appendix A for reference. Use of in situ photogrammetry, and/or high speed video or camera are recommended to better capture the behaviour of filamentous biofilms.

The results from this Chapter and Chapter 8 are further synthesised and discussed in chapter 9.

Chapter 8 Boundary Layer, Drag and Roughness Measurements for Clean and Fouled Rough Plates

8.1 Introduction

This chapter provides results of boundary layer and friction measurements for a clean rough plate and two fouled rough plates. Measurements of the surface were also made using close range photogrammetry.

The plates were made rough by coating with an artificial roughness consisting of fine grit imprinted and stuck to a tar undercoat. This surface coating was described in Chapter 4.

A description of the fouled plates is given first. Boundary layer results and total drag characteristics of each plate are then presented.

Measurements of fouled rough plates have not previously been studied in the way presented in this chapter. Lewkowicz and Das (1985) have studied only simulated fouled rough surfaces, while Schultz (1999; 2000) studied only fouled smooth plates.

Rougness information obtained from each of the measurement techniques are compared with each other and related back to the observed biofilm.

The chapter then finishes with a short summary.

8.2 Description of Fouled Plates

The rough plates were deployed in the Tarraleah No. 1 Canal system at field installations depicted in Figure 4.6. The rough plate was attached downstream of the large smooth plates presented in Chapter 7. This meant that the smooth plates provided a leading edge for the majority of the time the plates were deployed. However, when a smooth plate was retreived for laboratory testing, the rough plate was exposed for the duration (usually 1 week) the smooth plate was removed from the installation. This effectively meant that the rough plate acted as the leading edge for the (one) week before being retrieved for laboratory measurements.

The method for naming the various test plates in this chapter is the same as that used in Chapter 7.

The rough plate clean measurements were conducted on a control plate which remained in the laboratory at all times. All rough plates were prepared using the same method and same fine grit described in Chapter 4.

Rough plate fouling 1 was deployed for approximately 4 months and allowed to become fouled from an initially clean state. Growth on the plate was very skewed in much the same way as smooth plate fouling 1 described in Chapter 7. This resulted in relatively little fresh living biofilm, and mostly large clumps of old and dying biofilm. The nature of these large clumps resulted in the creation of large filament tufts when submerged in water. Figure 8.1 shows rough plate fouling 1 prior to testing in the water tunnel.

Fresh living biofilm was located only on the lower 30% of the plate. The old biofilm was on the top 60% of the plate. This reflects the frequent fluctuations of water level during the period of deployment which often left the top portion of the plate exposed to ambient air temperatures. There was generally thicker growth on the plate proportionate with distance downstream. Physical measurements of biofilm thickness are presented in section 8.5. Lines are drawn on Figure 8.1 separatings the two types of growth. Little growth was seen near the leading edge of the plate.

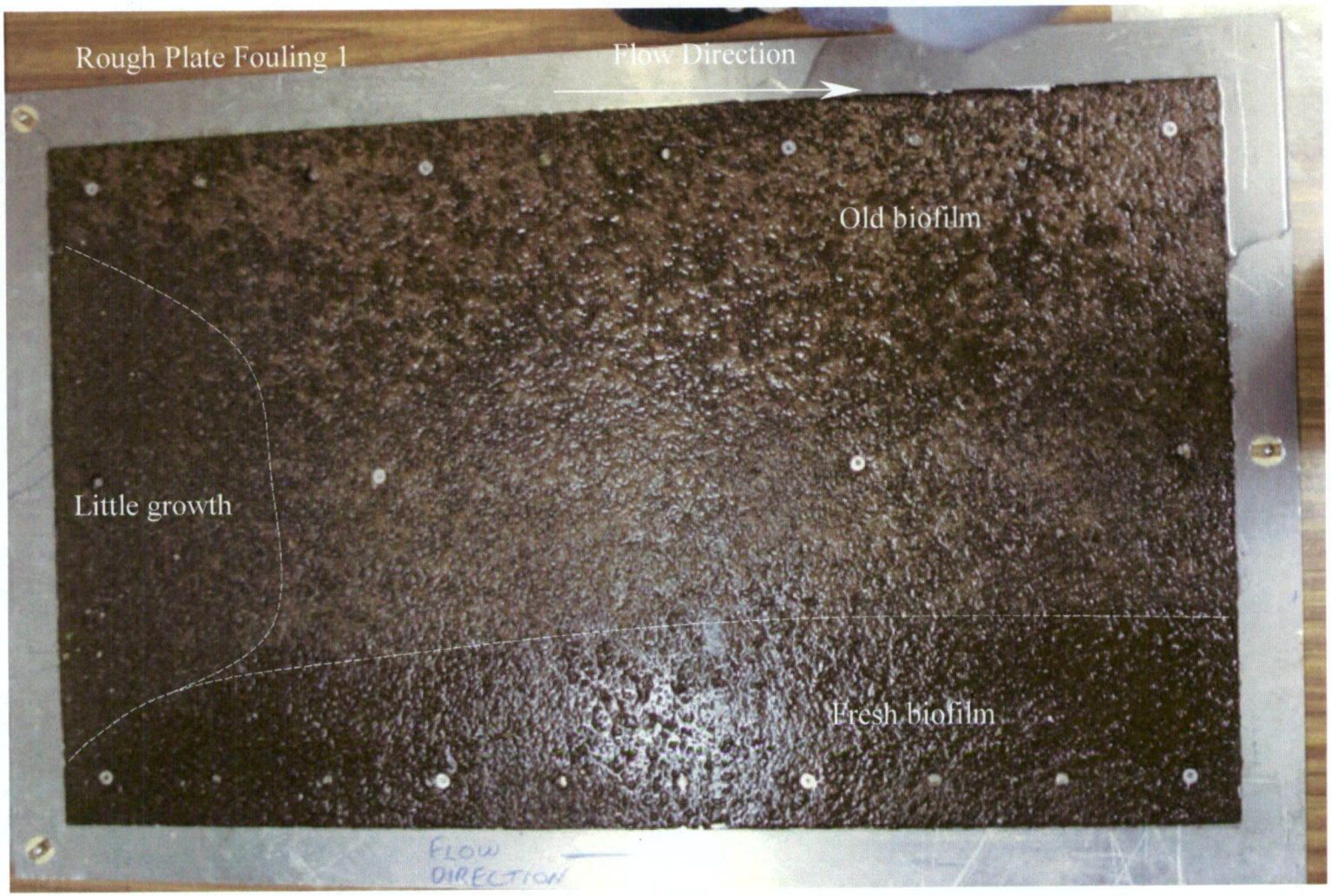

Figure 8.1: Rough test plate on the table ready for photography.

Figure 8.2 shows a photo of a section of old biofilm growth from the side with no flow. Large and numerous filaments were apparent. When water was flowing, these filaments laid flat against the rough wall as shown in Figure 8.3.

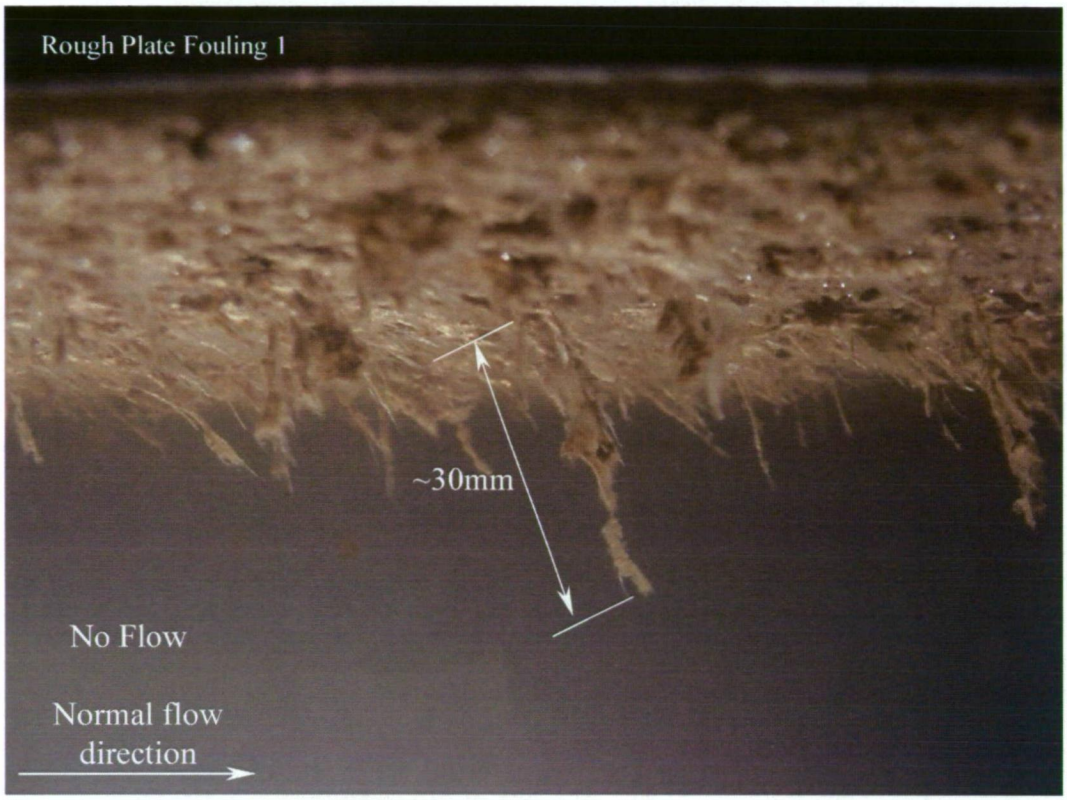

Figure 8.2: Side oblique view of rough plate fouling 1 biofilm showing large filaments.

The filaments were observed to be between approximately 10mm and 30mm in length. Figure 8.4 shows a photo from underneath in the downstream left hand corner where thick tufts of old biofilm were present. Filamentous streamers formed "tails" which moved about vigorously behind the biofilm clumps.

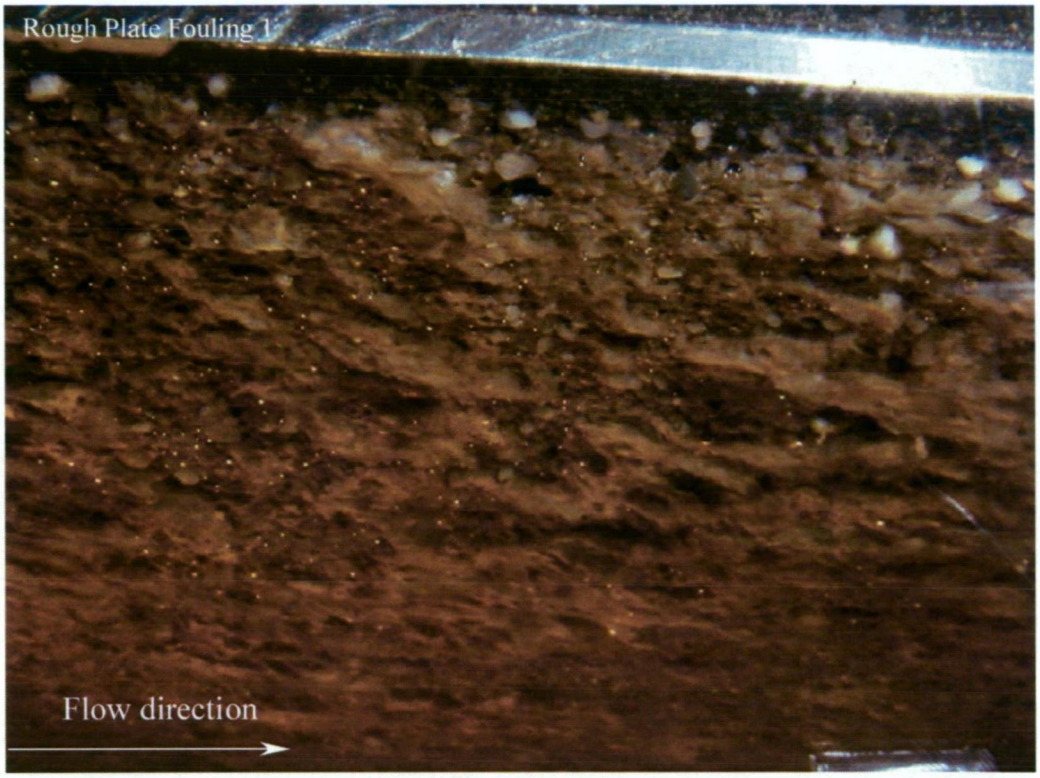

Figure 8.3: Photo from side of rough plate fouling 1 (oblique view) showing the biofilm laying flat in moving water. Flow speed is approximately 1m/s in this photo.

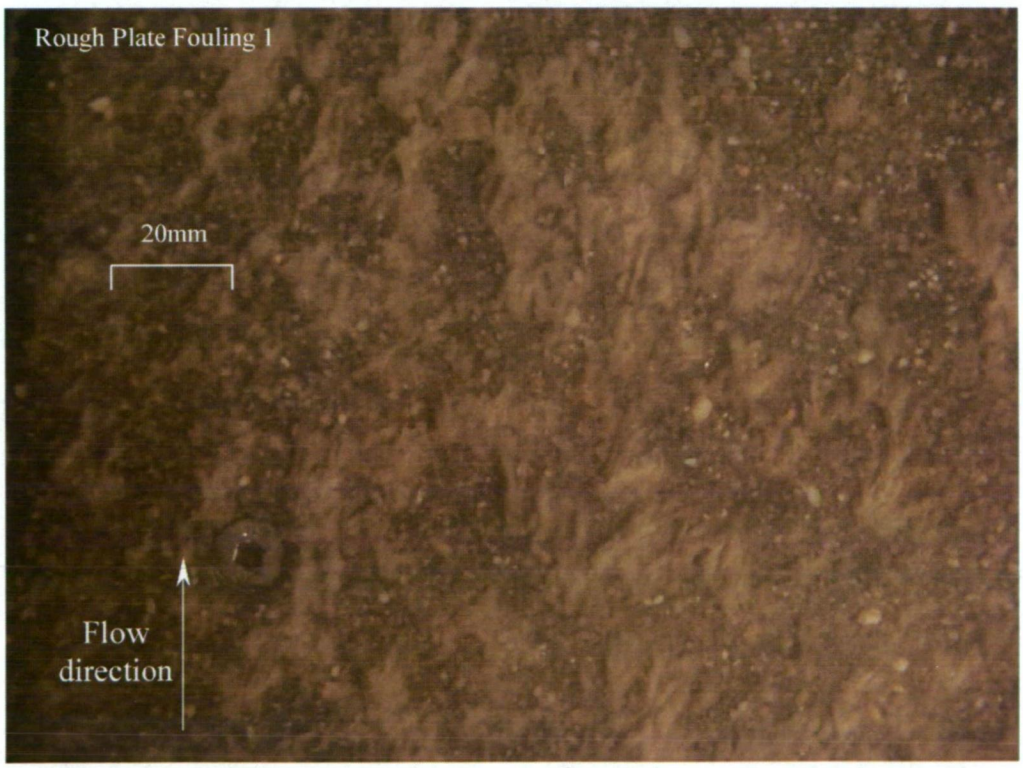

Figure 8.4: View from underneath of rough plate fouling 1 showing tufts of biofilm.

The rough plate fouling 1 was deployed for approximately 5 months at Tarraleah No. 1 Pond. After testing the plate was redeployed to No. 1 Pond without cleaning. The growth on the plate changed over time, with the dead clumps washed off. New growth became established and formed the biofilm for rough plate fouling 2 (Figure 8.5), which was taken out for measurement after an additional 4 months. The Tarraleah canal system ran full or near full for the duration of deployment allowing the plate to be fully submerged at all times.

Figure 8.5: The biofilm on rough plate fouling 2 was evenly distributed and healthy.

Rough plate fouling 2 had an even coverage of soft gelatinous growth, though it tended to form patches. Filaments were not immediately obvious, though some filaments approximately 2 to 10mm in length, distributed sparsely over the plate, were apparent when submerged in water.

Figure 8.6 shows the scale of the growth, and the size of the patches present. Figure 8.7 shows a more even area of growth, and interestingly, some of the larger grit particles can be seen to protrude through the biofilm.

After testing it was found that small portions of the artificially rough surface were missing at the leading edge of the plate (Figure 8.8). These had obviously come away from the plate during testing in the water tunnel. It is thought that at the water temperature of 23 – 28 deg C in the water tunnel during operation, the tar base becomes more prone to peeling. The missing areas of artificial roughness constituted less than 1% of the total plate area and would negligible affect on averaged results.

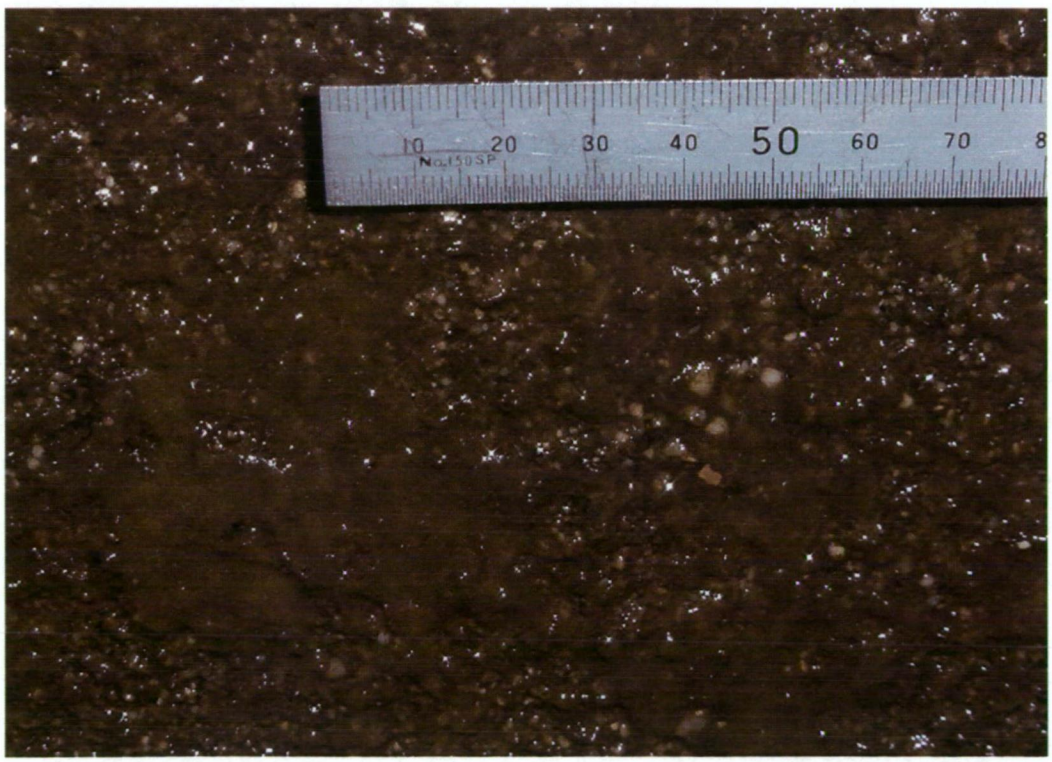

Figure 8.6: The scale of the growth for fouling 2 is shown. Many patches of biofilm approximately 30 to 50mm across are apparent across the entire plate.

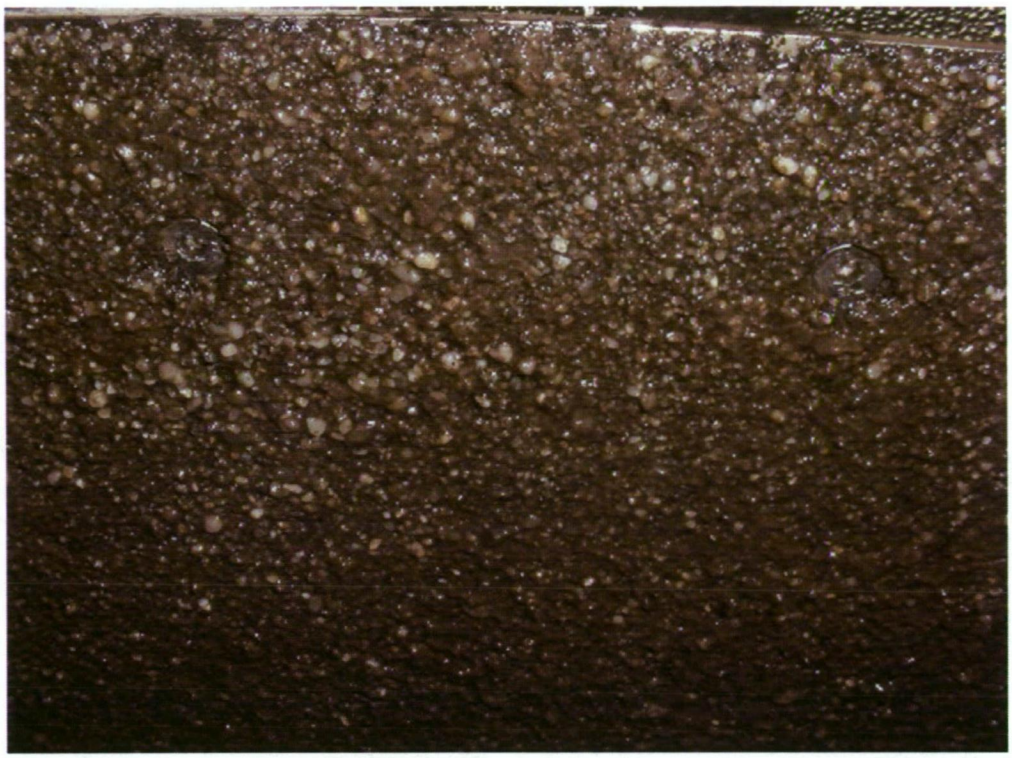

Figure 8.7: Wet growth clings to the plate when out of water. Grit particles protude though sections of the biofilm.

Figure 8.8 Rough plate fouling 2 ready to be re-deployed after testing. Seen at the leading edge of the plate (dashed ellipse) are missing portions of the rough surface.

After testing in the water tunnel the biofilm appearance had changed, with a more dull look. Some areas were starting to clump together and were dying. This was due to the effect of water temperatures and environmental shock to the biofilm.

A general identification of the biofilm on the rough plates was undertaken by Perkins and Hallegraeff (2006). Two types of diatom dominated the biofilm. They were a Tabellaria type diatom and a Gomphonema stalked diatom which were also found on the smooth plates and were previously shown in Chapter 7.

8.3 Boundary Layer Characteristics

Boundary layer profiles were obtained 95, 495 and 865mm downstream of the leading edge on the test plates on the working section centreline. Measurements were conducted at three Reynolds numbers of 1.2×10^6, 1.8×10^6, and 2.2×10^6 (based on test plate length of 997mm). This method is the same as for the smooth plates described in Chapter 7.

8.3.1 Mean Velocity Profiles

Table 8.1 presents a summary of results from the mean velocity boundary layer measurements. Results for the measurements are presented in Figures 8.9 to 8.17. Data for the rough plate clean, fouling 1 and fouling 2 are presented in each figure.

Table 8.1: Boundary layer parameters for clean and fouled rough plates.

Rough Plate - Clean																
	U (m/s)	δ (mm)	δ* (mm)	θ (mm)	u* (m/s)	c_f	H	Re_{XPlug}	Re_{XPlate}	Re_δ	Re_{δ^*}	Re_θ	k_s (mm)	Re_k	ε (mm)	Δu^+
x = 95mm (Plug 1)	1.04	23.44	3.63	2.79	0.0777	0.0111	1.30	1.17E+05	1.23E+06	2.88E+04	4.47E+03	3.43E+03	1.63	150	0.21	8.78
	1.60	22.03	3.48	2.62	0.1162	0.0105	1.33	1.80E+05	1.89E+06	4.17E+04	6.59E+03	4.96E+03	1.51	207	0.39	9.56
	1.94	21.33	3.36	2.54	0.1376	0.0100	1.32	2.18E+05	2.29E+06	4.90E+04	7.71E+03	5.83E+03	1.36	221	0.45	9.72
x = 495mm (Plug 2)	1.05	31.08	5.45	3.70	0.0614	0.0068	1.47	5.82E+05	1.17E+06	3.65E+04	6.41E+03	4.35E+03	1.79	123	0.87	8.17
	1.60	29.41	5.16	3.50	0.0904	0.0064	1.48	8.85E+05	1.78E+06	5.26E+04	9.23E+03	6.26E+03	1.46	147	0.83	8.71
	1.96	31.50	5.51	3.75	0.1028	0.0055	1.47	1.08E+06	2.18E+06	6.90E+04	1.21E+04	8.21E+03	1.05	121	0.58	8.23
x = 865mm (Plug 3)	1.06	38.22	7.01	4.55	0.0598	0.0064	1.54	1.08E+06	1.24E+06	4.76E+04	8.73E+03	5.67E+03	1.96	138	0.41	8.52
	1.63	38.67	7.05	4.60	0.0868	0.0057	1.53	1.51E+06	1.74E+06	6.73E+04	1.23E+04	8.01E+03	1.30	121	0.07	8.19
	1.98	37.92	6.90	4.51	0.1082	0.0060	1.53	1.83E+06	2.11E+06	8.02E+04	1.46E+04	9.54E+03	1.44	167	0.11	8.98

Rough Plate - Fouling 1 (Filamentous Biofilm)																
	U (m/s)	δ (mm)	δ* (mm)	θ (mm)	u* (m/s)	c_f	H	Re_{XPlug}	Re_{XPlate}	Re_δ	Re_{δ^*}	Re_θ	k_s (mm)	Re_k	ε (mm)	Δu+
x = 95mm (Plug 1)	1.05	16.47	2.89	1.96	0.0730	0.0097	1.47	1.10E+05	1.15E+06	1.91E+04	3.34E+03	2.27E+03	2.31	186	0.69	9.17
	1.61	17.08	2.96	2.03	0.1089	0.0091	1.45	1.69E+05	1.77E+06	3.03E+04	5.25E+03	3.61E+03	1.49	179	0.25	9.26
	1.96	15.66	2.73	1.86	0.1329	0.0092	1.47	2.05E+05	2.15E+06	3.37E+04	5.89E+03	4.02E+03	1.79	262	0.49	10.16
x = 495mm (Plug 2)	1.06	28.92	4.93	3.44	0.0667	0.0080	1.43	5.81E+05	1.17E+06	3.39E+04	5.78E+03	4.04E+03	2.41	179	1.33	9.13
	1.62	28.40	4.84	3.38	0.0932	0.0066	1.43	8.92E+05	1.80E+06	5.12E+04	8.72E+03	6.09E+03	1.70	176	1.30	9.10
	1.98	27.95	4.75	3.33	0.1091	0.0061	1.43	1.08E+06	2.19E+06	6.13E+04	1.04E+04	7.29E+03	1.42	172	1.27	9.03
x = 865mm (Plug 3)	1.05	37.55	6.64	4.47	0.0678	0.0084	1.49	1.02E+06	1.18E+06	4.45E+04	7.87E+03	5.30E+03	2.71	208	0.67	9.49
	1.61	36.86	6.57	4.39	0.0932	0.0067	1.50	1.58E+06	1.82E+06	6.72E+04	1.20E+04	8.00E+03	1.75	184	0.43	9.16
	1.96	34.99	6.23	4.17	0.1140	0.0067	1.50	1.92E+06	2.21E+06	7.76E+04	1.38E+04	9.24E+03	1.50	194	0.29	9.34

Rough Plate - Fouling 2 (Low-Form Gelatinous Biofilm)																
	U (m/s)	δ (mm)	δ* (mm)	θ (mm)	u* (m/s)	c_f	H	Re_{XPlug}	Re_{XPlate}	Re_δ	Re_{δ^*}	Re_θ	k_s (mm)	Re_k	ε (mm)	Δu+
x = 95mm (Plug 1)	1.03	14.42	2.40	1.72	0.0791	0.0117	1.40	1.08E+05	1.14E+06	1.64E+04	2.74E+03	1.96E+03	2.24	196	0.71	9.42
	1.60	15.01	2.48	1.79	0.1087	0.0093	1.39	1.67E+05	1.75E+06	2.64E+04	4.35E+03	3.14E+03	1.51	181	0.78	9.23
	1.93	14.04	2.33	1.67	0.1250	0.0084	1.39	2.02E+05	2.12E+06	2.99E+04	4.96E+03	3.56E+03	1.16	160	0.69	8.91
x = 495mm (Plug 2)	1.03	31.55	5.24	3.76	0.0626	0.0074	1.40	5.64E+05	1.14E+06	3.59E+04	5.97E+03	4.28E+03	2.17	151	1.31	8.50
	1.56	27.54	4.56	3.28	0.0936	0.0072	1.39	8.59E+05	1.73E+06	4.78E+04	7.92E+03	5.69E+03	1.41	146	0.87	8.64
	1.92	29.43	4.84	3.50	0.1101	0.0066	1.38	1.06E+06	2.13E+06	6.28E+04	1.03E+04	7.47E+03	1.23	150	0.80	8.72
x = 865mm (Plug 3)	1.02	34.04	6.13	4.05	0.0630	0.0077	1.51	9.94E+05	1.15E+06	3.91E+04	7.04E+03	4.66E+03	2.93	209	1.10	9.47
	1.56	33.86	5.91	4.03	0.0912	0.0068	1.47	1.53E+06	1.76E+06	5.97E+04	1.04E+04	7.11E+03	2.10	216	0.85	9.48
	1.91	32.66	5.84	3.89	0.1027	0.0058	1.50	1.86E+06	2.15E+06	7.03E+04	1.26E+04	8.37E+03	1.42	164	0.69	8.71

Figures 8.9, 8.10 and 8.11 show the mean velocity profiles for the clean and fouled rough test plates. The law of the wall is fitted to all of the velocity profiles (clean and fouled) in the form presented in Equation 2.3. Also plotted on the rough plate clean figure are the measured velocity profiles plotted using the rough law of the wall coordinates $\left(\frac{y+\varepsilon}{k_s}\right)$ of Equation 2.4. Finally, the $1/5^{th}$ power law is also plotted for comparison.

Results at x=95mm, display similar characteristics to those observed for the smooth test plate data, indicative of a thinning of the boundary layer due to flow leakage the plate leading edge. The profiles are depressed at this location compared to the law of the wall but quickly recover at x=495 and x=865mm.

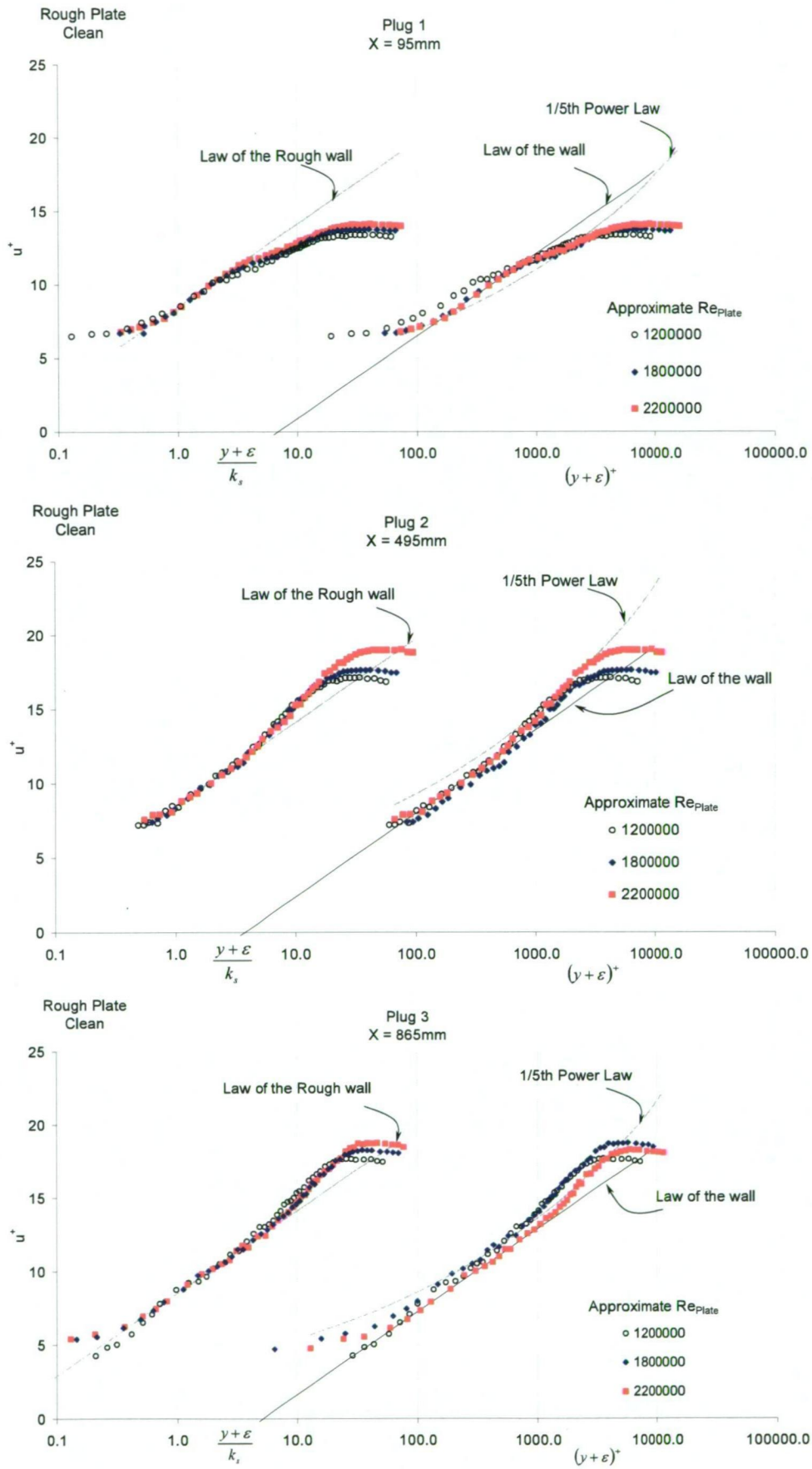

Figure 8.9: Velocity profiles for rough plate clean.

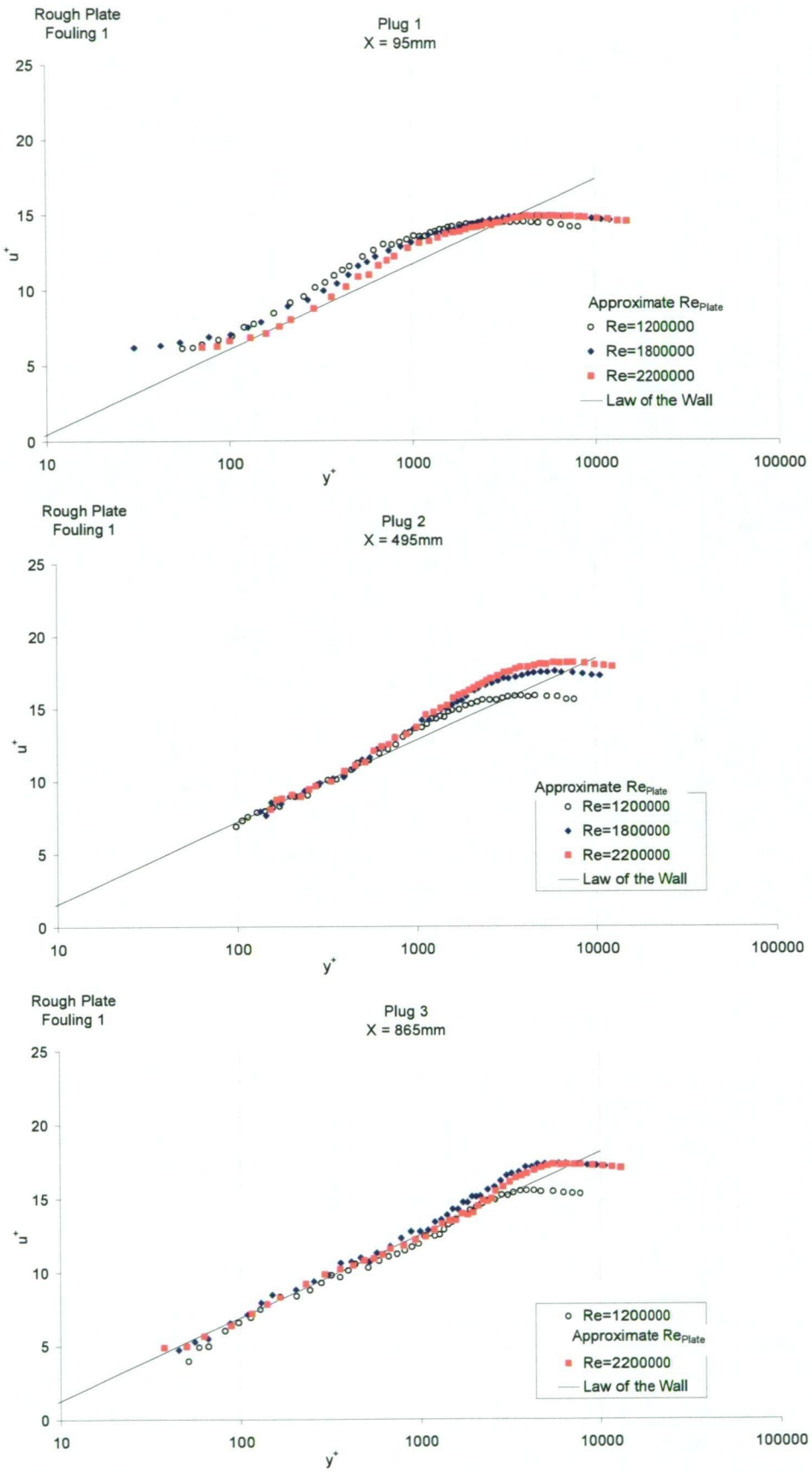

Figure 8.10: Velocity profiles for rough plate fouling 1 (filamentous biofilm).

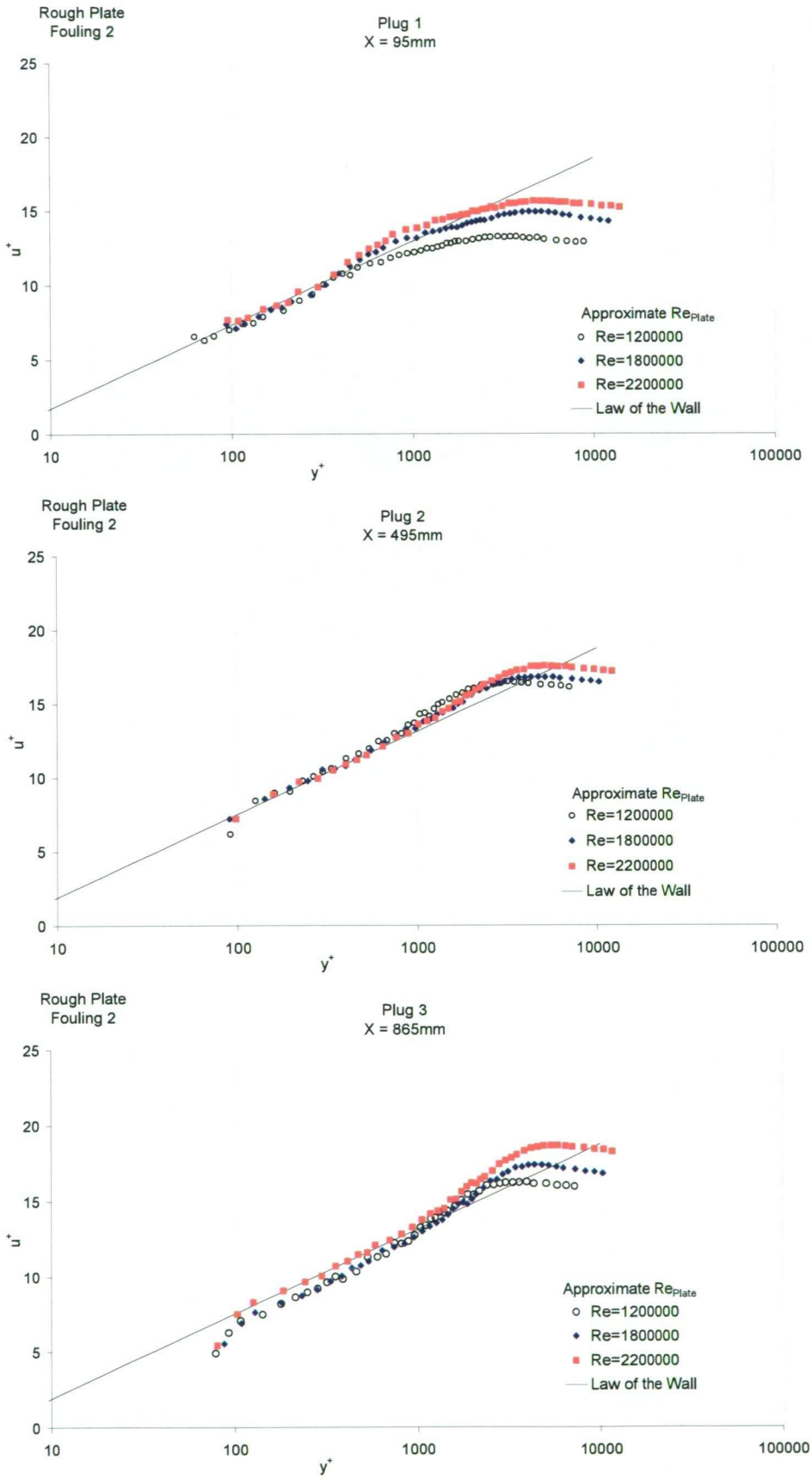

Figure 8.11: Velocity profiles for rough plate fouling 2 (low-form gelatinous biofilm).

Boundary layer shape factors shown in Figure 8.12 show the clean rough plate values changing rapidly over the length of the plate compared to the relatively constant valuesof the smooth plate clean in Chapter 7. Fouling 1 and 2 show the shape factor reaching a maximum at the most downstream location at x=865mm.

The momentum thickness measured along the rough plate clean are much greater than for smooth plate clean as shown in Figure 8.13. The lowest momentum thickness values were, consistently, very much lower at the leading edge of each rough plate. This value was influenced by the reduction in boundary layer fluid due to the gap at the leading edge of the plate.

The momentum thickness increased, from x=95mm to x=865mm, by 78%, 123% and 133% respectively for rough plate clean, fouling 1 and fouling 2 respectively at $\mathrm{Re}_{Plate} = 2.2 \times 10^6$.

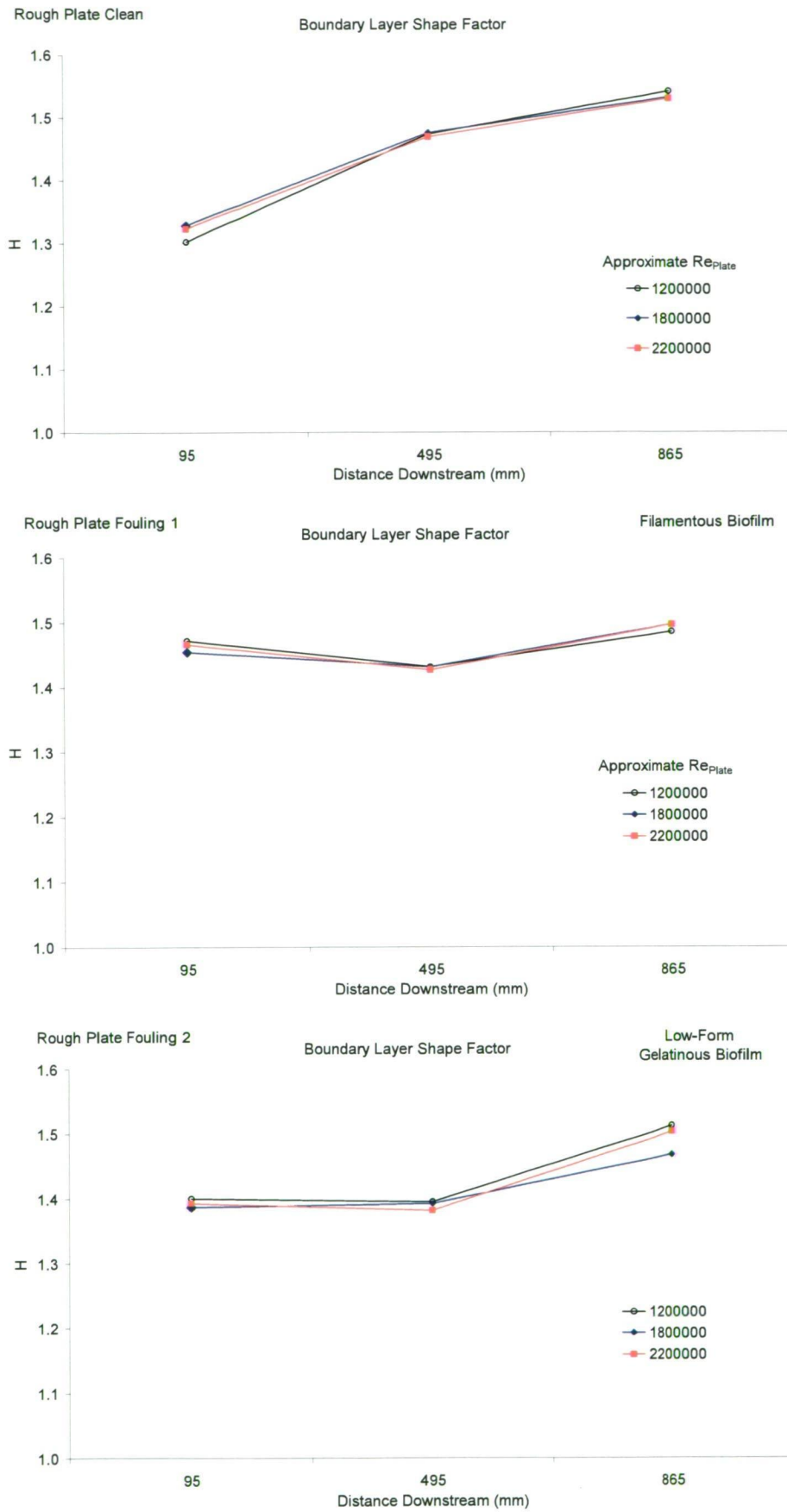

Figure 8.12: Boundary layer shape factor for the measured plates.

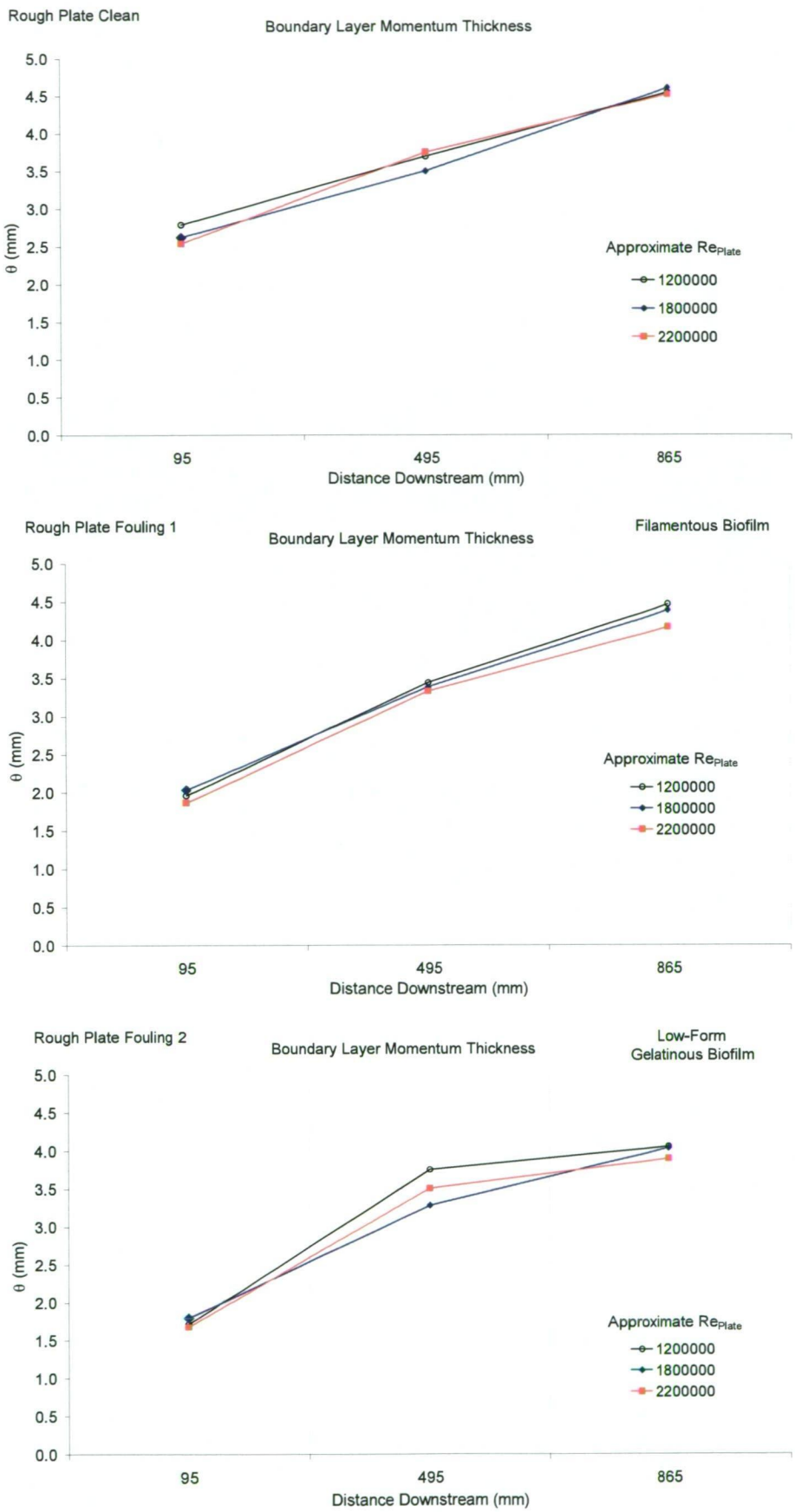

Figure 8.13: Boundary layer momentum thicknesses.

Local skin friction coefficients, c_f, reduced with distance downstream on each plate. This is in accordance with boundary layer growth at constant roughness (Figure 8.14). Rough plate fouling 1 displayed generally higher c_f values than the other rough plate measurements.

Wall shear velocities shown in Figure 8.15 for rough plate clean are higher than for the smooth plate clean results of Chapter 7. Importantly, rough plate clean wall shear velocities are representative of Tarraleah No. 1 Canal wall shear velocities presented in Chapter 6. Results are particularly good at the middle and downstream areas of the test plate.

Fouling causes a general increase in wall shear velocity, and interestingly for rough plate measurements, they compare well to the fouled smooth plates in Chapter 7.

Comparisons with the Tarraleah No. 1 Canal deployment conditions are also made by estimating the local skin friction by using Equation 8.1 (White, 2006), for a rough plate, where k_s was taken as 1.5mm.This is an approximate average from Table 8.1. It is assumed in using this equation that there is no initial laminar boundary layer region at the forward section of the plate and the leading edge flow velocity in the field at Pond No. 1 when flowing full is approximately 1m/s. x was taken as 95, 495 and 865mm representing the same locations where boundary layer measurements were taken in the water tunnel. Mean flow velocity at Pond No. 1 was taken as 1m/s and water temperature was taken as 10 deg C.

$$c_f = \left[2.87 + 1.58 \log \frac{x}{k_s}\right]^{-2.5} \qquad \text{Equation 8.1}$$

A comparison of the theoretical friction and wall shear velocities (Figure 8.14 and 8.15) for the rough plate clean (representing the initial state the plate was deployed in) show that the deployment conditions closely match the measured values at $\mathrm{Re}_{Plate} = 1.2 \times 10^6$. This validates the use of the field installation.

Chapter 9 further investigates the biofilm behaviour in relation to u^*, and looks at this result in the contact of field conduits.

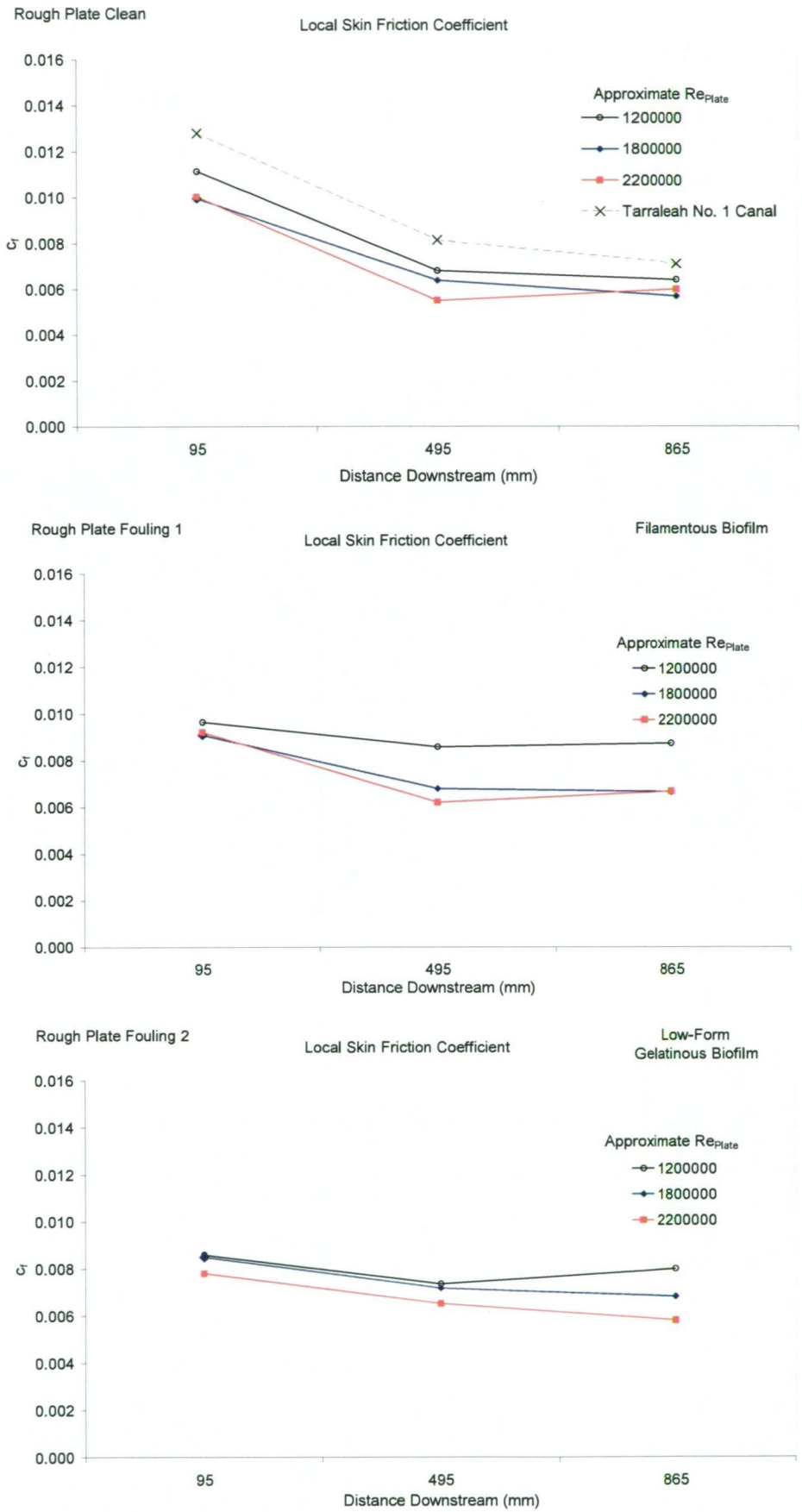

Figure 8.14: Local skin friction coefficient derived from log-law slope method.

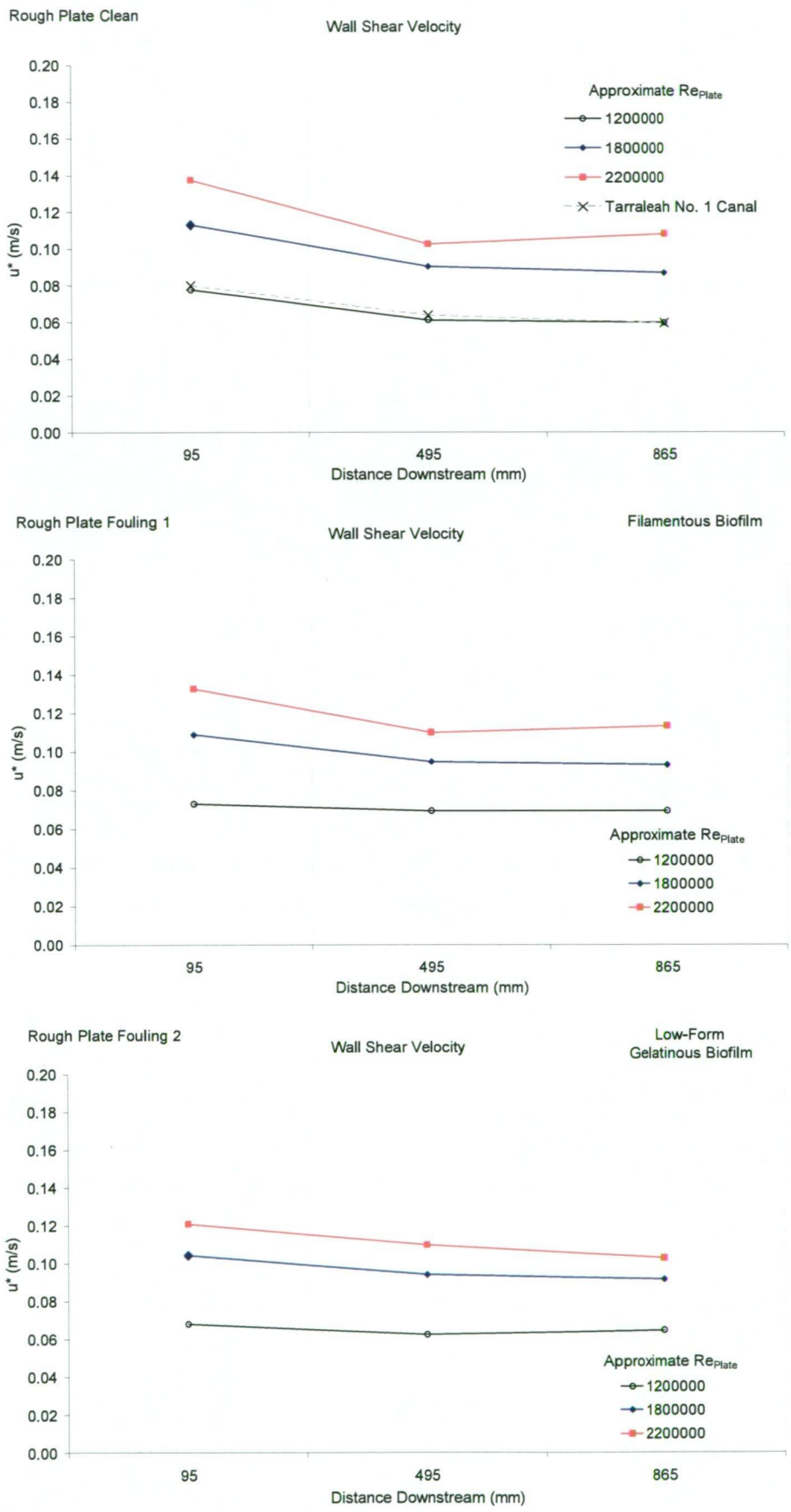

Figure 8.15: Wall shear velocity for clean and fouled plates.

The measured roughness is presented in Figure 8.16. Equation 2.4 (Chapter 2) was used to find k_s, which assumes there are fully hydraulic rough conditions. This is confirmed in Table 8.1 where the roughness Reynolds numbers are all greater than 100.

Similar roughness values were obtained for each plate at x=95mm. Rough plate clean then show relatively constant roughness, with fouling 1 and fouling 2 showing general increases in roughness.

It was observed (Figure 8.1) that the majority of biofouling occurred on the rear, lower half of the rough plate fouling 1. The boundary layer velocity profiles were taken at the plate longitudinal centreline and so did not measure effects of the more filamentous biofilm. Higher roughness values could be expected if data were taken over this more fouled region.

Rough plate fouling 2 shows perhaps the most interesting behaviour, as the measured roughness clearly increased with distance downstream, and the measured roughness was clearly different for each flow Reynolds number.

There is a measured decrease in k_s at higher flow speeds, which, as suggested in Chapter 7, may be related to the thinning of the biofilm, and changes in the effective wall position as a results of the biofilm thinning.

Compared to the rough plate clean, a 27% increase in roughness (average of all roughness data) was measured for rough plate fouling 1, and a 20% increase for rough plate fouling 2.

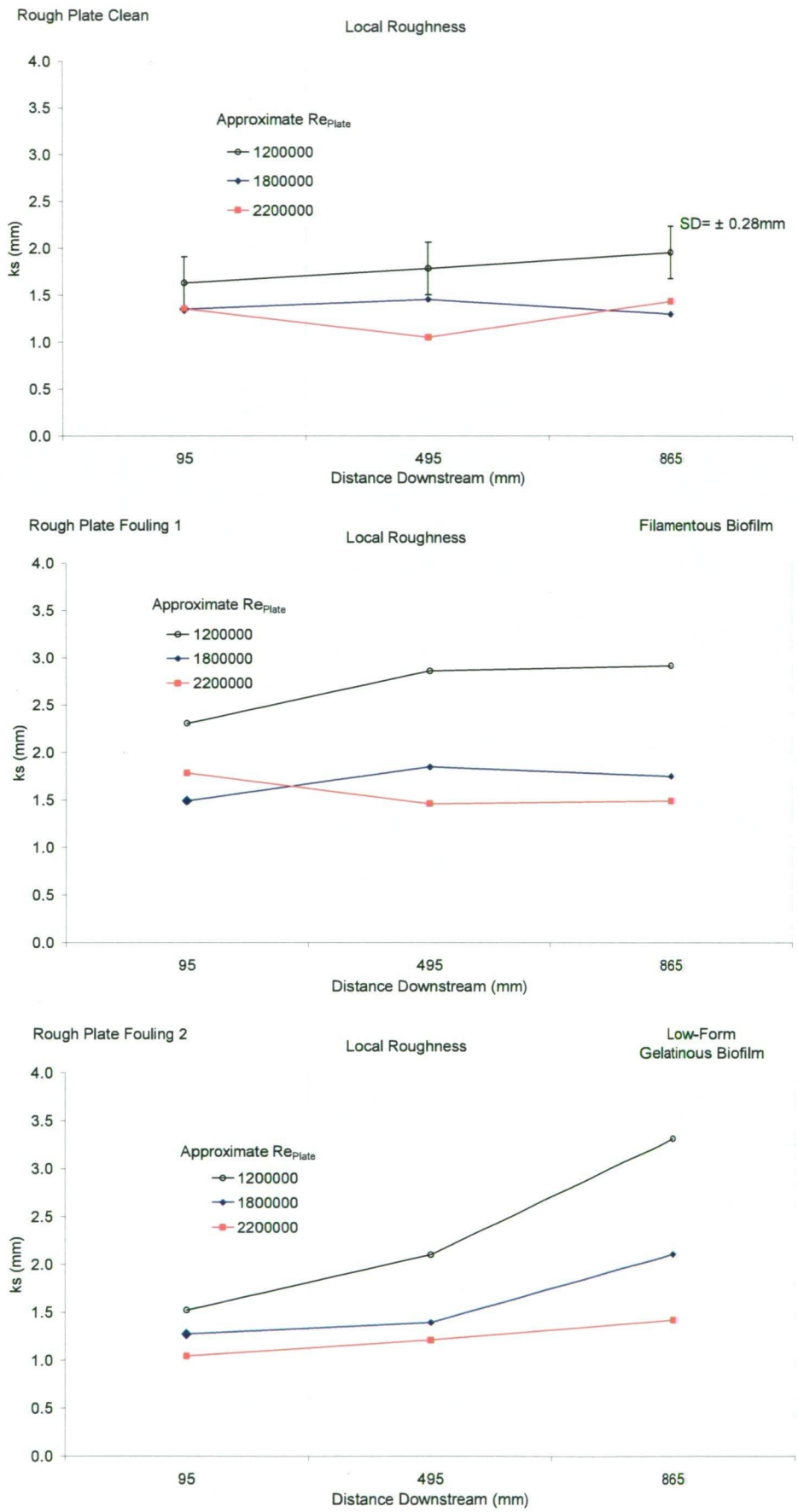

Figure 8.16: Local roughness values determined from velocity profiles.

An estimate of error in k_s was made by taking the average of the standard deviations (SD) of measured at each plug (x = 95, 495 and 865 mm) for the rough plate clean. This gave an SD of ± 0.28 mm. The values for rough plate clean at $Re_{Plate} = 1.2 \times 10^6$ are shown with error bars demonstrating this uncertainty.

To show how sensitive k_s values are to the effective wall position, ε was varied by ± 0.1 mm and the changes in friction and roughness values obtained. Table 8.2 presents these data, for plug 3 only at x = 865 mm from the plate leading edge. This analysis gives an SD in k_s of ± 0.41 mm for an error in ε of ± 0.1 mm (at plug 3 for $Re_{X\ Plate} = 2.11 \times 10^6$).

Table 8.2: Rough plate clean error analysis at plug 3.

Change in Wall Position	Re_{XPlate}	u* (m/s)	c_f	k_s (mm)	Re_k	ε (mm)	Δu+
	1.24E+06	0.0539	0.0052	1.21	77	0.31	7.09
- 0.1mm	1.74E+06	0.0814	0.0050	0.94	82	-0.03	7.24
	2.11E+06	0.1017	0.0053	1.05	115	0.01	8.07
	1.24E+06	0.0598	0.0064	1.96	138	0.41	8.52
Original	1.74E+06	0.0868	0.0057	1.30	121	0.07	8.19
	2.11E+06	0.1082	0.0060	1.44	167	0.11	8.98
	1.24E+06	0.0622	0.0069	2.37	174	0.51	9.08
+ 0.1mm	1.74E+06	0.0913	0.0063	1.66	162	0.17	8.91
	2.11E+06	0.1143	0.0067	1.87	229	0.21	9.75

A comparison of the rough plate clean, fouling 1 and fouling 2 velocity profiles at plug 3 at the three Reynolds numbers are shown in Figure 8.17. The velocity deficit is not as clearly seen in these profiles as it is for the smooth plates in Chapter 7.

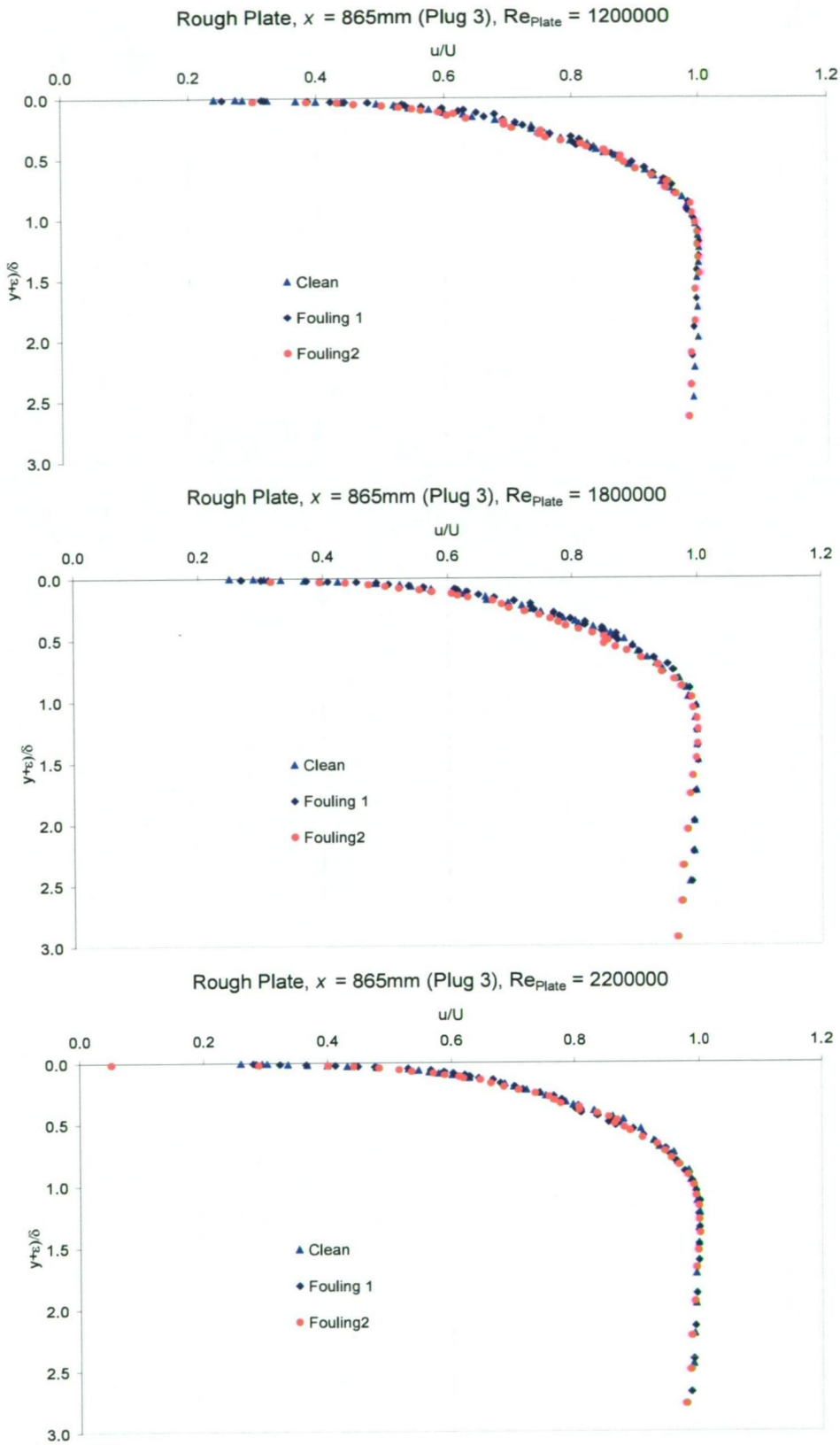

Figure 8.17: A comparison of velocity profiles for clean and fouled rough plates.

8.3.2 Turbulence Profiles

Despite the difficulties of turbulence measurement using hotfilm probes experienced in Chapter 6, boundary layer traverses were again made using a different hotfilm probe. A Dantec Dynamics hotfilm probe, type 55 R14 (Figure 8.18, where $l = 1.25mm$ and $d = 70\mu m$), and Dantec Dynamics 4mm 55H21 probe support was used for the rough plate clean measurements. The same 10 mm extended support was used for all measurements, which was securely clamped to the precision height gauge for manual traversing. A DISA 55M CTA was used in conjunction with all probe combinations.

Turbulence intentities were determined from the RMS of velocity fluctuations using the same methods and corrections described in Chapter 6.

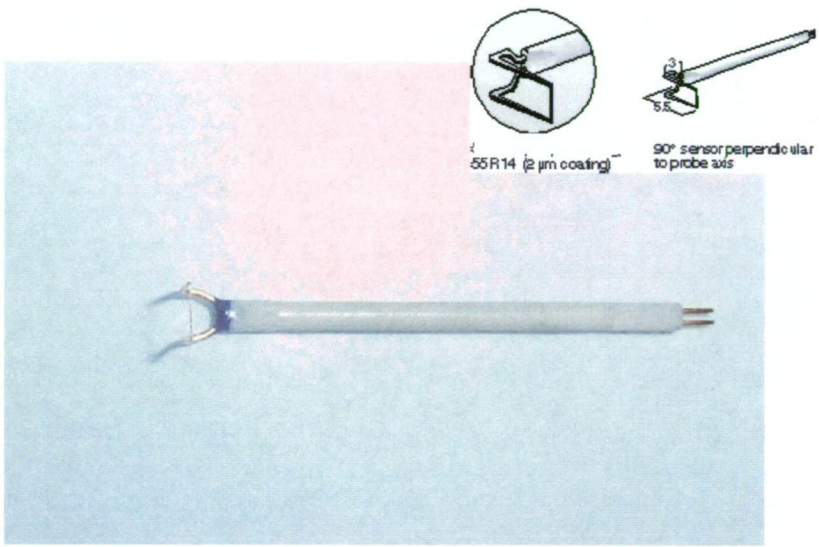

Figure 8.18: Dantec Dynamics hotfilm probe, type 55 R14.

The probe sensor for the rough plate measurements was 5.5mm upstream of the probe stem centreline. This made the measurements 109.5, 509.5 and 879.5 mm downstream of the test plate leading edge.

The turbulence intensities are presented in Figure 8.19, and are also shown with the smooth plate data of Klebanoff (1955) for comparison.

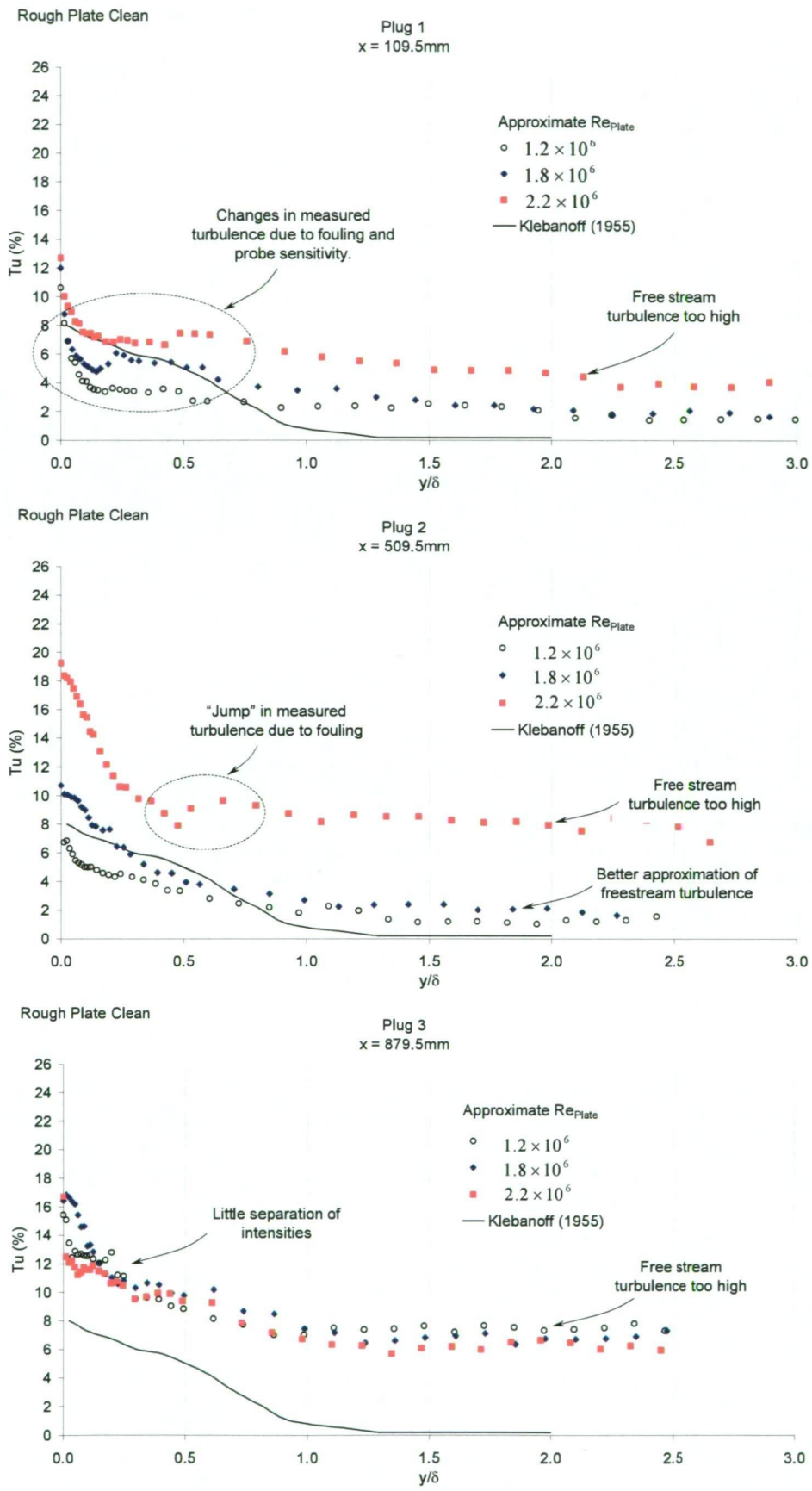

Figure 8.19: Turbulence intensities for rough plate clean using hotfilm probe.

The rough plate clean data show significant signal drift and shift problems due to fouling of the probe sensor. Water temperature variations also required temperature corrections to be made to the measured voltages using the correlation of Collis and Williams (1959). However the exponents stated for use for this correlation are only suggested for use up to probe Reynolds numbers of $\mathrm{Re}_{film} = 140$, and at these Reynolds numbers it is noted that eddy shedding may be apparent, further limiting the use of this correlation method. Bradshaw (1971) and Richardson and McQuivey (1968) both note that there are no general methods available for the calibration of hotfilm probes in water.

Due to the fouling problems using a hotfilm probe and subsequent inconclusive results, turbulence measurements using hotfilm probes were not sought for any biofouled test plates. Presented instead, for comparison purposes with the smooth acrylic plate data of Chapter 6, are the results from using a Pitot probe used to measure unsteady pressures. Figure 8.20 shows the results for these measurements, conducted at the downstream plug 3 at X=865 mm only. A free stream turbulence intensity of between 1 and 2% has been measured, consistent with that shown in Chapter 6. Much greater intensity levels have been measured nearer the wall, which indicates the greater turbulence production by the rough surface. The edge of the boundary layer is also indicated.

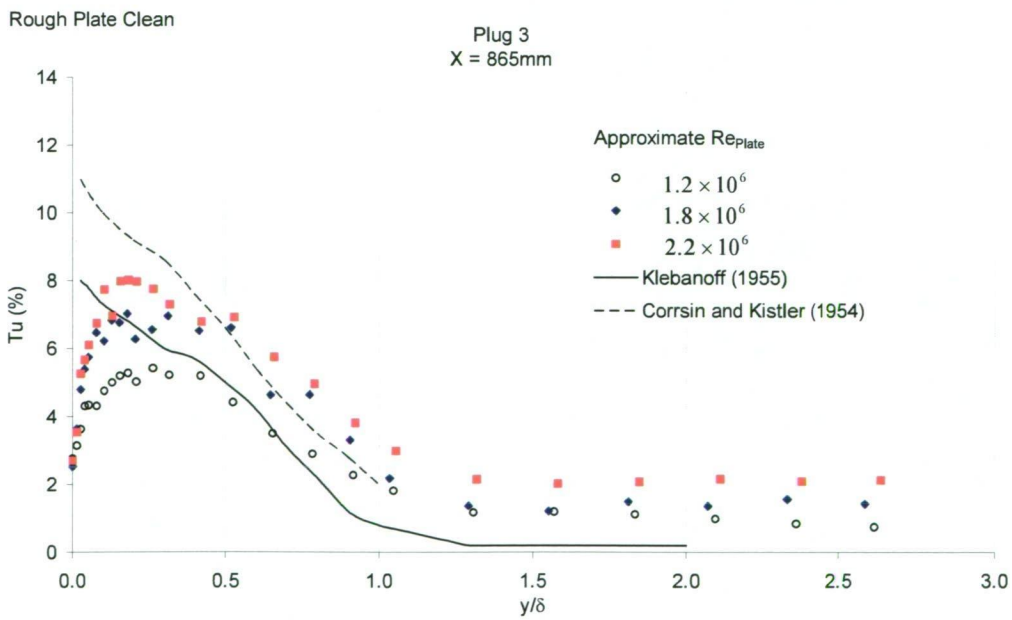

Figure 8.20: Turbulence intensities for rough plate clean using Pitot probe.

Streamwise turbulence intensities by Corrsin and Kistler (1954), from their work using rough walls, is provided (in addition to the data by Klebanoff) in Figure 8.20 for comparison. The data of Corrsin and Kistler (1954) shows similar properties as Klebanoff's except that turbulence intensities are generally increased in the near wall region, and maintain higher values to the edge of the boundary layer. This is what the rough wall data in Figure 8.20 obtained from the present study also shows.

The papers of Antonia and Luxton (1971; 1972) contain details on roughness effects on turbulence intensities in the near wall region and discuss similar properties as described.

Representative data traces are shown in Figure 8.21, with the probe at the wall (probe tip aligned approximately with the top of the roughness elements), 5mm from the wall (within the boundary layer), and 100 mm (within the bulk flow region). Spectral analyis of these data traces are shown in Figure 8.22 showing a frequency reponse of up to approximately 30Hz. Data frequencies are slightly greater than for the equivalent smooth wall (acrylic plate) data.

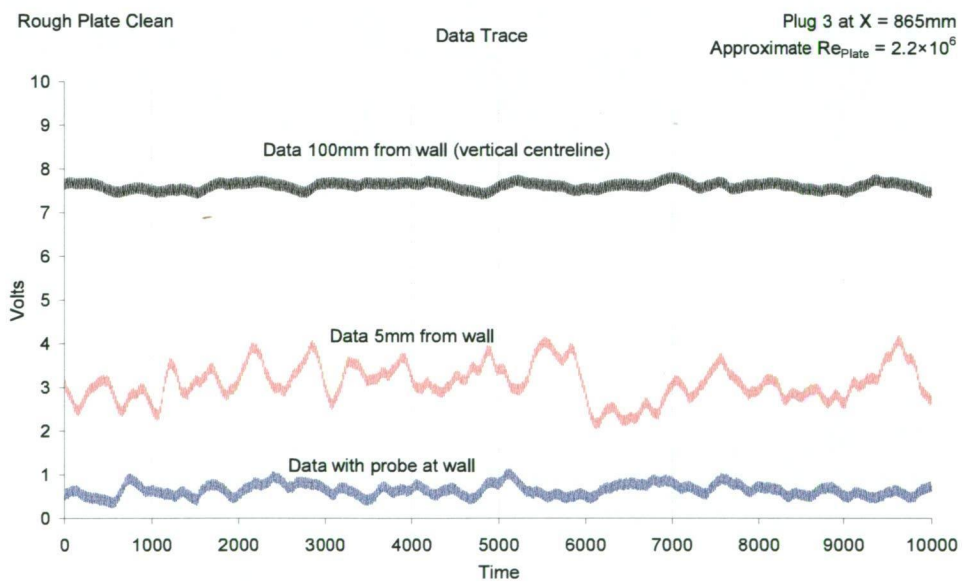

Figure 8.21: Data traces for rough plate clean.

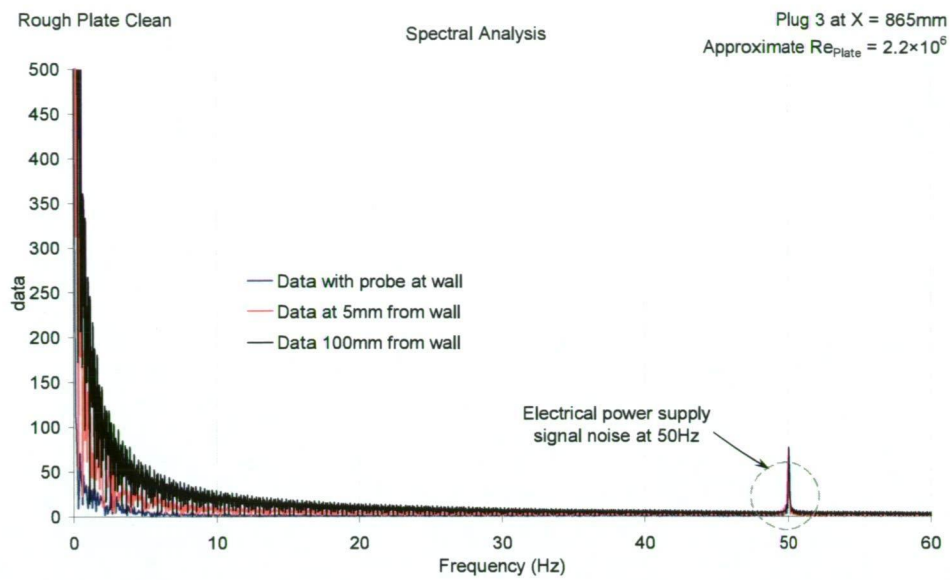

Figure 8.22: Spectral analysis of data trace for rough plate clean.

8.4 Total Drag Characteristics

Total drag measurements were undertaken on a clean rough plate, and two fouled rough plates denoted as fouling 1 and fouling 2. Corrections were made to the total drag measurements in the same manner as described in Chapter 7 for the smooth plates.

Figure 8.23 shows the results of the total drag measurements presented as coefficients of drag against plate Reynolds number.

The terminology of "Measured Drag 1" and "Measured Drag 2" is the same as used in Chapter 7. Differences between the two measurements are a result of changes in biofilm character.

Error bars are shown for the C_D values on the total drag plots. Error bars have only been included for Measured Drag 1 for the rough plate fouling cases for clarity of the plots. Values of $k_s \pm SD$ are also given on the figures.

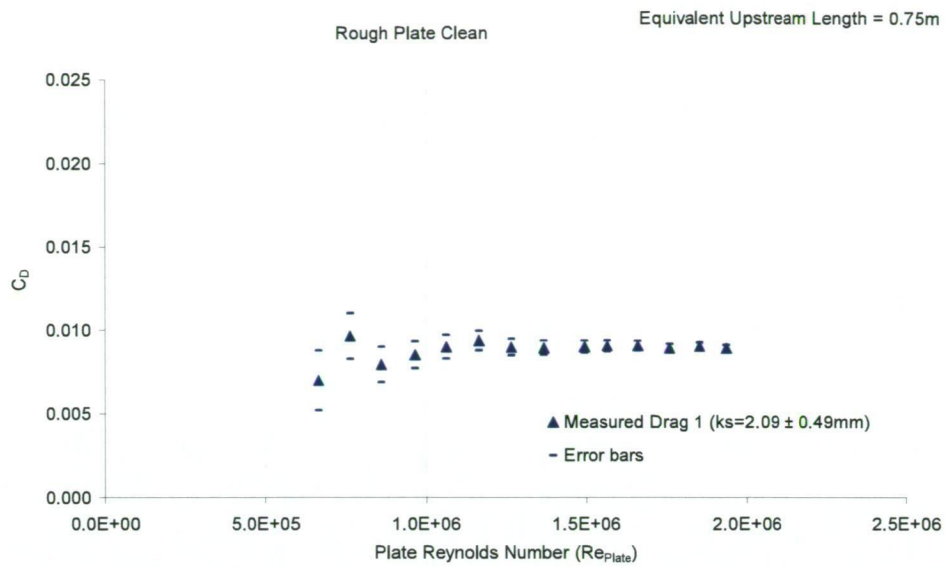

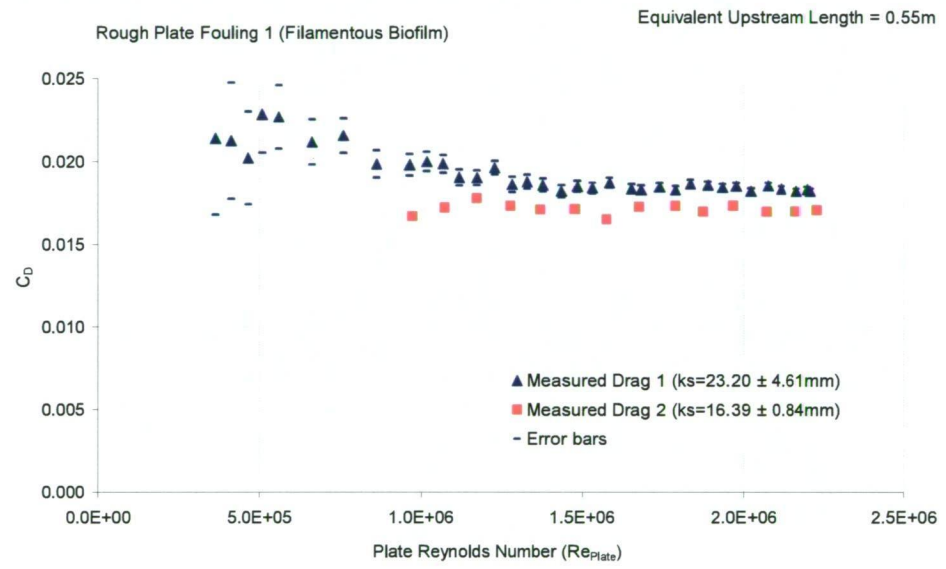

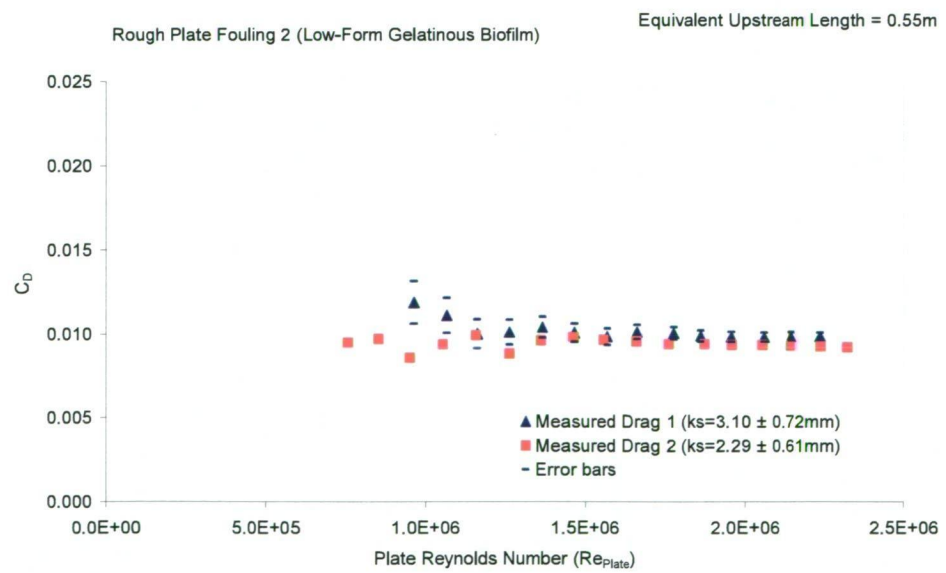

Figure 8.23: Total drag measurements for clean and fouled rough test plates.

The C_D values measured for rough plate clean show good agreements with the average of local skin friction values determined from the boundary layer measurements.

Total drag measurements for rough plate fouling 2 are slighty higher than the local skin friction measurements indicate. This suggests that either there was biofilm coverage elsewhere on the test plate different than that along the plate longitudinal centreline, or that there is an increased drag measured possibly due to flow leakage at the leading edge of the test plate, thinning the boundary layer and increasing drag on the forward section of the test plate.

Perhaps the most interesting results is that for rough plate fouling 1. The highest drag was measured on rough plate fouling 1 where the roughness was measured to be 23.2mm (±4.61mm) at the commencement of water tunnel testing. Figure 8.1 shows the rough plate fouling 1 and the highly skewed nature of the biofilm. It was observed that the thickest and "roughest" part of the biofilm was not on the plate longitudinal centreline (which was measured by the boundary layer profiles), but on the right hand side downstream half of the plate where the most numerous and longest filaments were found. It is clear that this area of biofilm had a large impact on the total drag measured on the plate.

Although the rough plate fouling 1 roughness was measured to be hydraulically rough (shown in Table 8.1), there still seemed to be a dependency on Reynolds number, particularly at lower Reynolds numbers. Figure 8.24 shows the sandgrain roughness derived from Equation 7.4. It is thought the filamentous biofilm may play a role in this roughness behaviour.

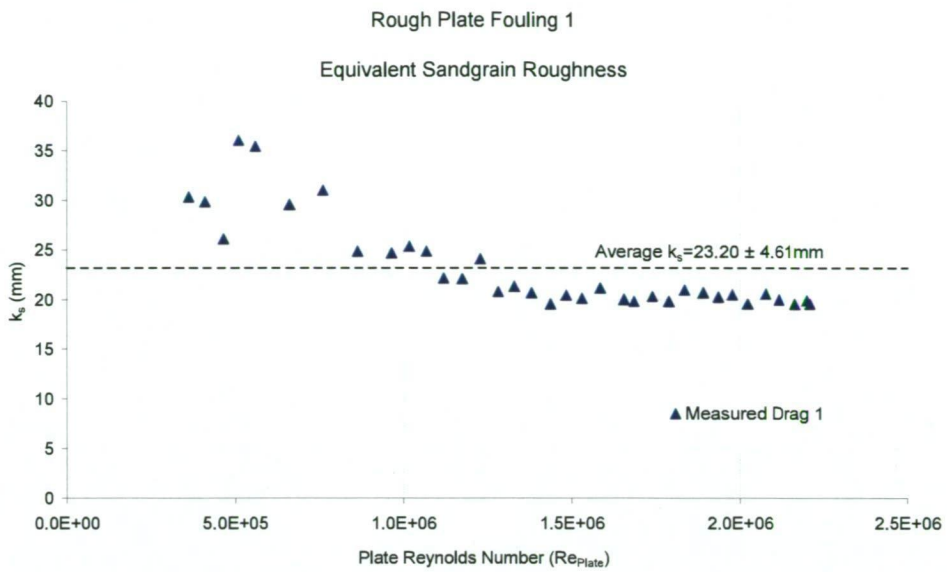

Figure 8.24: Measured roughness from total drag for rough plate fouling 1.

A 119.1% increase in total drag was measured for fouling 1 over rough plate clean conditions (using measured drag 1). An increase of 15.4% in total drag was recorded for fouling 2.

A general reduction in total drag was measured for both rough plate fouling 1 and fouling 2 over the course of testing due to loss of biofilm, as shown in Figure 8.23.

8.5 Surface Character from Photogrammetry

Using the same method as for the smooth plate studies in Chapter 7, the rough plates were photographed just prior to being placed in the water tunnel for testing. For the fouled plates cases, this was immediataly after being retrieved from the field.

For reference Figure 8.25 shows the where the photographs were taken over the plates.

Tables 8.3, 8.4 and 8.5 present the roughness information obtained from rough plate clean, fouling 1 and fouling 2 respectively.

All surface profiles used to derive the roughness information for rough plate fouling 1 and 2, presented in Tables 8.3 and 8.4 are included in the Appendix.

The clean plate data compares well to the measured roughness from the water tunnel, with the Rt paramater best providing a sandgrain diameter type length scale. Data also compares well with the fine grit small plate results from section 5.6 of Chapter 5 and particle size distribution of Chapter 4. Peak counts for rough plate clean are slightly higher than the results of Chapter 5, though this can be explained by the use of filtering to remove long wavelenght undulations.

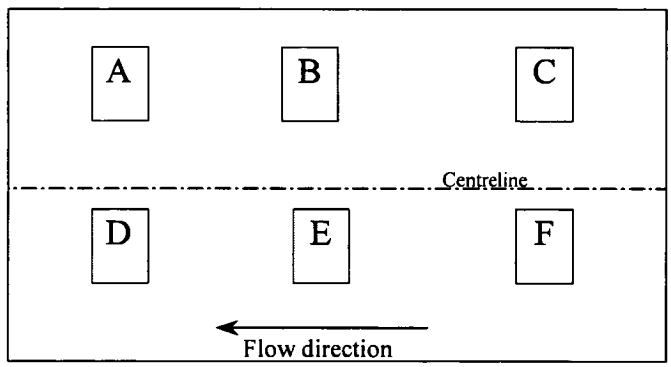

Figure 8.25: Layout of the photography windows for the large test plates.

Table 8.3: Summary of photogrammetry results for rough plate clean.

Photographed Area	Roughness Parameters (mm)					Statistical moments				Peak
	Ra	Rq	Rp	Rv	Rt	Mean	Variance	Skewness	Kurtosis	Count
Window A	0.24	0.31	0.88	-0.58	1.46	0.58	0.10	0.58	0.38	13.20
Window B	0.25	0.32	0.94	-0.80	1.74	0.80	0.11	0.11	0.12	14.40
Window C	0.20	0.26	0.90	-0.57	1.47	0.57	0.07	0.76	1.42	15.40
Window D	0.26	0.32	1.13	-0.78	1.91	0.78	0.10	0.47	1.66	14.80
Window E	0.18	0.22	0.62	-0.57	1.19	0.57	0.05	0.26	0.16	16.60
Window F	0.19	0.24	0.73	-0.67	1.39	0.67	0.06	0.25	1.57	16.40

Table 8.4: Summary of photogrammetry results for rough plate fouling 1.

Photographed Area	Roughness Parameters (mm)					Statistical moments				Peak	Mean Biofilm
	Ra	Rq	Rp	Rv	Rt	Mean	Variance	Skewness	Kurtosis	Count	Thickness (mm)
Window A	0.22	0.29	1.03	-0.73	1.76	0.74	0.09	0.74	2.11	11.80	0.16
Window B	0.21	0.26	0.72	-0.66	1.38	0.66	0.07	0.11	0.26	11.60	-0.14
Window C	0.29	0.36	1.08	-0.86	1.94	0.86	0.15	0.36	1.00	11.80	0.29
Window D	0.34	0.42	1.06	-0.76	1.82	0.76	0.17	0.53	-0.19	10.40	-0.02
Window E	0.29	0.37	1.61	-0.68	2.29	0.68	0.14	1.11	2.80	10.40	0.11
Window F	0.28	0.35	0.97	-0.75	1.72	0.75	0.13	0.44	0.14	12.00	0.09

Table 8.5: Summary of photogrammetry results for rough plate fouling 2.

Photographed Area	Roughness Parameters (mm)					Statistical moments				Peak Count	Mean Biofilm Thickness (mm)
	Ra	Rq	Rp	Rv	Rt	Mean	Variance	Skewness	Kurtosis		
Window A							No Data				
Window B							No Data				
Window C							No Data				
Window D	0.33	0.42	1.02	-0.98	2.00	0.98	0.18	0.09	0.61	9.40	0.20
Window E	0.36	0.47	1.40	-1.05	2.45	1.05	0.23	0.61	0.84	8.20	0.47
Window F	0.33	0.42	1.16	-0.91	2.07	0.76	0.18	0.54	0.15	8.60	0.09

Both rough plate fouling 1 and fouling 1 show generally greater Rt values and increased roughness mean than for rough plate clean. Peak counts are also significantly reduced, which corresponds to the findings of Chapter 5 for the fouling of fine grit surfaces. Here it was found that two types of behaviour influence this. The first is that the biofilms may fill in the valleys and gaps between roughness elements, "smoothing the surface." However, from the results in Tables 8.3 and 8.4, is more likely the second type of behaviour occuring here where clumps of biofilm significantly bias the mean line and Rq value of the surface profiles, so that the "cut-off" for peak counting is effectively increased. This is shown in Figure 8.27 where larger clumps of biofilm can be seen reprodeced in the surface profile plots.

The estimates of biofilm thickness on rough plates are difficult than for smooth plates, as a surface datum is not clearly defined. In addition, as shown in Chapter 5, grit on the surface can be washed off which reduces the efective surface mean. To measure the biofilm thickness for the rough plates, the clean plate mean Z height filtered data for each window was subtracted from the mean Z height fliltered data of the fouled plates. This was achievable as the photogrammetry rig for the large test plates (described in Chapter 5) allows all Z height data to be obtained referenced to the camera support as the datum.

Surface data for rough plate fouling 2 was difficult to obtain due to the heavy fouling present on the plate creating a very dark surface to photograph. Different lens appatures, film exposures and lighting arrangements were used, with the results being only windows D, E and F being satisfactorily resolved into the photogrammetric models. Third party software was also used to manipulated the digital images (scanned film) to change contrast and bightness with little success.

Figures 8.26, 8.27 and 8.28 shows digital images derived from the photogrammetry process, and surface profiles for a typical area of fouling. The Z height has been exaggerated in these Figures to better see the surface topography.

The most noticable difference between the smooth plate surface data of Chapter 7 and rough plate clean data presented here, is the more clearly defined surface, with roughness elements well represented. The surface "noise" evident with the smooth surface photogrammetry is not as apparent, as the surface texture is usually better.

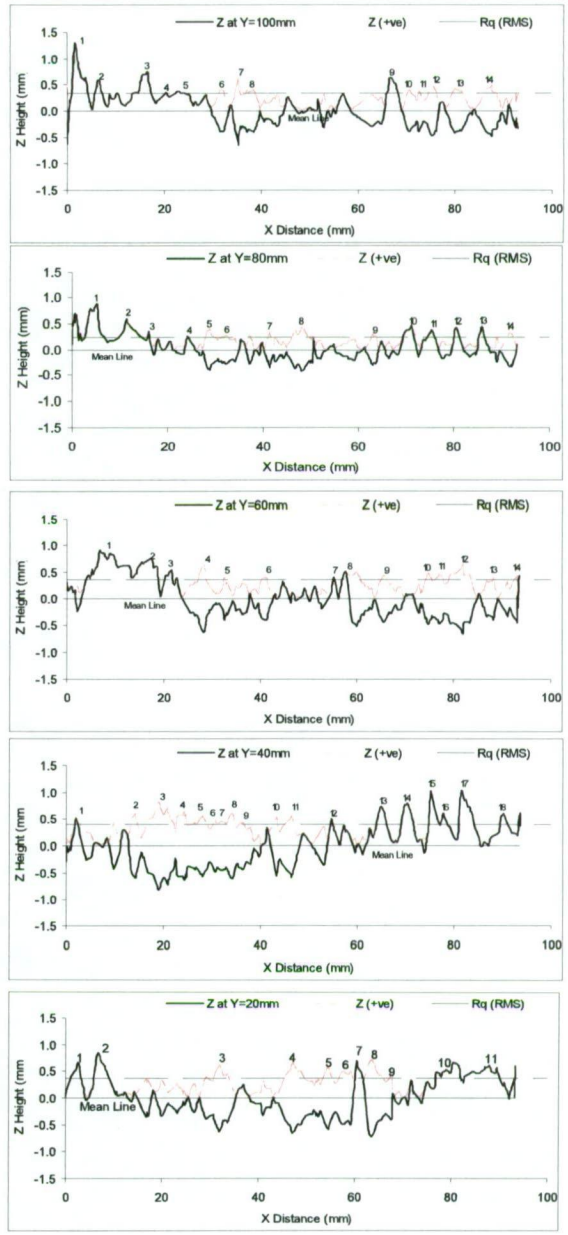

Figure 8.26: Digital reproduction of window D for rough plate clean.

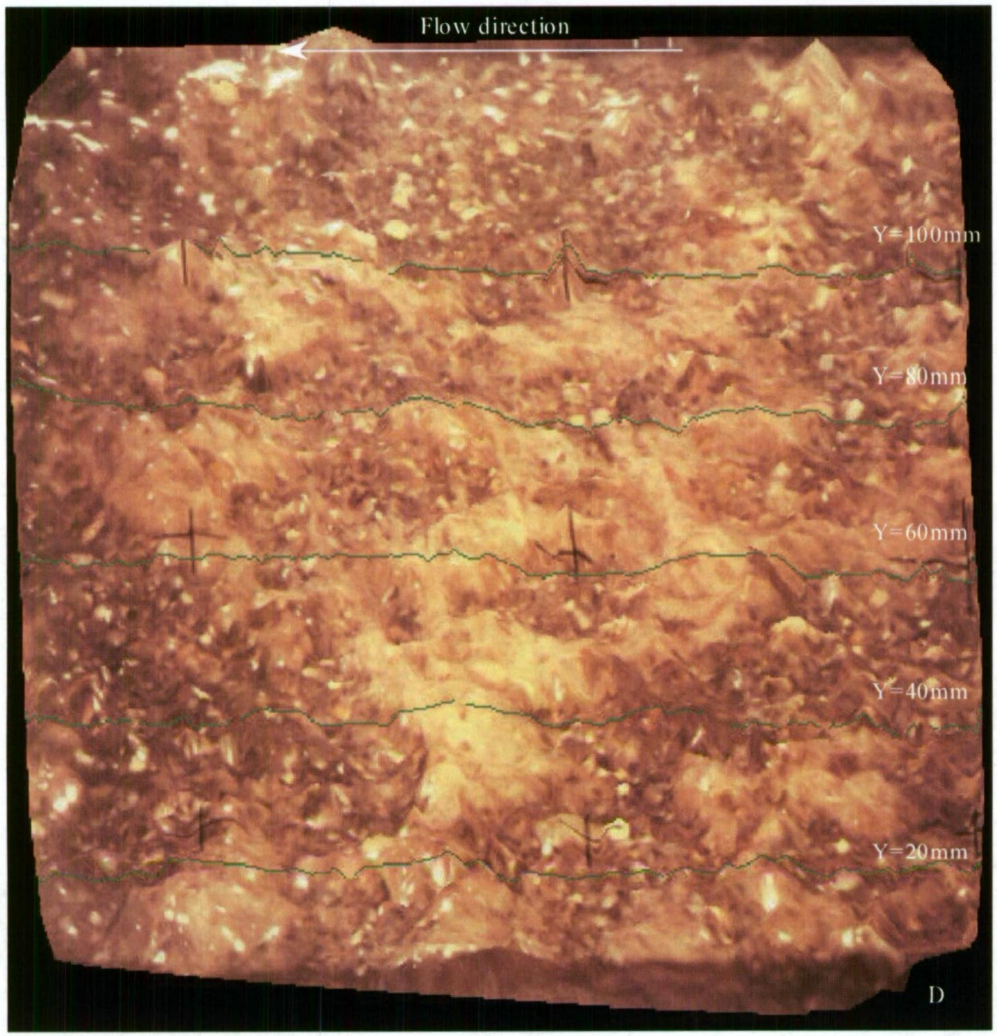

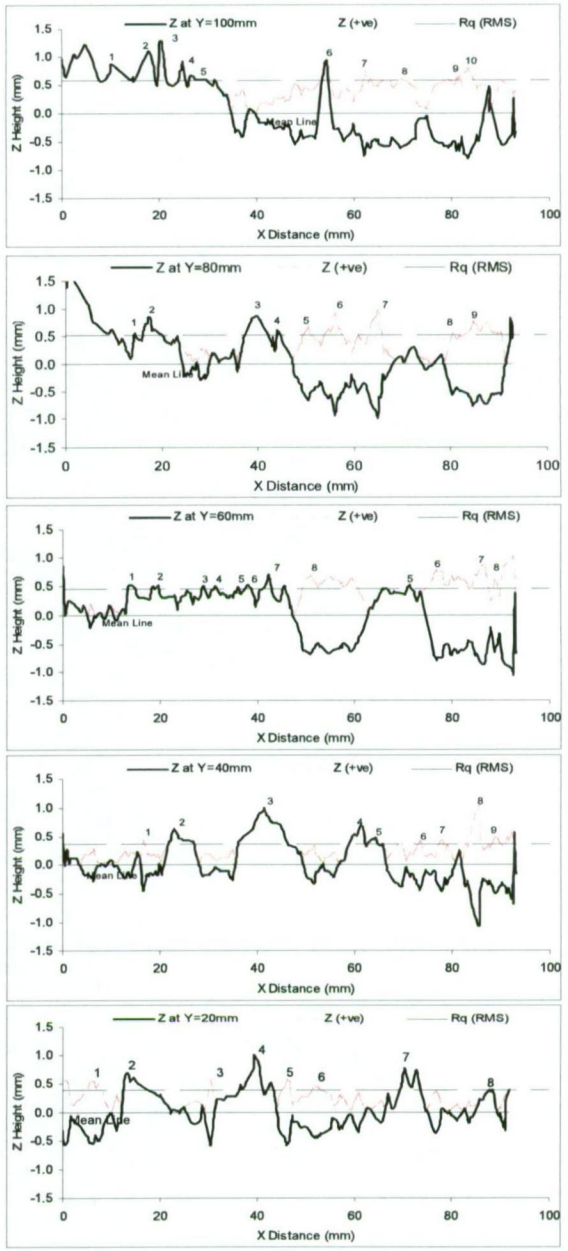

Figure 8.27: Digital reproduction of window D for rough plate fouling 1.

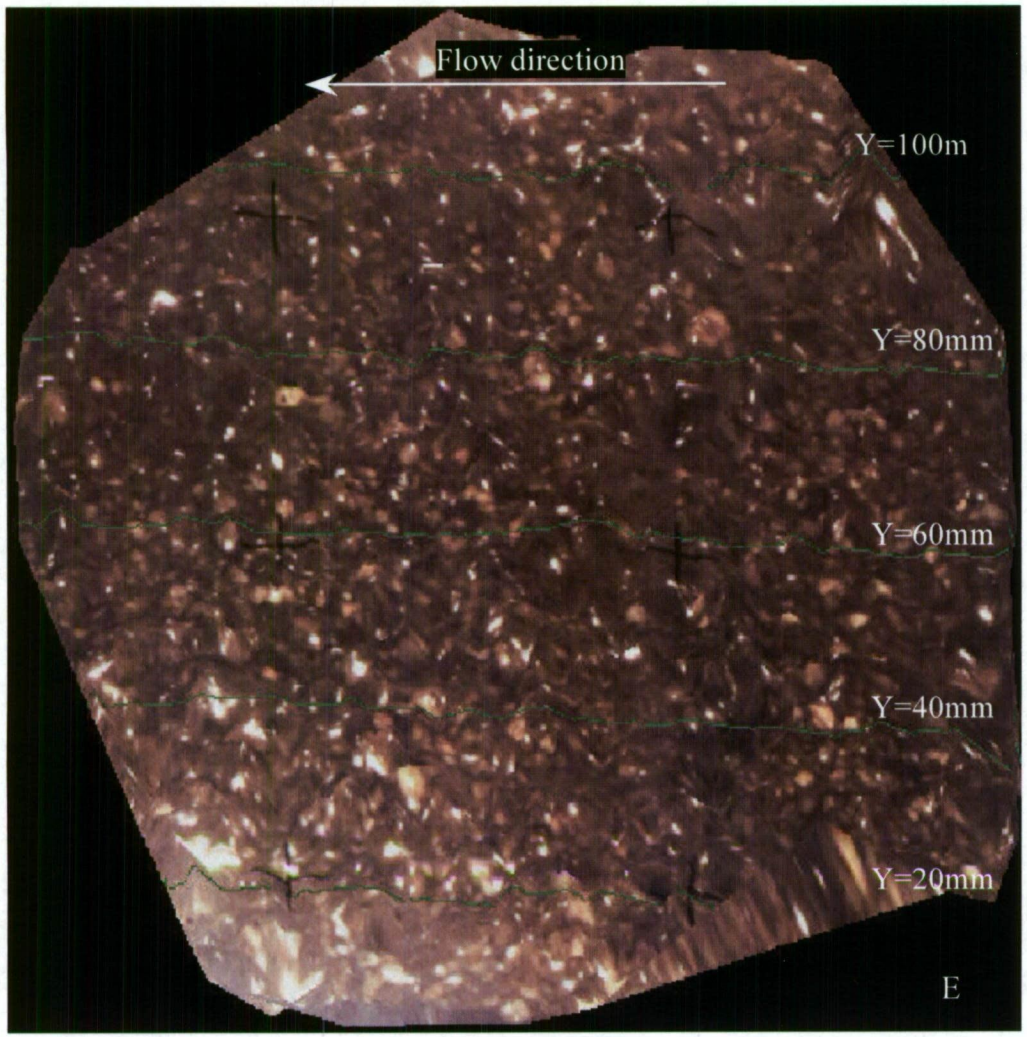

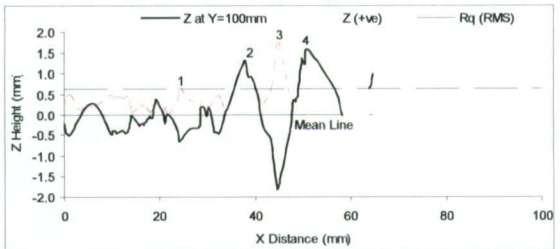

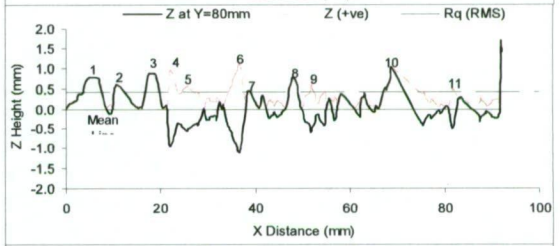

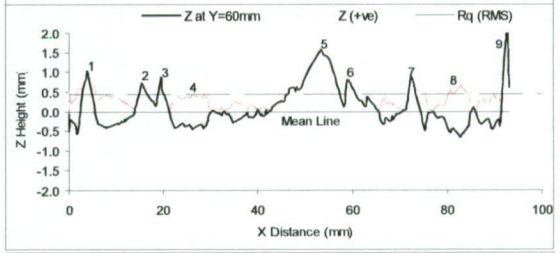

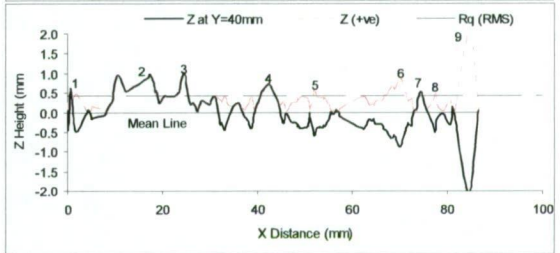

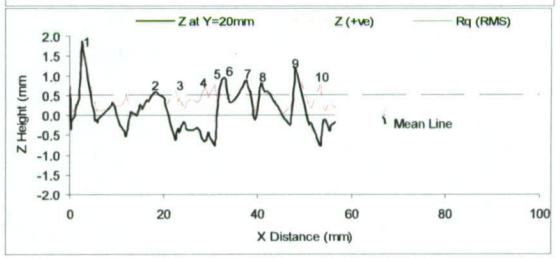

Figure 8.28: Digital reproduction of window E for rough plate fouling 2.

8.6 Chapter Summary

Results from water tunnel measurements and photogrammetry for an artificially roughned plate in an initial clean condition and two fouled states have been presented in this Chapter. The comprehensive approach detailed in the Chapter is well suited to understanding the roughness characteristics of freshwater biofilms. The roughness information reported significantly extends that previously available in studies such as those of Schultz (1998) and Picologlou *et al.* (1980).

Results show that biofilms in general create roughness effects well beyond those suggested by their geometrical surface character. Filamentous growths, in particular, produce large increases in drag and cannot be truly characterised while out of water. It was observed that filaments of biofilms display three-dimensional behaviour. This is an area that deserves particular attention in future research. Video footage of biofilm behaviour is included on CD in Appendix A.

Results show that the wall shear velocity on the plates during deployment in the field closely match that of the water tunnel at lower flow speeds. However, the field installation of the test plates may need to be revised to reduce the effects of leading edge flow behaviour, which resulted in biofilms not developing on the front corners of the plate. Plates flush with the canal wall would be more appropriate to encourage more even biofilm growth across the plate, but such an installation was not practicable for the present study.

Further work may need to be spent on developing a laboratory based apparatus to allow flow conditioned biofilms to grow on test plates. This should also provide better controll over biofilm variability of the plate, enable shorter growth times, and provide a more flexible schedule for testing.

There were two clearly different types of biofilm measured in the present study. A compact gelatinous biofilm which moves in water, but maintains its shape while out of water. This type of biofilm is ammendable to the photogrammetry type studies used in this thesis. The second type of biofilms is a filamentous biofilm. This type did not show a good characterisation by the photogrammetry methods used in this study.

Suggestions for the study of filamentous biofilms are made in the Chapter 9 along with further discussion and analysis of results is provided in Chapter 9, with conclusions from the work made in Chapter 10.

Chapter 9 Results Synthesis and Discussion

9.1 Introduction

The present study has used a broad range of measurements in the pursuit of information to describe the effects of freshwater biofilms on flow in hydraulic conduits. This involved comprehensive field studies, the use of close range photogrammetry to map surfaces, and the development of, and subsequent measurements from, a water tunnel. The results of these investigations are synthesised in this chapter and discussed in light of their findings.

9.2 Field Studies and Results

The field tests undertaken for the present investigation, reported in Chapter 3, demonstrated the industrial application of this research and identified the impact of biofouling on the operation of pipelines and canals. The principal biofilm species were identified with ongoing work being completed by Buia (2006) and Perkins (2006). Work is also continuing on the selection of paints for their antifouling and low friction properties by Andrewartha (2006).

Supporting earlier studies by Brett (1980) and McFie (1973; 1976) it was found that biofouling is a cause for significant energy loss within hydroelectric schemes. The present study also indicated a clear economic case for the regular cleaning of pipelines to minimise biological growths in pipelines amenable to it.

Better understanding of biofouling problems in pipelines requires the regular monitoring of headloss characteristics and ways to quantify the level of growth on internal surfaces. It is suggested that monitoring of problematic pipelines be undertaken at intervals of not more than 5 years.

It is acknowledged that accurate field tests of large conduits also pose significant problems. Care must be taken when measuring flow, and these observations should be corroborated with other data where possible. Improvements in the accuracy and reliability of flow measurement for large diameter pipes will reduce the uncertainty in headloss tests.

The results in Chapter 3 showed that the friction behaviour of biofouled surfaces may not follow a Colebrook-White type relationship in the smooth-rough transition regime. Designers and operators of hydraulic conduits should consider that the friction factors may be increasing with Reynolds number when dealing with biofouled conduits. If possible, hydroelectric schemes should be operated at flows where the biofouling causes less energy loss.

It was also found that biofilms are often location specific, with different species abundance, different morphology, and thicknesses in each pipeline studied. This means that headloss studies of individual conduits are the best way of determining roughness character and re-growth properties. This way, with enough historical data on the conduit, predictions can be made to better optimise operation, cleaning and other maintenance.

The trial of different paints to study their ability to curb biofilm growths was reported in Chapter 3 as part of the field study program. These trials are continuing (see Andrewartha, 2006) in the search for a suitable surface coating to reduce biofilm growth. This includes different surface finishes; from very smooth surfaces (preventing initial biofilm colonisation by increasing flow velocities near the wall) to different surface tension properties. The development of environmentally friendly biocides to impregnate paints is recommended for investigation to produce new, innovative kinds of antifouling surface coatings suitable for use in potable freshwater applications.

From the paint trial study it was found that a particular group of paints clearly out performed others in their ability to impede biofilm growth. The reasons why these paints worked better are not well understood, but may partially be due to their low friction properties. Further investigation into paint friction characteristics, along with cost-benefit analyses to determine the economic viability of relining various conduits

will provide a significant breakthrough in the solution to the biofouling problem, with applications beyond freshwater hydraulic conduits.

Water quality and temperature data was collected from the Tarraleah No. 1 Canal system, with results presented in Chapter 4. This type of information proved essential in understanding the character of the biofilms grown on the large test plates used for photogrammetry and water tunnel measurements. It was revealed that the operating regime of the canal where the plates were deployed had a significant impact on the type of biofilm on the plates. The temperature measurements revealed the plates were sometimes exposed to ambient air temperatures of between –2 °C and 20 °C, detrimentally affecting the biofilm, and creating a filamentous type of growth on the large test plates. Alteration of biofilm character by manipulating their environment in this way could be an area of further investigation, although in this study it was shown that a filamentous growth developed creating greater surface friction than more usual low-form gelatinous types of biofilm.

Although the filamentous biofilm studied in the present work was not the typical biofilm encountered at Tarraleah, it still represented a good contrast to the low-form gelatinous growths on the fouling 2 plates later on in the experimental program.

Water quality information showed that although the water of the central highlands of Tasmania is relatively nutrient poor, specialised biofilms still thrive and cause significant biofouling problems in hydraulic conduits. Although not well documented, there have been reported cases where algal blooms have occurred after particular events. One such event was the dewatering and maintenance of a canal, which was repaired at sections with cement. Shortly after the canal was brought back into operation, a diatomaceous algae bloom occurred, thought to be due to increased levels of Calcium in the water from the fresh cement (Line, 2003). Another reported event occurred after increased water levels of a supply lake from recent high rainfall, where water inundated nutrient laden embankments after a period of low water levels. Increased nutrient levels in the water resulted in increased levels of biofouling. These two cases show the complexity of controlling biofouling, and asset owners and operators should consult specialists to better understand and avoid these types of problems.

9.3 Photogrammetry Studies and Surface Roughness Information

The close range photogrammetry techniques used in this study were developed specifically to measure the surface character of biofilms and other complex rough surfaces. Photogrammetry is particularly suitable as it does not touch or interfere in any way with the biofilm.

This work showed that with the use of photogrammetry, high quality surface information and biofilm physical character could be obtained.

The most useful data proved to be the mean surface roughness, mean biofilm thickness, total peak to valley height (Rt), and peak count. Other parameters such as the surface RMS did not provide as useful information, though they were required for the surface peak counts.

Because the biofilms changed over the plate surface, roughness information had to be interpreted carefully for appropriate comparisons to be made with the water tunnel measurements.

It was found that the biofilms on the smooth plate produced a surface profile that was mostly positively skewed where the biofilm grew. Where there was little growth, the photogrammetry data displayed a more negative skewness. The kurtosis was mostly positive where there was more growth for both fouling 1 and fouling 2, meaning the biofilm modified the surface to display a "sharper" profile.

For the rough plates, the surface profile statistics were more diverse, and were complicated by the underlying surface roughness. The roughness parameters and peak counts were more useful in describing the effect the biofilms had on changing the character of the initially clean rough surface.

Chapter 5 presented results from studies looking at the development of biofilms over two scales of roughness (fine grit and a coarse grit). Results showed that a rough surface can become physically smoother by the biofilm growing within the valleys and gaps

between the roughness elements; then growing as a general mat over the surface. This is consistent with the growth characteristics of the stalked diatom, *Gomphonema*, described by Perkins (2005). However, results from the coarse grit test plates showed that biofilms can also develop to form peaks on roughness elements, further increasing the physical roughness (Rt values) of the surface. Results from one coarse grit plate, where much biofilm was present, also showed evidence of transverse ripples. These results add to the complex topography of biofilm surfaces, some of which were shown in Chapter 2.

However, the biofilms were not submerged in water during photography for this study, and it was observed that biofilms readily change their physical character in flowing water when placed in the water tunnel (see for example the videos in Appendix A). For the filamentous type of biofilm particularly, this limits the results of photogrammetry. However, it was one of the aims of the photogrammetry work to be able to provide a surface characterisation, which could then be related back to the biofilm effect on the flow. The ultimate goal of this would be the in situ characterisation of biofouling in an open channel or pipeline, which could then be readily used to determine the performance characteristics of the conduit. This represents a useful field application of the method. Underwater methods are not feasible for high velocity conduits, and would be limited to certain laboratory uses.

The photogrammetry methods presented have applications beyond that used in the present study. It is suggested that the photogrammetry used in this study could be applied to the surface mapping of other complex surfaces. Applications such as flow over rough beds or rough walls, and non-uniform surfaces could see large improvements in terms of the quantification of physical roughness in engineering studies.

9.4 Water Tunnel Design and Calibration

The water tunnel constructed for the present study was designed using a typical wind tunnel design approach. Measurements were made using a flat acrylic plate to calibrate the tunnel, and these showed that flow conditions generally matched the design values, and displayed good flow distribution characteristics in the working section.

It was noted that low energy fluid on the inside of the water tunnel may be producing a slight non-uniformity in the vertical direction. This non-uniformity influenced the use of the usual boundary layer thickness definition of $\delta = y$ at 99% of the free stream velocity. Instead the momentum thickness was used, where appropriate, as this was also less sensitive to an accurate wall position, important for rough wall studies.

The presence of longitudinal corner vortices and the movement of water between the edges of the test plate and the roof cavity in the working section were noted, but were determined not to significantly impact on results presented.

Special considerations were made so the facility could contain fresh or salt water. Water could be kept onsite using storage tanks, or carted in from the field where the measured biofilms were grown. This allows the use of water from the natural biofilm habitat which is particularly useful for biological studies on the biofilm.

It was shown that a purpose built water tunnel is a reliable instrument to measure the skin friction and total drag characteristics of biofilms found in hydraulic conduits. From these measurements, a hydraulic roughness could be inferred which was comparable to the physical roughness measured by photogrammetry.

A measurable reduction in biofouling and associated drag was observed over the course of testing in the water tunnel. Although the biofilms were grown and conditioned to flow in the field, the constant change in flow speeds and associated wall shear, sometimes above what the biofilm grew in, would have assisted in the sloughing process. Increases in water temperature, and changes in water quality over time would also have negatively affected the biofilm. These effects need to be better controlled for future studies.

9.5 The Biofouling on the Test Plates

The purpose of the water tunnel was to allow detailed measurements of the near wall flow over test plates of different surfaces. Near wall measurements of field conduits were not feasible in the present study.

As stated in Chapter 2 the problem of biofouling occurs at the wall, and so this is where investigations should be focussed. The water tunnel allowed for both detailed measurements of the boundary layer, and measurements of total drag due on test plates. This approach resulted in useful information to better understand the roughness effect of freshwater biofilms.

In general, the results show that biofilms create roughness effects beyond what their physical surface character may otherwise suggest, supporting the work of others (Picologlou *et al.*, 1980; Stoodley *et al.*, 1988; Schultz, 1999; Schultz, 2000; Towler, 2004). It was also found that filamentous biofilms create more drag than low form gelatinous type biofilms. It was observed that biofilm filaments moved about vigorously, and extended further into the boundary layer than the gelatinous types, consequently drawing more momentum from the flow.

A *Tabellaria* type diatom and a *Gomphonema* stalked diatom were the most abundant algae species present on the biofouled test plates in Tarraleah No. 1 Canal. Bacteria made up the majority of the biofilm biomass in the pipelines studied. Based on molecular analysis, members of the class Alphaproteobacteria were the most frequently detected followed by members of phylum Chloroflexi (Barton *et al.*, 2006). Greater detail of the microbiological content of the biofilms are the subject of other studies by Buia (2006) and Perkins (2006). Only a general description was provided in this thesis.

9.5.1 Skin Friction and Total Drag Measurements

Tables 9.1 and 9.2 present the measured skin friction coefficient, c_f, values for the smooth and rough plate respectively, and the changes in c_f relative to the clean plate condition. Data for the clean smooth plate are from the Preston method for the determination of wall friction velocity, u^*. All other values in both Table 9.1 and 9.2 are from the log-law slope method.

The most drag, and greatest measured roughness was for a rough plate fouling 1, which had large amounts of filamentous biofilm attached to an artificially roughened surface.

The greatest relative increase in drag from its clean condition was for smooth plate fouling 1 with a filamentous biofilm growth. This drag approached similar levels of drag measured on the rough plate fouling 2 with the gelatinous biofilm growth. This is significant from a design and operation point of view. For example, if an open channel is re-lined as a biofouling control option, there remains a potential biofouling effect that still requires a large free board to be maintained as a risk reduction measure.

For example, Table 9.1 shows an increase in c_f of approximately 50% for smooth plate fouling 2 from the clean plate condition, as shown in Table 9.2. For rough plate fouling 2, however, an increase of only between 10% and 20% was measured from the clean condition.

Table 9.1: Changes in c_f for smooth plate experiments.

		Smooth Plate				
			Fouling 1	Fouling 2	Fouling 1	Fouling 2
Measurement	Approximate	Clean	(Filamentous)	(Gelatinous)	Change in c_f	
Location	Re_{XPlate}	c_f	c_f	c_f	%	%
x = 95mm (Plug 1)	$1.2x10^6$	0.0045	0.0086	0.0085	93	90
	$1.8x10^6$	0.0039	0.0069	0.0063	78	62
	$2.2x10^6$	0.0036	0.0069	0.0056	88	54
x = 495mm (Plug 2)	$1.2x10^6$	0.0038	0.0088	0.0061	129	58
	$1.8x10^6$	0.0036	0.0081	0.0055	126	53
	$2.2x10^6$	0.0033	0.0086	0.0049	159	47
x = 865mm (Plug 3)	$1.2x10^6$	0.0040	0.0085	0.0065	110	61
	$1.8x10^6$	0.0036	0.0077	0.0052	113	46
	$2.2x10^6$	0.0034	0.0077	0.0048	125	40

Table 9.2: Changes in c_f for rough plate experiments.

Measurement Location	Approximate Re_{Plate}	Rough Plate Clean c_f	Fouling 1 (Filamentous) c_f	Fouling 2 (Gelatinous) c_f	Fouling 1 Change in c_f %	Fouling 2 Change in c_f %
x = 95mm (Plug 1)	$1.2x10^6$	0.0111	0.0097	0.0117	-13	5
	$1.8x10^6$	0.0105	0.0091	0.0093	-13	-12
	$2.2x10^6$	0.0100	0.0092	0.0084	-8	-17
x = 495mm (Plug 2)	$1.2x10^6$	0.0068	0.0080	0.0074	17	9
	$1.8x10^6$	0.0064	0.0066	0.0072	3	12
	$2.2x10^6$	0.0055	0.0061	0.0066	11	19
x = 865mm (Plug 3)	$1.2x10^6$	0.0064	0.0084	0.0077	31	20
	$1.8x10^6$	0.0057	0.0067	0.0068	17	20
	$2.2x10^6$	0.0060	0.0067	0.0058	12	-3

Total drag measurements for the smooth plate experiments show an increased change in skin friction from the clean plate conditions. Table 9.3 presents these data. Total drag measurements show a greater increase in drag (due to friction) than the local skin friction measurements do. The filamentous type biofilm growth of smooth plate fouling 1 shows the greatest level of drag amongst the smooth plate experiments.

Table 9.3: Increase in drag on smooth plates due to fouling.

Measurement	Smooth Plate Clean C_D	Fouling 1 (Filamentous) C_D	Fouling 2 (Gelatinous) C_D	Fouling 1 Change in C_D %	Fouling 2 Change in C_D %
Measured Drag 1	0.0036	0.0098	0.0082	173	128
Measured Drag 2	-	0.0102	0.0078	184	117

The total drag measurements for the rough plate experiments show very different information between fouling 1 (filamentous biofilm) and fouling 2 (low-form gelatinous). The skewed distribution of the biofilm towards the lower rear section of the test plate is described in Chapter 8. The heaviest fouling was not on the centreline and this was consequently not evident in the boundary layer measurements. The greatest increase in drag was for rough plate fouling 1 with the filamentous biofilm. The drag measurements of the low-form gelatinous biofilm of rough plate fouling 2 more closely

match the values determined from the boundary layer measurements, as there was a more even distribution of fouling over the plate.

Table 9.4: Increase in drag on rough plates due to fouling.

Measurement	Rough Plate Clean C_D	Fouling 1 (Filamentous) C_D	Fouling 2 (Gelatinous) C_D	Fouling 1 Change in C_D %	Fouling 2 Change in C_D %
Measured Drag 1	0.0088	0.0193	0.0102	119	15
Measured Drag 2	-	0.0171	0.0094	94	6

All the local skin friction values measured for the smooth and rough plates are shown in Figures 9.1 and 9.2 respectively. c_f is plotted against boundary layer momentum thickness Reynolds number, Re_θ, and the results show a general decrease in friction with an increase in Re_θ. The smooth plate results (Figure 9.1) show that filamentous biofilm growth creates greater local skin friction than gelatinous biofilm for the same Re_θ.

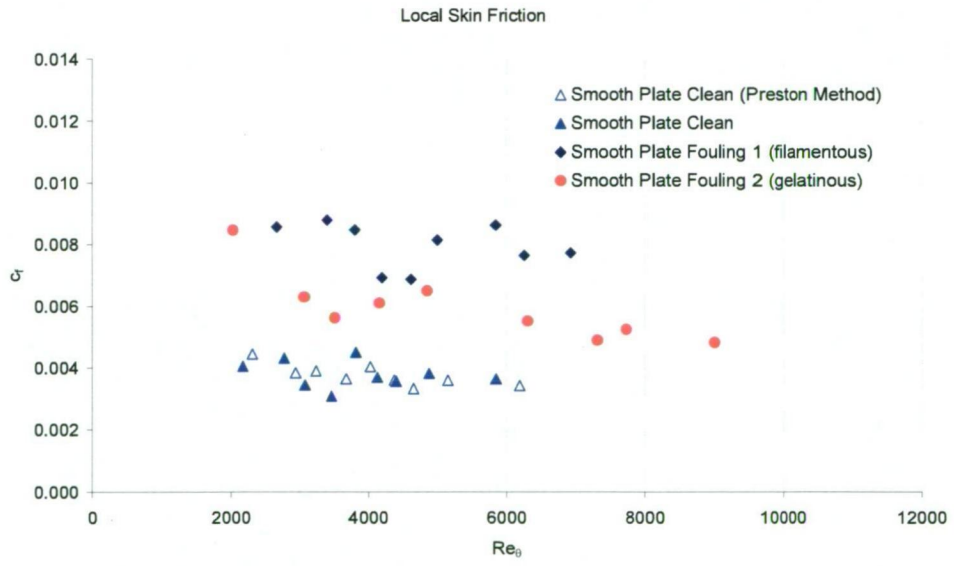

Figure 9.1: Local skin friction coefficient versus momentum Reynolds number for smooth plate experiments.

Figure 9.2 presents the results for the rough plate experiments. Local skin friction (c_f) results are generally similar for both rough plate fouling 1 (filamentous) and fouling 2 (gelatinous). Of interest are the three high c_f values for rough plate clean (indicated on the Figure) which are the data obtained from plug 1 at the forward section of the test plate. These c_f values are high due to the previously discussed thinning of the boundary layer at the leading edge gap of the test plate, and show the variability in measurements that can arise from the size of this gap.

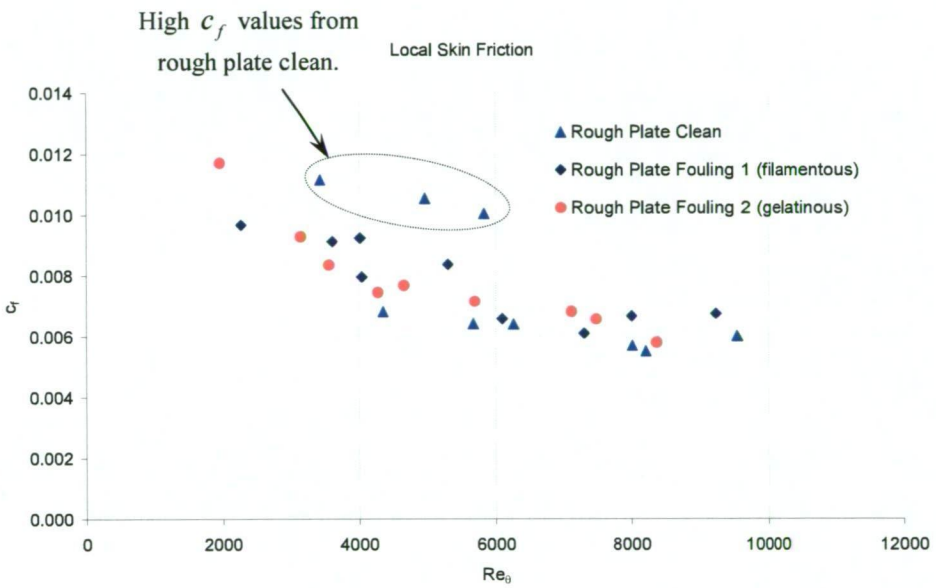

Figure 9.2: Local skin friction coefficient versus momentum Reynolds number for rough plate experiments.

The mean velocity profile in the outer layer (described by Schlichting, 1979) can be expressed as a relationship between the velocity defect, $\frac{U-u}{u^*}$, and a non-dimensional distance from the boundary, $\frac{y}{\delta}$ (or $\frac{y+\varepsilon}{\delta}$). This is called the velocity defect law. The velocity defect $(U-u)$ at a distance y from the wall is the result of the wall shear. For fully developed pipe flow with distributed sand roughness, the velocity defect law is valid for both smooth and rough boundaries. This implies that the outer layer is insensitive to the manner in which the wall shear is generated.

Velocity defect profiles are presented for the smooth plate and rough plate experiments in Figures 9.3 and 9.4 respectively. Data are shown from plug 3 (x = 865 mm) for

$Re_{Plate} = 2.2 \times 10^6$ only, and data from the smooth plate clean (Preston method) are shown on both Figures for comparison.

Results for both the smooth and rough plate experiments show a good collapse of data in the outer region of the boundary layer. The smooth plate results (Figure 9.3) do not collapse onto each other in the inner region suggesting some differences in large mixing eddy structure due to surface roughness effects. The smooth plate clean and smooth plate fouling 1 results exhibit less velocity deficit in the near wall region which contradicts the expectation that the results be independent of roughness level. The data from the gelatinous biofilm of smooth plate fouling 2 more resembles the character of the set of rough plate velocity defect results.

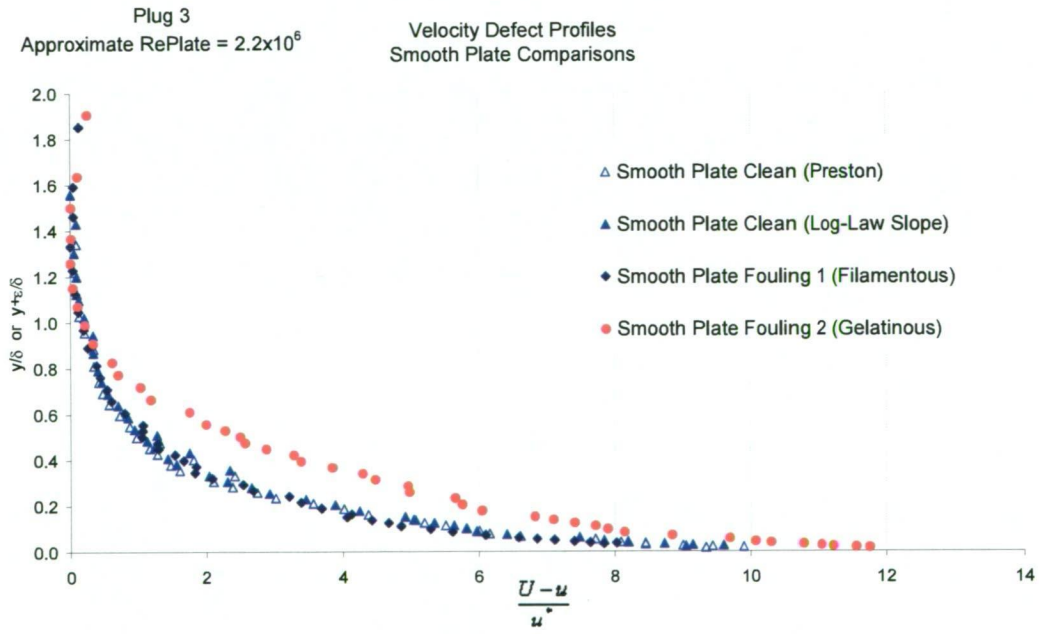

Figure 9.3: Comparison of velocity defect profiles for smooth plates.

Rough plate results (Figure 9.4) show less separation between profiles, and all show an increased velocity defect from the smooth plate clean data. There is a slight difference between the gelatinous and filamentous biofouling cases indicating that these biological roughness examples follow different velocity defect laws.

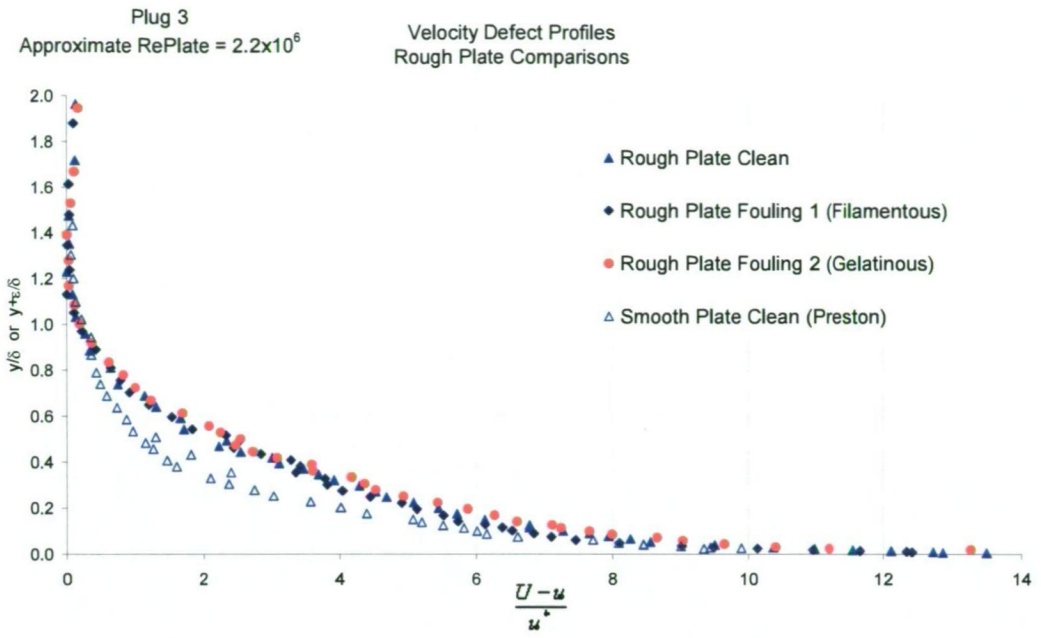

Figure 9.4: Comparison of velocity defect profiles for rough plates.

9.5.2 Comparison of Roughness Information

The roughness values determined from the boundary layer measurements depend on an average of upstream conditions to that measurement location, and so it can be reasoned that the most downstream measurement station (plug 3) is most representative of the conditions of the test plate. Total drag measurements represent mean conditions for the entire plate, but may include forces due to flow circulation around the plate edges, shown to be present in Chapter 6. The gap at the leading edge, in particular, causes a thinning of the boundary layer, and artificially increases the local skin friction on the forward section of the plate. Corrections were made to remove pressure forces on the plate ends due to boundary layer growth and associated longitudinal flow acceleration within the working section.

The photogrammetry measurements were designed to obtain representative surface information of the rough and fouled test plates from fixed locations. However, it was found that the biofilm varied considerably across the plate surface, and the photogrammetry consequently did not necessarily capture the diversity of the biofilm surface.

What the physical roughness data obtained from photogrammetry does not adequately describe is the filamentous properties of the biofilm, which was clearly observed on fouling 1 for both smooth and rough plates. This is because the filaments lay flat when out of water, and explains why a relatively small physical roughness is shown by the photogrammetry compared to the measured roughness effect from the water tunnel.

From the outset of this research project, it was never envisaged there would be filamentous type growths. This is because filamentous growths were never observed in Tarraleah No. 1 Canal until well after the photogrammetry equipment and methods were developed. Earlier paint trial studies (Chapter 3) showed only gelatinous, low form clumps and nodules of biofilm thought ideal for photogrammetry. The unanticipated operating regime of Tarraleah canal, due to low water storage levels, resulted in a skewed growth pattern for smooth and rough plate fouling 1, and no doubt facilitated development of the filamentous type of biofilm.

Recommended research for the future is to use photogrammetric techniques in situ in the water tunnel, and high speed photography to better capture the fluttering behaviour of filamentous biofilms.

A greater range of roughness information was foreshadowed by Schultz (1998) to better characterise biofilm surface properties. Schultz advised that something more than a simple biofilm thickness is required in the search for a suitable, descriptive roughness length scale. The present study agrees with this, and indicates that biofilm type (e.g. filamentous or gelatinous), mean thickness, approximate surface coverage of the biofilm, and the underlying surface condition are all important parameters. Peak counts and Rt values are also useful descriptors.

Tables 9.5 and 9.6 present the roughness information obtained from water tunnel and photogrammetric measurements. Results are averaged where more than one result is available. Photogrammetry data has been divided into three parts corresponding to an upstream third (averaged across windows C and F), the middle third (averaged across windows B and E) and the downstream third (averaged across windows A and D) of the plate. This better corresponds to the measurements made in the water tunnel at plug 1, plug 2 and plug 3 respectively. Total drag measurements are shown as Measured Drag 1 (at start of testing) and Measured Drag 2 (at end of testing).

Table 9.5: Comparison of roughness information for smooth painted plate.

Smooth Plate	Photogrammetry									Water Tunnel				
	Rt (mm)			Peak Count			Mean Biofilm Thickness (mm)			k_s (Plug 1) (mm)	k_s (Plug 2) (mm)	k_s (Plug 3) (mm)	ks (from C_D) (mm)	
	1st	2nd	3rd	1st	2nd	3rd	1st	2nd	3rd				1	2
Fouling 1	0.62	0.66	0.66	11.40	14.20	12.50	0.30	0.32	0.48	0.48	1.51	1.70	3.34	3.84
Fouling 2	1.32	1.12	1.17	10.80	9.40	11.70	0.48	0.48	0.39	0.99	1.33	1.26	1.90	0.72

Table 9.6: Comparison of roughness information for artificially rough plates.

Rough Plate	Photogrammetry												Water Tunnel				
	Rt (mm)			Peak Count			Mean Surface Roughness (mm)			Mean Biofilm Thickness (mm)			k_s (Plug 1) (mm)	k_s (Plug 2) (mm)	k_s (Plug 3) (mm)	ks (from C_D) (mm)	
	1st	2nd	3rd	1st	2nd	3rd	1st	2nd	3rd	1st	2nd	3rd				1	2
Clean	1.43	1.47	1.69	15.90	15.50	14.30	0.62	0.69	0.68	-	-	-	1.50	1.43	1.57	2.09	-
Fouling 1	1.83	1.83	1.85	11.90	11.00	11.10	0.81	0.67	0.75	0.19	-0.02	0.07	1.86	1.84	1.99	23.20	16.39
Fouling 2	2.07	2.45	2.00	8.60	8.20	9.40	0.76	1.05	0.98	0.09	0.47	0.20	1.64	1.60	2.15	3.10	2.29

Data for the smooth plate experiments (Table 9.5) clearly show low roughness values for fouling 1 from the photogrammetry (Rt and mean) compared to the measured roughness (k_s), which demonstrates that the filaments laid flat on the plate during photography. The gelatinous biofilm Rt data of smooth plate fouling 2 are nearer in value to the measured roughness, though the water tunnel roughness is still greater than the mean photogrammetry roughness.

The total drag measurements from both the smooth and rough plate fouling 1 (with the filamentous biofilm) show the greatest roughness of any measurement, and indicate the skewed biofilm growth away from the longitudinal centreline as similar levels of roughness was not measured at the plugs. Also, because of the filaments, the biofilm is not effectively measured by the photogrammetry.

Photogrammetry data best matches the water tunnel data for rough plate clean case shown in Table 9.6. This validates the photogrammetric methods, and in turn also compares well to the particle size distribution shown in Figure 4.20 in Chapter 4.

There is a generally lower peak count for the fouled rough plates compared to the clean rough plate. This supports the smoothing behaviour of the biofilm growth of the physical surface.

The mean thickness of a biofilm grown on a rough surface is not well defined, as the underlying surface roughness complicates the analysis. Some of the grit of the rough plate is removed over time, not significantly affecting the overall test plate surface roughness character, but affecting the surface where the photogrammetry takes place. As the photogrammetry requires, and analysis methods depend on, a high degree of repeatability, any change in the underlying surface roughness will alter the baseline condition, which is further disguised when biofilms are present. So biofilm thickness was not a good descriptive for fouled rough plate character in the present study, though the data for rough plate fouling 2 (gelatinous biofilm) shows generally greater thickness than fouling 1 (filamentous biofilm) due to the filaments laying flat. There was, however, an increase in the mean roughness for both rough plates fouling 1 and fouling 2 compared to the clean plate conditions.

9.5.3 Relating Roughness to Roughness Effects

The velocity profiles presented in Chapter 7 and 8 show a clear shift from smooth wall conditions. This is consistent with results from Hama (1954) who shows that this shift in the velocity profile, the roughness function (Δu^+), is the velocity decrement due to the increase in wall roughness.

It is possible to relate Δu^+ to the roughness character of the wall. This has been widely reported where it was found that, for geometrically similar sandgrain type surfaces, the roughness function collapses well, following the relation described in Equation 9.1 where C and a are constants.

$$\Delta u^+ = \frac{a}{\kappa}\ln(\mathrm{Re}_k) + C \qquad \text{Equation 9.1}$$

White (2006) suggests Equation 9.2 for sandgrain type data, and so this has been used here as comparison in Figures 9.5, 9.6. 9.8 and 9.9. Note that Equation 9.2 is asymptotic to $1+0.3\mathrm{Re}_k$ for large values of Re_k.

$$\Delta u^+ \approx \frac{1}{\kappa}\ln(1+0.3\mathrm{Re}_k) \qquad \text{Equation 9.2}$$

Different combinations of methods to determine Δu^+ and Re_k are plotted in these Figures to show the various relationships between the measured water tunnel roughness and physical roughness determined by photogrammetry.

Figures 9.5 and 9.6 both show the log-law slope method to derive Δu^+, but each respectively use k_s (from water tunnel measurements) and Ra (from photogrammetry measurements) to derive Re_k. The constants to fit Equation 9.1 to the data of Figure 9.5 are approximately $a = 0.99$ and $C = -3.5$.

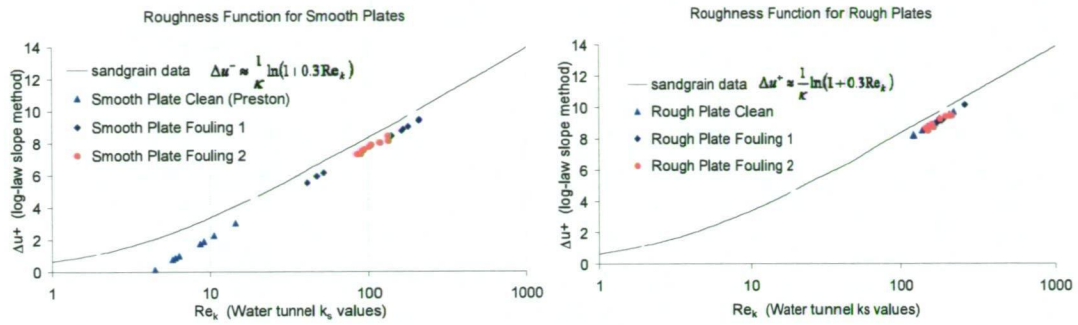

Figure 9.5: Log-law slope method roughness function and k_s values to calculate Re_k.

The data shown in Figure 9.5 displays a good similarity to the typical sandgrain roughness function. This is because the log-law slope method forces the data to a log-law fit, from which in turn was used to derive the roughness function. Figure 9.5 confirms the basic relationship between Δu^+ and k_s described by Equation 9.1.

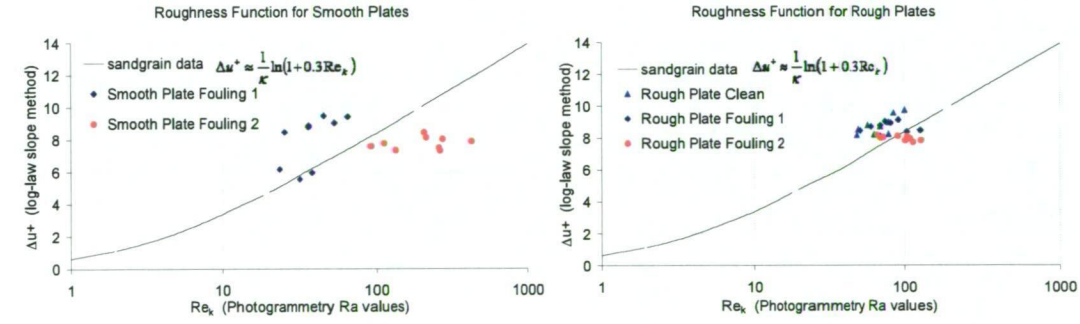

Figure 9.6: Log-law slope method roughness function and Ra values to calculate Re_k.

An alternative to measuring the shift in velocity profile on the semi-log velocity profile (log-law slope method) plots is to use Equation 9.3, from Hama (1954); this method was also used by Granville (1987). Equation 9.3 is only valid where c_f values are at the same Re_{δ^*}. Therefore data were plotted as shown in Figure 9.7, and power law regression curves were fitted. It was from the equations of these curves that Δu^+ values were determined at the measured Re_{δ^*}. Figures 9.8 and 9.9 show the roughness function plots using the Hama method to derive Δu^+; each respectively use k_s and Ra to derive Re_k.

$$\left(\sqrt{\frac{2}{c_f}}\right)_{Smooth} - \left(\sqrt{\frac{2}{c_f}}\right)_{Rough} = \frac{\Delta u}{u^*} = \Delta u^+ \qquad \text{Equation 9.3}$$

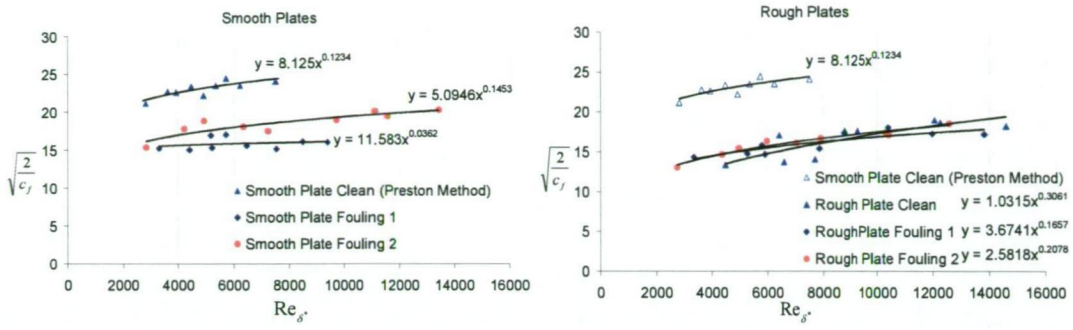

Figure 9.7: Hama roughness function from local skin friction coefficients.

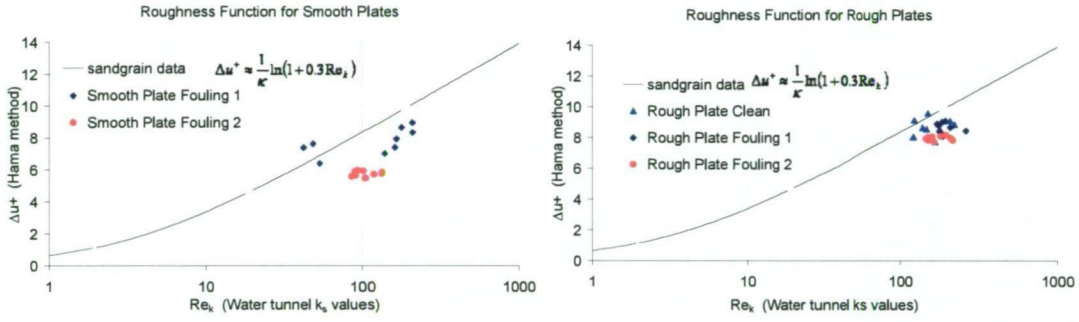

Figure 9.8: Hama method roughness function and k_s values to calculate Re_k.

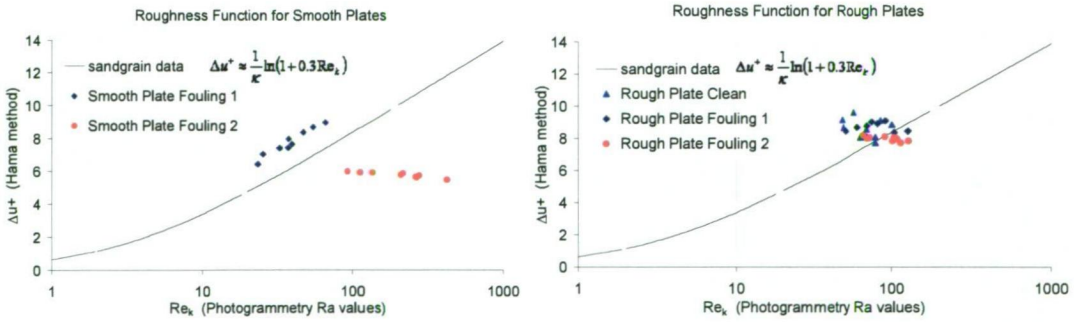

Figure 9.9: Hama method roughness function and Ra values to calculate Re_k.

Biofilms were not observed to be geometrically similar, particularly so for the filamentous biofilms on smooth plate fouling 1 and rough plate fouling 1. Smooth plate experimental data show more scatter than the rough plate data, suggesting the underlying surface roughness may have a moderating influence on the biofilm.

No discernable improvement can be seen in the Figures using either the log-law slope method or the Hama method to relate Δu^+ to Re_k. Both methods show approximately the same amount of scatter for the respective smooth and rough test plates.

Schultz (1998; 2000) also describes considerable scatter when plotting roughness functions from measurements of biofilms. White (2006) states that there is no unique function of Δu^+, as the nature of roughness varies greatly. This has been found the case in this study, where only very general relationships are seen with general clustering about typical sandgrain data.

Hama (1954) also relates the velocity profile shape factor, H, to the local skin friction coefficient in the form of $\sqrt{\frac{2}{c_f}}$. This has been completed in Figure 9.10 and shows a general trend of decreasing H with increasing $\sqrt{\frac{2}{c_f}}$ (corresponding to an increasing Re_θ). Equilibrium boundary layer values (at zero pressure gradient) are included for comparison with the smooth plate data. These data were obtained from the methods outlined in Chapter 6.

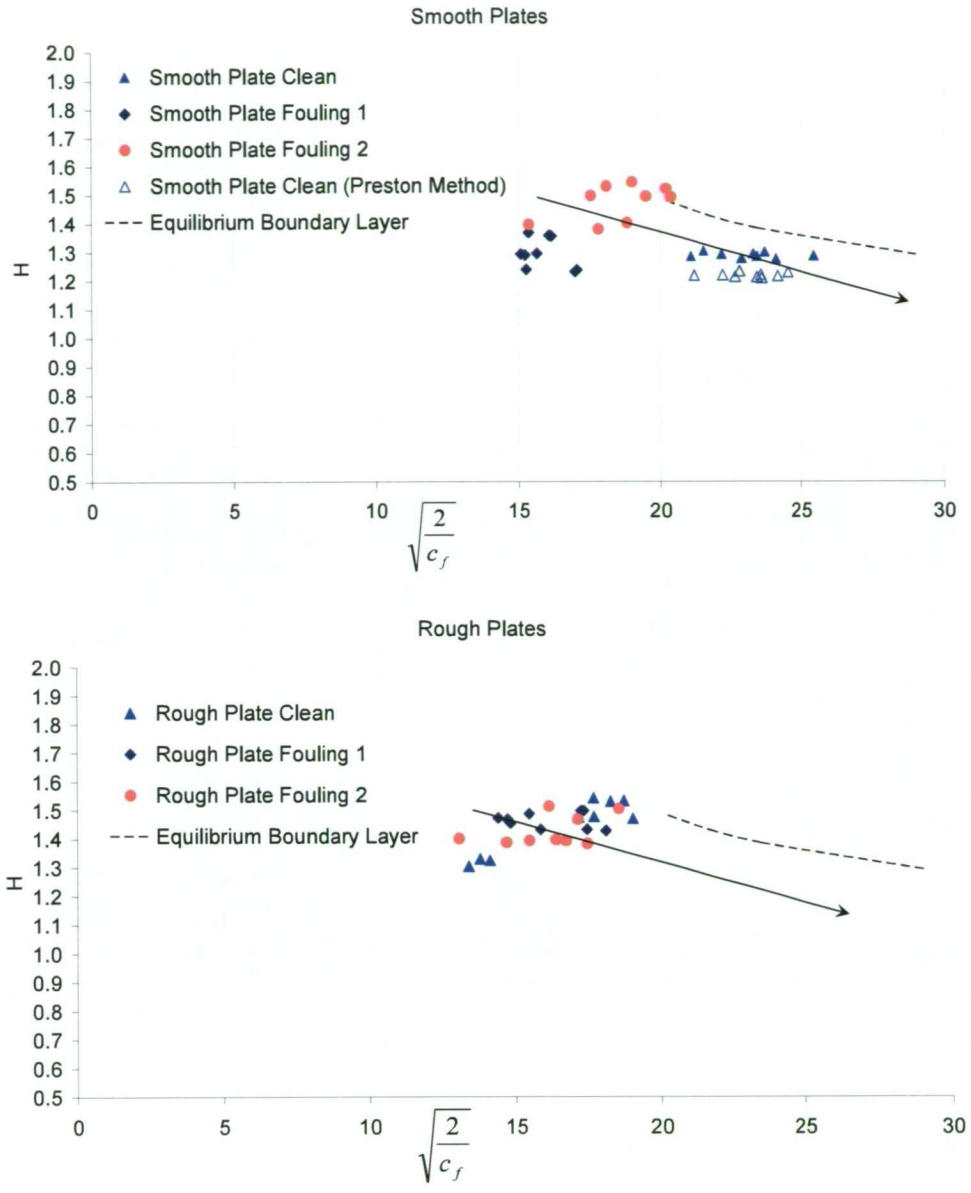

Figure 9.10: Velocity profile shape factor as a description of surface friction.

A relationship of the type described by Perry *et al.* (1969) where Δu^+ is proportional to $\frac{\varepsilon u^*}{\nu}$ where ε is the error in y, or the distance below the crest of the roughness elements, was found to show no relationship for the present study. This is because the peak of the roughness elements needs to be known to accurately to determine the distance ε below the roughness peaks. Complicating this is the general decrease in ε measured with increasing flow speed and associated Reynolds number for the fouled plates. This is thought to be related to the "thinning" of the biofilm surface with increased wall shear. As the biofilm is forced harder against the wall, the virtual origin

decreases, as the roughness elements flatten and reduce in size and so exposes the tip of the Pitot probe.

Of more practical interest is the relationship between the measured wall shear velocity, and the roughness effect of the biofilm. Figure 9.11 shows the results for smooth and rough test plate plotted as u^* against $\frac{k_s}{\delta}$. Here, k_s is the measured value, and δ was taken as $\frac{72\theta}{7}$ for the smooth plate clean ($1/7^{th}$ power law) and $\frac{42\theta}{5}$ for the rough plate clean, and all fouled test plates ($1/5^{th}$ power law). Data are plotted for the approximate Re_{Plate} values of 1.2×10^6, 1.8×10^6, 2.2×10^6, at which measurements were made in the water tunnel.

Figure 9.11 shows that $\frac{k_s}{\delta}$ increases with a decrease in u^*, again supporting the concept of biofilm thinning under higher shear forces. The other general relationship is that $\frac{k_s}{\delta}$ decreases as the flow Reynolds number decreases. This is observed to be particularly so for the measurements made at $\mathrm{Re}_{Plate}=1.2\times10^6$. Data for smooth plate fouling 2 is the only plate which shows a different behaviour of u^* versus $\frac{k_s}{\delta}$. This is consistent with results from Chapter 3 where bacterial biofilms cause increased friction with increasing Reynolds number in the transitional roughness regime.

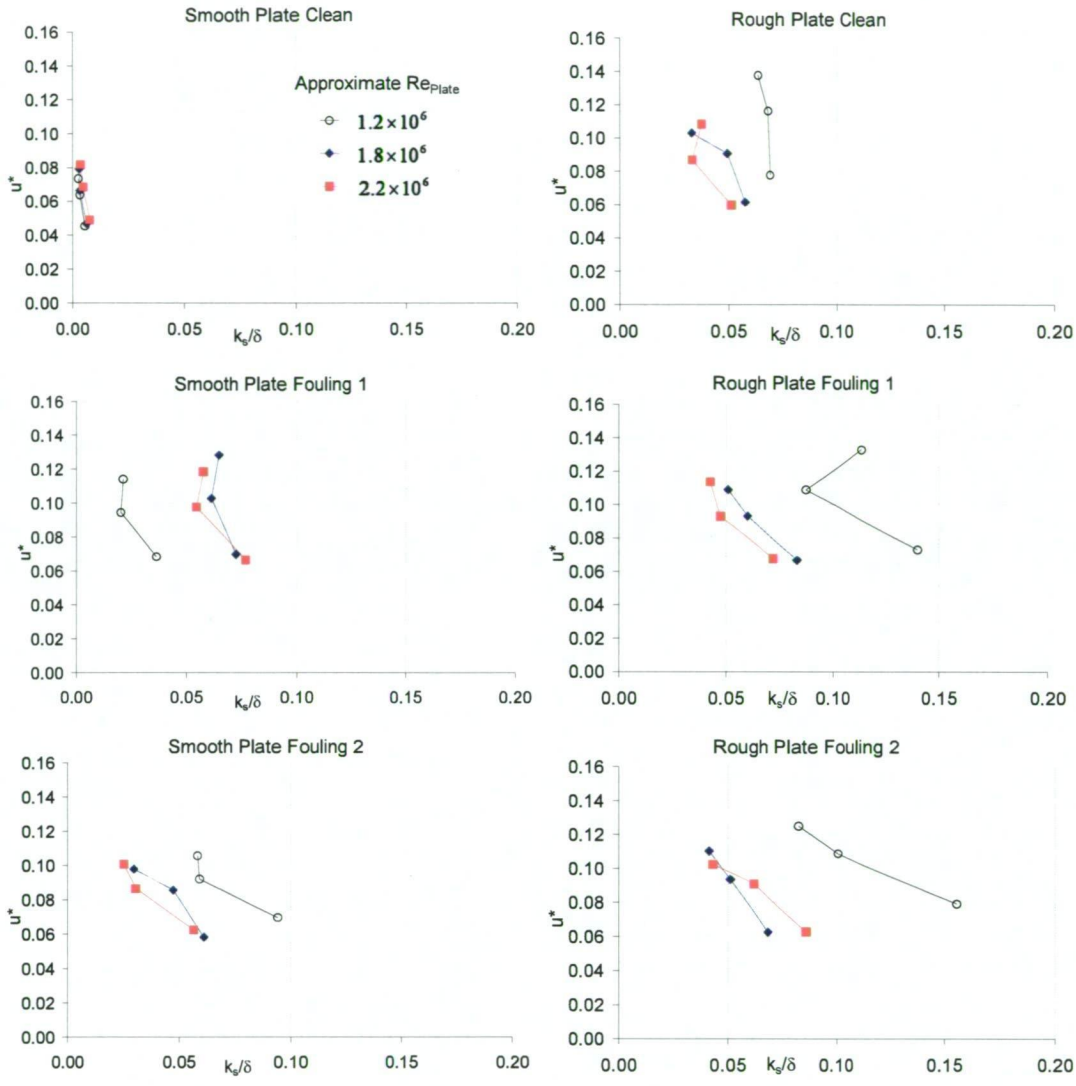

Figure 9.11: Biofilm roughness with different wall shear velocities.

Lau (1996) investigated the relative importance of mean flow velocity and bed shear on biofilm accumulation in open channels. Lau found that the mean flow had a greater influence on the biofilm accumulation rate than the bed shear stress. It was observed with the water tunnel experiments that the wall shear has a clear influence on the biofilm attachment and detachment. Although the mean flow velocity would be convenient method to determine the nature of the biofilm on a conduit wall, it was found in this study that biofilm behaviour is much more complicated and probably better described by wall shear stresses and associated boundary layer properties.

9.5.4 Filamentous and Gelatinous Biofilms

Several features are apparent in the results of the present study which warrant further discussion of filamentous and gelatinous biofilms. Smooth plate results (Chapter 7) show that there was greater skin friction and total drag for smooth plate fouling 1 (filamentous biofilm) yet reduced momentum thickness compared to the smooth plate fouling 2 (gelatinous biofilm). The velocity deficit, shown in Figure 7.21, is also less for the filamentous biofilm than for the gelatinous case. This may be due to differences in mode of drag causing behaviour, and requires further research.

The mass of the biofilm on each of the fouled test plate was not measured. But it stands to reason that although the filamentous biofilms cause greater drag and roughness effects, the photogrammetry results show that the filamentous biofilm is thinner than the gelatinous type when laying flat against the surface out of water. This means there may be less filamentous biofilm by mass than the gelatinous type to cause these effects.

The differences between the filamentous and gelatinous growths are not as evident in the rough plate results (Chapter 8) as it is for the smooth plates. This is due to the underlying rough substrate. The results do show, however, that the gelatinous type of biofilm is more like that of typical sandgrain roughness than the filamentous type, as the increases in friction were not as profound, and data compared better between physical photogrammetry data and water tunnel roughness.

More data is required to further investigate the specific differences in behaviour of filamentous and gelatinous types of biofilms.

9.6 Chapter Summary

The results presented herein demonstrate that a useful study of freshwater biofilms has been undertaken using a range of investigative techniques.

Results show that biofilms grown on rough or smooth surfaces generate greater drag than the equivalent clean surface. This was particularly evident for filamentous type biofilms. There seem to be quite important differences between filamentous and

gelatinous types of biofilms with regard to how they act as a wall roughness and how they impart their respective energy loss mechanisms, which requires further research.

The results from this research have implications for the design, operation and maintenance of hydraulic conduits susceptible to biofouling, particularly conduits in hydroelectric schemes. Biofouling in water supply, drainage networks and industrial systems may also benefit from the insight provided from the present study.

The complex and dynamic nature of biofilms mean that conducting experimental near wall measurements are more difficult than are most unfouled surfaces. Problems of probe fouling and the appropriate management of the biofilm to maintain a consistent surface for the duration of experimentation add to the uncertainty in results.

Chapter 10 Conclusions and Recommendations

10.1 Introduction

Biofouling is a problem that affects many hydraulic conduits. For the problem to be better understood, the mechanisms that cause the energy loss must be investigated. The present study has shown some of the effects freshwater biofilms have on flow.

Conclusions for the present study and recommendations for future research are presented in this Chapter.

10.2 Conclusions

With reference to results for the field studies in Chapter 3, the following conclusions are drawn:

1. Biofouling can be a significant cause of energy loss for hydraulic conduits.
2. Bacterial biofilms are dominant in closed conduit systems.
3. The present study indicates an economic case for the regular cleaning of pipelines to minimise biological growths.
4. Better understanding of biofouling problems requires regular monitoring of pipeline headloss characteristics, and further efforts to quantify the level of growth on internal surfaces, as biofilms are often location specific.
5. Accurate field tests of large conduits can pose significant problems.
6. The friction behaviour of biofouled surfaces may not follow a Colebrook-White type relationship in the in the smooth-rough transition regime, and the friction coefficient may increase with increasing Reynolds number.
7. Headloss tests of individual conduits are the best method for determining roughness character and biofilm re-growth properties.
8. The limits of hydraulically smooth and rough behaviour are important when considering the best operating regime for the conduit.

9. There is a small group of surface coatings that clearly impede biofilm growth, a group that has a moderate to poor ability to resist fouling, and many others that fail.

With reference to results for the photogrammetry studies on the small test plates presented in Chapter 5, the following conclusions are drawn:

10. For immovable rough surfaces, such as concrete, photogrammetry is an excellent technique to derive roughness information.
11. Photogrammetry is useful to map the complex surface character of biofilms.
12. Biofilms tend to grow in the gaps and valleys of rough surfaces, and may actually create a physically smoother outer surface.
13. Biofilms growing on coarse surfaces may colonise peaks of the roughness elements.
14. Heavy biofouling may form ripples transverse to the flow direction, similar to a compliant surface.

With reference to results for the water tunnel in Chapter 6, the following conclusions are drawn:

15. A recirculating water tunnel is a useful facility to quantify the effects of biofilms on flow.
16. Flow conditions within the purpose built water tunnel generally matched the design aims, and displayed good flow distribution characteristics.
17. Edge effects were present around the test plates used in the water tunnel, most likely due to longitudinal corner vortices and the movement of water between the edges of the test plate and the roof cavity in the working section. These non-uniformities were well within usable limits.
18. A boundary layer discontinuity was present at the leading edge of the test plate due to the small gap required to isolate the plate for total drag measurements. This size of this leading edge gap is a source of variability in results.
19. Low energy fluid may exist on the inside of the water tunnel, which may be producing a slight non-uniformity in the vertical velocity distribution.
20. The working section of the water tunnel proved useful for the observation of biofilm behaviour in water.

With reference to smooth plate experiments in Chapter 7, the following conclusions are drawn:

21. Results show that biofilms in general create roughness effects beyond what their physical surface character suggest.
22. Filamentous biofilms create more drag than gelatinous type biofilms.
23. The physical character of filamentous biofilms cannot be adequately described while out of water.
24. Biofilm filaments were observed to display three-dimensional flapping behaviour.
25. Low form gelatinous biofilms were observed to vibrate in the flow.
26. The *Tabellaria* type diatom and a *Gomphonema* stalked diatom were the most abundant algae species in the present study for the smooth plate experiments.
27. The operating regime of a hydraulic conduit greatly influences the type and character of the biofilms present on a smooth surface.
28. Biofilms grown on a smooth painted surface cause a large velocity deficit in the near wall flow region.
29. There are differences in the amount of velocity deficit caused by filamentous and gelatinous biofilms.

With reference to results from Chapter 8, the following conclusions are drawn:

30. The most drag, and greatest roughness measured in the present study was observed for an artificially rough plate with large amounts of filamentous biofilm present.
31. The smallest relative increase in drag from clean plate conditions was observed for a low form gelatinous biofilm on a rough plate.
32. In general, rough surfaces allow a faster rate of accumulation of biofilms, probably as rough surfaces have greater surface area and are may be more suitable for initial biofilm colonisation.
33. The *Tabellaria* type diatom and a *Gomphonema* stalked diatom were the most abundant algae species present for the rough plate experiments.
34. Experimental measurements of rough surfaces produce greater uncertainty in results.
35. The operating regime of a hydraulic conduit greatly influences the type and character of the biofilms present on a rough surface.

36. Biofilms grown on an artificially rough surface cause a slight increase in the velocity deficit in the near wall flow region.
37. Differences in the amount of velocity deficit caused by filamentous and gelatinous biofilms grown on an artificially rough surface are more difficult to determine than for smooth plate fouling.

10.3 Recommendations

It is recommended that further investigations be carried out to improve the understanding of the effects freshwater biofilms have on hydraulic conduits.

The photogrammetry methods used in this study are new and innovative, but have only just started to be used to their full extent. Underwater photography methods should be developed to better capture the complexities of biofilms, moving in three dimensions, in water, at different flow speeds. Filamentous biofilms (and to a lesser extent low-form gelatinous biofilms) were seen to move while under the influence of flow in the present study. This is an area that is in need of further research. Large amounts of information can quickly, accurately and repeatably be obtained with the digital methods now becoming available.

It is recommended that a greater range of biofouled surfaces should be measured to continue the study into the effects biofilms have on near wall flow. Biofilms with different properties should be investigated, including filamentous and low-form gelatinous growths, A greater range of species should be studied, as biofilm visco-elasticity and attachment and detachment processes would be different for each species, and are important for understanding control options. Further research into the behaviour of biofilms growing on either rough surface peaks or within valleys is also recommended to investigate the interaction of the boundary sublayer and roughness elements.

Further investigation into the friction characteristics of paints is recommended, along with cost-benefit analyses to determine the economic viability of relining conduits with various surface coatings. A greater range of painted surfaces should be studied as an extension of the clean smooth painted plate studies and the paint trials of the present

investigation. The identification of a cost-effective paint with low friction properties, also able to impede biofilm growth, would bring great benefits to hydraulic conduits prone to biofouling.

The temperature of the water in the water tunnel needs to be better controlled to maintain biofilm condition. A cooling system should be incorporated into the water tunnel return pipe to maintain water temperatures below 15°C.

The use of an automated probe traversing arrangement would considerably reduce the time spent taking the measurements. This would lessen the time spent by the biofilm in the water tunnel, increase probe placement accuracy, and increase the turn around time of results.

Improvements to the water tunnel working section lid arrangement, which incorporates the load cell for drag measurement, should be made, aimed at:

a) Reducing the time-consuming process of removing/changing test plates;
b) Allowing for more precise alignment of the test plates; and
c) Possible modifications to allow for the incorporation of high speed photography or video of the test plate surface while in the water tunnel.

The use of micro Acoustic Doppler Velocimetry, Laser Doppler Velocimetry or similar measurement techniques for velocity and turbulence measurements may be beneficial as Pitot probes are subject to fouling and hotfilm probes are subject to both fouling and damage when making near wall measurements of biofilms. Field measurements in open channels would also prove useful in validating water tunnel results.

The detailed investigation of a uniformly rough plate, both clean and fouled, is recommended, using both the water tunnel and photogrammetric techniques, to further refine the methods used to derive friction and roughness information. Measurements of a uniformly rough plate may assist in understanding and reducing experimental error.

Of particular interest would be the investigation of near wall velocity measurements coupled with concentrations of oxygen and nutrient levels. The interplay between the velocity boundary layer and concentration boundary layer could significantly affect biofilm growth and character.

References

Ackers, P. (1961). "The hydraulic resistance of drainage conduits." Proceedings of the Institute of Civil Engineers 19(July): 307-336.

Ackers, P., Crickmore, M. J. and Holmes, D. W. (1964). "Effects of use on the hydraulic resistance of drainage conduits." Proceedings of the Institute of Civil Engineers 28(July): 339-360.

Altchul, S. F., Madden, T. L., Schaffer, A. A., Zhang, J., Miller, W. and Lipman, D. J. (1997). "Gapped blast and Psi-blast: A new generation of protein database search programs." Nucleic Acids Research 25: 3389-3402.

Andrewartha, J. (2006). University of Tasmania, School of Engineering. Personal Communication to Andrew Barton. Hobart, Tasmania.

Andrewartha, J., Sargison, J., Barton, A. F., Denne, T. and Cribbin, N. (2006). Roughness issues in Hydro Tasmania water conveyance structures. Corrosion & Prevention 2006, "Steel & Concrete - Nothing Lasts Forever", Hotal Grand Chancellor, Hobart, Tasmania, Australia.

Antonia, R. A. and Luxton, R. E. (1971). "The response of a turbulent boundary layer to a step change in surface roughness part 1. Smooth to rough." ASME Journal of Fluid Mechanics. 48(4): 721-761.

Antonia, R. A. and Luxton, R. E. (1972). "The response of a turbulent boundary layer to a step change in surface roughness part 2: Rough to smooth." ASME Journal of Fluid Mechanics. 53(4): 737-757.

ASCE (1965). "Factors influencing flow in large conduits." Proceedings A.S.C.E., Report of the task force on flows in large conduits of the committee on hydraulic structures 91.(HY6 Nov.): 123-152.

Bae, Y.-S., Osborn, J. E. and Sprent, A. (2002). Unpublished report. Hobart, Australia., School of Geography and Environmental Studies, University of Tasmania.

Baier, R. E. (1980). Substrata influences on adhesion of microorganisms and their resultant new surface properties. Adsorption of microorganisms to surfaces. G. Bitton and K. C. Marshall. New York, John Wiley and Sons: 60-104.

Barmuta, L. (2005). University of Tasmania, School of Zoology. Personal Communication to Andrew Barton. Hobart, Tasmania.

Barton, A. (2004). Poatina Power Scheme - penstock cleaning and power conduit headloss estimation. Report No. 21/04. Reviewed by, J. Sargison, G. Walker, C. Ludlow and M. Wallis, University of Tasmania, Hobart.

Barton, A. and Sargison, J. (2003). Wilmot Power Station - penstock cleaning and power conduit headloss estimation. Report No. 17/03. Reviewed by, G. Walker and M. Wallis, University of Tasmania, Hobart.

Barton, A. and Sargison, J. (2004). Tarraleah Headworks - paint trials in Canal No. 1 and Pond No. 1. Report No. 20/04. Reviewed by, G. Walker and T. Denne, University of Tasmania, Hobart.

Barton, A. F. and Buia, A. (2005). Tarraleah Power Station - hilltop pipeline cleaning and headloss estimation. Report No. 18/03. Reviewed by, J. Sargison, G. Walker, C. Ludlow and M. Wallis, University of Tasmania, Hobart.

Barton, A. F., Sargison, J. E., Walker, G. J., Osborn, J. E. and Brandner, P. A. (2005). A baseline study of the effect of freshwater biofilms in hydraulic conduits. XXXI IAHR Congress, Seoul, Korea, Conference Proceedings. CD ROM.

Barton, A. F., Wallis, M., Sargison, J. E., Buia, A. and Walker, G. J. (2007). "Hydraulic roughness of biofouled pipes, biofilm character, and measured improvements from cleaning." ASCE Journal of Hydraulic Engineering (Accepted for publication).

Bendall, T. (2005). "Application of photogrammetric techniques to the mapping of biofouled surfaces. Bachelor of Geomatics (Honours) thesis." University of Tasmania, School of Geography and Environmental Studies. Hobart

Bendall, T. (2006). Research assistant. University of Tasmania, School of Geography and Environmental Studies. Personal Communication to Andrew Barton. Hobart, Tasmania.

Bland, C. E. G., Bayley, R. W. and Thomas, E. V. (1975). "Some observations on the accumulation of slime in drainage pipes and the effects of these accumulations on the resistance to flow." Public Health Engineering: 21-28.

Bradshaw, P. (1971). An introduction to turbulence and its measurement. Germany, Pergamon Press.

Bradshaw, P. and Pankhurst, R. C. (1964). "The design of low-speed wind tunnels." Prog. Aero. Sci. 5: 1.

Brandner, P. (2004). Manager cavitation tunnel, Australian Maritime College. Personal Communication to Andrew Barton. Hobart, Tasmania.

Brandner, P. A., Clarke, D. B. and Walker, G. J. (2004). Development of a fast response pressure probe for use in a cavitation tunnel. 15th Australasian Fluid Mechanics Conference, The University of Sydney, Sydney, Australia, 13-17 December, CD-ROM.

Brauer, H. (1963). "Stromungswiderstand riffelrauher rohre (flow resistance in pipes with rippled roughness)." Chemiker-Zig. / Chemische Apparatur 87(6): 199-208.

Brett, T. (1980). "Head-loss measurements on hydroelectric conduits." ASCE Journal of the Hydraulics Division. 106(1): 173-190.

Brown, J. C. (1903-1904). "Deposits in pipes and other channels conveying potable water." The Institution of Civil Engineers - Minutes of Proceedings CLVI(Part II): 1-17.

Buia, A. (2005). Univeristy of Tasmania, School of Agricultural Science. Personal Communication to Andrew Barton. Hobart, Tasmania.

Buia, A. (2006). "Draft PhD thesis: Microbiological aspects of biofouling in hydroelectric water conduit." University of Tasmania, School of Agricultural Science. Hobart, Tasmania, Australia

Callow, M. E. (1993). "A review of fouling in freshwaters." Biofouling 7: 313-327.

Candries, M. (2001). "Drag, boundary-layer and roughness characteristics of marine surfaces coated with antifoulings" Doctor of Philosophy. University of Newcastle-Upon-Tyne, Department of Marine Technology.

Candries, M. and Atlar, M. (2003). "On the drag and roughness characteristics of antifoulings." RINA Transactions - International Journal of Maritime Engineering(Part A2): 35-60.

Candries, M. and Atlar, M. (2005). "Experimental investigation of the turbulent boundary layer of surfaces coated with marine antifoulings." ASME Journal of Fluids Engineering 127: 219-232.

Carling, A. (1992). "The nature of the fluid boundary layer and the selection of parameters for benthic ecology." Freshwater Biology 28: 273-284.

Chamberlain, A. H. L. (1992). The role of adsorbed layers in bacterial adhesion. Biofilms science and technology. L. F. Melo, T. R. Bott, M. Fletcher and B. Capdeville. The Netherlands, Kluwer Academic Publishers.

Chanson, H. (2006). University of Queensland, School of Engineering. Personal Communication to Andrew Barton. Queensland, Australia.

Characklis, W. G. (1973). "Attached microbial growths - ii. Frictional resistance due to microbial slimes." Water Research 7: 124

Chenier, M. R., Beaumier, D., Roy, R., Driscoll, B. T., Lawrence, J. R. and Greer, C. W. (2003). "Impact of seasonal variations and nutrient inputs on nitrogen cycling and degradation of hexadecane by replicated river biofilms." Applied and Environmental Microbiology 65: 5170-5177.

Chezy, A. (1775). "Report unpublished." Ecole Nationale des Ponts et Chaussees.
Clauser, F. H. (1954). "Turbulent boundary layers in adverse pressure gradients." Journal of the Aeronautical Sciences 21(February): 91-108.

Cloeta, T. E., Westaard, D. and Vuuren, S. J. v. (2003). "Dynamic response of biofilm to pipe surface and fluid velocity." Water Science and Technology 47(5): 57-59.

Cochran, D. L. and Kline, S. J. (1958). Use of short flat vanes for producing efficient wide angle two dimensional subsonic diffusers. Technical note 4309. Washington, National Advisory Committe for Aeronautics: pp. 136.

Colebrook, C. F. (1939). "Turbulent flow in pipes, with particular reference to the transition between the smooth and rough pipe laws." Journal of Civil Engineers 11: 133-157.

Colebrook, C. F. and White, C. M. (1937). "Experiments with fluid-friction in roughened pipes." Proceedings of the Royal Society of London (A) 161: 367-381.

Colebrook, C. F. and White, C. M. (1937-38). "The reduction of carrying capacity of pipes with age." Intstitution of Civil Engineers 7: 99-118.

Colin, R. J., Churchill, P. F. and Roden, E. E. (2001). "Successional changes in bacterial assemblage structure during epilithic biofilm development." Ecology 82(2): 555-566.

Collis, D. C. and Williams, M. J. (1959). "Two-dimensional convection from heated wires at low reynolds numbers." Journal of Fluid Mechanics 6: 357-384.

Corrsin, S. and Kistler, A. L. (1954). "The free-stream boundaries of turbulent flows." NACA TN 3133.

Costerton, J. W., Lewandowski, Z., Caldwell, D. E., Korber, D. R. and Lappin-Scott, H. M. (1995). "Microbial biofilms and their role in the induction and inhibition of invertebrate settlement." Annual Review of Microbiology 49: 711-745.

Darcy, H. (1857). "Recherches experimentales relatives au mouvement de l'eau dans les tuyaux." Paris.

Davis, J. A. and Barmuta, L. A. (1989). "An ecologically useful classification of near bed flows in streams and rivers." Freshwater Biology 21: 271-282.

Denne, T. (2005). Principle asset engineer, Hydro Tasmania. Personal Communication to Andrew Barton. Hobart, Tasmania.

Druck Limited (2002). PTX/PMP 1400 industrial pressure sensors.

Flemming, H.-C., Wingender, J., Moritz, R., Borchard, W. and Mayer, C. (1999). Physico-chemical properties of biofilms - a short review. Biofilms in the aquatic environment. C. W. Keevil. Cambridge, Royal Society of Chemistry.

Gordon, N. D., McMahon, T. A., Finlayson, B. L., Gippel, C. J. and Nathan, R. J. (2004). Stream hydrology: An introduction for ecologists, 2nd edition. Chichester, England, John Wiley & Sons Ltd.

Granville, P. S. (1987). "Three indirect methods for the drag characterization of arbitrarily rough surfaces on flat plates." Journal of Ship Research 31(1): 70-77.

Grenness, M. J., Osborne, J. E. and Tyas, M. J. (2005). "Stereo-photogrammetric mapping of tooth replicas incorporating texture." Photogrammetric Record 20(110): 1-15.

Groenenboom, M. D. (2000). "Increase of frictional resistance in closed conduit systems fouled with biofilms." Master of Science. Montana State University. Bozeman

Hallegraeff, G. (2005). University of Tasmania, School of Plant Science. Personal Communication to Andrew Barton. Hobart, Tasmania.

Hama, F. R. (1954). "Boundary layer characteristics for rough and smooth surfaces." Transactions Society of Naval Architecture and Marine Engineering 62: 333-351.

Haslbeck, E. G. and Bohlander, G. (1992). Microbial biofilm effects on drag - lab and field. Proceedings 1992 S.N.A.M.E. Ship production symposium.

Holt, J. G., Krieg, N. R., Sneath, P. H. A., Staley, J. T. and Williams, S. T. (1994). Bergey's manual of determinative bacteriology. Baltimore, Williams and Wilkins.

Hydro Consulting (2000). Pre feasibility study - regular cleaning of the Fisher conduit system. Hobart, Hydro Tasmania.

Jones, D. F. (1999). "Controlling marine fouling with antifouling paints and underwater hull cleaning." Protective Coatings Europe: 24-27.

Kennedy, J. F. (1963). "The mechanics of dunes and antidunes in erodible-bed channels." Journal of Fluid Mechanics 16: 521-544.

Kim, W. J. and Patel, V. C. (1994). "Origin and decay of longitudinal vortices in developing flow in a curved rectangular duct." ASME Journal of Fluids Engineering 116: 45-52.

Klebanoff, P. S. (1955). Characteristics of turbulence in boundary layer with zero pressure gradient. Washington, DC, United States, National Bureau of Standards, National Advisory Committee for Aeronautics, Report 1247.

Kline, S. J., Moore, C. A. and Cochran, D. L. (1957). "Wide-angle diffusers of high performance and diffuser flow mechanisms." Journal of Aeronautical Science 24: 469.

Krogstad, P. A., Antonia, R. A. and Browne, L. W. B. (1992). "Comparison between rough and smooth wall turbulent boundary layers." Journal of Fluid Mechanics 245: 599-617.

Larsen, E. I., Sly, L. I. and McEwan, A. G. (1999). "Manganese(ii) adsorption and oxidation by whole cells and a membrane fraction of pedomicrobium sp. Acm 3067." Archives of Microbiology 171: 257-264.

Lau, Y. L. (1996). "Relative importance of mean velocity and bed shear on biofilm accumulation in open-channel flows." Water Science and Technology 32(8): 193-198.

Lee, T., Fisher, M. and Schwarz, W. H. (1993). "Investigation of the stable interaction of a passive compliant surface with a turbulent bundary layer." Journal of Fluid Mechanics 257: 373-401.

Lewandowski, Z. and Stoodley, P. (1995). "Flow induced vibrations, drag force, and pressure drop in conduits covered with biofilm." Water Science and Technology 32(8): 19-26.

Lewkowicz, A. K. and Das, D. K. (1985). "Turbulent boundary layers on rough surfaces with and without a pliable overlayer: A simulation of marine fouling." International Shipbuilding Progress, Marine Technology Monthly 32(December): 174-186.

Lewthwaite, J. C., Molland, A. F. and Thomas, K. W. (1985). "An investigation into the variation of ship skin frictional resistance with fouling." Transactions of the Royal Institute of Naval Archetects 127: 269-284.

Liehr, S. K., Suidan, M. T. and Eheart, J. W. (1989). "Effect of concentration boundary layer on carbon limited algal biofilms." Journal of Environmental Engineering 115(Part 1): 320-335.

Ligrani, P. K. a. M., R.J. (1986). "Structure of transitionally rough and fully rough turbulent boundary layers." Journal of Fluid Mechanics 162: 69-98.

Line, M. (2003). University of Tasmania, School of Agricultural Science. Personal Communication to Andrew Barton. Hobart, Tasmania, Australia.

Lopez, F. and Garcia, M. H. (2001). "Mean flow and turbulence structure of open channel flow through non-emergent vegetation." ASCE Journal of Hydraulic Engineering 127(5): 392-402.

Manning, R. (1889). "On the flow of water in open channels and pipes." Transactions of the Institution of Civil Engineers of Ireland: 161-207.

Masurat, P., Fru, E. C. and Pedersen, K. (2005). "Identification of meiothermus as the dominant genus in a storage system for spent nuclear fuel." Journal of Applied Microbiology 98: 727-740.

McEntree, W. (1915). "Variation of frictional resistance of ships with condition of wetted surface." Transactions of the Society of Naval Architects and Marine Engineers 23: 37-42.

McFie, H. (1956). Report - algae and moss in canals. Hobart, Tasmania, Hydro-Electric Commission.

McFie, H. (1973). Biological, chemical and related engineering problems in large storage lakes of Tasmania. Man-made lakes: Their problems and environmental effects. W. C. Ackermann, White, G.F. and Worthington, E.B. Washingston, D.C., American Geophysical Union. 17: 56-62.

McFie, H. (1976). Power storage lakes: Biological depositions and energy losses in Tasmania. 47th ANZAAS Congress, Hobart.

Mehta, R. D. (1977). "The aerodynamic design of blower tunnels with wide-angle diffusers." Progress in Aerospace Science 18: 59-120.

Mehta, R. D. and Bradshaw, P. (1979). "Design rules for small low speed wind tunnels." Aeronautical Journal: 443-449.

Milltronics (2001). The probe level monitor: Instruction manual pl-517, Siemens Milltronics Process Instruments Inc.

Minkus, A. J. (1954). "Deterioration of the hydraulic capacity of pipelines." New England Water Works Association LXVIII(1): 1-10.

Mitchell, H. L., Kniest, H. T. and Oh, W. J. (1999). "Digital photogrammetry and microscope photographs." Photogrammetric Record 16(94): 695-704.

Mokhtari, S. and Bradshaw, P. (1983). "Longitudinal vortices in wind tunnel wall boundary layers." Aeronautical Journal(June / July): 233-236.

Moody, L. F. (1944). "Friction factors for pipe flow." Transactions of the American Society of Mechanical Engineers 66: 671-684.

Morris, H. M. (1955). "Flow in rough conduits." Transactions of the American Society of Civil Engineers, Paper No. 2745 120: 373-398.

Nave, C. R. (2000). Methods for producing polarisation, [Online] HyperPhysics, Georgia State University, Accessed: September 2005, Available: http://hyperphysics.phy-astr.gsu.edu/hbase/phyopt/polar.html#c1.

Nikora, V. (2004). Hydrodynamic effects in aquatic ecosystems. 8th National conference on hydraulics in water engineering, ANA Hotal, Gold Coast, Australia, 13-16 July, The Institution of Engineers Australia.

Nikora, V. I., Goring, D. G. and Biggs, B. J. F. (2002). "Some observation of the effects of micro-organims growing on the bed of an open channel on the turbulence properties." Journal of Fluid Mechanics 450: 317-341.

Nikuradse, J. (1933a). Laws of flow in rough pipes. Washington, National Advisory Committee for Aeronautics. Technical Memorandum 1292.

Nikuradse, J. (1933b). "Stromungsgesetze in rauhen rohren." Ver. Dtsch. Ing. Forschungsheft 361.

On-Solution (2004). Etemperature logger.

Osborn, J. E. (2003). University of Tasmania, School of Geography and Envrironmental Studies. Personal Communication to Andrew Barton. Hobart, Tasmania, Australia.

Osborn, J. E. (2006). University of Tasmania, School of Geography and Envrironmental Studies. Personal Communication to Andrew Barton. Hobart, Tasmania, Australia.

Osborn, J. E., Bae, Y.-S., Grenness, M. J., Sargison, J. E., Barton, A. F., Sprent, A. S., Walker, G. J. and Bendall, T. (2005). Mapping surface biofilms to improve the efficiency of water conveyance. Spatial Sciences Congress, Melbourne, Spatial Sciences Institute of Australia, September 2005. CD ROM.

Panametrics (2001). Transport pt868 flowmeter: Options and specifications.

Patel, V. C. (1965). "Calibration of the preston tube and limitations on its use in pressure gradients." Journal of Fluid Mechanics 23(Part 1): 185-208.

Perkins, J. A. and Gardiner, I. M. (1985). "The hydraulic roughness of slimed sewers." Intstitution of Civil Engineers 79: 87-104.

Perkins, K. (2005). "Bachelor of Science (Honours) thesis. Part A: Literature review - the adhesion of fouling diatoms: Function, structure and physiology. Part B: Experimental thesis - the ecophysiology of the fouling diatom, gomphonema, from the central Tasmanian hydro canals: The role of temperature, light and nutrients." University of Tasmania, School of Plant Science. Hobart.

Perkins, K. (2006). University of Tasmania, School of Plant Science. Personal communication to Andrew Barton. Hobart, Tasmania, Australia.

Perkins, K. and Hallegraeff, G. (2006). University of Tasmania, School of Plant Science. Personal communication to Andrew Barton. Hobart, Tasmania, Australia.

Perry, A. E. and Joubert, P. N. (1963). "Rough-wall turbulent boundary layers." Journal of Fluid Mechanics 37: 383-413.

Perry, A. E., Schofield, W. H. and Joubert, P. N. (1969). "Rough wall turbulent boundary layers." Journal of Fluid Mechanics 37(Part 2): 383-413.

Picologlou, B. F., Zelver, N. and Charaklis, W. G. (1980). "Biofilm growth and hydraulic performance." ASCE Journal of the Hydraulics Division HY5: 733-747.

Pollard, A. L. and House, H. E. (1959). "An unusual deposit in a hydraulic tunnel." ASCE Journal of the Power Division December: 163-171.

Richardson, E. V. and McQuivey, R. S. (1968). "Measurement of turbulence in water." ASCE Journal of the Hydraulics Division 94(HY2): 411-430.

Rickard, A. H., Leach, A. S., Hall, L. S., Buswell, C. M., High, N. J. and Handley, P. S. (2002). "Phylogenetic relationships and coaggregation ability of freshwater biofilm bacteria." Applied and Environmental Microbiology 68: 3644-3650.

Rouse, H. (1965). "Critical analysis of open channel resistance." Proceedings A.S.C.E. 91(HY4 July): 1-25.

Sargison, J. (2004). University of Tasmania, School of Engineering. Personal Communication to Andrew Barton. Hobart, Tasmania, Australia.

Sargison, J. E., Walker G.J., Rossi, R. (2004). Design and calibration of a wind tunnel with a two dimensional contraction. 15th Australasian Fluid Mechanics Conference, University of Sydney, Sydney.

Schlichting, H. (1979). Boundary layer theory, McGraw-Hill.

Schultz, M. P. (1998). "The effect of biofilms on turbulent boundary layer structure, phd thesis." Doctor of Philosophy. Florida Institute of Technology, Department of Ocean Engineering. Melbourne

Schultz, M. P. (2000). "Turbulent boundary layers on surfaces covered with filamentous algae." Journal of Fluids Engineering 122: 357-363.

Schultz, M. P. (2004). "Frictional resistance of antifouling coating systems." ASME Journal of Fluids Engineering 126: 1039-1047.

Schultz, M. P. and Swain, G. W. (2000). "The influence of biofilms on skin friction drag." Biofouling 15(1-3): 129-139.

Schultz, M. P., Swain, G.W. (1999). "The effect of biofilms on turbulent boundary layers." ASME Journal of Fluids Engineering 121: 44-51.

Stanborough, J. (2003). "Mapping algal accumulation and sandpaper using close-range photogrammetry. Undergraduate studio project." University of Tasmania, School of Geography and Environmental Studies. Hobart

Stoodley, P., Boyle, J., Cunningham, A. B., Dodds, I., Lappin-Scott, H. M. and Lewandowski, Z. (1999a). Biofilm structure and influence on biofouling under laminar and turbulent flows. Biofilms in the aquatic environment. C. W. Keevil. Cambridge, Royal Society of Chemistry.

Stoodley, P., Dodds, I., Boyle, J. D. and Lappin-Scott, H. M. (1999b). "Influence of hydrodynamics and nutrients on biofilm structure." Journal of Applied Microbiology 85: 19S-28S.

Stoodley, P., Lewandowski, Z., Boyle, J. D. and Lapin-Scott, H. M. (1988). "Oscillation characteristics of biofilm streamers in turbulent flowing water as related to drag and pressure drop." Biotechnology and Bioengineering 57(5): 536-544.

Stoodley, P., Lewandowski, Z., Boyle, J. D. and Lappin-Scott, H. M. (1999c). "Structural deformation of bacterial biofilms caused by short term fluctuations in fluid shear: An in situ investigation of biofilm rheology." Biotechnology and Bioengineering 65(1): 83-92.

Stoodley, P., Wilson, S., Cargo, R., Piscitteli, C. and Rupp, C. (2001). "Detachment and other dynamic processes in bacterial biofilms." Surfaces in Biomaterials Foundation: 189-190.

Streeter, V. L. and Wylie, E. B. (1986). Fluid mechanics, first si metric edition. Singapore, McGraw-Hill.

Towler, B. W. (2004). "Modeling the non-linear response of mixed culture biofilm structures to turbulent flow - doctor of philosophy thesis." Montana State University. Bozeman

Townsin, R. L. (2003). "The ship hull fouling penalty." Biofouling 19(Supplement): 9-15.

Tyler, P. A. (1967). "Microbiological deposition of manganese in freshwater distribution systems." Doctor of Philosophy. University of Tasmania, Faculty of Agricultural Science. Hobart

U.S. Bureau of Reclamation (1965). Friction factors for large conduits flowing full, engineering monograph no. 7, U.S. Govt. Printing Office.

Walker, G. (2004). University of Tasmania, School of Engineering. Personal Communication to Andrew Barton. Hobart, Tasmania, Australia.

White, F. M. (2006). Viscous fluid flow, 3rd edition. New York, McGraw Hill.

Whitehouse, D. (2002). Surfaces and their measurement. London, Hermes Penton Science.

Winter, K. G. (1977). "An outline of the techniques available for the measurement of skin friction in turbulent boundary layers." Prog. Aerospace Sci. 18: 1-57, Pergamon Press. Printed in Great Britain.

Wolf, P. R. and Dewitt, A. (2000). Elements of photogrammetry with applications in gis, 3rd edition, McGraw-Hill.

Yen, B. C. (2002). "Open cannel flow resistance - Hunter Rouse award lecture." ASCE Journal of Hydraulic Engineering 128(1): 20-39.

Young, W. J. (1992). "Clarification of the criteria used to identify near-bed flow regimes." Freshwater Biology 28: 383-391.

Zelver, N. (1979). "Biofilm development and associated energy losses in water conduits." Master of Science. Rice University. Houston, Texas

Zhang, H., Sekiguchi, Y., Hugenholtz, S., Kim, H., Kamagata, Y. and Nakamura, K. (2003). "Gemmatimonas aurantica gen. Nov., sp. Nov., a gram-negative, aerobic, polyphosphate-accumulating micro-organism, the first cultured representative of the new bacterial phylum gemmatimonadetes phyl. Nov." International Journal of Systematic and Evolutionary Microbiology 53: 1155-1163.